



HAL
open science

An in situ kinetic investigation of the selective dissolution mechanism of Cu alloys

Peng Zhou

► **To cite this version:**

Peng Zhou. An in situ kinetic investigation of the selective dissolution mechanism of Cu alloys. Chemical Physics [physics.chem-ph]. Université Pierre et Marie Curie - Paris VI, 2017. English. NNT : 2017PA066251 . tel-01691570

HAL Id: tel-01691570

<https://theses.hal.science/tel-01691570>

Submitted on 24 Jan 2018

HAL is a multi-disciplinary open access archive for the deposit and dissemination of scientific research documents, whether they are published or not. The documents may come from teaching and research institutions in France or abroad, or from public or private research centers.

L'archive ouverte pluridisciplinaire **HAL**, est destinée au dépôt et à la diffusion de documents scientifiques de niveau recherche, publiés ou non, émanant des établissements d'enseignement et de recherche français ou étrangers, des laboratoires publics ou privés.

Université Pierre et Marie Curie

L'École doctorale de Chimie Physique et de Chimie Analytique de Paris Centre

Equipe Electrochimie, Interfaces et Energie-Institut de Recherche de Chimie Paris

An *in situ* kinetic investigation of the selective dissolution mechanism of Cu alloys

Par Peng ZHOU

Thèse de doctorat de [Chimie physique et chimie analytique]

Dirigée par Kevin Ogle

Présentée et soutenue publiquement le [13 octobre 2017]

Devant un jury composé de :

[Noms, Prénoms, fonctions (ex : Maître de conférences) et rôle (ex : Rapporteur) des
membres du jury]

Ogle, Kevin	Professeur à ChimieParistech	Directeur de thèse
Ryan, Mary	Professeur à Imperial College London	Rapporteur
Rohwerder, Michael	Directeur de recherche à Max-Planck-Institut	Rapporteur
Vivier, Vincent	Directeur de recherche à l'UPMC	Examinateur

Acknowledgements

Time passes quickly when you are absorbed in something whether it is meaningful or meaningless. I am lucky in that I have reaped a meaningful experience in terms of science and life, rather than idle away the past three years. On October 2nd 2014, I first set my foot in France. As a young man who had never been abroad before, living in a strange country itself is a challenge, not to mention a country that has French as the official language. Besides the language barrier and cultural barrier, the most challenging difficulty came from my Ph. D. project: as a graduate student majoring at Materials Science, I had minimal knowledge of electrochemistry. The first few months after my arrival in France were devoted to the self-study of electrochemistry, as well as my struggling against maladaptation to new life. *No pain, no gain*. During the last three years, I enjoyed the pleasure of publishing my first article in an international journal; I managed to conquer my nervousness during my first talk at an international conference; I benefited a lot from the discussion with my advisor, coworkers, and visitors from outside the group. Now my Ph. D. work has come to an end, and I am ready to defend my work. But before that, I'd like to express my gratitude to people who helped me directly or indirectly in finishing my project.

First, I want to express my gratitude to my thesis advisor, Prof. Kevin Ogle. Without his invitation, I could never have won the scholarship from the Chinese government. The door to Prof. Ogle's office was always open whenever I ran into a trouble spot or had a question about my research or writing. He consistently allowed the research to be my own work, but steered me in the right direction whenever he thought I needed it. His immense knowledge, patience and motivation are indispensable in helping me finish my thesis. His professional dedication to electrochemistry and corrosion science, especially during and after the recovery period of a major operation, mobilized me to rise to severe challenges.

I would also like to acknowledge the China Scholarship Council (CSC) for the 36-month financial support to my Ph.D. project. I hereby pay my respect to my country and wish my country a prosperous future.

I would also like to thank Dr. Johann Wilhelm Erning from German Federal Institute for Materials Research and Testing (Bundesanstalt für Materialforschung und –prüfung, BAM). I could never have finished my thesis without his constructive advice, passionate participation and fruitful discussion.

My sincere thanks also go to Professor John R. Scully from University of Virginia. My one-month experience as a visiting scholar in Center for Electrochemical Science and Engineering (CESE) was short but precious. Special thanks go to Mr. Michael John Hutchison for cordially orientating me into local community. Also, I'd like to thank Leslie, Chao, Marilyn, Rebecca, Fu and other friends in CESE for a beautiful life in Charlottesville. The collaborative project between the two Labs broadened my eyesight into the corrosion field and enriched my experience in international collaboration.

I am also gratefully indebted to the whole research group of the *Equipe Interfaces, Electrochimie et Energie* (I2E). My sincere thanks go to Michel Cassir, the director of our group, and to Armelle Ringuede, Virginie Lair, and Valerie Albin, who helped me a lot for my orientation after my first arrival in Paris. I would thank Elisabeth Brochet, Marjorie Sadaoui-Eudier and Soobrayen Koonavadee for their help with administrative work and their patience with my poor French. Special thanks go to Junsoo Han, who helped me with many important things that were beyond my capability, and to Slava, Deborah, Alina, Nour, Thomas, who shared such a narrow office with me. My gratitude also goes to Ouma ñna, Arturo, and other members in our group, both of whom helped me with manipulating the machine, arranging instruments in good order.

Further, I must express my very profound gratitude to my parents, and sister for providing me with unfailing support and continuous encouragement throughout my years of study and through the process of researching and writing this thesis. I am greatly indebted to my wife, who not only encouraged me to pursue my goal three years ago, but encouraged me again to take a one-year postdoc. This accomplishment would not have been possible without them.

Finally, please allow me to express my sincere gratitude to my thesis referees: Mary Ryan and Michael Rohwerder, and to the whole jury members. Their helpful and enlightening advice significantly improved the quality of my thesis.

Nomenclature

A	reaction area of the sample (cm^2)
f	flow rate (mL s^{-1})
i_{ap}	applied current during anodization experiment (nA cm^{-2})
E	potential (V vs. SCE)
t	time (s)
F	Faradaic constant ($= 96500 \text{ C mol}^{-1}$)
τ	empirical parameter for log-normal fit (s)
β	empirical parameter for log-normal fit (no unit)
v_e	applied current expressed as transfer rate of electrons ($\text{nmol s}^{-1} \text{ cm}^{-2}$)
v_e^*	v_e convoluted ($\text{nmol s}^{-1} \text{ cm}^{-2}$)
n	stoichiometry factor of Cu (no unit)
$v_{\text{Zn(aq)}}$	dissolution rate of soluble Zn species in STW ($\text{nmol s}^{-1} \text{ cm}^{-2}$)
$v_{\text{Cu(aq)}}$	dissolution rate of soluble Cu species in STW ($\text{nmol s}^{-1} \text{ cm}^{-2}$)
v_{Σ}	sum of dissolution rate of soluble Cu and Zn in STW ($\text{nmol s}^{-1} \text{ cm}^{-2}$)
$Q_e(pstat)$	the quantity of electricity obtained by integrating the current transient (nmol cm^{-2})
$Q_e(ICP)$	the quantity of electricity obtained by calculating the electrochemical reaction assuming a known reaction factor (nmol cm^{-2})
$n_{m, aq}$	stoichiometry factor of aqueous species for Cu, Zn or Si (no unit)
$n_{m, s}$	stoichiometry factor of solid species for Cu, Zn or Si (no unit)
$Q_{m, an}$	the quantity of elemental dissolution of a metal, m (Cu, Zn and Si), contributed to either aqueous species (aq) or solid species (s) (nmol cm^{-2})
$Q_m(STW) (i_{ap} = 0)$	total quantity of elemental dissolution in STW during open circuit (nmol cm^{-2})
$Q_m(CBS) (i_{ap} = 0)$	total quantity of elemental dissolution in CBS during open circuit (nmol cm^{-2})
$Q_m(STW)$	total quantity of elemental dissolution in STW during anodization (nmol cm^{-2}).
$Q_m(CBS)$	total quantity of elemental dissolution in CBS during anodization (nmol cm^{-2}).
δ_{Cu}	thickness of dezincified layer (nm)
δ_{Cu_2O}	thickness of oxide layer (nm)
M_{Cu}	atomic weight of Cu (g mol^{-1})
ρ_{Cu}	density of Cu (8.90 g cm^{-3})
M_{Cu_2O}	atomic weight of Cu_2O (g mol^{-1})
ρ_{Cu_2O}	density of Cu_2O (6.04 g cm^{-3})
K	the molar ratio of Cu / Zn in the bulk
K'	the molar ratio of total oxidized Cu/Zn in tap water
$\sum v_{m(aq)}$	the sum of elemental dissolution rates, such as $v_{Cu(aq)}(STW)$, $v_{Zn(aq)}(STW)$ and $v_{Si(aq)}(STW)$ ($\text{nmol s}^{-1} \text{ cm}^{-2}$)
Z	dezincification factor.
$v_{Cu(aq)}$	dissolution rate of Cu into aqueous species ($\text{nmol s}^{-1} \text{ cm}^{-2}$)
v_{corr}	open circuit dissolution rate of Cu ($\text{nmol s}^{-1} \text{ cm}^{-2}$)
v_{Cu_2O}	growth rate of residual oxide film on alloy surface ($\text{nmol s}^{-1} \text{ cm}^{-2}$)
v_{Cu}	growth rate of dezincified layer on alloy surface ($\text{nmol s}^{-1} \text{ cm}^{-2}$)

List of acronyms

AESEC	atomic emission spectroelectrochemistry
ICP-AES	inductively coupled plasma-atomic emission spectroscopy
LOD	limit of detection for a specific element ($\mu\text{g mL}^{-1}$)
STW	synthetic tap water
CBS	citrate buffer solution
SPS	synthetic perspiration solution
GIXRD	grazing incidence X-Ray diffraction
OCP	open circuit potential
SCE	saturated calomel electrode

Contents

Acknowledgements	1
Nomenclature	3
List of acronyms	4
Contents	5
Résumé de la thèse	8
1.1 Origine et objective de cette thèse	8
1.2 Les résumé et la structure de la thèse de doctorat	10
A. Introductory Section	18
Introduction	19
1.1 Origin and objective of this Ph. D work	19
1.2 Summary and structure of the dissertation	21
1.3 List of publications	24
2. The corrosion of Cu based alloys	26
2.1 The corrosion of copper	26
Cathodic Reactions on Cu	27
Anodic corrosion of copper	28
2.2 The corrosion of Cu-Zn alloys: dezincification	29
Dezincification structure	31
Dezincification mechanism	31
2.3. The corrosion of Cu-Sn alloys: its antimicrobial efficacy.	38
2.3.1 Antimicrobial efficacy of copper	38
2.3.2 The use of Cu alloys as antimicrobial material	39
2.4 Summary	40
B. Experimental Section	42
3. Materials and experiments	43
3.1 Materials	43
3.2 Atomic emission spectroelectrochemistry (AESEC)	45
3.2.1 Electrochemical flow cell	46
3.2.2 Inductively coupled plasma-atomic emission spectroscopy (ICP-AES)	47
3.2.3 Fast electronics	48
3.2.4 Data treatment	49
3.3 Corrosion product identification and morphology characterization	51
C. Results Section	53
4. The anodic dissolution of copper alloys in synthetic tap water: Pure copper	54
4.1. Introduction	54
4.2. Experimental	55
4.2.1 Materials	55
4.2.2 Instrumentation	56
4.2.3 Data Analysis	57
4.3. Results	58
4.3.1 Mass and charge balance in acid electrolytes	58
4.3.2 The STW – CBS Dissolution Experiment	60
4.3.3 Mass and Charge Balance for Anodic Dissolution of Cu in STW	64
4.3.4 Kinetic analysis	68

4. 4. Conclusion	69
5. An in situ kinetic study of brass dezincification and corrosion	70
5.1. Introduction	70
5.2. Experimental.....	72
5.2.1 Materials	72
5.2.2. Dezincification test.....	73
5.2.3. Instrumentation	73
5.2.4. Electrochemical experiments and data analysis.....	74
5.3. Results	74
5.3.1. Dezincification test result.	74
5.3.2. Elemental dissolution behavior in synthetic tap water (STW)	75
5.3.3. Analysis of insoluble corrosion products	80
5.3.4. Characterization of residual oxides	82
5.3.5. Surface morphology	84
5.3.6. Mass and Charge Balance	86
5.3.7. Growth of the dezincification and the oxide layers	88
5.4. Kinetic analysis and Discussion	90
5.5. Conclusions	94
6. The dissolution of Cu-Zn alloys in synthetic tap water: effect of Zn content on the elemental release, scale formation and dissolution mechanism.....	96
6.1 Introduction	96
6.2 Experimental.....	97
6.3 Results	99
6.3.1 Potentiodynamic polarization of Cu-Zn alloys.....	99
6.3.2 Galvanostatic dissolution behavior of Cu-Zn alloys in tap water.....	105
6.3.3 Validation of the fate of elements by the mass/charge balance calculation	110
6.3.4 Effect of current on the formation of Cu^{2+} , Cu_2O and Zn^{2+}	112
6.3.5 Effect of Zn content on dissolution behavior	114
6.4 Discussion	116
6.4.1 Summary of findings.....	116
6.4.2. Dezincification mechanism	119
6.5 Conclusions	122
7. Effect of alloying elements on the electrochemical Cu release from Cu-Sn alloys to artificial perspiration solution	124
7.1 Introduction	124
7.2 Materials and experiments	125
7.3 Results.....	127
7.3.1 Synthetic perspiration solution-citrate buffer solution experiment (SPS-CBS)....	127
7.3.2. Characterization of solid species	133
7.3.3. Mass/charge balance calculation.....	135
7.3.4 Potentiodynamic polarization experiments	136
7.4 Discussion	137
7.5 Conclusions	139
D. Concluding remarks.....	141
8. Conclusions and perspectives.....	142
8.1 Conclusions	142
8.2 Perspectives	146
Appendix A: ISO-6509 dezincification test of Cu-Zn alloys.	148
Appendix B: Investigation into the dissolution mechanism of Cu-Zn alloys in deaerated citrate buffer solution.	152

Appendix C: Curriculum vitae of the author163
Bibliography.....166

Résumé de la thèse

1.1 Origine et objective de cette thèse

Le cuivre, en tant qu'un premier métal utilisé par l'homme [1], joue un rôle essentiel dans la civilisation des êtres humains. Son utilisation remonte à la préhistoire avec la découverte de nombreux objets de cuivre et de bronze [2]. C'était le début de l'ère du cuivre. Les progrès techniques et la demande croissante de matériaux ont conduit à l'émergence du premier alliage d'aluminium artificiel, qui a également ouvert une nouvelle ère : l'âge du bronze. Bronze est un alliage Cu-Sn qui a été fabriqué en armes, pièces de monnaie, articles ménagers, ornements ainsi que des ustensiles rituels, en raison de ses excellentes propriétés mécaniques et de sa couleur agréable [3]. Son utilisation dure depuis les premiers outils de l'âge du bronze jusqu'aux applications industrielles modernes. Des milliers d'années plus tard, les cuivres ont été utilisés à grande échelle [4]. Laiton est un alliage Cu-Zn, sa première émergence remonte au 5^{ème} millénaire en Colombie-Britannique. Cet alliage a été largement utilisé en Asie de l'Est et en Asie centrale au 2^{ème} et 3^{ème} siècle av. J.-C. [5]. L'utilisation du laiton est plus tard que du bronze. Cela a été attribué à la difficulté à fondre Zn en Cu en considérant la grande différence de température de fusion entre Zn et Cu. Cependant, l'utilisation de l'alliages Cu-Zn est aussi populaire que l'alliages Cu-Sn aux jours moderne.

Maintenant, la consommation mondiale d'alliages du cuivre dépasse 18 millions de tonnes par an [6]. Parmi eux, environ 47% sont consommés par l'industrie de la construction, 23% par l'électronique, 10% par transport, 11% et 9% par les produits de consommation et les machines industrielles [7]. Indépendamment de leur utilisation, la corrosion est un problème commun qui soulève des inquiétudes : la corrosion des alliages de Cu peut entraîner une catastrophe à cause de la rupture des composants de contrainte en alliages de Cu [8], une fuite inattendue des tubes de Cu [9] ainsi qu'une défaillance des composants électroniques [10]. Une étude menée par les États-Unis en 2002 a déclaré que le coût direct en raison de la corrosion ou à la prévention de la corrosion est de 267 milliards de dollars [11], cela représente une proportion considérable du produit intérieur brut (PIB) des États-Unis. Ainsi, l'étude sur le mécanisme de corrosion des alliages de Cu ne permet pas seulement une utilisation plus efficace de ceux-ci, mais aussi contribue au développement économique.

Les alliages Cu-Zn, lesquels sont également connus sous le nom de laiton, sont les alliages à base de cuivre les plus représentatifs de l'industrie moderne. L'addition de Zn dans Cu conduit à une amélioration significative des propriétés mécaniques des alliages de Cu. Cependant, Zn est plus électro-négatif que Cu, cela conduit à une lixiviation sélective de Zn à partir d'alliages Cu-Zn, c'est-à-dire la dézincification. La dézincification est le problème le plus gênant qui entrave l'utilisation du laiton dans la tuyauterie pour l'eau potable, l'ingénierie d'échange de chaleur et l'ingénierie maritime. Au cours des dernières décennies, de nombreuses recherches ont porté sur l'explication mécaniste de la dézincification et son inhibition. Deux théories majeures, la dissolution préférentielle [12,13] et la dissolution-redéposition [14,15] ont été largement favorisées par différents chercheurs. Cependant, un consensus n'est pas encore à faire, parce qu'il existe des complexités de la structure de la couche de dézincification, et en plus les conditions expérimentales ne sont pas uniformes. Dans ces conditions, ses données sont moins comparables, donc ils conduisent à diverses conclusions. Surtout dans le cas de la dissolution de l'eau du robinet, un environnement neutre conduit à la formation de l'échelle d'oxyde, à la libération des cations et à la formation simultanée d'une couche riche en Cu à forte teneur en Zn qui complique le processus de corrosion. Nombreuses littératures précédentes portaient sur l'interprétation du mécanisme, la caractérisation des produits de corrosion et la structure de la dézincification. Par contre, qu'il y a peu d'attention particulière qui a été accordée à la réaction élémentaire à l'interface et à la relation quantitative (stoechiométrie) de la dissolution et de la formation du film. Ce sont d'une importance cruciale dans l'explication du processus de corrosion.

Les alliages Cu-Sn sont une famille d'alliage largement utilisée dans la société moderne. Contrairement aux alliages Cu-Zn, qui ont une courte histoire d'application depuis l'époque médiévale, les alliages Cu-Sn ont une longue histoire d'utilisation à grande échelle qui remonte à 4500 av. J.-C.. Il y a deux raisons pour cela : a) les alliages de Cu-Sn étaient plus faciles d'obtenir dans les temps anciens, et b) ils montrent généralement une bonne performance de corrosion sous l'atmosphère en raison de la passivité de Sn [16]. Malgré que la corrosion soit inévitable, pour la raison des esthétiquement agréables verdoyantes patines formées après d'une longue exposition atmosphérique, elle est irremplaçable dans les constructions architecturales et artistiques. Cependant, l'étude de la corrosion du bronze est largement limitée à la corrosion atmosphérique du bronze, appliqué à la restauration et à la conservation des antiquités en bronze excavées. L'utilisation moderne du bronze nécessite plus de connaissances sur la corrosion du bronze. Par exemple, la capacité des ions Cu à tuer les bactéries et les superbactéries permet aux alliages de Cu comme matériaux biologiques. Le bronze est ainsi

largement utilisé dans des environnements qui ont un accès facile aux bactéries, comme les hôpitaux et les entreprises biologiques. Cette utilisation spéciale nécessite le bronze ayant un équilibre entre une libération facile de Cu à l'environnement ambiant et la résistance à la corrosion, ce qui est négligé et le manque de littérature.

Dans ce travail, le mécanisme de dissolution des alliages de Cu, de Cu-Zn dans l'eau de robinet synthétique (STW) et les alliages de Cu-Sn dans la solution synthétique de transpiration ont été étudiés respectivement en utilisant la spectroélectrochimie à émission atomique (AESEC). Une expérience qui s'appelle STW-CBS et une expérience qui s'appelle SPS-CBS ont été utilisées dans l'étude des alliages Cu-Zn et Cu-Sn. Ces expériences permettent quantifier des espèces solubles et des espèces solides. Divers alliages Cu-Zn avec une composition différente ont été utilisés pour identifier le comportement de dissolution de différentes phases et divers alliages Cu-Sn contenant Sn différent ont été utilisés pour explorer l'effet de la teneur en Sn de la libération de Cu. La relation quantitative de la libération des cations, de la formation d'échelle et de l'évolution de la structure de surface sur une échelle du temps, du courant électrique appliqué et de la composition des alliages peut être obtenue par AESEC.

Cette dissertation vise à aborder les points suivants :

1. Comprendre le mécanisme de dissolution du cuivre pur et des alliages Cu-Zn dans l'eau du robinet : libération d'ions, formation d'échelle ainsi que la croissance de la couche de Cu pure appauvrie Zn;
2. Distinguer la différence dans le comportement de dissolution de la phase α et de la phase β dans les alliages Cu-Zn respectivement; Identifier l'effet du contenu Zn sur la dissolution;
3. Identifier l'effet de la teneur en Sn à libérer l'ions Cu dans les alliages Cu-Sn : la formation d'échelle et le mécanisme de dissolution;

1.2 Les résumés et la structure de la thèse de doctorat

Cette thèse se compose de quatre parties principales: **Section d'introduction (A)**, **Section expérimentale (B)**, **section de résultats (C)** et **Conclusions(D)**.

La section d'introduction (**partie A**) se compose de deux chapitres: **chapitre 1** et **chapitre 2**. Le **chapitre 1** donne le contexte du travail pendant la thèse et les points techniques à traiter. Le **chapitre 2** donne une revue de la littérature générale concernant la corrosion de l'alliage Cu-Zn et la fonction antimicrobienne des alliages Cu-Sn.

Au **chapitre 2**, la réaction anodique et la réaction cathodique de Cu en solution aqueuse ont été présentées; la formation de Cu_2O pensait qu'un mécanisme à un électron ou un mécanisme à deux électrons a été élaboré. Deux types différents de mécanismes de la

d'azincification ont été présentés : a) mécanisme de dissolution-redéposition et b) dissolution préférentielle. Le mécanisme de dissolution-redéposition représente une dissolution simultanée de Cu et Zn et une redéposition subséquent de Cu à la surface. Le mécanisme de dissolution préférentielle représente une réaction électrochimique impliquant seulement Zn, elle se compose de trois sous-mécanismes: diffusion de surface, diffusion de volume et percolation. La fonction antimicrobienne des alliages Cu-Sn a été introduite en termes de la fonction jouée par les ions Cu dans l'élimination/inactivation des bactéries/superbactéries, et l'importance d'améliorer la libération d'ion Cu en analysant l'effet des additions d'alliage.

La section expérimentale (**Partie B**) comprend le **chapitre 3**. Dans ce chapitre, les matériaux utilisés dans ce travail de Ph. D., et leur composition, méthode de prétraitement ont été élaborés. La spectroélectrochimie d'émission atomique (AESEC) a été introduite en fonction de son principal fonctionnement et de sa structure schématisée.

La section Résultats se compose de trois chapitres: **le chapitre 4** (dissolution anodique de Cu pur), **chapitre 5** (comportement de dissolution de deux alliages commerciaux), **chapitre 6** (effet du contenu de Zn sur le comportement de dissolution), **le chapitre 7** (effet du contenu de Sn sur la libération d'ions Cu d'alliages Cu-Sn) et **le chapitre 8** (comportement de dissolution des alliages Cu-Zn dans la solution tampon citrate).

Du **chapitre 4** au **chapitre 6**, la dissolution anodique du cuivre pur, des alliages Cu-Zn avec les compositions différentes ont été étudiés dans de l'eau du robinet synthétique naturellement aérée (STW) par spectroélectrochimie d'émission atomique in situ (AESEC). Le schéma de l'expérience STW-CBS est démontré à la Figure 1. L'expérience consiste en quatre étapes : a) une dissolution en circuit ouvert d'alliages de Cu dans STW a été appliquée; B) une dissolution galvanostatique à courant varié a été appliquée pour accélérer la dissolution élémentaire; C) une autre dissolution en circuit ouvert a été mise en œuvre; D) l'électrolyte a été remplacé par un CBS désaéré pour dissoudre les espèces solides formées lors que la polarisation est anodique. Cette technique mesure directement le taux de la dissolution de Cu et la formation de l'échelle de Cu indirectement par l'équilibre de masse entre le courant anodique et le taux de dissolution.

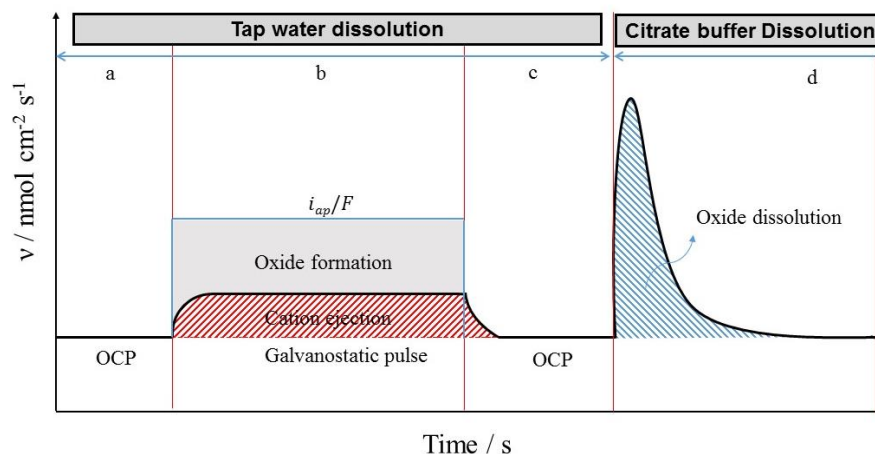


Figure 1. Schéma de l'expérience STW-CBS: a) dissolution du circuit ouvert en STW pendant 5 min; B) impulsion galvanostatique en STW pendant 20 min; C) circuit ouvert en STW pendant 5 min; D) dissolution en circuit ouvert d'oxyde dans CBS pendant 25 min.

Le chapitre 4 présente l'étude du mécanisme de dissolution du cuivre pur dans l'eau du robinet. Les conditions étudiées ont été effectuées dans les deux conditions spécifiques à discuter l'effet du temps et du courant appliqué: l'une étudie l'effet du temps et du courant appliqué (0 à $80 \mu\text{A cm}^{-2}$) pendant 20 min, et l'autre étudie l'effet du courant appliqué (0 à $40 \mu\text{A cm}^{-2}$) pendant 0 à 20 min. L'échelle d'oxyde formée lors de l'exposition à STW, a été dissoute dans une solution tampon de citrate déshydraté (CBS) et suivie par AESEC in situ. Un bilan de masse/charge a confirmé la prédiction que la plupart des espèces de Cu (II) sont solubles et sont libérées dans STW, en laissant derrière elles un film de Cu_2O comme produit insoluble à la surface. La spectroscopie Raman *ex situ* et l'analyse de la diffraction par des rayons X (GIXRD) corroborent cette conclusion. Une analyse quantitative des espèces Cu (I) et Cu (II) par rapport au courant appliqué et en fonction du temps pendant une impulsion galvanostatique est présentée. Une analyse cinétique suggère que le mécanisme de dissolution implique une dissolution simultanée de Cu et une formation de film plutôt qu'un mécanisme séquentiel (voir Figure 2).

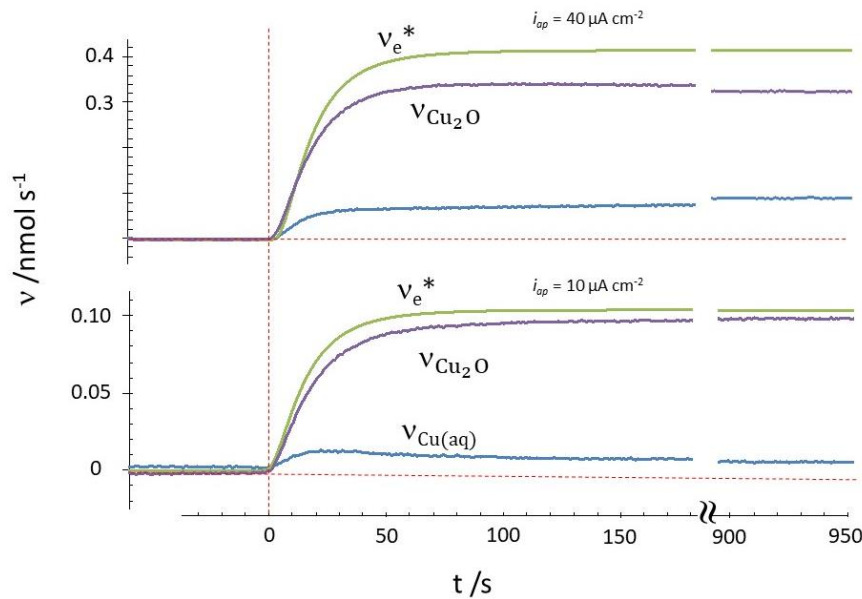


Figure 2. Analyse cinétique de la dissolution du Cu dans l'eau synthétique du robinet.

Au **chapitre 5**, la cinétique de la dissolution anodique du laiton (Cu-42Zn et Cu-21Zn-3SiP) dans l'eau du robinet synthétique a été étudiée par la même expérience STW-CBS comme le chapitre précédent. Les taux de dissolution de Cu élémentaire et de Zn ont été mesurés in situ et en temps réel lors de la dissolution galvanostatique. Une balance complète de masse/charge pour le système a donné, en fonction du courant appliqué et en fonction du temps, la quantité de Cu dans la couche de dézincification et la quantité de Cu et de Zn dans la couche d'oxyde. De cette manière, une première caractérisation cinétique des processus chimiques fondamentaux survenant lors de la dézincification a été réalisée pour la première fois. La couche d'oxyde était composée principalement de Cu_2O comme indiqué par l'incidence rasante XRD et l'analyse Raman. On a déterminé que le produit d'oxydation de Cu soluble était Cu (II) par un équilibre masse / charge. Zn a été oxydé en Zn soluble (II) en laissant derrière lui une quantité de produit de corrosion Zn solide. L'analyse cinétique représente un processus de dissolution en deux étapes de la dézincification: une première étape d'une croissance rapide de la couche dézincifiée et une deuxième étape où la croissance de la couche dézincifiée était beaucoup plus lente. La couche Cu_2O se développe continuellement pendant l'exposition.

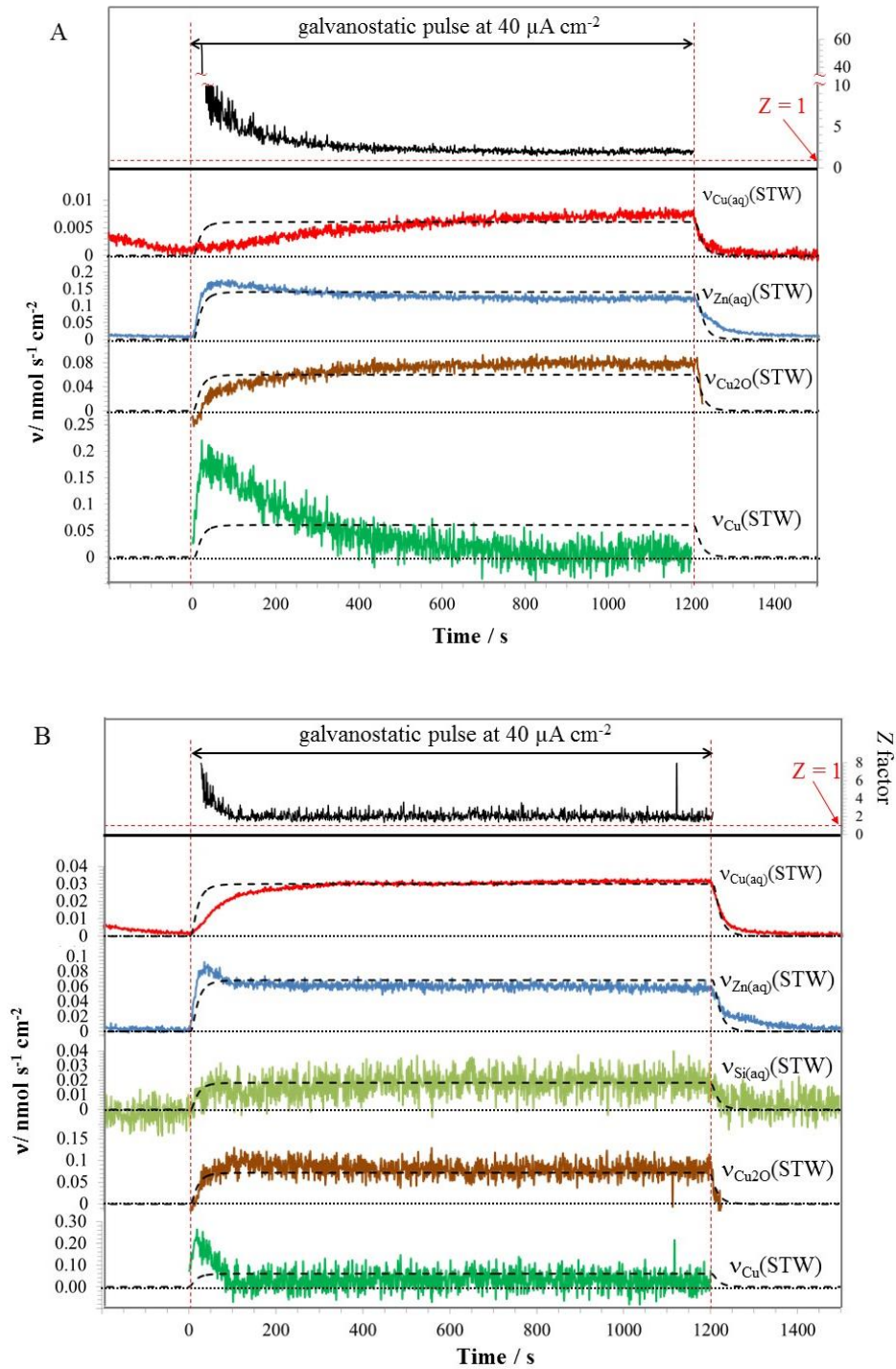


Figure 3. Analyse cinétique de la dissolution élémentaire, du film d'oxyde et de la croissance de la couche de cuivre pure d'zincifié Cu-42Zn (A) et Cu-21Zn-3Si-P (B) à $i_{ap} = 40 \mu\text{A cm}^{-2}$. La ligne d'échappée représente la courbe hypothétique pour une fonction d'échappée après correction de la constante de temps AESEC.

Au **chapitre 6**, des mêmes expériences au **chapitre 4** et au **chapitre 5** ont été étendues à l'étude du comportement de dissolution des alliages Cu-Zn avec une teneur en Zn allant de 0% en poids à 45% en poids, avec une variation de phase métallurgique à partir de la phase α pure, via dual Phase $\alpha + \beta'$, à la phase β pure. Les relations quantitatives de Cu (II), de Zn (II) et de

Cu_2O par rapport au courant appliqué et contre le contenu de Zn ont été présentés et discutés. En outre, la polarisation potentiodynamique des alliages Cu-Zn a été réalisée dans de l'eau du robinet. La relation du courant partiel Cu et Zn contre le potentiel a été présentée et discutée. Les résultats ont montré que, lors de la dissolution anodique des alliages de Cu-Zn, un mécanisme à deux étapes a été vérifié la première étape où une oxydation simultanée de Cu et de Zn s'est produite, mais Zn a été oxydé en Zn soluble (II) et Cu a été oxydé en Cu_2O solide ; Et une deuxième étape que le Cu (II) soluble a commencé à libérer (Figure 4). Le comportement de dissolution en deux étapes pourrait être observé sur les deux alliages contenant la phase α , à l'exception de la phase β pure. Dans la dissolution de la phase β' , il n'y avait pas d'espace de Cu (II) trouvé au cours de la deuxième étape. Les résultats de la polarisation potentiodynamique des alliages contenant la phase α ont également montré qu'il existait une région potentielle dans laquelle seul Zn soluble (II) était détectable, le Cu (II) a commencé à être détecté après un certain surpoids. Cependant, la polarisation potentiodynamique de la phase β ne montre pas de Cu (II) tout au long du balayage potentiel. Ainsi, un mécanisme de dissolution différent entre la phase α et β a été proposé. L'effet de l'addition de Zn dans les alliages de Cu-Zn annulera la dissolution du début de Cu (II).

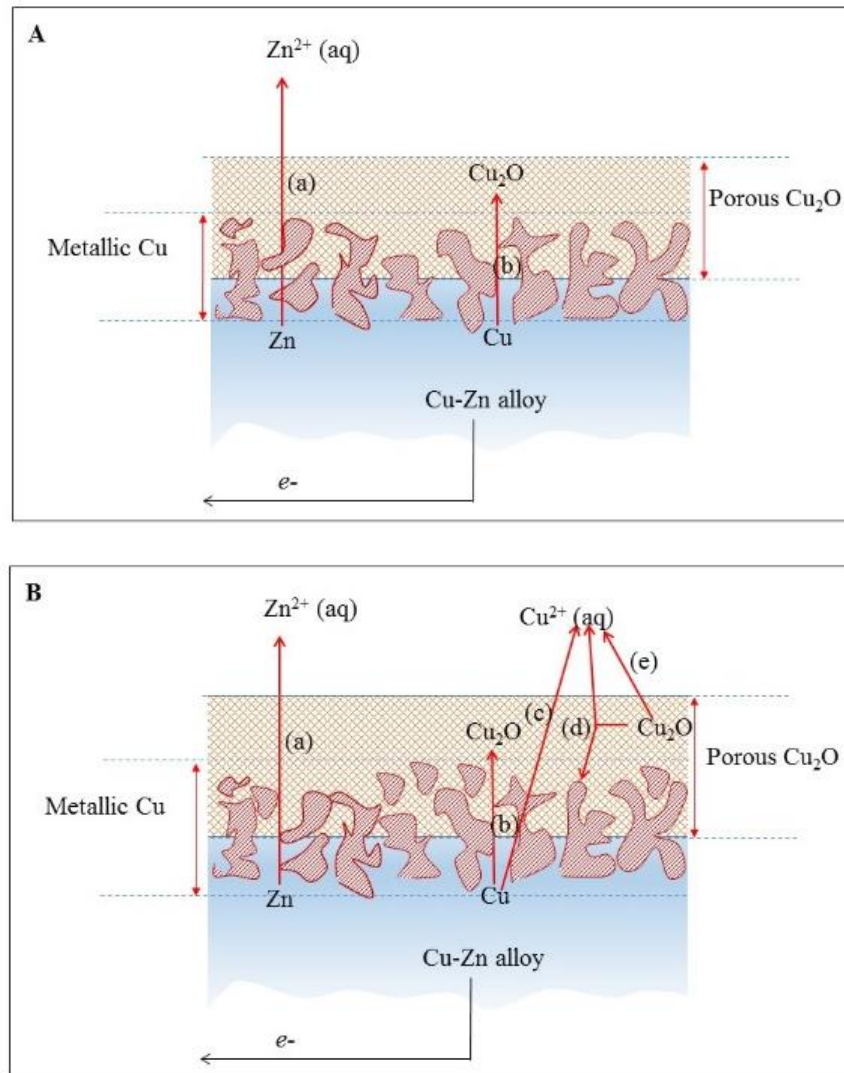


Figure 4. Schematic diagram of the dissolution of Cu-Zn alloy in tap water.

Au **chapitre 7**, le comportement de dissolution des alliages de Cu-Sn a été étudié en fonction de l'effet du contenu de Sn sur la libération d'ion Cu dans une solution synthétique de transpiration. On a étudié le Cu pur, Cu-4.5Sn-0.1Zn et Cu-9.7Sn-0.1Zn. L'expérience synthétique de solution de transpiration-citrate tampon (SPS-CBS) a été effectuée à un courant appliqué de 0 à 80 $\mu\text{A cm}^{-2}$. Cette expérience est envisagée de déterminer l'état de la valence des espèces solubles et des espèces insolubles, en comparant la quantité de charges effectives (Q_e (ICP)) et la somme des espèces solides/solides oxydés. Les résultats montrent que le Cu libéré était Cu (I), et l'échelle solide à la surface est une structure multicouche constituée d'une couche de CuCl extrême, d'une couche de Cu₂O intermédiaire et d'une couche de Sn₂O interne. Les Cu-4.5Sn-0.1Zn et Cu-9.7Sn-0.1Zn ont montré une libération d'ion Cu plus élevée par rapport au cuivre pur, mais Cu-4.5Sn-0.1Zn a montré l'effet renforcé le plus élevé des ions Cu.

L'effet améliorant joué par Sn n'est pas proportionnel au contenu, car la formation de la couche Sn_2O passivera la surface et inhibera finalement la libération d'ion Cu, entraînant une diminution de la fonction antimicrobienne des alliages Cu-Sn de Cu-4.5Sn-0.1Zn à Cu-9.7Sn-0.1Zn.

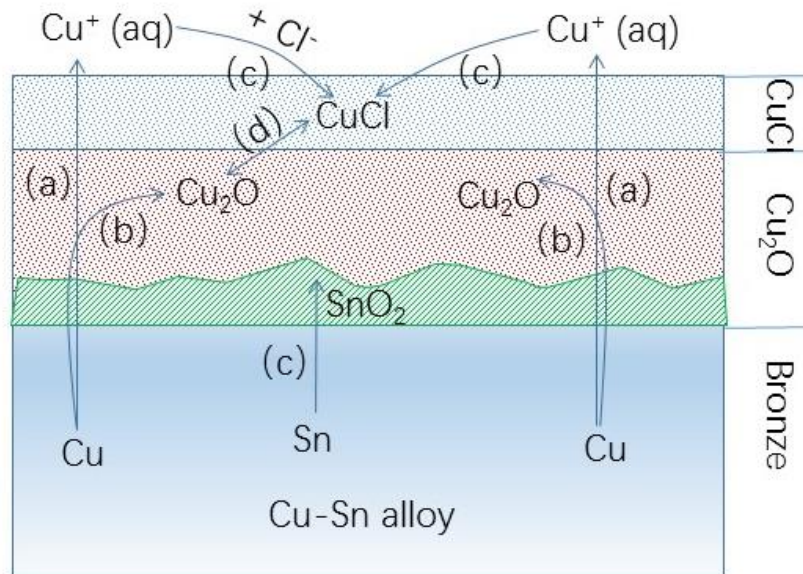


Figure 5. Diagramme schématique illustrant la structure et les réactions électrochimiques impliquées lors de la dissolution des alliages Cu-Sn dans la solution de transpiration.

La **partie D** de la dissertation comprend le chapitre 8. Dans ce chapitre, les conclusions générales ont été résumées et les perspectives futures ont été discutées.

A. Introductory Section

In this section the context of the Ph.D. thesis is introduced and the scientific questions, which should be answered in the thesis, are raised.

Parts of the content presented in **Chapter 2** have been summarized and accepted as a book chapter: **P. Zhou**, K. Ogle, *Corrosion of Cu and Cu Alloys* in *Encyclopaedia of Interfacial Chemistry - Surface Science and Electrochemistry*, 2017.

Introduction

1.1 Origin and objective of this Ph. D work

Copper, as the first metal used by man [1], plays a vital role in the civilization of human beings. Its use dates back to prehistoric times with the discovery of many copper and bronze objects [2]. This was the beginning of the “Copper Age”. Technical advances and growing demanding for materials led to the emergence of the first man-made alloy—bronze, which also opened a new era: the “Bronze Age”. Bronze is a Cu-Sn alloy and it was fabricated into weapons, coins, household articles, ornaments as well as ritual utensils, due to its excellent mechanical properties and pleasing colour [3]. Its use lasts from early Bronze Age tools to modern day industrial applications. Thousands of year later, brass came into a large-scale use [4]. Brass is a Cu-Zn alloy, its first emergence dates back to the 5th millennia BC in China and were widely used in east and central Asia by the 2nd and 3rd century BC [5]. The relative late use of brass was attributed to the difficulty in melting Zn into Cu considering the large difference of melting temperature between Zn and Cu. However, the use of Cu-Zn alloys is as popular as the use of Cu-Sn alloys in modern days.

The worldwide consumption of copper alloys now exceeds 18 million tons per annum [6]. Among them, about 47% is consumed by building industry, 23% by electronics, 10% by transportation, 11% and 9% by consumer products and industrial machinery [7]. Regardless of the usage of them, corrosion is a common problem that raises concern: the corrosion of Cu alloys may result in a disaster due to the break of stress components made of Cu alloys [8], an unexpected leakage of Cu tubes [9] as well as a failure of electronic components [10]. A US study conducted in 2002 stated that the direct cost due to corrosion damage or corrosion prevention is 267 billion dollars [11], which accounts for a considerable proportion of the US Gross Domestic Product (GDP). So the investigation into the corrosion mechanism of Cu alloys not only allows a more efficient use of them, but contributes to the economic development.

Cu-Zn alloys, also known as brass, are the most representative Cu-based alloys that are popular in modern industry. The addition of Zn into Cu leads to a significant improvement of mechanical properties of Cu alloys. However, Zn is less noble than Cu, leading to a selective leaching of Zn from Cu-Zn alloys, *i.e.*, dezincification. Dezincification is the most annoying problem that hinders the utilization of brass in water plumbing, heat exchange engineering and

marine engineering. During the past decades, numerous investigations have been focused on the mechanistic explanation of dezincification and its inhibition. Two major theories, preferential dissolution [12,13] and dissolution-redeposition [14,15], have been widely favoured by different researchers. However, a consensus is yet to be made, mostly due to the complex dezincification structure and the less comparable experimental conditions leading to various conclusions. Especially in the case of tap water dissolution, a neutral environment leads to the formation of oxide scale, the release of cations and the simultaneous formation of a Zn depleted Cu rich layer which complicate the corrosion process. Much of the previous literature focused on the interpretation of mechanism, the characterization of corrosion products and the dezincification structure. Less attention had been paid to the elemental reaction at the interface and the quantitative relationship (stoichiometry) of dissolution and film formation, which are of critical importance in the explanation of corrosion process.

Cu-Sn alloys are another alloy family that are widely used in modern society. Differing from Cu-Zn alloys, which has a relative short history of application since medieval times, Cu-Sn alloys have a rather long history of large-scale utilization which dates back to 4500 BC. There are two reasons for that: a) Cu-Sn alloys were easier to obtain in ancient times, and b) they usually show a good corrosion performance under atmosphere due to Sn passivity [16]. And although corrosion is inevitable, due to the aesthetically pleasing greenish patinas formed after a long time atmospheric exposure, it is irreplaceable in architectural and artistic constructions. The investigation of bronze corrosion, however, is largely limited to the atmospheric corrosion of bronze, applied to the restoration and conservation of excavated bronze antiques. The modern use of bronze, requires more knowledge about the corrosion of bronze. For instance, the ability of Cu ions to kill bacteria and superbugs entitles Cu alloys as biological materials. So bronze is widely used in environments that have easy access to bacteria, such as hospitals and biological enterprises. This special use requires bronze to have a balance between an easy Cu release to the ambient environment and corrosion resistance, which is neglected and lack of literature.

In this work, the dissolution mechanism of Cu, Cu-Zn alloys in synthetic tap water (STW) and Cu-Sn alloys in synthetic perspiration solution were investigated using atomic emission spectroelectrochemistry (AESEC). A synthetic tap water – citrate buffer solution (STW-CBS) and a synthetic perspiration solution – citrate buffer solution (SPS-CBS) experiment were conducted respectively in the study of Cu-Zn and Cu-Sn alloys. These experiments allow a quantification of both soluble species and solid species. Various Cu-Zn alloys with different composition were used to identify the dissolution behaviour of different phase and various Cu-

Sn alloys with different Sn content were used to explore the effect of Sn content of the Cu release. The quantitative relationship of cation release, scale formation and surface structure evolution on a scale of time, of applied current and of composition of alloys can be obtained through AESEC.

This Ph.D. project aims at addressing the following points:

1. To understand the dissolution mechanism of pure copper and Cu-Zn alloys in tap water: ion release, scale formation as well as the growth of Zn depleted pure Cu layer;
2. To distinguish the difference in the dissolution behaviour of α phase and β' phase in Cu-Zn alloys respectively; identifying the effect of Zn content on the dissolution;
3. To identify the effect of Sn content in the Cu ion release from Cu-Sn alloys: the scale formation and the dissolution mechanism;

1.2 Summary and structure of the dissertation

This Ph.D. work is composed of four main parts: **(A) Introductory section, (B) Experimental section, (C) Results section and (D) Conclusions.**

The introductory section (**Part A**) consists of two Chapters: **Chapter 1** and **Chapter 2**. **Chapter 1** gives the context of the Ph.D. work and the technical points to be addressed. **Chapter 2** gives a general literature review regarding the corrosion of Cu-Zn alloy, and the antimicrobial function of Cu-Sn alloys.

In **chapter 2**, the anodic reaction and cathodic reaction of Cu in aqueous solution was presented; the formation of Cu_2O through a one-electron mechanism or a two-electron mechanism was elaborated. Two different types of dezincification mechanisms were presented: a) dissolution-redeposition mechanism and b) preferential dissolution. The dissolution-redeposition mechanism depicts a simultaneous dissolution of Cu and Zn and a subsequent redeposition of Cu on the surface. The preferential dissolution mechanism depicts an electrochemical reaction that involves only Zn, it consists of three sub-mechanisms: surface diffusion, volume diffusion and percolation. The antimicrobial function of Cu-Sn alloys was introduced in terms of the function played by Cu ions in kill/inactivating bacteria/superbugs, and the importance of enhancing Cu ion release by analysing the effect of alloying additions.

The **Experimental section (Part B)** comprises **Chapter 3**. In this chapter, the materials used in this Ph. D. work, and their composition, pre-treatment method were elaborated. Atomic

emission spectroelectrochemistry (AESEC) was introduced in terms of its working principal and schematic structure. Surface characterization measurements and parameters were listed.

The **Results section** is composed of three chapters: **Chapter 4** (anodic dissolution of pure Cu), **Chapter 5** (dissolution behaviour of two commercial alloys), **Chapter 6** (effect of Zn content on the dissolution behaviour), **Chapter 7** (effect of Sn content on the Cu ion release from Cu-Sn alloys).

In **Chapter 4**, the anodic dissolution of pure copper was investigated in naturally aerated synthetic tap water (STW) by *in situ* atomic emission spectroelectrochemistry (AESEC). This technique measures the Cu dissolution rate directly and the formation of the Cu scale indirectly by mass balance between the anodic current and the dissolution rate. The conditions investigated include the effect of applied current (0 to 80 $\mu\text{A cm}^{-2}$) and time duration at 40 $\mu\text{A cm}^{-2}$ (0 to 20 min). Oxide scale formed during exposure to STW was dissolved in a de-aerated citrate buffer solution (CBS) and followed by *in situ* AESEC as well. A mass/charge balance confirmed the predication that most Cu(II) species are soluble and are released into STW, leaving behind a Cu_2O film as an insoluble product on the surface. *Ex situ* Raman spectroscopy and grazing incidence X-Ray diffraction analysis (GIXRD) also corroborate this conclusion. A quantitative analysis of Cu(I) and Cu(II) species vs. applied current and vs. time during a galvanostatic pulse are presented. A kinetic analysis suggests that the dissolution mechanism involves simultaneous Cu dissolution and film formation rather than a sequential mechanism.

In **Chapter 5**, The kinetics of the anodic dissolution of brass (Cu-42Zn and Cu-21Zn-3Si-P) in synthetic tap water were investigated following the same STW-CBS experiment as previous chapter. Elemental Cu and Zn dissolution rates were measured *in situ* and in real time during galvanostatic dissolution. A complete mass/charge balance for the system yielded, as a function of applied current and a function of time, the quantity of Cu in the dezincification layer and the quantity of Cu and Zn in the oxide layer. In this way a complete kinetic characterization of the fundamental chemical processes occurring during dezincification was realized for the first time. The oxide layer was composed primarily of Cu_2O as indicated by grazing incidence XRD and Raman analysis. The soluble Cu oxidation product was determined to be Cu(II) by a mass/charge balance. Zn was oxidized to soluble Zn(II) leaving behind a trivial amount of solid Zn corrosion product on the surface. The kinetic analysis depicts a two-stage dissolution process of dezincification: a first stage of a rapid growth of the dezincified layer and a second stage where the growth of dezincified layer was much slower. The Cu_2O layer grows continually during the exposure.

In **Chapter 6**, identical experiments to **Chapter 4** and **Chapter 5** were extended to the investigation of dissolution behavior of Cu-Zn alloys with Zn content ranging from 0 wt% to 45 wt%, with a metallurgical phase variation from pure α phase, via dual $\alpha + \beta'$ phase, to pure β' phase. The quantitative relationships of Cu(II), Zn(II) and Cu_2O against applied current and against Zn content was presented and discussed. Besides, the potentiodynamic polarization of Cu-Zn alloys was conducted in tap water. The relationship of partial Cu and Zn current against potential was presented and discussed. Results showed that during the anodic dissolution of Cu-Zn alloys, a two stage mechanism was revealed: a first stage that a simultaneous oxidation of Cu and Zn occurred, but Zn was oxidized into soluble Zn(II) and Cu was oxidized into solid Cu_2O ; and a second stage that soluble Cu(II) started to release. The two stage dissolution behavior could be observed on both alloys containing α phase, except for pure β' phase. In the dissolution of β' phase, there was no Cu(II) species being found during the second stage. The potentiodynamic polarization results of alloys containing α phase also showed that there was a potential region that only soluble Zn(II) was detectable, Cu(II) started to be detected after a certain overpotential. However, the potentiodynamic polarization of β' phase shown no Cu(II) at all throughout the potential scan. So a different dissolution mechanism between α and β' phase was proposed. The increase of Zn addition in Cu-Zn alloys will put off the onset dissolution of Cu(II).

In **Chapter 7**, the dissolution behavior of Cu-Sn alloys was investigated in terms of the effect of Sn content on the Cu ion release into synthetic perspiration solution. Pure Cu, Cu-4.5Sn-0.1Zn and Cu-9.7Sn-0.1Zn were investigated. Similar to the STW-CBS experiment in previous chapters, the synthetic perspiration solution-citrate buffer solution experiment (SPS-CBS) was conducted at applied current from 0 to 80 $\mu\text{A}/\text{cm}^2$, aiming at determining the valence state of soluble species and insoluble species by the comparison between the quantity of effective charges ($Q_e(\text{ICP})$) and the total charges consumed by oxidizing of soluble/solid species. Results show that the released Cu ion was Cu(I), and the solid scale on the surface is a multilayered structure consisting of an outmost CuCl layer, an intermediate Cu_2O layer and an inner Sn_2O layer. Both Cu-4.5Sn-0.1Zn and Cu-9.7Sn-0.1Zn showed enhanced Cu ion release compared with pure copper, but Cu-4.5Sn-0.1Zn showed the highest enhanced effect of Cu ions. The enhancing effect played by Sn is not proportional to the content, since the formation of Sn_2O layer will passivate the surface and finally inhibit Cu ion release, resulting a diminishing antimicrobial function of Cu-Sn alloys.

Part D of the dissertation comprises **Chapter 8**. In this chapter, the general conclusions were summarized and future perspectives were discussed.

1.3 List of publications

Full text articles

1. **P. Zhou**, M. J. Hutchison, J. R. Scully, K. Ogle, *The anodic dissolution of copper alloys: Pure copper in synthetic tap water*. *Electrochimica Acta*, 191 (2016), 548-557.
2. **P. Zhou**, M. J. Hutchison, J.W. Erning, J. R. Scully, K. Ogle. *An in situ ICP-AES study of brass dezincification in synthetic tap water*, *Electrochimica Acta*, 229(2017), 141-154.
3. M. J. Hutchison, **P. Zhou**, J. R. Scully, K. Ogle, *Effect of Al and Sn on Corrosion Response and Cu Ion Release of Copper-Based Alloys, Implications towards Tarnish Resistant Antimicrobial Surfaces*, *Electrochimica Acta*, 241(2017) 73-88.

Article in preparation

1. **P. Zhou**, M. J. Hutchison, J.W. Erning, J. R. Scully, K. Ogle. *The dissolution of Cu-Zn alloys in synthetic tap water: effect of Zn content on the elemental release and scale formation and dissolution mechanism*.
2. **P. Zhou**, J.W. Erning, K. Ogle. *Anodic dissolution mechanism of Cu-Zn alloys in citrate buffer solution*.

Book chapter

1. **P. Zhou**, K. Ogle, *Corrosion of Cu and Cu Alloys in Encyclopaedia of Interfacial Chemistry - Surface Science and Electrochemistry*, 2017, accepted.

Presentation in international conferences

Oral presentation:

1. **P. Zhou**, Kevin Ogle, *A new look into the selective dissolution of Cu-Zn alloys in tap water: elemental release, scale formation and dissolution mechanism*, European Corrosion Congress (Eucorr) September 11-15, 2016. Montpellier, France. Abstract No. 59657.
2. **P. Zhou**, M. J. Hutchison, J.W. Erning, J. R. Scully, K. Ogle, *Dissolution of Cu-Zn alloys in tap water: effect of metallurgical phase on the elemental release, scale formation and dissolution mechanism*, NACE Corrosion, March 26-30, 2017. New Orleans, USA. Abstract No. C2017-12038.

Poster / Participant:

1. K. Ogle, V. Shkirskiy, P. Volovitch, **P. Zhou** and A. Maltseva, *A Novel Coupling Between Atomic Emission Spectroelectrochemistry and Electrochemical Impedance Spectroscopy: Application to Zn, Zn-Cu and Zn-Al-Mg Alloys*, 228th ECS Meeting, Oct. 11-15, 2015, Phoenix, USA.
2. K. Ogle, **P. Zhou**, *The dezincification of brass: in situ measurement of Zn and Cu dissolution with atomic emission spectroelectrochemistry*, 228th ECS Meeting, Oct. 11-15, 2015, Phoenix, USA.
3. M. J. Hutchison, **P. Zhou**, K. Ogle, J. R. Scully, *Effect of Sn on the Fate of Copper during Dissolution: A Comparison between Copper and Bronze Commercial Alloys*, July 10-15, 2016, New London, New Hampshire, USA.
4. **P. Zhou**, M.J. Hutchison, J.W. Erning, J.R. Scully, K. Ogle, *In situ kinetics of the dezincification of Cu-Zn alloys: Uncovering the effect of phase structure and composition*, ISE 68th Annual Meeting - International Society of Electrochemistry, August 27-September 1st, 2017, Providence, Rhode Island, USA

2. The corrosion of Cu based alloys

Copper has the longest history of use by human beings of any metallic material. Its earliest use dates back to circa 4500 BC in Mesopotamia [17] as building tools fashioned from bronze which were a pivotal underpinning for urbanization. In recent centuries, due to their excellent corrosion resistance, Cu alloys are popularly utilized in disciplines like architecture [18], automotive [19], electrical [20], tube, pipe & fittings [9,21-33] and seawater [34]. Modern advances in technique see the use of Cu alloys in more sophisticated fields such as nuclear engineering [35] and microelectronics [36], in which corrosion is a critical issue to be addressed: the former requires a precise prediction of corrosion rate of nuclear waste canister that is made of Cu over many thousands of years; the latter requires an atomic level understanding of corrosion process because of the small amount of material. So the mechanistic investigation of corrosion of Cu alloys is indispensable for manufacturing industry.

Cu alloys are most popularly used as tube, pipe & fittings, due to their excellent corrosion performance. The corrosion of copper and its alloys is a troublesome problem due to their large-scale use. Corrosion may result in the premature failure of tubes and fittings, blue water problems, toxicity due to unwashed copper release and costly expenses involved in waste water disposal. Besides the sporadic tubercle blockages due to the deposition of scales, superfluous soluble copper release into water not only causes serious health problems [21], but induces accelerated corrosion elsewhere in iron pipelines [32] and tanks which may also be present in the water distribution system. To date, much work has been conducted to investigate factors that affect corrosion of copper and its alloys. Water chemistry [23,31,32], surface states of samples [22], temperature [26,37] and pretreatment work [38], all affect the corrosion of copper and its alloys in a complex way. However, data from field work often contradicts results from laboratory work. An in-depth, systematic investigation into the corrosion mechanism of Cu alloys will allow a better use of Cu alloys.

2.1 The corrosion of copper

Copper has its natural attributes that make it ideal for plumbing. It creates a biostatic atmosphere which makes it difficult for bacteria to grow inside of it. It also resists corrosion and is unaffected by ultraviolet rays, which permits both indoor use and outdoor use.

Nevertheless, the corrosion of copper tubes is an important issue because it leads to the release of Cu cations into the ambient environment, which will either deteriorate the environment, or jeopardize human health since drinking water is the most important pathway of copper into human body. The ‘Lead and Copper Rule (LCR)’ promulgated in the US regulates an action when a level of 15 ppb of Pb or 1.3 ppm of Cu is found in more than 10% of customer taps sampled. The *World Health Organization* (WHO) and the Europe Union (EU) defined the maximum safe level of Cu ion in drinking water at 2 mg l⁻¹ [21]. Besides, dissolved Cu in water will also result in its redeposition elsewhere in the plumbing system in the presence of Fe via a displacement reaction, to form highly localized galvanic couples [39]:



Cathodic Reactions on Cu

Due to the nobility of Cu, it is most frequently the cathode when in contact with other metallic materials and therefore, the cathodic properties of Cu are very important. Oxygen reduction by a four-electron mechanism is by far the most important cathodic reaction for the corrosion of pure Cu [40, 41]:



The cathodic properties of Cu are also important for other materials such as high strength Al alloys for which the corrosion rate may be determined by the presence of Cu intermetallic particles [42]. The corrosion may spread via the Cu ions released from the intermetallic particles which redeposit at other areas of the surface by a displacement reaction, similar to Eq. 1 [43]. An important strategy for the corrosion protection of high strength Al alloys is to block oxygen reduction on Cu with the appropriate inhibitor molecule [44]. The removal of surface Cu is an important goal of Al alloy surface pretreatment [45].

The spontaneous reaction of Cu with H₂O or H⁺ is conventionally considered to be thermodynamically impossible. However, Hultquist [46,47] measured hydrogen gas formation, attributed to the reaction of Cu with anoxic pure water; and Cleveland *et al.* [48] measured a corrosion rate of 1 nm/day in water with an O₂ concentration on the order of, or less than, 1 ppb. Although this corrosion rate is extremely small, it could have important consequences on the choice of Cu for nuclear waste storage, extending the necessary estimated canister thickness from 0.05 m to 1 m [49]; and for the use of copper nanostructures as heat exchangers for liquid-cooling of high-performance electronics. These results have generated some controversy [50].

Anodic corrosion of copper

In aqueous solution, Cu will oxidize to either Cu(II) or Cu(I). The latter is only slightly soluble in water, and therefore a film of Cu_2O is the predominant insoluble product during Cu corrosion [46, 49, 51] while Cu^{2+} is the predominant soluble species. In the presence of Cl^- , or other complexing agents, the solubility of Cu(I) is enhanced and becomes the dominant species in solution for example in the form of CuCl_2^- .

In early work, Ives and Rawson [52] proposed a two-layer cuprite (Cu_2O) film consisting of a compact, epitaxial grown inner layer and a porous outer layer. A hypothetical structure of the Cu/ Cu_2O /electrolyte interface based on the Ives and Rawson model is shown in Figure 2.1. The compact cuprite film is a p-type semiconductor in which Cu(II) replaces Cu(I) in the crystal lattice giving rise to electron transport via a shift between the Cu(II) and Cu(I) species as confirmed by photocurrent measurements [53,54]. Ives and Rawson proposed the existence of a large electrical barrier at the interface between the compact and the porous film, creating an electrical disconnection of the later from the metal rendering the porous film susceptible to further oxidation by oxygen reduction at the oxide /electrolyte interface (Reaction (c) in Figure 2. 1).

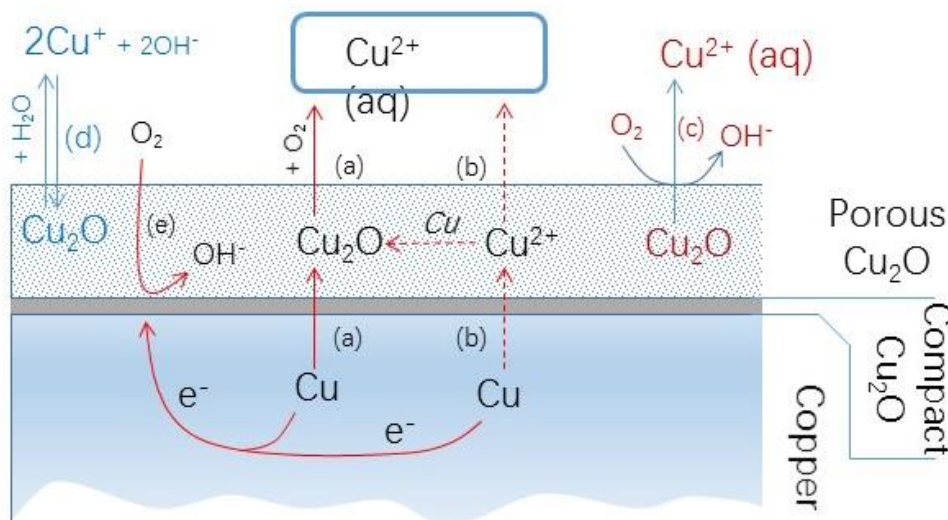
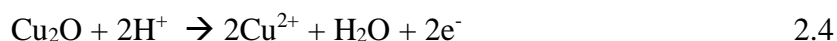
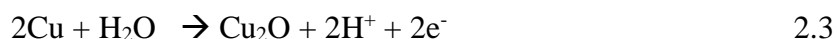


Figure 2.1. Schematic diagram of copper corrosion

One-electron and two-electron reaction mechanisms for Cu dissolution and film formation have been proposed in the literature [55-57] and are illustrated in Figure 2.1. The *one-electron reaction mechanism* (mechanism (a) in Figure 2.1), involves the stepwise formation of slightly soluble cuprite (Cu₂O), followed by the subsequent oxidation of cuprite into a soluble Cu(II) species [40,41]



The two electron mechanism (mechanism (b) in Figure 2.1), also known as the *dissolution-redeposition* mechanism, involves the direct formation of Cu²⁺ followed by a synproportionation between Cu(0) and Cu(II) [2,4,8,58-59 60]



Current interest in Cu corrosion is for the most part focused on the characterization of the corrosion structure, factors that affect corrosion, and methods of corrosion inhibition. The reaction sequence of soluble Cu, Cu₂O and sometimes CuO or other Cu containing salts at the interface is of critical importance in explaining the corrosion process.

2.2 The corrosion of Cu-Zn alloys: dezincification.

Though unalloyed copper has been used in a wide range of products due to its excellent electrical and thermal conductivity, good strength, good formability and resistance to corrosion, its softness and high fabricating cost hinder its application in fields that require a good combination of cost and mechanical property. The addition of Zn into Cu matrix, not only maintains the good electrical and thermal properties, but grants excellent forming and drawing characteristics, making brass amenable to an extended range of applications. Figure 2.2 shows the Cu-Zn equilibrium phase diagram. Cu and Zn have an atomic size of 1.27 Å and 1.37 Å respectively. Their relative small atom size difference (about 4%) leads to a high solid solubility of Zn in Cu solid solution up to 35% at 20 °C [61], this face centered cubic (FCC) substituted solid solution is the α phase with a chemical formula of Cu₃Zn. The further increase of Zn leads to the formation of an intermetallic phase, *i.e.*, β phase with Zn content up to 55 wt%. This body

centered cubic (BCC) phase is disordered at high temperature but then becomes ordered with the cooling process. The ordered phase is usually denoted as β' with a chemical formula of CuZn . Unlike the α phase which is ductile, the β' phase contributes to the toughness of the alloy. The mechanical properties of brass depend on tuning the composition of the two phases, their size and distribution in the matrix. The further increase of Zn will result in the formation of other intermetallic phases: γ and ϵ . Since these phases are brittle and do not contribute to the improvement of mechanical properties, they are rarely sought after, and will not be discussed here.

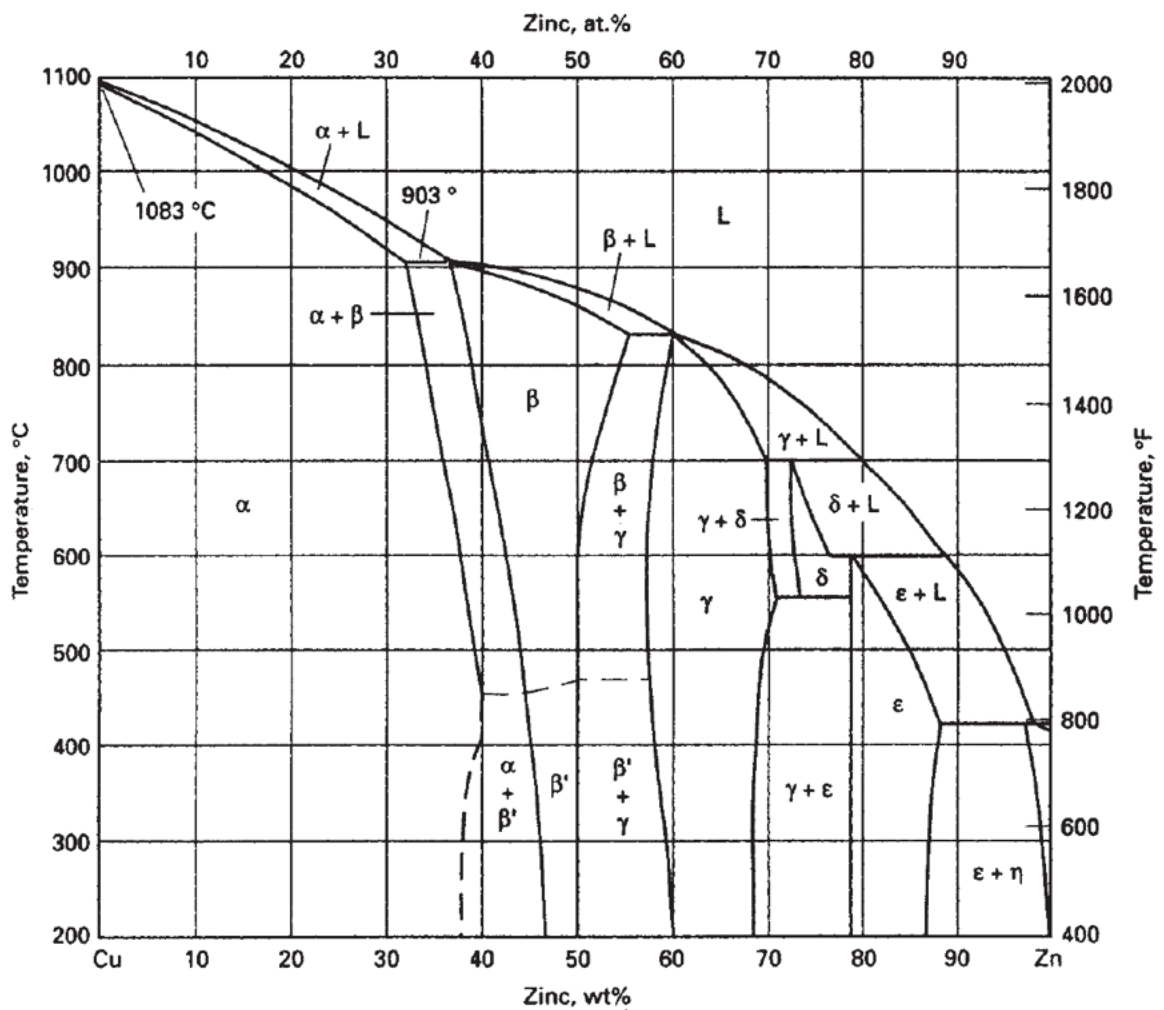


Figure 2.2. The equilibrium Cu-Zn phase diagram. [61]

Besides improved mechanical properties, brasses also have excellent corrosion resistance in most natural environment such as soil, water, air, etc. [62]. However, Zn has a standard potential of $-0.76 \text{ V}_{\text{SHE}}$, a value that is -1.04 V more negative than Cu [63]. So the coexistence

of the two elements results in the preferential oxidation of Zn leaving behind Cu metal. This is known as the selective (or preferential) dissolution of Zn or *dezincification*.

Dezincification structure

The selective leaching of Zn from Cu results in the formation of a dealloyed layer that is Cu-rich and defect rich, this is normally the case of the dissolution of brass in acidic media where little oxide is formed [64-66]. However, in neutral electrolyte a multi-layered dezincification structure consisting of a Zn depleted layer and a corrosion product layer composed of Zn and Cu corrosion products [67] is formed. The composition and structure of the oxide layer varies with testing condition, chemical composition of the alloy and the electrolyte, but typically Cu_2O , CuO , $\text{Cu}(\text{OH})_2$, ZnO and $\text{Zn}(\text{OH})_2$ are the most representative species that constitute the altered layer.

Dezincification mechanism

The mechanisms of selective dissolution have been intensively investigated during the past decades, many representative theories have been proposed, however a consensus has yet to be reached. The biggest argument remains on the role played by Cu in the dissolution of brass. Many authors believe that since Cu is a noble component, it will not directly participate in the electrochemical process, leading naturally to the *mechanism of selective dissolution*. However, others found that in the corrosion/dissolution of brass in certain environments, the involvement of Cu oxidation could be supported by many experimental phenomenon, which leads them to conclude another category of theory, *dissolution-redeposition*.

The theory of preferential dissolution of zinc, depicts a dezincification process in which only zinc is involved in the electrochemical reaction during corrosion, the surrounding Cu atoms on the material and are not directly involved in the electrochemical process [68]. The fact that Zn has an equilibrium potential more negative to Cu, results in a preferential dissolution of Zn from the Cu-Zn lattice. However, the continuity of this preferential dissolution process remains doubtful since the selective oxidation process of Zn will result in a defect-rich, porous layer replete with vacancies, which will finally block the Zn reaction path. Moreover, this Zn depletion layer will change neither the physical structure nor the lattice parameters if the selective dissolution of Zn was the only transport mechanism. Whereas numerous investigations had shown that in the free corrosion or anodic dissolution for brass, both physical

structure and surface phase transformed significantly compared with their original surface state. Horton [69] and Natarajan [70] found that the morphology of corroded brass samples being deformed lost their characteristics of prior deforming work. Pickering [13] also reported that the lattice parameter of surface phases altered greatly from their matrix by XRD analysis. So some sub-mechanisms describing different atom transport mechanism were introduced to account for these changes.

Surface diffusion

Surface diffusion process was proposed by Forty et al [71, 72]: in the anodic dissolution of duplex alloy, the initial selective leaching of less noble atoms from the surface resulting in surface roughening, leaving a disordered structure that contains vacancies (removal of less noble atom) and adatoms (residual more noble atom). The adatoms then start to diffuse across the surface by an uphill diffusion, forming a small island that mainly contains noble atoms [72,73]. The interconnection of these islands renders a reordered porous maze-like structure. This surface re-arrangement has been observed by TEM in the corrosion of Au-Ag alloy in strong acid [71] and Forty *et al.* [72] reported a model regarding this surface recrystallization in explaining the corrosion pitting. Burstein et al [74] drew the conclusion that this surface transport of Cu atoms is the rate-determining step for the continuity of the early stages of dezincification.

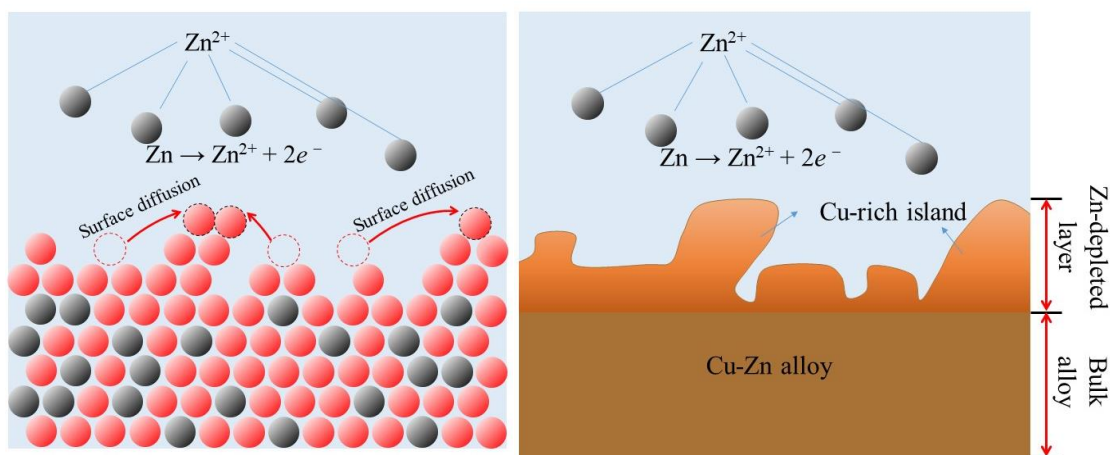


Figure 2.3. Schematic diagram of surface diffusion mechanism

Volume diffusion

The theory of volume diffusion, as proposed by Pickering et al [12,13], originates from the research of the anodic dissolution of Cu-Au Alloys [75]. It depicts a transport mechanism that is not only located at the reaction front, but penetrates a certain depth into the bulk, forming a gradual variation of chemical composition and lattice parameter. Unlike the surface diffusion which depicts a surface re-arrangement of the noble element in a duplex alloy, the volume diffusion theory differs in that the interdiffusion/counterdiffusion of both noble and less noble atoms occur through the migration of vacancies/divacancies. Pickering used X-Ray diffraction to corroborate the volume diffusion of Cu-Au [75], Cu-Zn[13] alloys during anodic dissolution in sulfuric acid, by detecting two characteristic features of the diffraction patterns: (a) the emergence of new peaks due to the formation of new phases during anodic dissolution, such as the peak of α phase in the dissolution of β' brass, γ and ϵ brass [13]; and (b) the evolvement of the broad diffraction ring, which was due to the gradual variation of lattice parameter - a direct evidence of the existence of a composition transitional region that was produced by the interdiffusion of atoms. In the interpretation of this transport mechanism, many researchers cited the remarkable mobility difference between the vacancy and divacancy, which is normally proposed for the solid transformation during the vaporization of Zn from Cu-Zn alloys in elevated temperature environment. A monovacancy forms from the surface through a kink-ledge-terrace model [13], a divacancy can be formed either by the joining of two monovacancies, or directly from the removal of two adjacent atoms under a strong driving force. The diffusivity coefficient of monovacancy at room temperature, as reported by many authors, varies from the order of $10^{-19} \text{ cm}^2 \text{ s}^{-1}$ to $10^{-16} \text{ cm}^2 \text{ s}^{-1}$ [76] in copper alloys at room temperature, virtually negligible compared with a diffusion coefficient of the order of 10^{-15} - $10^{-13} \text{ cm}^2 \text{ s}^{-1}$ [76,77] for a divacancy. However, though some researchers utilized the positron annihilation spectroscopy (PAS) [76,77] to correlate the dezincification behavior and the movement of divacancies, detailed investigation regarding the kinetics of divacancy movement is still lacking. Besides, research from other authors contradicts the theory proposed by Pickering: Fort [78] found that in the dissolution of Cu-30Zn, the diffusion coefficient based on the Auger electron spectroscopic depth profiling was 8 orders higher than the extrapolated value from high temperature leading them to the conclusion that volume diffusion alone could not be the only transport mechanism for dezincification. Similar results were also reported by Laurent et al [79,80] in the dissolution of Cu-30Au. The feature of the formation of new phases with transitional chemical composition can also be explained by the previous percolation theory [81].

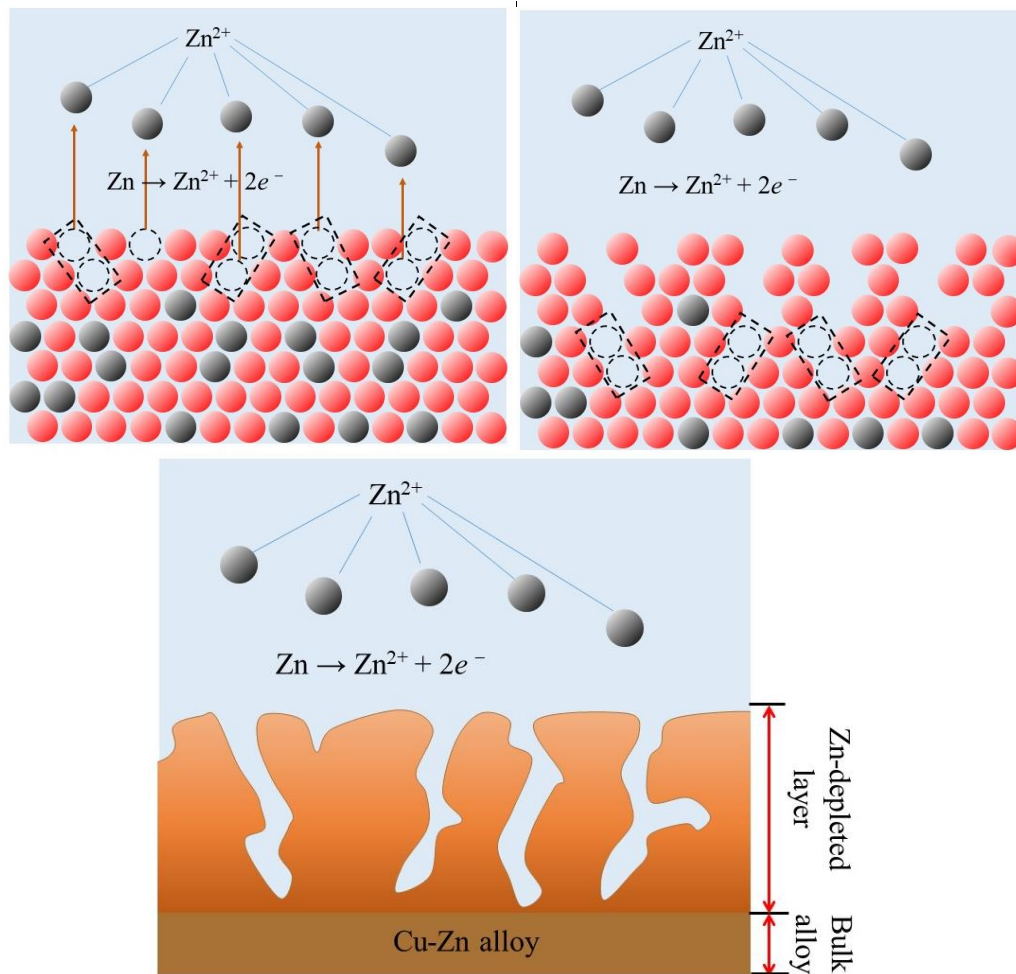


Figure 2.4. Schematic diagram of the volume diffusion mechanism.

Percolation

Some researchers found that Cu-Zn alloys containing less than 20 wt% of Zn are seldom sensitive to dezincification [81], which is beyond the explanation of a single surface reordering process. In this case, Sieradzki et al [81,82] proposed a percolation theory, which serves as an extension of the aforementioned surface diffusion theory [83]: after the selective leaching of the less noble atoms from the reaction front, the surface re-arrangement proceeds via a mobility of several adjacent atoms, rather than a long-range diffusion among the surface. Also, the dissolution is only able to initiate within several nearest atom lengths from the reaction frontier. This short-ranged diffusion & dissolution allows a kinematic formation of interconnected paths of the less noble elements in a binary phase, constructing an infinite Zn cluster that allows the continuity of selective leaching from the surface to a certain depth of the bulk [84]. The Monte Carlo model proposed by Sieradzki et al [81], reported a three-dimensional percolation process for Cu-Zn alloy with a dealloying threshold (p) of 0.2, indicating that a minimum of 20 at% of

the less noble atom allowing the dealloying through a percolation process. This theory is able to interpret the propensity of pitting corrosion of brass alloys with different Zn content [81], and the function that alloying additions, such as arsenic, boron[85], played in the improvement of dezincification resistance by a blockage of the continuous Zn reaction clusters. However, there is no up-to-date experimental evidence supporting this theory.

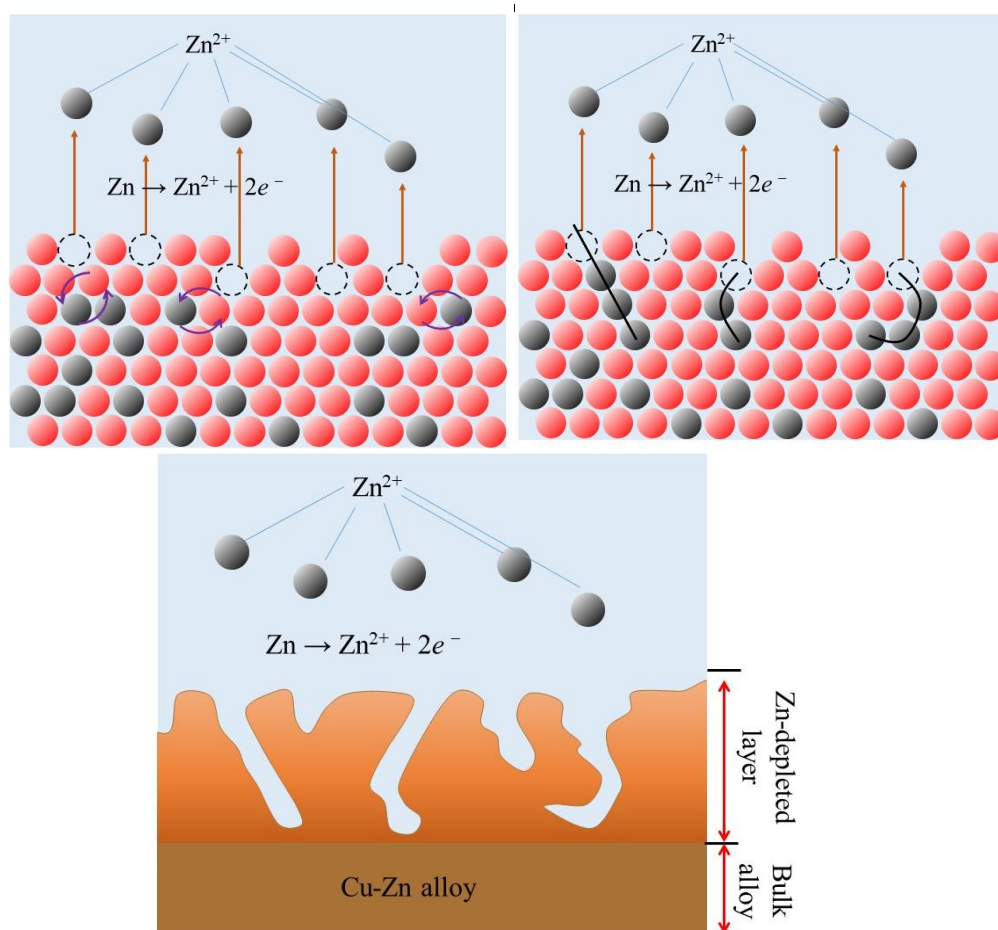


Figure 2.5. Schematic diagram of percolation theory.

Dissolution-redeposition

The theory of dissolution-redeposition depicts a completely different electrochemical reaction process, in which a simultaneous oxidation of both Cu and Zn is followed closely by the precipitation of the Cu ions back onto the surface [70]. To date, the major controversy lies in two aspects: a) the possibility of simultaneous dissolution and b) the kinetics of the Cu redeposition process. For Cu-Zn alloys, the large difference of the equilibrium reduction potential suggests a strong propensity for Zn selective removal. As to Cu, a simultaneous

oxidation is possible to initiate, considering the complex structural change and lattice change, which may increase the activity of Cu below its oxidation potential. However, there is no direct evidence proving that Cu and Zn oxidized and dissolved faradaically as compared to the ratio of Cu/Zn in the bulk alloy. Many authors tried to obtain the real-time concentrations of the ions by chemically analyzing the electrolyte composition [86]. Their results showed a clearly higher Zn/Cu dissolution ratio compared to the bulk Zn/Cu ratio. Another question regarding the possibility of the redeposition of oxidized Cu back onto the surface is also controversial. Polunin and Pchel'nikov [14,15] used a brass sample labeled with isotopes, aiming at following the atom transport mechanism. Their results favored the redeposition of Cu process. Heidersbach [87] and Saber [38] also found an isolated Cu particle included in a residual oxide layer, a result which is hardly compatible with a solid transport mechanism. However, a large amount of data shows that an ideal congruent dissolution of Cu and Zn strictly complying to their bulk ratio cannot be achieved in free corrosion or at a low overpotential [12]. This result leads more and more researchers to interpret the dezincification in a combined mechanism of the previously mentioned theories.

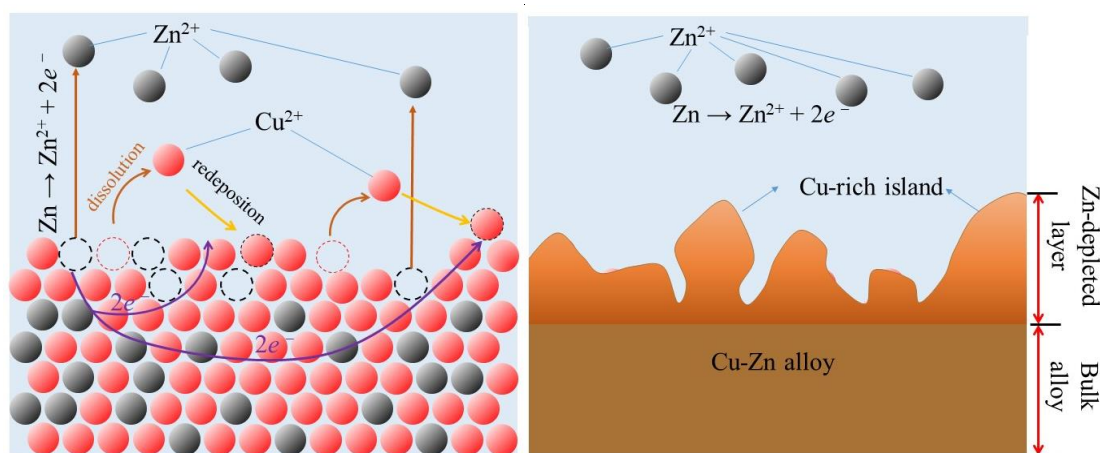


Figure 2.6 Schematic diagram of dissolution-redeposition mechanism.

A major problem in understanding the dezincification of brass in tap water lies in the complexity of the dezincification process itself: the formation of a Zn depleted layer, the precipitation of the residual oxide and the simultaneous Cu and Zn release into water. The dezincification structure varies from testing condition to the chemical composition of the alloy and the electrolyte. The application of *in situ* techniques such as Raman spectroscopy [88], infrared reflection absorption spectroscopy (IRAS) [89], near normal incidence reflectance spectroelectrochemical technique (NNIRS) [90] and ultraviolet-visible (UV-vis) reflectance

spectroscopy [91] in combination with conventional electrochemical methods such as potentiodynamic polarization [92] and electrochemical impedance spectroscopy (EIS) [93, 94] have been used to identify the solid species during corrosion / dissolution and prediction of the interfacial structure change. However, they provide insufficient quantitative information in terms of different species, nor do they offer reliable evidence showing the evolvement of the interface such as the growth of residual oxide and the Zn depleted layer, which altogether contributes a lot to predicting the dezincification resistance and a better understanding of the mechanism. In this effort, some researchers also developed new technique in exploring the corrosion process: Hoshi et al. [95,96] developed a *channel flow double electrode* (CFDE) for the investigation of Cu alloys. The CFDE permits distinguishing Cu(I) and Cu(II) release in real time during the anodic dissolution of Cu and Cu-Zn. This technique has recently been coupled with a video microscopy system to correlate the elemental dissolution rates with the initiation of pits on Cu [102]. Cerrato *et al.* [97] proposed a laser induced breakdown spectroscopy (LIBS) to monitor *in situ* and in real time the dealloyed structure by a three-dimensional mapping.

Another aspect of the problem which has received very little attention is the role of different metallurgical phases - α , β' , γ , ϵ , etc. and the effect of the increasing concentration of Zn has yet to be clarified. Some researchers mentioned the difference in dissolution mechanism among different phases. Pickering [13] investigated the anodic dissolution of α brass (Cu-30Zn), γ brass (Cu-65Zn) and a ϵ brass (Cu-86Zn), in a complex buffered solution with a pH = 5.0, and found that no Cu was released into the electrolyte from the ϵ brass, and no porous Cu-rich layer can be found on the α brass. Lucey [98,99] exposed α brass in deaerated CuCl₂ solution, and found that cuprous ions could be formed due to the reduction of cupric ions, but no cuprous ions can be formed in an similar experiment with a β' brass. Polunin and Pchel'nikov [14,15] used isotopes to follow the dissolution of α brass and β brass: their results showed that in the dissolution of β' brass there is no Cu released into the electrolyte whereas in α brass both Cu and Zn ion release were found. Can [100] utilized the rotating ring disk to investigate the effect of rotating speed on the electrode current of different alloys and found that the current of an α brass was independent of the rotating speed whereas the current was dependent on an α , β' brass. Langenegger [68] found a different dezincification structure between an α brass and an α , β' brass in the dissolution in an acidic solution.

The various results proposed by these authors emphasized the importance of identifying the detailed dissolution differences among the different phases in the alloy. Especially in the dissolution of brass in a neutral electrolyte, *i.e.*, tap water, the coexistence of both soluble,

insoluble species, combined with a complex interfacial structure, greatly complicate the dezincification process. A series of detailed comparable experiments on the dissolution of brass alloys with various chemical composition that can provide a precise quantitative relationship among different species, will help understand the elemental dissolution kinetics, dezincification structure evolution and the mechanism.

2.3. The corrosion of Cu-Sn alloys: its antimicrobial efficacy.

It has long been acknowledged that Cu exhibits excellent ability of killing/inactivating bacteria, yeasts, and viruses. The first recorded medical use of Cu can be found in Egyptian books written between 2600 and 2200 B.C., which describes the utilization of Cu in sterilizing chest wounds and drinking water [101]. Similar documented medical application of copper can also be found in the history of Greeks, Romans and Aztecs. And a historic finding of Cu's medical potency was observed in 1832 that coppersmiths appeared to be immune to cholera outbreaks in Paris, France [101]. This finding led to the popular use of Cu in medicine in the 19th and 20th century [102], such as the treatment of chronic adenitis, eczema, impetigo, scrofulosis, tubercular infections, lupus, syphilis, anemia, chorea, and facial neuralgia [101, 102].

The advent of commercial antibiotics in 1932, facilitated the control of bacteria without Cu, but also spawned the subsequent spread of antibiotic-resistant bacteria ubiquitous in hospitals, nursing homes, food processing plants, and animal breeding facilities. Therefore, different approaches are needed to keep pathogenic microorganisms at bay. One such alternative is the use of copper surfaces in hygiene-sensitive areas. Lately, Kuhn reported the beneficial effects of using brass and bronze on doorknobs to prevent the spread of microbes in hospitals [103], and Sudha reemphasized that using Cu vessels rendered water drinkable [104]. Currently, Cu and its alloys are being developed as a self-sanitizing material, and Cu has recently been registered at the U.S. Environmental Protection Agency as the first solid antimicrobial material [105]. They are fabricated into door handles, bathroom fixtures, or bed rails, in attempts to curb nosocomial infections on touch surfaces.

2.3.1 Antimicrobial efficacy of copper

Copper is an essential trace element for humans as well as bacteria, and more than 30 types of copper-containing proteins are known today, such as *lysyl oxidase*, *tyrosinase*,

dopamine β-hydroxylase, etc. In high doses, Cu ions can cause a series of negative events in bacterial cells. The precise chemical and molecular mechanisms responsible for copper's antimicrobial capabilities are still being researched, however, several molecular mechanisms had been proposed by different researchers.

1. Alteration the structure of proteins, thus deactivate their normal functions.

The accumulation of Cu ions or intracellular release of free Cu ions from proteins causes cell damage. Free Cu ions are able to oxidize *sulphydryl* groups, such as cysteine, in proteins or the cellular redox buffer glutathione [106]. Specifically, Cu ions inactivate proteins by damaging Fe-S clusters in cytoplasmic hydratases. In *Escherichia coli*, these are *dihydroxy-acid dehydratase* (DHAD) [107] in the branched-chain amino acid synthesis pathway, *isopropylmalate dehydratase* (IMD) [108] in the leucine-specific branch, *fumarase A* (FumA) [109] in the tricarboxylic acid cycle, and *6-phosphogluconate dehydratase* (6-PGD) [110] in the pentose phosphate pathway (Edd).

2. Compromising the integrity of cells

The excess Cu ions result in the imbalance of osmotic balance and disrupt the cell membrane wall, leading to leakage of specific essential cell nutrients, such as potassium and glutamate, and subsequent cell death [111].

3. Capturing electrons from the lipids in the cell membrane, causing oxidative degradation.

Copper readily catalyzes reactions that result in the production of hydroxyl radicals through the Fenton and Haber-Weiss reactions [112]. The highly reactive oxygen intermediates cause lipid peroxidation and oxidation of proteins [113,114].

There are many other theories explaining the function of Cu in killing bacteria, and the exact mechanism by which copper kills bacteria is still unknown. However, this does not affect the use of Cu alloys as self-sterilized material.

2.3.2 The use of Cu alloys as antimicrobial material

The feasibility of using Cu alloys as self-sterilizing materials depends on the release of Cu ions into the ambient environment. The soluble release of ions from metallic copper requires a critical control of corrosion. Besides, most Cu alloys remain undesirable for used in high-touch applications such as doorknob and bed rails, because they require both the sustainability of antimicrobial function and an aesthetically pleasing surface aspect. Since the corrosion of Cu

alloys also tarnishes the surface by forming a green oxide, the aesthetic function of Cu alloys needs to be settled. The use of Cu-Al alloys and Cu-Ni alloys allow a compact passive scale that is aesthetically pleasing, however, the passive layer inhibits the antimicrobial efficacy by slowing down Cu ion release. A critical balance is needed between corrosion and Cu ion release where corrosion rate is sufficient to enable the release Cu while simultaneously avoiding undesired tarnish/oxide layer formation. Cu-Sn alloys have been shown to have an enhanced Cu ion release despite a lower content of Cu due to the addition of Sn. However, the dose-response relationships of alloying effect on the corrosion and cation release of Cu-Sn in simulative high touch environments on remains as a question that lacks understanding.

2.4 Summary

This chapter gives a literature review of the corrosion of Cu-Zn alloys. The corrosion mechanisms of copper and Cu-Zn alloys are introduced, and the antimicrobial function of Cu-Sn alloys is described.

The corrosion of copper involves the formation of solid Cu_2O and soluble Cu^{2+} , either through a one-electron mechanism or by a two-electron mechanism (dissolution- redepositon).

The corrosion mechanism of Cu-Zn alloy, *i.e.* dezincification, could be achieved by two different mechanisms: a dissolution-redepositon mechanism and a preferential dissolution mechanism. As to the dissolution-redeposition mechanism, Cu and Zn dissolve simultaneously but Cu is subsequently redeposited on the surface. As to the preferential dissolution mechanism, only Zn is selectively dissolved, while Cu is not directly involved in the electrochemical process. The continuity of the process could be achieved by either a surface/volume diffusion of Cu atoms, an inward movement of vacancy and/or divacancy from surface to the depth of the alloy, or the formation of percolation due to the kinematic movement of Cu and/or Zn atoms, allowing a pathway of Zn dissolution. However, a consensus has yet to be reached.

The release of Cu ions from Cu-Sn alloys enables Cu alloys to be used as antimicrobial materials. The function played by Cu ions to kill/inactivate bacteria or bugs are: a) deactivating functions of cells by altering the structure of proteins; b) compromising the integrity of cell and c) capturing electrons from the lipids in the cell membrane, causing oxidative degradation. But the effect of alloying elements, such as Sn, on the efficacy of antimicrobial function is not clear.

This Ph.D. work attempts to address the following questions:

- ✓ **What is the dissolution behavior of Cu: the electrochemical reactions, the quantitative and qualitative information regarding the anodic dissolution products? (Chapter 4)**

- ✓ **What are the differences of dissolution behavior in tap water between a dezincification sensitive alloy (Cu-42Zn) and a dezincification resistant Cu-Zn alloy (Cu-21Zn-3Si-P)? (Chapter 5)**
- ✓ **How does the applied current, Zn content, metallurgical phase composition affect the dissolution behavior of Cu-Zn alloys? (Chapter 6)**
- ✓ **How does the Sn content in Cu-Sn alloys affect the Cu ion release? (Chapter 7)**

B. Experimental Section

In this section the composition of materials and electrolytes were presented, the pretreatment methods were elaborated. Specially, the most important technique, atomic emission spectroelectrochemistry (AESEC) was presented in terms of fundamental principle and data treatment. Surface identification measurements and their parameters were also presented.

3. Materials and experiments

3.1 Materials

In this thesis, Cu-Zn alloys and Cu-Sn alloys were investigated respectively, their elemental composition is listed in Table 3.2.

For the dezincification investigation of Cu-Zn alloys, synthetic tap water (STW) with a neutral pH of 7.5 ± 0.1 was prepared with the chemicals listed in Table 3.1. For the antimicrobial efficacy investigation of Cu-Sn alloys, synthetic perspiration solution (sweat solution) with a pH of 6.5 ± 0.05 was used as an appropriate analogue to a high-touch environment, its chemical composition is listed in Table 3.1. Citrate buffer solution with a pH buffered at 4.9 ± 0.1 was used in this project to dissolve the residual scale formed on the Cu-Zn and Cu-Sn alloys respectively. It was prepared by mixing a 0.1M citric acid ($C_6H_8O_7$) with a 0.1M trisodium citrate solution ($Na_3C_6H_5O_7$). The solutions were prepared by mixing reagent grade reagents into deionized water (Millipore™ system, $18.2 \Omega \text{ cm}$ at $25 \text{ }^\circ\text{C}$).

Table 3.1. Chemical composition of synthetic tap water

	Chemical name	mg/L	Molarity (mM)
Synthetic tap water	$Mg_2SO_4 \cdot 7H_2O$	31.92	0.12
	$CaCl_2 \cdot 7H_2O$	102.90	0.43
	$NaHCO_3$	36.00	0.43
	Na_2SO_4	275.50	1.94
Sythetic perspiration solution	$NaCl$	5000	85.6
	CH_4N_2O	1000	16.7
	$C_3H_6O_3$	1000	11.1
	NH_4OH	To adjust pH	~11

Table 3.2. Elemental composition of Cu-Zn alloys and Cu-Sn alloys

Alloy		Pure metal		Cu-Zn alloys							Cu-Sn alloys		
ISO	Zinc	Copper	Cu-10Zn	Cu-20Zn	Cu-30Zn	Cu-33Zn	Cu-37Zn	Cu-21Zn-		Cu-42Zn	Cu-45Zn	Cu-4.5Sn-0.1Zn	Cu-9.7Sn-0.1Zn
								3Si-P					
UNS ⁽¹⁾	--	C10100	C22000	C24000	C26000	C26800	C27400	C69300	--	--	C51000	C52480	
CEN ⁽²⁾	--	CW009A	CW501L	CW503L	CW505L	CW506L	CW508L	CW724R	CW510L	--	CW451K	CW458K	
Elemental composition (wt%)	Cu	--	99.9	89.0-91.0	78.5-81.5	68.5-71.5	65.5-68.5	62.5-65.5	76.00	57-57.5	55.0	95.06	89.63
	Fe	--	--	0.1	0.1	0.1	0.1	0.2	--	--	--	0.02	0.16
	Pb	--	--	0.05	0.05	0.05	0.02	0.3	0.09	--	--	0.05	0.02
	Si	--	--	--	--	--	--	--	3.00	--	--	--	--
	Sn	--	--	--	--	--	--	--	--	--	--	4.52	9.72
	P	--	--	--	--	--	--	--	0.05	--	--	--	--
	Zn	99.9	--	remaining	remaining	remaining	remaining	remaining	remaining	remaining	remaining	remaining	0.08

(1) Unified numbering system.

(2) Comité Européen de Normalisation, *i.e.*, European Committee for Standardization.

3.2 Atomic emission spectroelectrochemistry (AESEC)

The conventional electrochemical method such as potentiodynamic polarization and electrochemical impedance spectroscopy (EIS) [115], are convenient methods in predicting the corrosion rate, the evolution of the interfacial structure by constructing reliable equivalent circuits. But they lack quantitative information separating the anodic/cathodic reaction. Moreover, in the corrosion/dissolution of complex alloys, which is the case for most practical problems, the elemental corrosion/dissolution could not be identified by these methods. Spectroscopy, such as Raman spectroscopy [116], near-infrared spectroscopy (NIRS) [90], glow-discharge optical emission spectroscopy (GDOES) [117] and inductively coupled plasma-atomic emission spectroscopy (ICP-AES) [118], had been widely used in the characterization and quantification of matters. Among them, ICP-AES is a perfect analytic technique used for the detection of trace metals [119]. It is a type of emission spectroscopy that uses the inductively coupled plasma to produce excited atoms and ions that emit electromagnetic radiation at wavelengths characteristic of a particular element [120]. It is a flame technique with a flame temperature in a range from 6000 to 10000 K. The intensity of this emission is indicative of the concentration of the element within the sample. The combination of electrochemistry and ICP-AES constitutes the atomic emission spectroelectrochemistry [121]. This technique not only allows a current-potential response on the working electrode, but offers precise quantitative information regarding the elemental concentration change of the electrolyte, which can further be converted into partial elemental current. This information is of critical importance in distinguishing the passivation of stainless steel [121,122], the breakdown of coatings [123], the detachment of intermetallic particles from Al alloys [124]. In this project, this technique is demonstrated to investigate the selective dissolution of Cu alloys.

Figure 3.1 demonstrates the scheme of the AESEC technique. It will be introduced by dividing it into three parts: (A) the electrochemical reaction system; (B) the ICP-AES system and (C) the fast electronics.

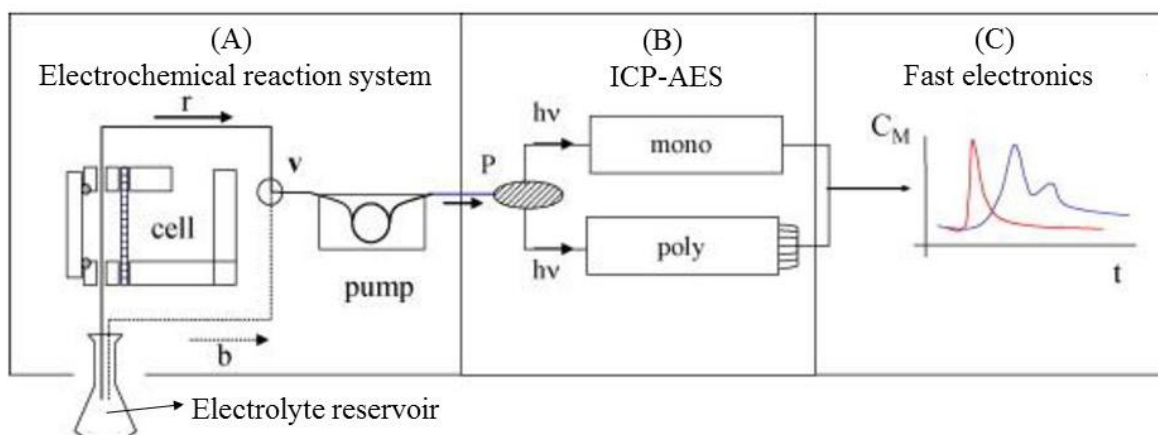


Figure 3.1. Schematic diagram of AESEC, adapted from ref [121].

3.2.1 Electrochemical flow cell

The sectional scheme of the flow cell is shown on the left side in Figure 3.2 and the picture of the real cell is shown on the right side. A conventional three-electrode system consisting a working electrode (WE), a counter electrode (CE, platinum foil) and a reference electrode (RE, saturated calomel electrode), was used. It was connected to a Gamry Reference 600™ potentiostat to measure the current-potential response. Differing from the conventional cell, the electrolyte chamber was separately into two compartments by a cellulos membrane (ZelluTrans/Roth). This membrane has a low absorption capacity that permits the conductivity between the two compartments but avoids major diffusion of ions through the membrane to another compartment. The left compartment has a small volume of ca.0.30 cm², it was directly exposed to the WE. When the electrolyte was introduced from the bottom inlet, driven by a peristaltic pump, corrosion/dissolution occurs. The electrolyte containing the kinetic information of the ion release from the WE was further driven to the ICP-AES system, allowing an online measurement of the concentration change of the electrolyte.

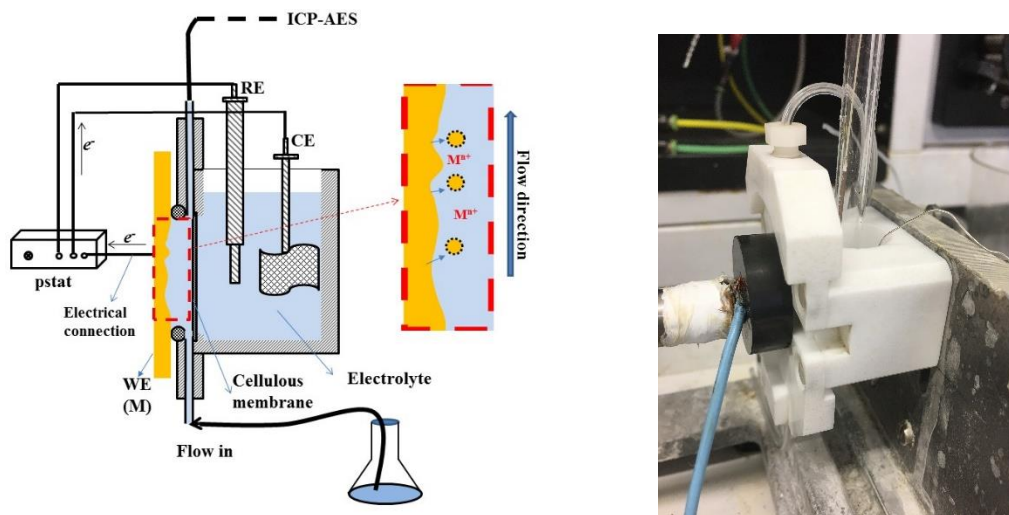


Figure 3.2. Sectional drawing of the flow cell (left) and the picture of the real cell (right)

3.2.2 Inductively coupled plasma-atomic emission spectroscopy (ICP-AES)

Inductively coupled plasma-atomic emission spectroscopy (ICP-AES) is a powerful technique detecting the trace amount of elements in the electrolyte. In this project an Ultima 2C™ ICP-AES (Horiba Jobin Yvon) was used. It uses the inductively coupled plasma to produce excited atoms and ions that emit electromagnetic radiation at wavelengths characteristic of a particular element. The emission spectrum is produced by an electronic transition from high energy level (E_2) to a low energy level (E_1) (Figure 3.3). The emitted radiation can be easily detected when it is in the vacuum ultraviolet (VUV, 120–185 nm), ultraviolet (UV, 185–400 nm), visible (VIS, 400–700 nm), and near infrared regions (NIR, 700–850 nm) [125].

Radiation ($h\nu$) emitted from the plasma are introduced through the optical system and be split by the diffraction grating (between 1800 and 4320 lines/mm). It is further introduced to the monochromator (mono) with a Czerny-Turner configuration, and a polychromator (poly) with a Paschen-Runge configuration (Figure 3.4). In the mono, the dispersing grating is flat and rotates on its axis, which gives a higher analytical accuracy; in the poly, the grating is fixed and concave, but is able to break the radiation into up to 30 different wavelengths, allowing a simultaneous detection of 30 different elements.

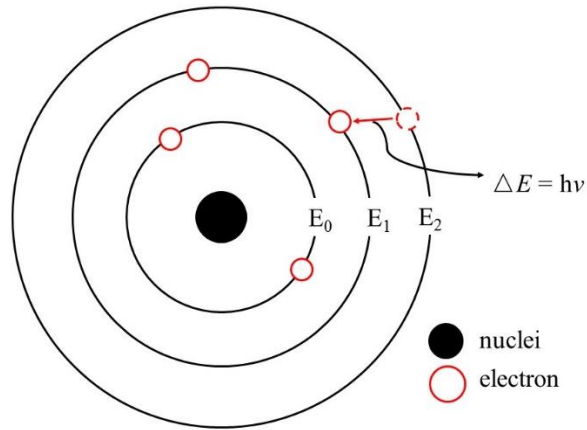


Figure 3.3. Schematic diagram of emission of radiation upon relaxation from high energy level.

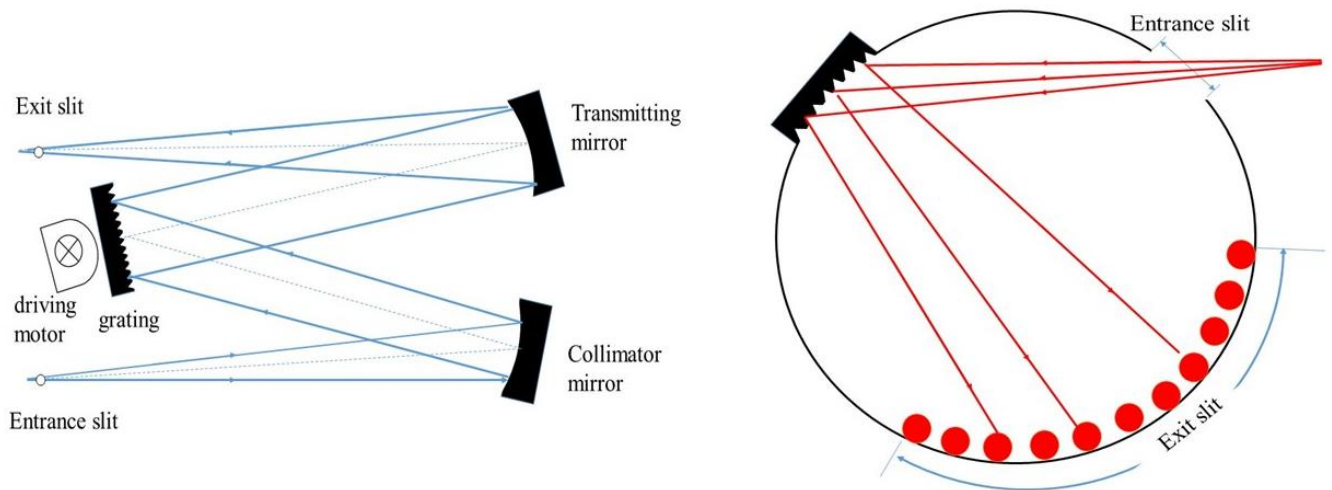


Figure 3.4. The schematic diagram of monochromator (left) and polychromator (right).

3.2.3 Fast electronics

The light diffracted from the exit slit of the poly or mono will be converted into an electrical current by photomultiplier tubes (PMT). A PMT is a vacuum tube containing a photosensitive called photocathode. This material emits electrons when subject to light. The electrons are accelerated to a dynode and causes further ejection of second electrons. These second electrons are then accelerated and multiplied, being collected on the anode. The current

measured on the anode will be proportional to the quantity of light reaching the cathode and the voltage (V) applied to the dynode.

The signal from the 31 PMTs (30 ploy + 1 mono) will further be processed by three 16-bit A/D converters operating at a frequency of 250 kHz, then transferred to the Quantum™ software and data acquisition system. The data acquisition time in this PhD project was set to be 1.0 s, which means that the signal intensity at each second corresponds to the average value of the previous 25000 data within the second. The use of these A/D converters significantly improves the time resolution.

3.2.4 Data treatment

ICP-AES data

The signal obtained through the Quantum™ software express the elemental concentration as Intensity (I) with an arbitrary unit. Since the data acquisition time is set to be 1 point/s, an $I-t$ curve will be obtained. However, in order to convert the signal intensity into the concentration of each element, a calibration curve is indispensable: 3 × 10 ml of electrolyte containing a known concentration of the target elements were prepared; they were passed into the ICP-AES and a set of intensity $I_1 \sim I_3$ were obtained; before this step a blank solution which contains no target elements was passed and the intensity I_0 was obtained. A linear relationship between ($I - I_0$) and concentration (C) was obtained (Figure 3.5), so a relationship between the intensity and the concentration was established:

$$C = \frac{I - I_0}{\alpha} \quad 3.1$$

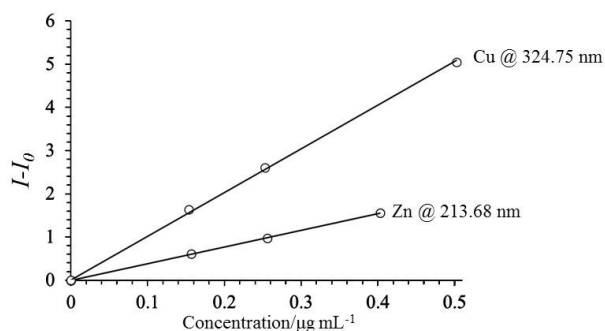


Figure 3.5 Calibration curve of Cu and Zn in synthetic tap water.

where α represents the sensitivity for the element. Note that the concentration in the electrolyte can further be converted into the dissolution rate (v) from the working electrolyte (WE) considering the flow rate and the exposure area. Take the element Cu as an example:

$$v_{Cu} = \frac{fC_{Cu}}{A} \quad 3.2$$

v_{Cu} is the dissolution rate ($\text{mol s}^{-1} \text{ cm}^{-2}$) of elemental Cu into the electrolyte, f is the flow rate ($\text{cm}^3 \text{ s}^{-1}$) of electrolyte driven by the pump, A is the exposure area (cm^2) of the sample. Note that this dissolution rate only represents the average value within the exposure area, the possible uneven distribution of corrosion could not be identified. This dissolution rate could further be expressed as equivalent current using Faraday's law, assuming a known valence state of the element:

$$j_{Cu} = nFv_{Cu} \quad 3.3$$

where j_{Cu} represents the partial current (A cm^{-2}) of Cu; n is the number of electrons passed during the reaction and F is the Faraday constant (96500 C mol^{-1}).

Convolution

The kinetic information obtained directly from the ICP-AES represents only the soluble species, the kinetics of insoluble species could not be immediately obtained by the QuantumTM software. However, they can be indirectly obtained comparing the total current j_e and j_{Cu} . Note that during the passage of electrolyte through the flow cell, the hydrodynamics in the cell leads to a non-ignorable broadening of the signal, this is demonstrated in Figure 3.6. A certain volume of pure water was fed into ICP-AES without passing through the flow cell, no element could be detected so the intensity was zero for simplification; when $t = 0 \text{ s}$, a 10 M Cu containing electrolyte was injected into the capillary, resulting in an immediate response of intensity increase (peak *a*). when the identical electrolyte was fed into ICP through the flow cell, the peak would be broadened, as is shown as peak *b* in the figure.

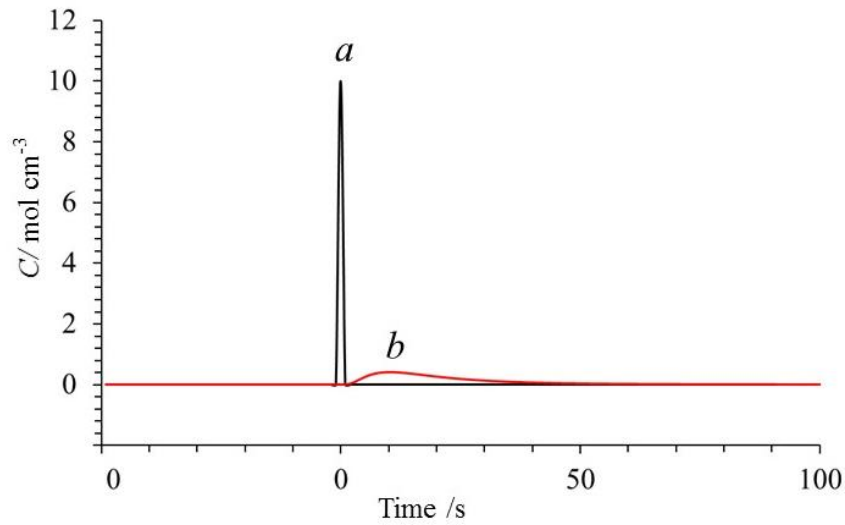


Figure 3.6. scheme showing the hydrodynamic effect within the flow cell.

All the kinetic data obtained directly from the AESEC system had been broadened due to the hydrodynamic effect, which differs from the instantaneous signal such as current and potential signal, a direct comparison among them is thus not possible. In order to solve the problem, a convolution of the current signal (v_e) was conducted.

$$v_e^* = \int_0^t v_e h(t - \tau) dx \quad 3.4$$

where $h(t)$ is the residence time distribution (RTD) of the electrochemical flow cell. Experimental measurement of the RTD has shown that it closely follows a log normal distribution:

$$h(t) = \sqrt{\frac{\beta}{\pi\tau^2}} e^{-\frac{1}{4\beta}} e^{-\beta \ln^2(t/\tau)} \quad 3.5$$

where τ and β are empirically determined parameters for the log-normal fit parameters. In this work, $\tau = 10.23$ s and $\beta = 0.99$ were used determined from a previously published variation of $h(t)$ with flow rate [126].

3.3 Corrosion product identification and morphology characterization

Crystalline products were identified using grazing incidence X-ray diffraction (GIXRD) using a PANalytical X'Pert diffractometer with copper $K\alpha$ radiation. Incident grazing angle gave optimal signal/noise at $\omega=0.5^\circ$ with a 10 mm width limiting mask. 2Θ ranged from 20 to 100 °. Compounds were identified by comparison to powder diffraction database (ICDD® PDF-

4+). Detection limits of crystalline compounds for this instrument and methodology are approximately 5 vol%.

Raman spectroscopy measurements performed post-exposure were acquired using a Renishaw InVia Raman microscope, utilizing a 514 nm line of an argon laser with 180 ° back scattering geometry and a 3000 1/mm grating. For compound identification, Raman spectra were compared with prepared in-house cold-pressed powder samples of known molecular identity and structure. To avoid thermal heating and conversion of sample corrosion products by laser illumination, low laser intensities with long (~minutes) acquisition times were used.

X-ray Photoelectron Spectroscopy (XPS) was also employed to investigate the corrosion products formed on Cu-Sn alloys. A Thermo-Scientific K-Alpha™ XPS system was equipped with an Al K α monochromatic X-ray source and an Ar ion gun for sputtering. High-resolution scans were taken with a pass energy of 20 eV and a spot size of ~0.5 mm². Au 4f_{7/2} was used as an energy reference assigned to 84.0 eV. Peak fits were made using a Shirley background and a Gaussian-Lorentzian shape. Spin orbit energy splits were set as the only constraint with all other parameters unconstrained for the best software fit.

A Zeiss Leo 1530 field emission scanning electron microscope (FE-SEM) was used to observe the surface morphology of brass samples after being exposed to STW. An in lens second electron detector was used to capture the image; the extra high tension (EHT) was fixed at 5 kV.

C. Results Section

This section presents the most important results of the thesis. The synthetic tap water – citrate buffer solution experiment (STW-CBS) was firstly utilized in the anodic dissolution of pure Cu (**Chapter 4**), aiming at identifying quantitative and qualitative relationships of solid/soluble species. Then the same technique was applied to the dissolution of two commercial Cu-Zn alloys: Cu-42Zn (dezincification sensitive) and Cu-21Zn-3Si-P (dezincification resistance) (**Chapter 5**). The dissolution behaviour of two alloys were compared and discussed in this chapter. In **chapter 6** the technique was extended to the dissolution of Cu-Zn alloys with Zn content ranging from 0 to 45 wt%. Effect of Zn content on the formation of different species was presented and discussed. A different dissolution mechanism regarding α and β' phase was proposed. Finally, the effect of Sn content on the release of Cu ions in synthetic perspiration solution (SPS) was investigated, the results are presented in **Chapter 7**.

Chapter **4 and 5** has been published as full text article in *Electrochimica Acta* in 2016 and 2017. Results from **Chapter 6** are under preparation for another full text article that will be submitted to *Electrochimica Acta* as well. Results from Chapter 7 belongs to an international collaboration project with University of Virginia, these results have also been published as a full text article in *Electrochimica Acta*.

4. The anodic dissolution of copper alloys in synthetic tap water: Pure copper

4.1. Introduction

The corrosion of copper (Cu) and its alloys is a troublesome problem due to their large-scale use in potable water plumbing systems [9,21-33] resulting in the premature failure of tubes and fittings, toxicity due to Cu release, and costly expenses involved in waste water disposal. Besides the sporadic tubercle blockages due to the deposition of scales, superfluous soluble Cu release into water not only causes serious health problems [21], but induces accelerated corrosion elsewhere in iron pipelines [29], which are also largely utilized in water distribution system. To date, much work has been conducted to investigate factors that affect corrosion of copper and its alloys. Water chemistry [29,31], surface states of sample [22], temperature [37] and pretreatment [38], all affect the corrosion of Cu and its alloys in a complicated way, to the extent that data from field work often contradicts results from laboratory work. In order to unravel the source of these controversies, a clear mechanistic explanation of the corrosion process is indispensable.

There are many mechanistic explanations of copper corrosion in the literature including the one-electron and the two-electron reaction mechanisms [55,56]. The one-electron reaction mechanism describes the corrosion behavior of Cu such that cuprite is the direct reaction product deposited on copper, and soluble species are released by further reaction of cuprite into Cu(II) species [40,41]. However, other workers have inferred that copper was oxidized into Cu(II) species directly [26], resulting in an equilibrium state between the Cu(II) species and Cu(I) species by disproportionation of Cu(I) or synproportionation between Cu(0) and Cu(II) [58-60]. It is commonly accepted that cuprite (Cu_2O) forms on the surface and constitutes a non-protective scale during the corrosion of copper in tap water [51]. Some researchers found trace amount of precipitated Cu(II) species such as $\text{Cu}(\text{OH})_2$ and malachite ($\text{Cu}_2\text{CO}_3(\text{OH})_2$) [33], however these species were mostly produced in high alkalinity water or after a long period of immersion. The theory that cuprite is the predominant insoluble corrosion product has been popularly proposed. But the origin of Cu_2O , its interrelationship to soluble species, together with its kinetic information is still unclear.

The addition of some saline constituents into water, together with dissolved oxygen, organic and inorganic matter, altogether exacerbate the corrosivity of typical tap water [127-, 128, 129, 130, 131]. Cations such as K^+ , Na^+ and Ca^{2+} exhibit a minor effect on water corrosivity [132], though Ca^{2+} is believed to form calcium carbonate that can mitigate corrosion [133, 134]. Anions such as Cl^- and SO_4^{2-} are oxidants that improve copper corrosion [135]. However, the synergistic effect among these anions is complex [128], and these mechanistic speculations are less reliable in predicting Cu corrosion. Some researchers have tried to quantitatively explore the relationship of insoluble and soluble species [136]: Xiao et al [28] tried to explain copper corrosion by differentiating peaks among the XPS spectra; Feng [57], M. Drogowska [137], Nakayama [138] used a small cathodic current to dissolve the solid corrosion products and to identify the corrosion products based on the potential features of the potential vs. time curve, and determine their relative proportions through charge conservation. However, XPS analysis is only a semi-quantitative method and galvanostatic cathodic reduction has poor time resolution [138]. In addition, the nature of the residual oxide film may play an important role in the dissolution mechanism, especially for a porous or defect-rich structure [51]. Hultqvist and Szakalos proposed the existence of hydrogen evolution via water reduction during Cu corrosion in anoxic pure water [46,49,139,140], which was considered to be thermodynamically unlikely and thereby disputed [50,141]. In principle, this phenomenon could be explained by the catalytic property of the corrosion product produced through the one-electron mechanism [141]. A similar idea was proposed by Jacobs and Edwards [142], who evoked the catalyzing nature of sulfide in Cu corrosion.

In this chapter, the anodic dissolution of Cu in synthetic tap water (STW) ($pH = 7.5 \pm 0.1$) was investigated using in situ atomic emission spectroelectrochemistry to monitor Cu dissolution directly and scale formation by mass balance. In this way it is possible to access the question of Cu dissolution stoichiometry directly. In the next chapter, the approach described here will be extended to investigate the dezincification of Cu-Zn alloys.

4.2. Experimental

4.2.1 Materials

Oxygen-free, high thermal conductivity Cu (Goodfellow, purity: 99.95+ %) was used in this work. The material was cut into 25 mm \times 25 mm \times 3 mm specimens and ground with 400

and 600 grit SiC paper, rinsed with deionized water, degreased with acetone, ethanol, and then dried under flowing nitrogen.

Synthetic tap water (STW) [143] containing $200 \text{ mg L}^{-1} \text{SO}_4^{2-}$, $50 \text{ mg L}^{-1} \text{Cl}^-$, $30.5 \text{ mg L}^{-1} \text{HCO}_3^-$, $27.9 \text{ mg L}^{-1} \text{Ca}^{2+}$, $3.4 \text{ mg L}^{-1} \text{Mg}^{2+}$, and $101.2 \text{ mg L}^{-1} \text{Na}^+$ was prepared using reagent grade chemicals and deionized water (Millipore™ system, $18.2 \text{ } \Omega \text{ cm}$ at $25 \text{ } ^\circ\text{C}$). The anion composition in this STW was taken from [143], however, cations like Ca^{2+} and Mg^{2+} were partially replaced by Na^+ so as to simulate a soft tap water after being ion exchanged from a hard tap water. The STW has an alkalinity of 84 mg L^{-1} as CaCO_3 and its pH and conductivity were 7.5 ± 0.1 and $479 \text{ } \mu\text{S cm}^{-1}$, respectively.

A citrate buffer solution (CBS) with $\text{pH} = 4.9 \pm 0.1$ was used to dissolve corrosion products formed on the surface after exposure to STW. It was prepared with 0.1 M citric acid solution (AppliChem) and 0.1 M sodium citrate solution (Amresco), and then mixed to achieve the target pH value. Unless otherwise noted, all the citrate buffer solutions were de-aerated for at least 30 min by Ar bubbling and were used under flowing Ar.

4.2.2 Instrumentation

A custom designed flow cell, described in detail elsewhere [118, 126,144], was used for these experiments. A platinum plate with a geometry area of 5 cm^2 and a saturated calomel electrode (SCE) were used as the counter and reference electrode, respectively. The Cu specimens were used as the working electrode with a surface area of 1 cm^2 defined by the geometry of the o-ring. The flow rate $f = 3 \text{ cm}^3 \text{ min}^{-1}$. All experiments were conducted at ambient temperature of approximately 25°C . A potentiostat (Gamry Reference 600™) was used to control current or potential and monitor the open circuit potential.

Atomic emission spectroelectrochemistry (AESEC) was used to monitor the instantaneous concentrations of Cu and other ions downstream from the flow cell using an inductively coupled plasma optical emission spectroscope (Jobin Yvon Horiba, Ultima 2™). Details of this system may be found in previous work [144]. The copper dissolution was followed using a monochromator to detect the emission intensity of the 324.75 nm line of atomic Cu with a typical detection limit of less than 1 ppb (defined as three times the standard deviation of the blank with a 1 s integration time) under the conditions of our experiment. All the AESEC experiments were calibrated using three standards (10 ppb , 20 ppb , 30 ppb of Cu in STW and 20 ppb , 50 ppb , 80 ppb of Cu in CBS) with a correlation coefficient $R^2 \geq 0.99$.

Bulk sample X-ray diffraction (XRD), grazing incidence X-ray diffraction (GIXRD) and Raman spectroscopy were used to analyze the residual Cu oxide film following exposure of Cu to STW with a galvanostatic current of $80 \mu\text{A cm}^{-2}$ for 1200 s. Diffraction experiments were performed on a PANalytical X'Pert Diffractometer with a Cu target ($K\alpha = 1.54 \text{ \AA}$). A fixed incident angle of 0.5° ($\omega=0.5^\circ$) was used to limit the excitation depth into the sample. Crystalline surface oxides can be detected using GIXRD. Bulk XRD of samples was performed using a spinning sample stage. The same sample was also used to obtain Raman spectra with a Renishaw InVia Raman microscope consisting of a 514 nm Ar ion Laser in 180° backscattering geometry, and a 3000 g/mm grating. The laser illuminated spot diameter was approximately $1 \mu\text{m}$ focused through a 50×0.75 NA objective. Pressed Cu_2O powder reference was prepared and investigated with a 488 nm laser.

4.2.3 Data Analysis

We may assume that Cu oxidation leads to the formation of both soluble and insoluble corrosion products. The formation of soluble corrosion products is monitored via the Cu dissolution rate, $v_{\text{Cu(aq)}} \text{ (nmol s}^{-1}\text{)}$. This value is determined directly from the downstream Cu concentration by Eq. 4.1:

$$v_{\text{Cu(aq)}} = fC_{\text{Cu}} \quad 4.1.$$

where f is the flow rate of the electrolyte ($\text{cm}^3 \text{ s}^{-1}$) and C_{Cu} is the downstream concentration of Cu determined from the spectral emission at 324.75 nm using standard analytical ICP-AES procedures. The electrical current was measured simultaneously, and in order to compare the two values on a quantitative scale, it is useful to convert the current to an electron transfer rate ($\text{nmoles e}^- \text{ s}^{-1}$):

$$v_e = i_{ap}/F \quad 4.2.$$

where i_{ap} is the electrical current (nA cm^{-2}) and F is the Faraday constant. This conversion is used for stoichiometric analysis since converting the dissolution rates into equivalent currents requires an assumption of the oxidation state of the dissolved Cu. For a mass balance it is often of interest to use an integrated form of the Eqn. 4.1 and 4.2 which will refer to the total quantity, Q , of either copper or electrons. For example, the total quantity of Cu dissolved in CBS will be referred to as $Q_{\text{Cu(CBS)}}$ while the total quantity of electrons passing through the potentiostat will be referred to as $Q_e(\text{pstat})$. Other terms useful for mass/charge balance will be defined as needed.

For kinetic measurements, it is important to consider the time resolution of the experiment. Eq. 4.1-4.2 are written in terms of instantaneous variables. Indeed, the electrical current may be considered as an instantaneous measurement on the time scale of these experiments, however Cu dissolution will be broadened by the residence time in the electrochemical flow cell [126]. The extensive diffusion layer and low convection rate result in a significant broadening of the concentration transient with respect to v_e , leading to a convolution integral relationship between v_e and v_e^* :

$$v_e^* = \int_0^t v_e h(t - \tau) dx \quad 4.3.$$

where $h(t)$ is the residence time distribution (RTD) of the electrochemical flow cell. Experimental measurement of the RTD has shown that it closely follows a log normal distribution:

$$h(t) = \sqrt{\frac{\beta}{\pi\tau^2}} e^{-\frac{1}{4\beta}} e^{-\beta \ln^2(t/\tau)} \quad 4.4$$

where τ and β are empirically determined parameters for the log-normal fit parameters. In this work, $\tau = 10.23$ s and $\beta = 0.99$ were used determined from a previously published variation of $h(t)$ with flow rate [126].

4.3. Results

4.3.1 Mass and charge balance in acid electrolytes

It was of interest to validate Eq. 4.1 and 4.2 under conditions in which the oxidation states of dissolved Cu are well known. This was achieved via dissolution experiment of Cu in de-aerated 0.6 M HCl and 1.5 M H₂SO₄, for which an $n = 1$ and an $n = 2$ dissolution mechanism have been observed [49], respectively. Typical dissolution profiles are given in Figure 4.1. These profiles are divided into three periods: For $t < 0$ and for $t > 300$ s, the Cu specimen reacted with the electrolyte at open circuit and the corrosion rate, v_{corr} , was estimated from the steady state Cu concentration by Eqn. 4.1 during the open circuit periods, assuming only soluble Cu corrosion products. The open circuit dissolution rate was measured for 20 minutes prior to $t = 0$, although Figure 1 shows only the final 50 s of this exposure. At $t = 0$, a galvanostatic pulse of $40 \mu\text{A cm}^{-2}$ was applied for a duration of 300 s, followed by a return to the open circuit potential for 300 s. The spontaneous corrosion rate was determined to be $0.015 \text{ nmol s}^{-1}$ in HCl and $0.014 \text{ nmol s}^{-1}$ in H₂SO₄ prior to the anodic pulse, and was nearly identical within

experimental error after the anodic pulse, following a several hundred second waiting period post anodic pulse.

Figure 4.1 shows both the original current, v_e , and the convoluted current, v_e^* . The dashed curve shows $v_e^* + v_{corr}$ which allows a comparison between the dissolution rate and the current corrected for the background corrosion rate. For 0.6 M HCl electrolyte, it is observed that $v_{Cu(aq)}$ and v_e^* follow each other closely indicative of an $n = 1$ mechanism. For 1.5 M H_2SO_4 the AESEC results are compared with $v_e^*/2$ in anticipation of an $n = 2$ mechanism and again the good correlation between v_{Cu} and v_e^* confirms this hypothesis.

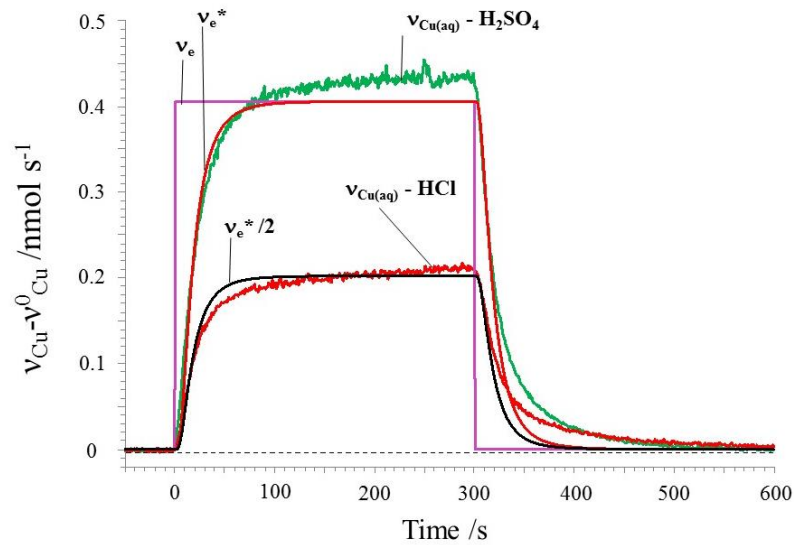


Figure 4.1 Typical Cu dissolution transients at open circuit and during a $40 \mu A \cdot cm^{-2}$ for 300 s galvanostatic pulse in deaerated 1.5 M HCl and 0.6 M H_2SO_4 .

The ability of the AESEC technique to quantitatively estimate the n value for anodic dissolution is demonstrated by the mass balance in Figure 4.2. To produce this analysis, a series anodic galvanostatic pulses of $\Delta t = 300$ s were applied to the sample ranging from $i_{ap} = 5 \mu A \cdot cm^{-2}$ to $100 \mu A \cdot cm^{-2}$ with a 300 s open circuit delay between each pulse. The quantity of electricity, Q_e (pstat), was obtained by integrating the current transient, which under galvanostatic conditions is simply

$$Q_e(\text{pstat}) = i_{ap} \Delta t / F \quad 4.5$$

To determine the n value, it is necessary to compare $Q_e(\text{pstat})$ with the quantity of Cu released by the anodic current, $Q_{an, aq}$. The latter is determined from the total amount of Cu dissolved during the experiment, Q_{aq} (integrated from $t = 0$ s to 600 s), by subtracting the integral of the corrosion rate, $Q_{an, corr}$:

$$Q_{an, aq} = Q_{Cu} - Q_{an, corr} \quad 4.6$$

where $Q_{an, corr}$ is estimated by assuming that the dissolution rate is identical during the anodic pulse:

$$Q_{an, corr} = v_{corr} \Delta t \quad 4.7$$

From a mass / charge balance:

$$Q_e(pstat) = n Q_{an, aq} = Q_e(ICP) \quad 4.8$$

The experimental data are shown as discrete data points. The hypothetical lines predicted for an $n = 1$ and $n = 2$ mechanism are shown as solid lines. The average experimental stoichiometry factor in this current range was 1.81 for copper dissolution in H_2SO_4 , while $n = 1.06$ was measured in 1.5 M HCl.

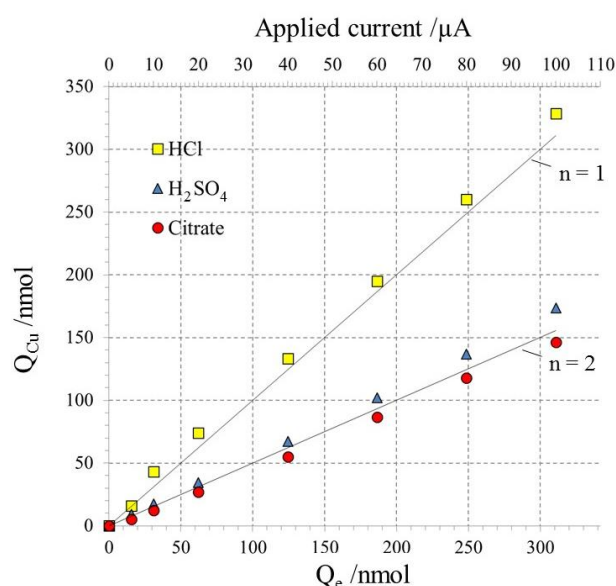


Figure 4.2. Total copper dissolution quantity (Q_{Cu}) in the range of applied current from 0 $\mu A cm^{-2}$ to 100 $\mu A cm^{-2}$, in HCl (\square) H_2SO_4 (Δ), and citrate buffer solution (\circ) respectively, vs. total quantity of electrons (Q_e) as measured from stepwise galvanostatic dissolution experiments.

4. 3.2 The STW – CBS Dissolution Experiment

The experimental protocol for Cu in STW was identical to that previously presented for Cu dissolution in acid solutions however a direct mass balance may not be performed because a significant quantity of insoluble Cu corrosion products was formed. Therefore, following the STW experiment, the electrolyte was changed to the CBS electrolyte with the idea of dissolving any residual oxide films that may have formed on the surface during the STW experiment.

A typical dissolution profile for a STW-CBS experiment is shown in Figure 4.3. Again, v_e , v_e^* , and $v_{Cu(aq)}$ are given as a function of time along with the potential, E (vs. SCE). The experiment is divided into four periods. (I) Firstly, the Cu specimen was allowed to react with

STW for 300 s at open circuit during which period the spontaneous rate of Cu dissolution, v_{corr} , was measured. (II) Then a galvanostatic pulse of $i_{\text{ap}} = 40 \mu\text{A}$ was applied for $\Delta t = 1200$ s. This period is associated with a large positive shift in E due to the high resistivity of the STW electrolyte. Note that throughout this period, $v_{\text{Cu(aq)}} \ll v_e^*$, which implies that an insoluble film is formed during this experiment. (III) Next, the sample returned to the open circuit potential again for 300 s. (IV) Finally the dissolution of the residual oxide film was performed at open circuit in the CBS electrolyte.

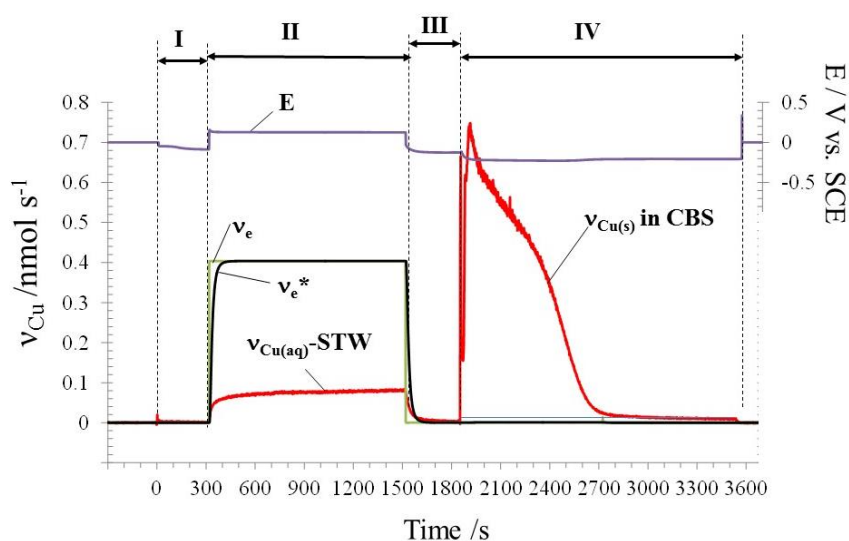


Figure 4.3. Typical anodic dissolution of copper in STW, followed by open circuit dissolution in citrate buffer solution (STW- CBS experiment). I, initial open circuit for 300 s in STW; II, Anodic polarization of copper in STW, $i = 40 \mu\text{A cm}^{-2}$, $t = 1200$ s; III, second open circuit dissolution for 300 s in STW. IV, CBS was introduced to naturally dissolve the residual scale on surface.

The initial open circuit dissolution of copper in STW (see the expanded scale version in Figure 4.4) was very slow with an average value of $v_{\text{Cu(aq)}}$ of approximately $2 \pm 1 \times 10^{-3} \text{ nmol s}^{-1}$ during this period, corresponding to an average steady state concentration of about 2.6 ppb Cu. This is very close to the detection limit of approximately 1 ppb, although clearly detectable as seen in Figure 4.4.

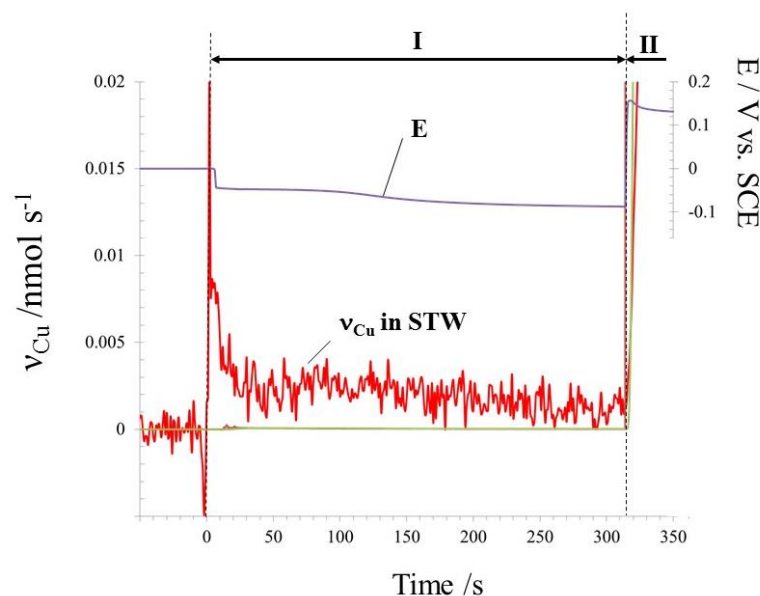


Figure 4.4. Enlarged view of open circuit dissolution (stage I and II in Figure 4.3).

During the galvanostatic pulse (stage II), $v_{Cu(aq)}$ increased rapidly during the first 100 s and then rose very slowly to obtain $0.080 \pm 0.004 \text{ nmol s}^{-1}$ by the end of the experiment. However, $v_{Cu(aq)}$ is much less than v_e^* throughout the anodic pulse indicative of the formation of insoluble Cu oxidation products. The second open circuit delay in STW (stage III) showed a rapid decrease of Cu to a value that is comparable to the initial open circuit dissolution rate. The result suggests that the scale formed during anodic polarization does not significantly alter the corrosion rate of Cu.

In order to estimate the quantity of scale formed during the polarization, the sample was then exposed to de-aerated citrate buffer solution (CBS) (stage IV). This electrolyte was chosen because citrate is a common reagent used in Cu and brass descaling formulations [145]. Cu dissolution reached a maximum within 50 s, followed by a sharp decrease for 900s. A subsequent steady state dissolution of Cu was observed afterwards. The onset of scale dissolution also coincided with a sharp drop of E to about -0.22 V vs. SCE, followed by a slight rise to -0.20 V vs. SCE. By the end of the experiment, the average $v_{Cu(aq)}$ was approximately 0.01 nmol s^{-1} .

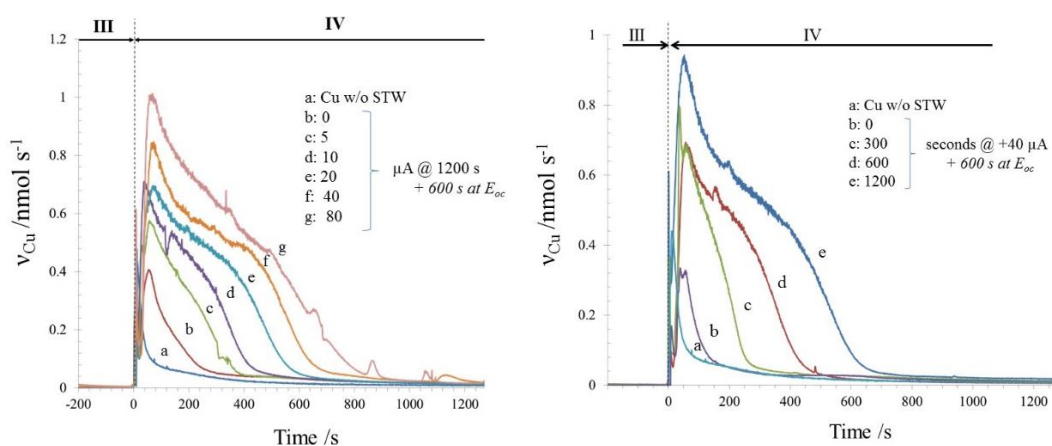


Figure 4.5. Superimposition of stage III + IV from Figure 4.3. Left: variation of applied current; Captions a-g represent: a: fresh copper in CBS; b: 0 $\mu\text{A cm}^{-2}$ in STW; c: 5 $\mu\text{A cm}^{-2}$ in STW; d: 10 $\mu\text{A cm}^{-2}$ in STW; e: 20 $\mu\text{A cm}^{-2}$ in STW; f: 40 $\mu\text{A cm}^{-2}$ in STW; g: 80 $\mu\text{A cm}^{-2}$ in STW;

The experiment of Figure 4.3 was conducted for variable applied current, i_{ap} , for a constant anodic polarization time, $\Delta t = 1200$ s (Figure 4.5A); and a variable Δt at $i_{ap} = 40$ $\mu\text{A cm}^{-2}$ (Figure 5B). For clarity, only the CBS dissolution step is shown in Figure 5. The dissolution profile of pure Cu exposed to CBS electrolyte without any exposure to STW (curve a) is also shown as a reference. For all experiments involving STW exposure, the total duration of the open circuit period (I + III) was maintained constant at 600 s as in Figure 4.3.

At least three distinct features are observed in the dissolution profiles of Figure 4.5 which for convenience we have labelled α , β and γ . A sharp peak (α) occurs immediately when the CBS electrolyte contacts the Cu surface. This is particularly noticeable, and is in fact the only peak observed, for the uncorroded Cu specimen. This is followed by a slow and broad dissolution that is itself divided into two features: a rather rapid maximum (β) and a very broad shoulder (γ). Following this, ultimately $v_{Cu(aq)}$ returns to a steady state value of 0.014 ± 0.003 nmol s^{-1} where the error represents the standard deviation of all the experiments of Figure 4.5. Note that this value is comparable to open circuit dissolution rates observed in deaerated 0.6 M H_2SO_4 and 1.5 M HCl . The unexposed Cu surface shows only a sharp peak at the origin and falls off slowly to obtain $v_{Cu(aq)} = 0.01 \pm 0.002$ nmol s^{-1} , somewhat lower but comparable to that of the other surfaces.

The second, broad peak undergoes a systematic growth with either increasing applied current or increasing time and is absent for the surface without exposure to STW. This clearly demonstrates that Cu dissolution in the second peak in the CBS electrolyte may be attributed to the formation of a residual film during open circuit or galvanostatic exposure to STW electrolyte.

4. 3.3 Mass and Charge Balance for Anodic Dissolution of Cu in STW

The systematic increase of the CBS dissolution peak with the growth of the residual oxide film suggest that the integral of the peak may be used as a quantitative measure of the oxide film. The mass balance is however more complex than was the case for 0.6 M H₂SO₄ and 1.5 M HCl in the previous section as both a soluble and an insoluble species are formed during the TW exposure. The oxidation of Cu in the STW solution may occur via either spontaneous corrosion or by the applied anodic current and in both cases may lead to a soluble and an insoluble component:

$$\text{Total Cu oxidized} = Q_{corr, aq} + Q_{corr, s} + Q_{an, aq} + Q_{an, s} \quad 4.9$$

As in the previous section, it is possible to investigate the stoichiometry of dissolution by a mass/charge balance. However, the situation is more complex, as the solid and aqueous forms of Cu may have different oxidation states. The quantity of soluble Cu released by the anodic reaction, $Q_{an, aq}$, may be estimated by analogy to Eqn. 4.5 and 5.6. (For this case however, the spontaneous corrosion is negligible.) Likewise, the solid component of the anodic reaction, $Q_{an, s}$, may be determined from:

$$Q_{an, s} = Q_{Cu (CBS)} - Q_{Cu (CBS)}(i_{ap} = 0 \mu\text{A cm}^{-2} \text{ or } \Delta t = 0 \text{ s}) \quad 4.10$$

A mass balance for the system gives:

$$Q_e(pstat) = n_{aq} Q_{an, aq} + n_s Q_{an, s} = Q_e (ICP) \quad 4.11$$

Following the lead of previous investigations, it is reasonable to assume that the solid oxide film is Cu₂O, formed by an $n = 1$ mechanism and that the soluble component is Cu(II) in aqueous solution. To verify these two hypothesis, a charge balance was performed comparing $Q_e(ICP)$ with $Q_e(pstat)$ for variable applied current (Figure 4.6A) and variable time (Figure 4.6B). The excellent convergence of both $Q_e(pstat)$ and $Q_e(pstat)$ to the line with a slope $n = 1$, demonstrates the validity of this assumption. Of course, this does not rule out the possibility of minor components, Cu(II) in the residual film or Cu(I) in the soluble component.

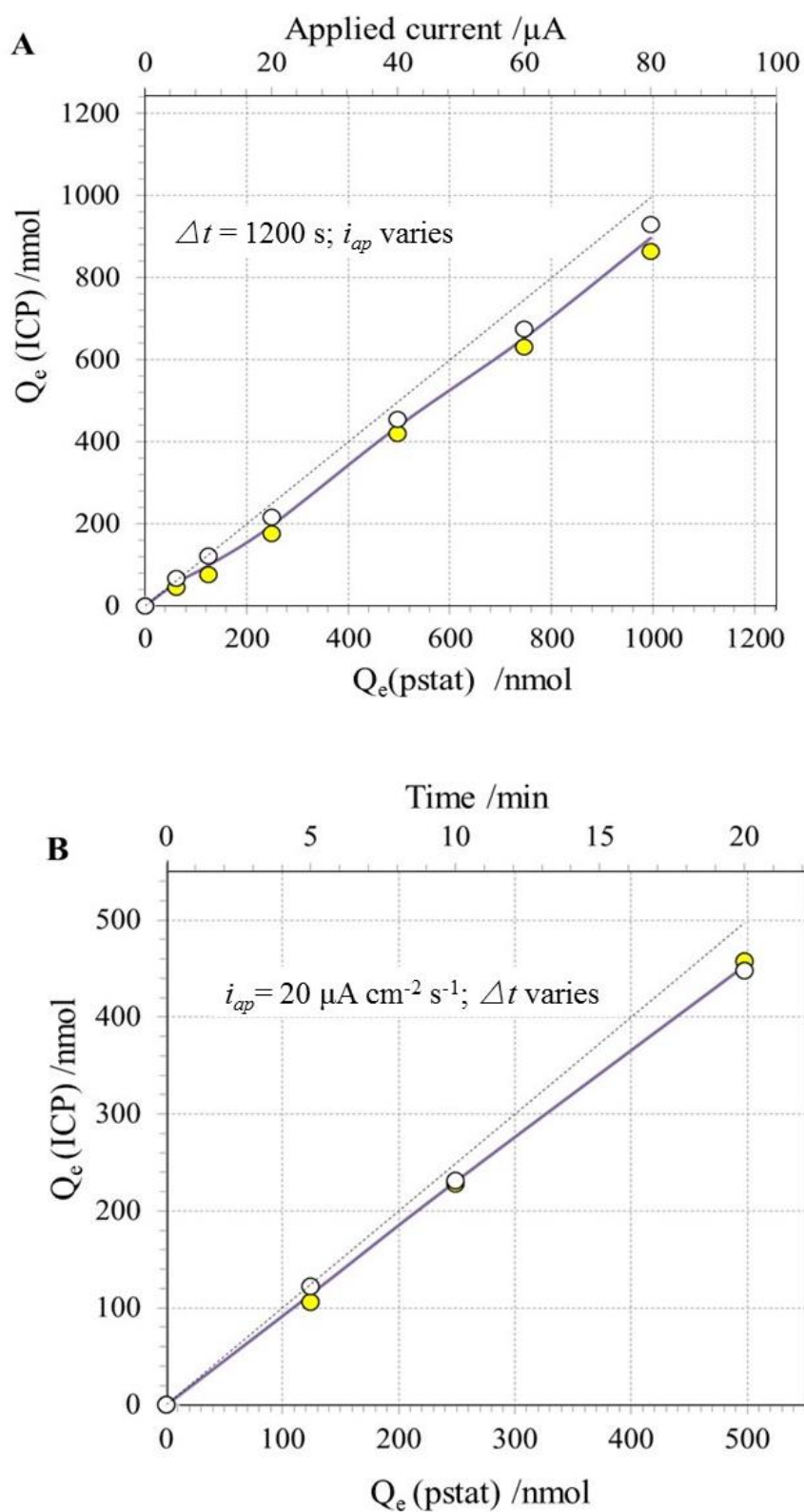


Figure 4.6. Relationship of Q_{Cu} to Q_e as a function of applied current (A) and a function of time (B). Replicate experiments (marked as colored and hollow \circ) were conducted individually. Trend lines were plotted by averaging the replicate experimental data at each current.

Following these results, it is possible to give a kinetic result for Cu dissolution in STW as a function of current at 1200 s (Figure 4.7A) and as a function of time at 40 μA (Figure 4.7B). Shown is the quantity of dissolved Cu and the quantity of the residual film. In Figure 4.7A we see that Cu_2O is formed preferentially at low current.

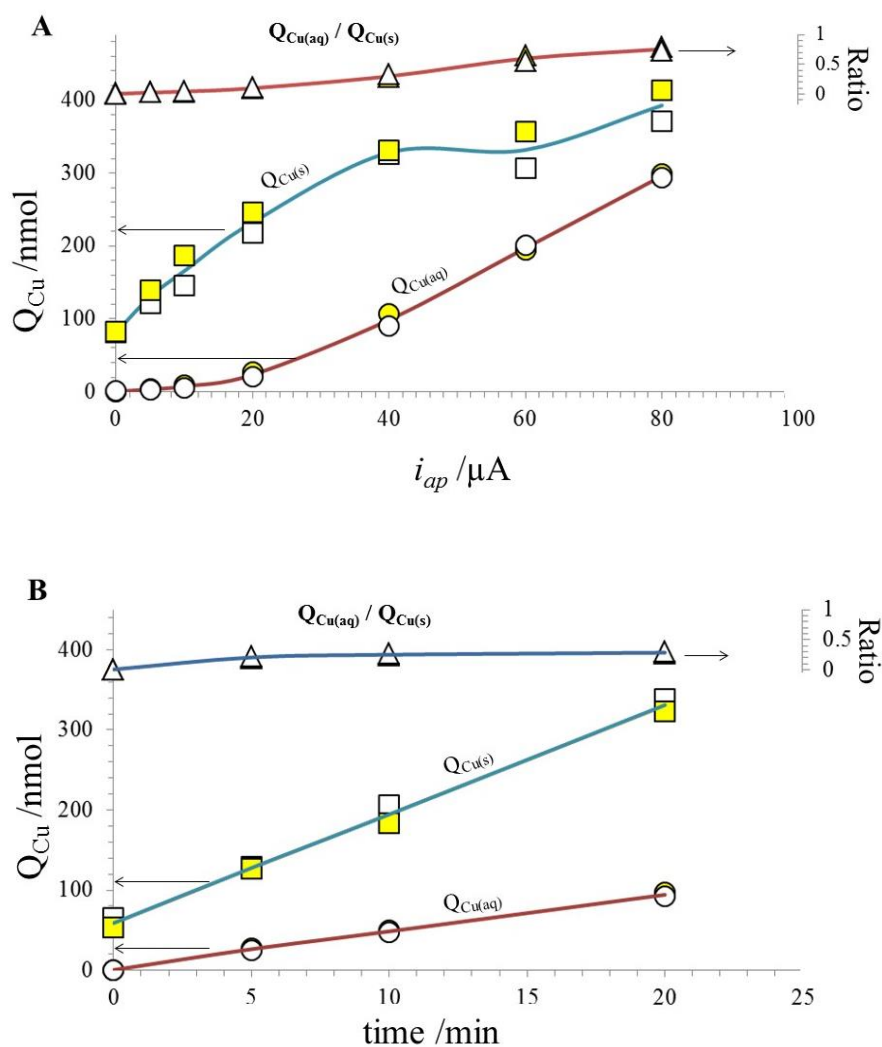


Figure 4.7. Comparison between soluble species $Q_{\text{Cu(aq)}}$ (marked as ○), and solid species $Q_{\text{Cu(s)}}$ (□) as a function of applied current (A) and a function of time (B). Ratio of $Q_{\text{Cu(sol)}}$ to $Q_{\text{Cu(insol)}}$ (△) was also plotted in the second axis. Their trend lines were plotted using averages values of the replicate experiments.

To further verify the formation of the Cu_2O film, XRD and Raman experiments were conducted. Figure 8 gives the GIXRD pattern for Cu after an anodic pulse of $80 \mu\text{A cm}^{-2}$ for 20 min. It is clear from Figure 4.8, that the brown scale on the surface is mainly cuprite. However, we cannot rule out the presence of cupric species either in an amorphous form or present at a

depth beyond the penetration of the X-ray photons; the presence of Cu fcc peaks confirm that the X-rays penetrated to the substrate, rather than been isolated by a thick oxide film. *Ex situ* Raman spectroscopy (Figure 4.9) was obtained on the same sample, to analyze possible crystalline or amorphous species, together with their stoichiometry information. The peaks at 150 cm^{-1} , 220 cm^{-1} , and 650 cm^{-1} proved the existence of Cu_2O , but the main peak of CuO at 650 cm^{-1} is close to that of Cu_2O [116], so identification of CuO is not reliable through this Raman analysis. Yohai *et al.* [67, 115,116] proposed that the existence of CuO in Cu_2O would significantly decrease the peak intensity. However, no sign of peak weakness was observed in Figure 9, which corroborates the AESEC experiment.

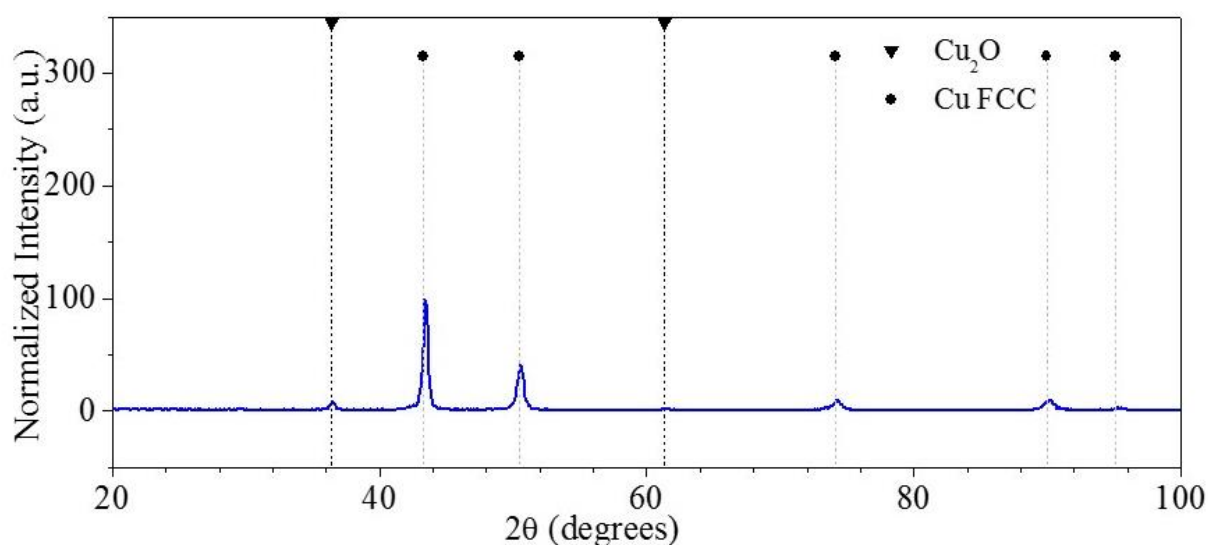


Figure 4.8. Grazing incidence X-ray diffraction analysis of copper exposed to STW, being anodically polarized at $80\ \mu\text{A cm}^{-2}$ for 20 min.

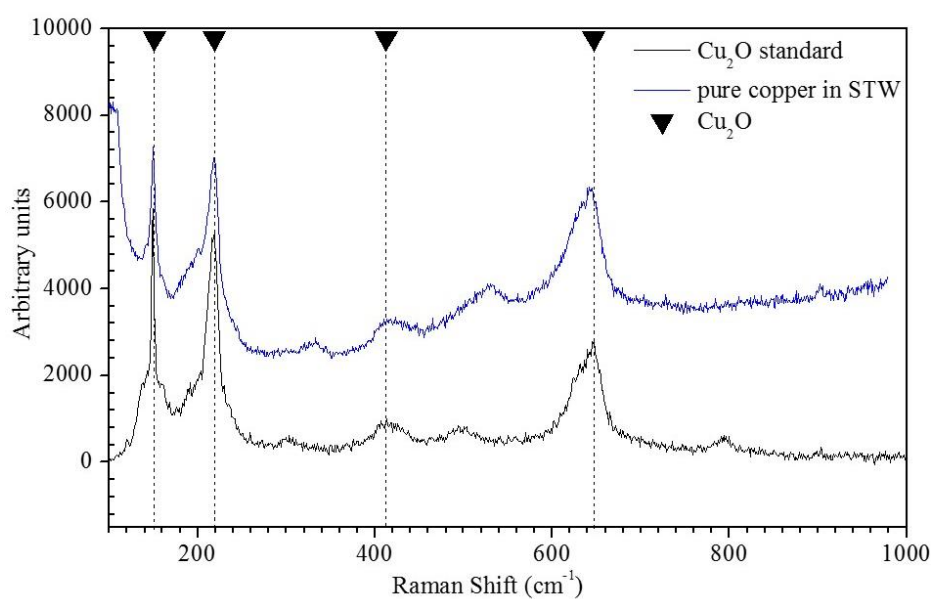


Figure 4.9. Ex-situ Raman analysis of copper exposed to STW with applied current $i = 80\ \mu\text{A cm}^{-2}$ for 20 min.

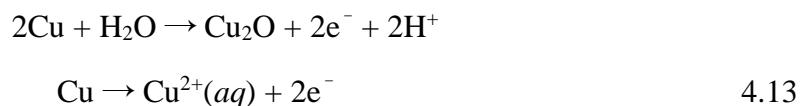
4. 3.4 Kinetic analysis

In the previous section we demonstrated that $\text{Cu}_2\text{O}(\text{s})$ and $\text{Cu}(\text{II})(\text{aq})$ are the major products of Cu corrosion either at open circuit or under anodic polarization in STW. Therefore, from a mass balance, we can write the rates of the elementary reactions for Cu dissolution as:

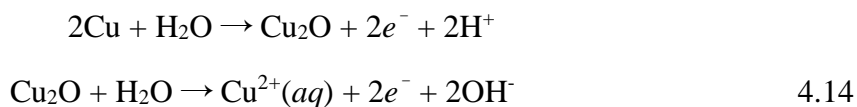
$$v_{\text{Cu}_2\text{O}} = [v_e^* - 2v_{\text{Cu}(\text{aq})}(\text{STW})] / 2 \quad 4.12$$

The variation of v_e^* , $v_{\text{Cu}_2\text{O}}$ and $v_{\text{Cu}(\text{aq})}$ with time is given in Figure 4.10 for two values of applied current: $40 \mu\text{A cm}^{-2}$ and $10 \mu\text{A cm}^{-2}$. In both cases it is observed that all three rates increase simultaneously at $t = 0$ within the time resolution of these experiments. Following the review of Section 1, we may describe three different mechanisms for Cu dissolution:

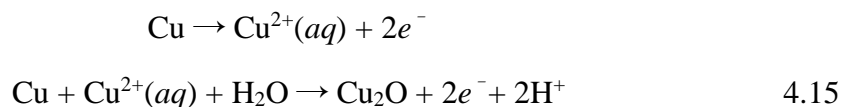
a simultaneous mechanism,



a sequential mechanism,



and a redeposition mechanism,



Of course these mechanisms represent global reactions that are accessible by AESEC. Intermediate steps involving for example, surface complexation and short lived adsorbed intermediates are not accessible through the measurements presented here and will not be discussed.

It is clear that in both cases of Figure 4.10, the dissolution rate rises simultaneously with the electrical current. This would strongly suggest a simultaneous mechanism as proposed in Eq. 13, or at least that the sequential mechanisms are happening on a time scale that is larger than the time scale of these experiments. Curiously for $10 \mu\text{A cm}^{-2}$, the dissolution rate rises through a maximum which might be consistent with the dissolution redeposition mechanism of Eq. 4.15.

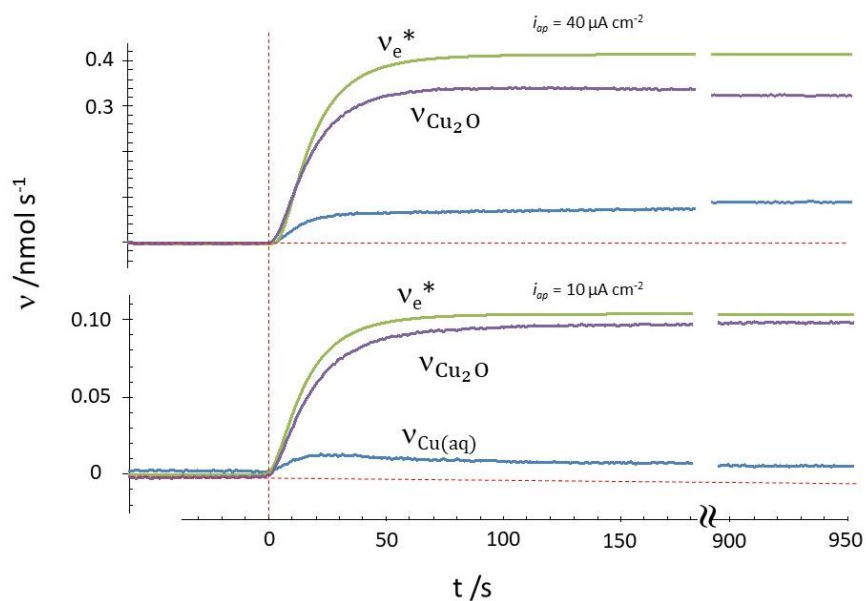


Figure 4.10. Superimposition of copper dissolution in STW at various current.

4. 4. Conclusion

The results presented here demonstrate that the AESEC method may be used to monitor the kinetics of anodic Cu dissolution. The instantaneous dissolution rate of Cu was measured in real time and compared with the simultaneous measurement of electrochemical current. From a mass/charge balance, it was revealed that the majority species formed during anodic polarization are soluble Cu(II) and insoluble Cu(I). The insoluble species was quantified after the experiment by dissolution in a citrate buffer solution.

The solid corrosion products were characterized by Raman and XRD analysis which confirmed that a Cu_2O film forms on the Cu surface at open circuit and during anodic polarization. Quantitative relationships of Cu(I), Cu(II) species vs. applied current and vs. time duration of galvanostatic pulse were presented.

5. An in situ kinetic study of brass dezincification and corrosion

5.1. Introduction

The corrosion process of brass often involves a mechanism of dezincification in which Zn is selectively dissolved leaving behind a porous metallic Cu enriched layer. Dezincification is a major limiting factor for the use of brass in numerous applications and is also a model system for the selective dissolution of a binary alloy. It is not surprising that much attention has been paid to the mechanistic explanation of dezincification [12,64,75,87,146,147,148,, 149, , 150, 14,15,78, 151, 152] and the characterization of the dezincification structure [89, 91,92, , , 153]. Numerous theories have been proposed, though, during the last decades, they can ultimately be categorized into two major groups: mechanism of selective dissolution and mechanism of dissolution-redeposition. As to the first group, theories such as volume diffusion of Zn [151] and/or Cu [152], surface diffusion [72], sometimes in conjunction with divacancy movement [148-150], as well as the percolation mechanism [81], are most representative. They depict a selective dissolution process of Zn without the electrochemical involvement of atomic Cu. The dissolution-redeposition of Cu [147], however, describes an simultaneous dissolution of both Cu and Zn, followed by a process of Cu plating back onto the surface, thus forming a defective metallic Cu layer.

A difficulty in identifying the underlying mechanisms of brass corrosion has been the fact that the oxidation of the brass, frequently measured as an anodic current in an electrochemical experiment, usually involves at least two different elements and results in both soluble and insoluble species. Various methods have been proposed to measure the partial dissolution rates of Zn and Cu. Intermittent chemical analysis of Cu and Zn in the electrolyte was used by Pickering *et al.* [149,150], and the radioactive emissions of isotopes of Zn and Cu were followed by Polunin [14] and Pchel'nikov *et al.* [15]. However, these methodologies have various drawbacks: intermittent electrolyte analysis neglects important transitional concentration changes, and the irradiation effect of radioactive indicators may cause the radiolysis of the electrolyte, thus affecting the corrosion process [154] and in any case, is only applicable to special alloys produced with isotopic Cu and Zn.

Another problem is the complex nature of the oxide and zinc depleted metallic layers that are formed during corrosion. Most academic research of dezincification has been performed in acidic media where no oxide is formed [65,66]. However, the nearly neutral pH of tap water leads to a more complicated corrosion process and more severe dezincification [57] despite the lower corrosion rate. This dezincification severity and complexity is due to the formation of a multi-layered dezincification structure consisting of a Zn depleted layer and a corrosion product layer composed of Zn and Cu oxides [5].

Conventional electrochemical methods such as potentiodynamic polarization [93] and electrochemical impedance spectroscopy (EIS) [93,94] have been used to predict the corrosion rate and to characterize the electrical properties of the interfacial structure. *In situ* techniques such as Raman spectroscopy [88], infrared reflection absorption spectroscopy (IRAS) [89], near normal incidence reflectance spectroelectrochemical technique (NNIRS) [90] and ultraviolet-visible (UV-vis) reflectance spectroscopy [91] can be used to observe the molecular identity of the oxide. But no quantitative kinetic information about Cu release into water, the growth of oxide layers, or the growth of the zinc depleted layer, has obtained through these methods.

In this work the kinetics of dezincification are quantified using the atomic emission spectroelectrochemical (AESEC) methodology [121]. This technique permits us to measure directly the rates of Cu and Zn dissolution *in situ* and in real time, and indirectly the rate of oxide and metallic Cu film formation. In the previous chapter [155], we established the feasibility of using *in situ* AESEC [118,126] to analyze copper dissolution in synthetic tap water in which a detailed quantitative relationship between the soluble Cu(II) ions and the insoluble Cu₂O film was obtained as a function of applied current. In this chapter these previous studies are extended to the anodic dissolution of two commercial plumbing brasses in synthetic tap water.

The kinetic methods are demonstrated using two types of commercial brass: A conventional dual α , β' phase low-leaded Cu-42Zn alloy that is fairly sensitive to dezincification, and a lead-free Cu-21Zn-3Si-P which is considered to be much more resistant. These commercial plumbing alloys are largely utilized in North America, Europe and Asia. The microstructure of Cu-42Zn are characterized by an even distribution of α (Cu₃Zn) phase within the β' (CuZn) phase matrix [156, 157]; the microstructure of Cu-21Zn-3Si-P shows about 60% of α phase with some silicon-rich kappa (κ , Cu₈Zn₂Si [158]) phase and gamma (γ , Cu₄ZnSi) phase dispersed within the matrix and the boundary respectively [159]. The corrosion performance of the two alloys had not yet been thoroughly investigated. It is well known that

Cu-42Zn, as it contains a large amount of β' phase, is sensitive to dezincification due to the existence of β' phase; Cu-21Zn-3Si-P, as a new Pb-free alloy that shows an excellent dezincification resistance, forms complex triple-phase structure due to the addition of Si and P. Seuss *et al.* [146] investigated the corrosion resistance of Cu-21Zn-3Si-P in aggressive tap water and found that dezincification initiates from these less noble κ and γ phases, and then being inhibited by a “phosphorous cycle”. However, no further information regarding the dissolution kinetics and the mechanism can be provided.

5.2. Experimental

5.2.1 Materials

Brass discs of low-leaded Cu-42Zn and lead-free Cu-21Zn-3Si-P of Φ 24 mm \times 2 mm were used in this work. Their elemental composition can be found in Table 5.1. Unless otherwise specified, samples for electrochemical experiments were dry ground up to P1200 (600 grit) silicon carbide paper, rinsed with deionized water ($0.0549 \mu\text{S cm}^{-1}$ at 25 °C) using a Millipore™ system), degreased with acetone, ethanol, and then dried under flowing nitrogen.

Synthetic tap water (STW) [160] containing $\text{MgSO}_4 \cdot 7\text{H}_2\text{O}$ (31.92 mg L^{-1}), NaHCO_3 (36.00 mg L^{-1}), $\text{CaCl}_2 \cdot 7\text{H}_2\text{O}$ (102.9 mg L^{-1}), Na_2SO_4 (275.5 mg L^{-1}), was prepared utilizing deionized water, with a pH of 7.5 ± 0.1 and a conductivity of $479 \mu\text{S cm}^{-1}$. Citrate buffer solution (CBS) was used to dissolve the solid corrosion products formed during dissolution in STW, it was prepared by adjusting the pH value of 0.1 M citrate acid (AppliChem) solution to 4.9 ± 0.1 , using 0.1 M citrate trisodium solution (Amresco), and deaerated for at least 30 min with an argon bubbling system before use.

Table 5.1 Compositions of brass samples

Alloy	Cu	Si	P	Zn	Pb	Fe	Ni	Sn	Al	Mn
Cu-42Zn	57.5	< 0.01	< 0.01	42	0.17	0.12	0.01	0.27	< 0.01	< 0.01
Cu-21Zn-3Si-P	75.8	3.06	0.05	21	0.05	0.02	0.01	0.01	< 0.01	< 0.01

5.2.2. Dezincification test.

The ISO 6509 dezincification test [161, 162] was performed in a 1 g l⁻¹ CuCl₂ solution, with the sample being exposed to the electrolyte for 24 hours at 75 ± 5°C and then observed under optical microscope to measure the dezincification depth.

5.2.3. Instrumentation

The atomic emission spectroelectrochemistry (AESEC) technique was used to follow elemental dissolution kinetics during the corrosion and electrochemical polarization of brass. Details of this technique can be found in previous publications [126,163]. Cu dissolution was followed using a monochromator to detect the atomic Cu emission intensity at 324.75 nm. Zn and Si were followed using a polychromator detecting the atomic emission intensity at 213.68 nm and 251.61 nm respectively. A conventional three-standard calibration was conducted for each element. The detection limit (LOD) was defined as three times the standard deviation of background noise divided by the sensitivity (α), which can be determined from the intensity – concentration calibration line. The LOD for Cu in STW and CBS was less than 1 ppb, for Zn it was 6 ppb and for Si it was 17 ppb. A Gamry Reference 600TM potentiostat was used to control and/or measure the current and potential. The analog output of the potentiostat was routed into the data acquisition system of the ICP spectrometer so that spectroscopic intensity and electrochemical data were on an identical time scale.

A two compartment flow cell was used in this work with a reaction area of $A = 1.0 \text{ cm}^2$, and a flow rate $f = 3.0 \text{ mL min}^{-1}$. Details of the cell can be found elsewhere [126]. A platinum foil with an area of 5.0 cm^2 was used as a counter electrode and a saturated calomel electrode (SCE) was used as reference electrode.

A PANalytical X'Pert X-ray Diffractometer using a Cu target ($K\alpha = 1.54 \text{ \AA}$) was used to analyze the sample following anodization at $80 \mu\text{A cm}^{-2}$ in STW. Grazing incidence X-ray diffraction (GIXRD) with an incidence angle (ω) of 0.5 ° was performed on the oxidized sample. Bulk sample X-ray diffraction (XRD) was performed on a spinning stage.

A Renishaw InVia Raman microscope equipped with a Renishaw CCD camera detector was used to characterize the oxide composition: An Ar ion laser was used with an excitation line at 514 nm focused through a 50×0.75 NA objective, in conjunction with a grating of 1800 g / mm. Reference Cu₂O spectra were obtained by analyzing the Cu₂O powder (Sigma Aldrich).

A Zeiss Leo 1530 field emission scanning electron microscope (FE-SEM) was used to observe the surface morphology of brass samples after being exposed to STW. An in lens second electron detector was used to capture the image; the extra high tension (EHT) was fixed at 5 kV.

5.2.4. Electrochemical experiments and data analysis

Anodic polarization of brass samples was conducted in STW at an applied current (i_{ap}) ranging from 0 to 80 $\mu\text{A cm}^{-2}$ for 1200 s, or with a time duration (Δt) of 0 s, 300 s, 600 s, 1200 s respectively at $i_{ap} = 40 \mu\text{A cm}^{-2}$. Before and after the polarization, a 300 s open circuit delay was also imposed respectively. After that, STW was replaced by CBS for a further open circuit dissolution of 1500 s, aiming at dissolving the residual solid corrosion products on the surface.

A detailed description of the data analysis, including the conversion of the emission intensity profile into dissolution rate profile and the convolution of applied current, was given in a previous publication [155].

5.3. Results

5.3.1. Dezincification test result.

The ISO6509 accelerated corrosion test confirmed that the Cu-21Zn-3Si-P was significantly less sensitive to dezincification as compared to Cu-42Zn, Figure 5.1. In the micrographs of Figure 5.1A, the β' phase of Cu-42Zn shows a preferential dezincification as compared to the α matrix, with the dezincification front penetrating along the dezincified β' phase. As expected, the test of Cu-21Zn-3Si-P (Figure 5.1B) shows a better dezincification performance under identical test conditions, with an undetectable dezincification structure visible at the magnification of Figure 5.1B.

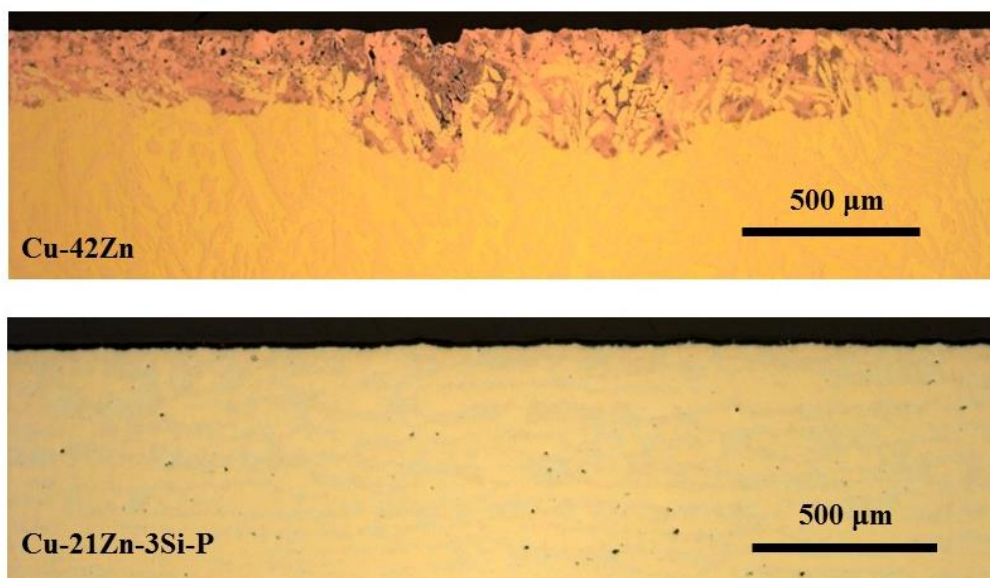


Figure 5.1. Optical microscope observation of the dezincification structure of Cu-42Zn (upper) and Cu-21Zn-3Si-P (lower) following an ISO 6509 dezincification test. The red defect-rich structure on the cross section is the dezincification structure.

5.3.2. Elemental dissolution behavior in synthetic tap water (STW)

The differences in dezincification kinetics of the two alloys, exemplified by Figure 5.1, is also apparent in the transient elemental dissolution rates during accelerated dezincification tests in synthetic tap water (Figure 5.2). A typical full experiment is given in Figure 5.2 for Cu-42Zn (A) and Cu-21Zn-3Si-P (B) respectively. The experiment is divided into four stages: (a) an open circuit dissolution in STW for 300 s; (b) a galvanostatic pulse for 1200 s; (c) another open circuit dissolution for 300 s; and finally (d) dissolution of residual oxide films formed during (a – c) by exposure to CBS at open circuit dissolution for 1500 s. Prior to $t = 0$ s, the pure electrolyte was fed into the plasma permitting a measurement of the background intensity and detection limit for each element. These experiments were performed with either an applied anodic galvanostatic current ranging from 0 to $80 \mu\text{A cm}^{-2}$ for 1200 s, or a time duration ranging from 0 to 1200 s at $40 \mu\text{A cm}^{-2}$.

The Cu and Zn dissolution rates, $(v_{\text{Zn}(aq)}, v_{\text{Cu}(aq)})$ and the electron transfer rate, v_e , are given as a function of time in Figure 5.2. This type of presentation will be referred to as a dissolution profile. Also shown is the electron transfer rate convoluted with the hydrodynamic distribution of time constants in the flow cell, v_e^* . This corrects for the different time resolution between the electrochemical data which is essentially instantaneous, and the elemental dissolution rates which are broadened by mixing in the cell, capillaries, and nebulization system [42]. Also presented is the sum of the elemental dissolution, $v_{\Sigma} = v_{\text{Zn}(aq)} + v_{\text{Cu}(aq)}$. This data set has been

multiplied by a factor of 2 to facilitate comparison with ν^*_e (see below.) Si dissolution was also followed, but it is not shown due to a poor signal to noise ratio.

The open circuit dissolution rates of Zn and Cu in STW were readily measured for both alloys, although it is not apparent on the scale of Figure 5.2. An enlarged view of the open circuit dissolution STW is shown in Figure 5.3A and 5.3B. The average open circuit dissolution rates for each alloy in STW (stage *a*) are listed in Table 5.2. Also listed in the table are the theoretical congruent dissolution rates of Cu and Si in STW and CBS, with reference to the experimental Zn partial corrosion rate, based on the component ratio of the bulk. For both alloys in STW (Table 5.2), the Cu partial corrosion rate is significantly lower than the congruent value calculated from the Zn dissolution rate. This rate discrepancy is indicative of a selective Zn dissolution process leaving behind either an oxidized Cu film or a metallic Cu layer.

Table 5.2. Steady dissolution rate of brass alloys in STW (upper) and deaerated CBS (lower).

		Zn	Cu	Cu (congruent)
		pmol s ⁻¹	pmol s ⁻¹	
STW	Cu-42Zn	9.59 ± 5.22	0.60 ± 0.85	13.43
	Cu-21Zn-3Si-P	5.22 ± 1.02	1.67 ± 1.11	18.84
CBS	Cu-42Zn reference	1.82 ± 2.11	2.32 ± 0.78	2.55
	Cu-42Zn	3.28 ± 1.68	5.40 ± 0.78	4.59
	Cu-21Zn-3Si-P reference	1.39 ± 1.83	3.13 ± 0.92	5.13
	Cu-21Zn-3Si-P	1.65 ± 0.69	6.98 ± 1.28	6.09

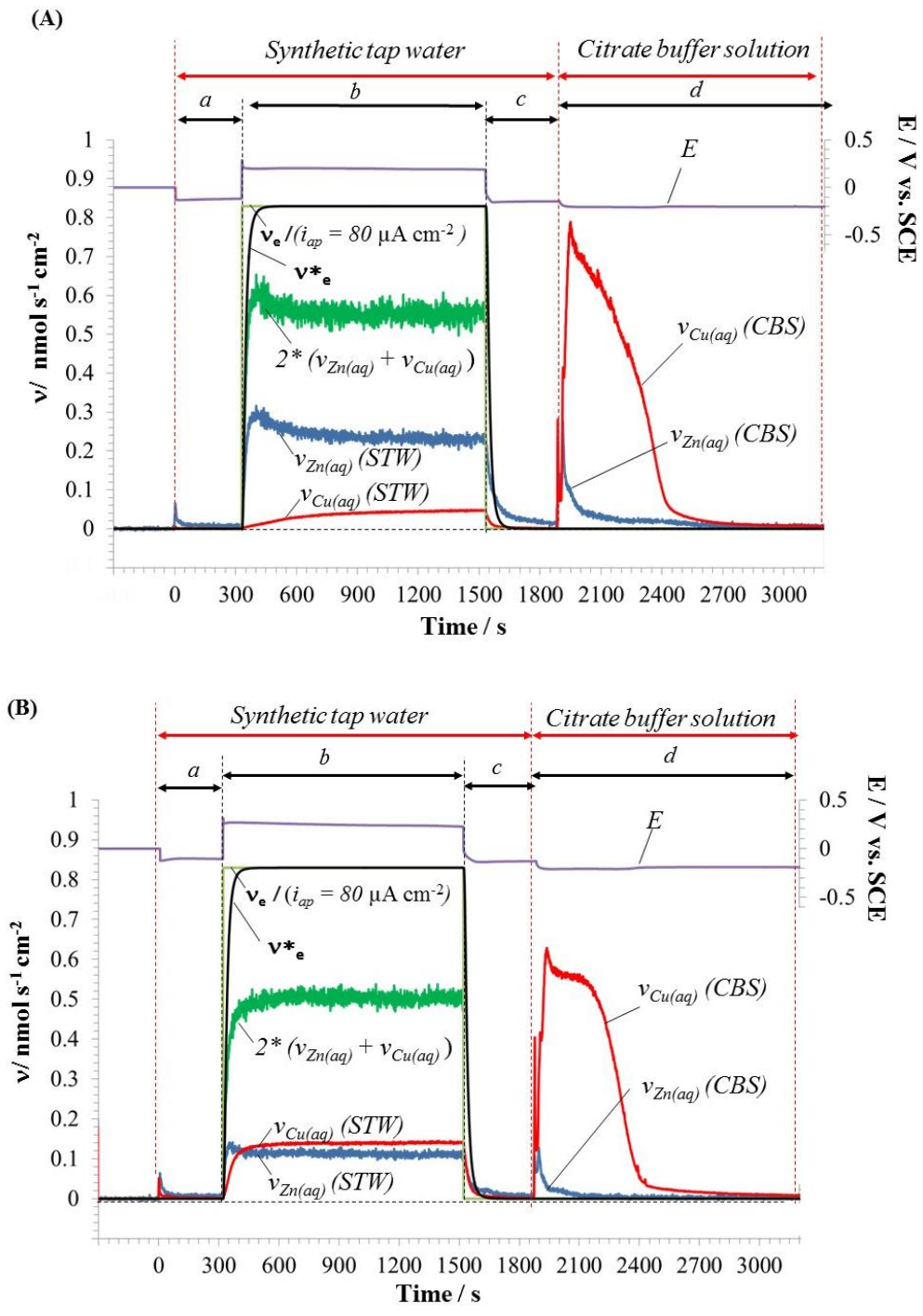


Figure 5.2. S STW-CBS experiment of Cu-42Zn (A) and Cu-21Zn-3Si-P (B) at $i_{ap} = 80 \mu\text{A}$. a: open circuit in STW for 300 s; b: galvanostatic dissolution in STW at $80 \mu\text{A}$ for 1200 s; c: open circuit in STW for 300 s; d: open circuit in CBS for 1500 s.

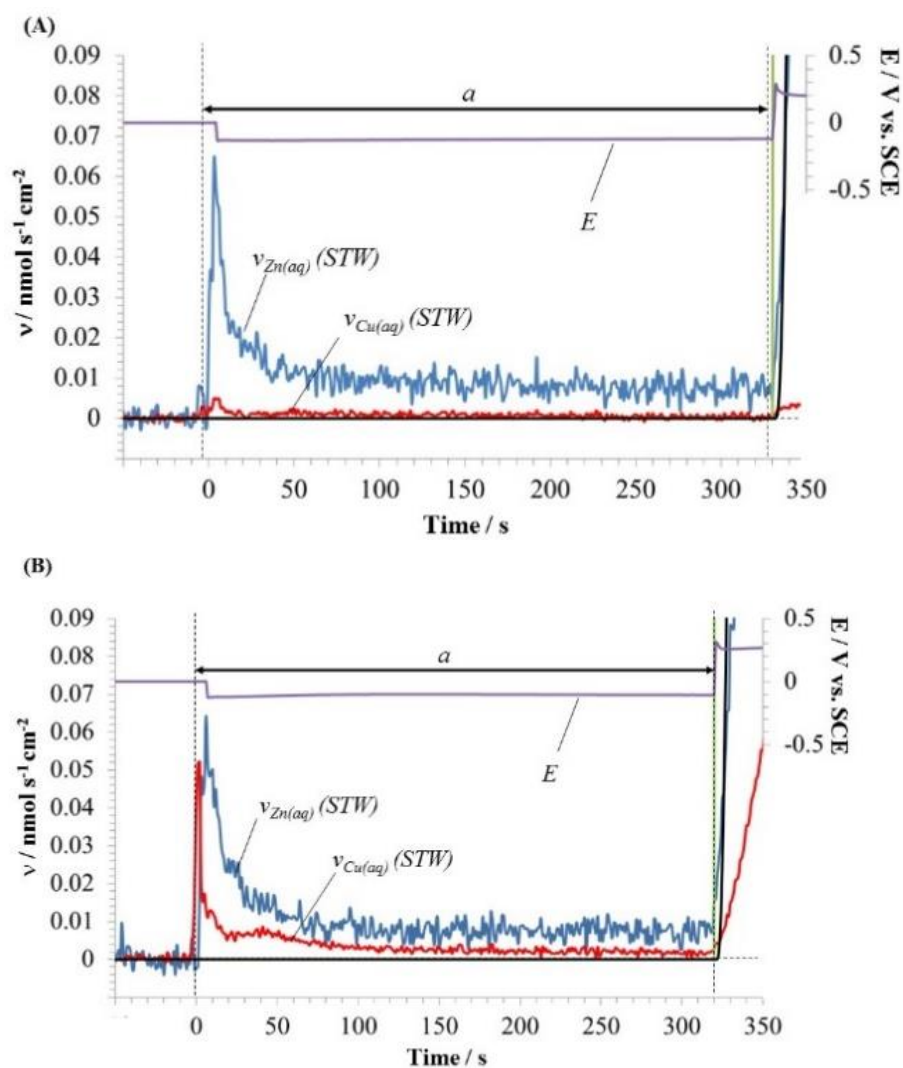


Figure 5.3. Enlarged view of the open circuit dissolution transient of Cu-42Zn (A) and Cu-21Zn-3Si-P (B).

It is of interest to compare this Zn selective leaching with that observed in the CBS electrolyte directly at the end of the experiment, (stage d in Figure 5.2). This data is also given in Table 5.2. In this case, the Cu dissolution rate was equivalent to or slightly higher than the estimated congruent dissolution rate indicating that Cu corrosion products were soluble in this electrolyte.

Insight into the formation of oxide films during the galvanostatic pulse may be derived from a quantitative consideration of the dissolution rates as compared to the electron transfer rate during the anodic stage b of Figure 5.2. The sum of the elemental dissolution rates is well below the electron exchange rate, v_e , even when the former is multiplied by 2, the highest valence that one would reasonably expect for either Cu or Zn in this electrolyte. The difference between the oxidative electron transfer and elemental dissolution may be explained by the

formation of insoluble oxidized Cu and/or Zn species since no other significant oxidation reactions would be expected in this electrolyte at the potentials used.

Table 5.2. Steady dissolution rate of brass alloys in STW (upper) and deaerated CBS (lower).

		Zn	Cu	Cu (congruent)
		pmol s ⁻¹	pmol s ⁻¹	
STW	Cu-42Zn	9.59 ± 5.22	0.60 ± 0.85	13.43
	Cu-21Zn-3Si-P	5.22 ± 1.02	1.67 ± 1.11	18.84
CBS	Cu-42Zn reference	1.82 ± 2.11	2.32 ± 0.78	2.55
	Cu-42Zn	3.28 ± 1.68	5.40 ± 0.78	4.59
	Cu-21Zn-3Si-P reference	1.39 ± 1.83	3.13 ± 0.92	5.13
	Cu-21Zn-3Si-P	1.65 ± 0.69	6.98 ± 1.28	6.09

Figure 5.4 shows the superimposition of Cu and Zn dissolution at various galvanostatic currents. A remarkable feature of the Zn dissolution profiles shown in this figure is the transient response to the anodic polarization, leading to a rapid increase in the Zn dissolution rate, which decreased gradually throughout the remainder of the anodic pulse. This curious behavior coincides with the results observed by Pchel'nikov [15] using Zn isotopes and Pickering [12] using quantitative chemical analysis of the electrolyte. The Cu dissolution rate, however, increased gradually, though at different rates for different alloys: for Cu-42Zn, a sluggish increase of Cu dissolution rate was observed with no steady state till the end of the 1200 s anodic period. In contrast, for Cu-21Zn-3Si-P, a steady state dissolution rate was reached after about 300 s after the initiation of anodic polarization. This was followed by a rapid decrease (stage *c*), identical for both alloys. Also, for Cu-42Zn, during the first few seconds of the anodization, no soluble Cu species were detected, while Zn dissolution increased rapidly. This period will be referred to as an induction period. The induction period was not observed on Cu-21Zn-3Si-P.

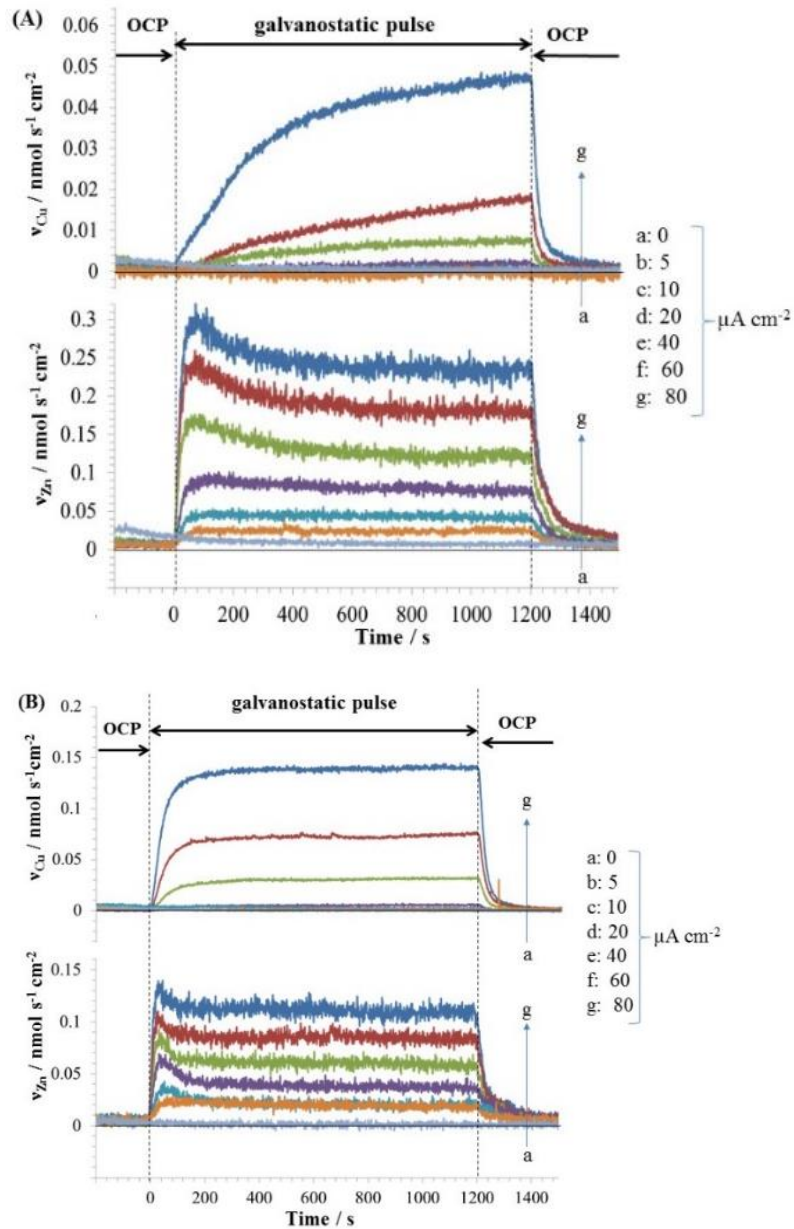


Figure 5.4. Elemental dissolution of Cu-42Zn (A) and Cu-21Zn-3Si-P (B) in exposure to STW. Upper: dissolution of Cu; lower: dissolution curve of Zn. Curves from upper to lower in $\mu\text{A cm}^{-2}$: 80, 60, 40, 20, 10, 5, 0.

5.5.3. Analysis of insoluble corrosion products

The formation of insoluble corrosion products during the galvanostatic pulse was clearly demonstrated by the significant mismatch between the sum of the elemental dissolution rates and the electrical current (stage *b* in Figure 5.2). It has been previously proven the feasibility of using CBS to dissolve insoluble copper corrosion products with minimal corrosion of the substrate [155]. In this paper, the same methodology was used. Dissolution profiles of the corrosion products in deaerated CBS electrolyte are given in Figure 5.5. The integral of the Cu

and Zn dissolution transients in Figure 5.5, gives the total amount of each element in the corrosion product film present at the surface following the exposure to STW, referred to as $Q_{Cu}(CBS)$ and $Q_{Zn}(CBS)$. It is clear from the figure that the corrosion product layer was mainly composed of Cu oxides [168], with Zn oxide and/or hydroxides as a minor constituent. The value of $Q_{Zn}(CBS)$ showed no statistically significant variation in quantity with either galvanostatic time or current [167-168].

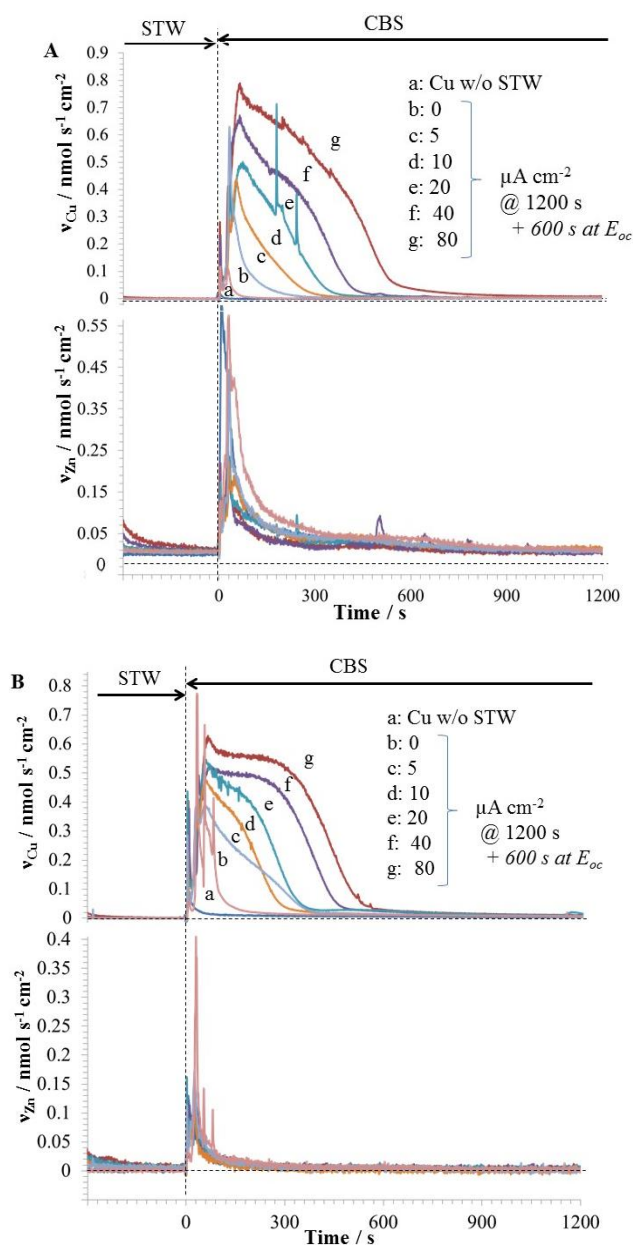


Figure 5.5. Superimposition of residual film dissolution of Cu-42Zn (A) and Cu-21Zn-3Si-P (B) in CBS. Captions a – g: a: fresh brass exposed to CBS; b - g represents $i_{ap} / \mu\text{A cm}^{-2} = 0, 5, 10, 20, 40$ and 80 respectively.

To further verify that the dissolution waves of Cu and Zn were from the dissolution of the oxides rather than the dissolution of the substrate, a reference experiment was conducted with a fresh brass sample in deaerated CBS, curve *a* in Figure 5.5. For Cu-42Zn, a large peak of Zn and a negligible peak of Cu were observed when exposed to CBS for a few seconds; for Cu-21Zn-3Si-P, relatively comparable peaks of Cu and Zn were observed. These peaks were significantly different from the dissolution wave of the alloys after STW exposure, and demonstrate that curve *b-g* were indeed the dissolution profile of the oxides rather than the substrate or the metallic component of the dezincification layer. Note that the quantity of Cu in this peak is negligible as compared to the other experiments so it is safe to ignore the corrosion of the substrate during the determination of the quantity of residual oxides.

For both Cu-42Zn and Cu-21Zn-3Si-P, a salmon colored layer was visually observable after removal of the oxide layer by CBS corresponding to the Zn depleted metallic Cu layer which was not soluble in the CBS. The presence of this metallic Cu film affected the steady state open circuit dissolution rates in CBS (Table 5.2). For the reference experiments with freshly ground samples (no preexisting oxide layer) both alloys show a slight preferential dissolution of Zn as compared to their bulk composition (curve *a* in Figure 5.5). This was much less significant than in STW due no doubt to the solubility of the solid Cu oxidation products. However, when the alloy had been subjected to a galvanostatic treatment, the corrosion rate in CBS after oxide dissolution, yielded a Cu dissolution rate larger than that predicted for congruent dissolution attributed to the excess Cu content of the material exposed to the electrolyte. Nevertheless, the Zn dissolution rate is not negligible indicating that the dezincification layer did not protect the underlying substrate from corroding.

5.3.4. Characterization of residual oxides

It has been previously demonstrated that the residual oxide film formed on pure Cu in STW was almost entirely composed of Cu₂O [155]. To verify whether or not this was the case for the brass samples, GIXRD and Raman spectrometry were used to analyze the oxide layer formed after anodic polarization at various applied current for 1200 s. Figure 5.6 presents the GIXRD results of both alloys with pure Cu as a reference [155]. Consistent with the case of pure Cu, crystallized Cu₂O was detected on both alloys after anodic polarization. However, no peaks corresponding to a pure Cu dezincified layer could be detected by GIXRD as would be evidenced by Cu fcc lattice peaks shifted due to the change in lattice parameter from lack of substitutional Zn, even though the Cu film was visually observable. Similarly, the Raman

spectra (Figure 5.7) show peaks at 150 cm^{-1} , 220 cm^{-1} , 411 cm^{-1} and 650 cm^{-1} supporting the existence of Cu_2O . Nonetheless, the existence of CuO cannot be excluded since the Raman shift of CuO at 633 cm^{-1} is very close to that of Cu_2O at 635 cm^{-1} [116,164-, , 165]. Moreover, it is possible that some thin amorphous CuO species cannot be detected by GIXRD or Raman spectroscopy [165]. The Raman shift at 525 cm^{-1} was due to Cu-OH vibration in defective Cu_2O [166]. It is thermodynamically possible that some Cu_2O can be further oxidized into CuO by exposure to air. However, since neither GIXRD nor Raman spectroscopy detected any Cu(II) species, it is reasonable to conclude that even if CuO exists at the surface, its quantity is still far smaller than the Cu_2O in the surface oxide film.

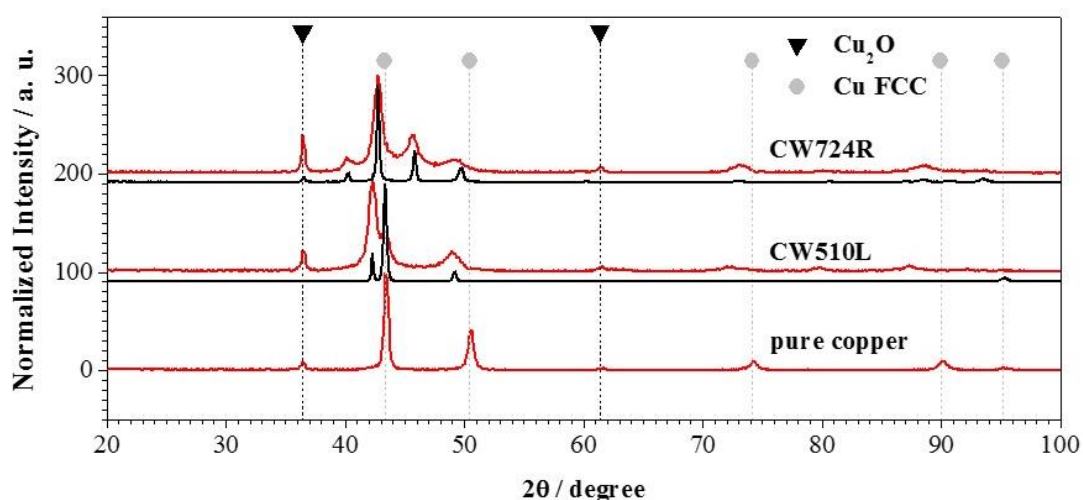


Figure 5.6. GIXRD results of Cu-42Zn and Cu-21Zn-3Si-P after exposure to STW at $i_{ap} = 80\ \mu\text{A cm}^{-2}$.

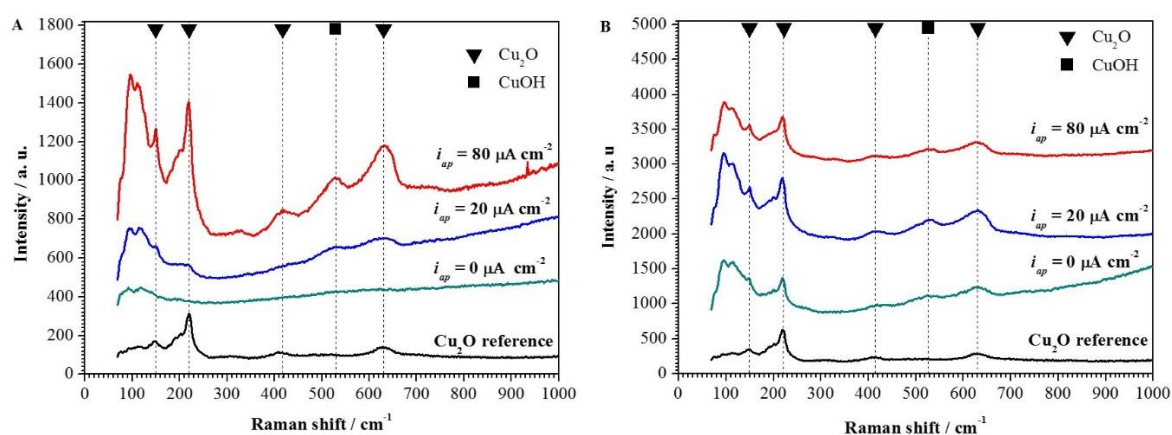


Figure 5.7. Raman spectra of Cu-42Zn (A) and Cu-21Zn-3Si-P (B) after exposure to synthetic tap water at different anodic current.

5.3.5. Surface morphology

Based on the previous analysis, it's clear that cuprite (Cu_2O) is the primary solid corrosion product deposited on the surface. The distribution of the corrosion product on the surface was investigated by SEM observations of the brass samples before and after exposure to STW at $i_{ap} = 5 \mu\text{A cm}^{-2}$ and $t = 1200 \text{ s}$ (Figure 5.8-5.9). Note that samples used for SEM observation were polished to 1 μm diamond paste to a mirror finish. Such a low current was chosen to enable the formation of Cu oxides among different phases after the induction period, as is shown in Figure 5.4 (A). Further, a larger applied current will produce more oxide film on the surface, thus covering the surface, minimizing differentiation of oxide distribution that might exist among different metallurgical phases. For these samples, the oxide layer of Cu-42Zn was formed in the center of the reacting zone, and the layer of Cu-21Zn-3Si-P was evenly distributed on the exposure area. Only the region where shows a complete coverage of oxide film was observed by SEM. Both figures show cubic solid crystalline products distributed on the surface. These cubic-shaped crystals were assumed to be Cu_2O based on GIXRD and Raman analysis. However, the distribution of cubic Cu_2O on the surface is completely different among the two alloys: in Figure 5.8, cubic crystals were evenly formed on the surface and no clear sign of preferential deposition of Cu_2O on the different metallographic phase structures was found, with respect to the duplex structure of Cu-42Zn. However, the distribution of Cu_2O on Cu-21Zn-3Si-P shows a remarkable preferential distribution: in Figure 5.9, a clear crystal boundary based on the distribution of Cu_2O can be distinguished; more than 50% of the area was covered with evenly distributed cubic particles with the rest being covered with a less dense and an incomplete coverage of Cu_2O cubic particles.

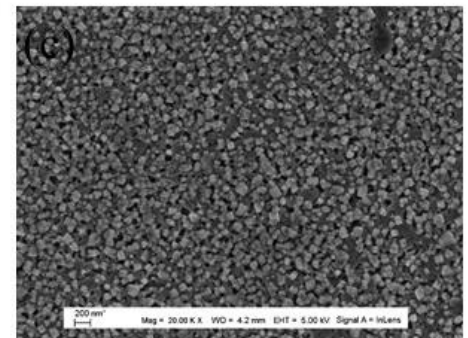
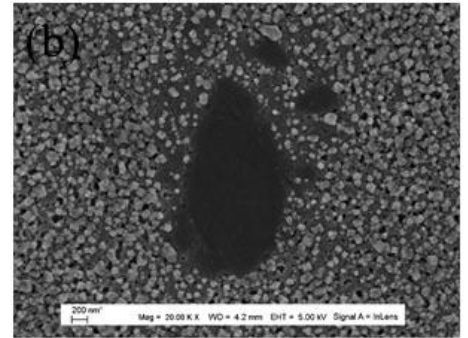
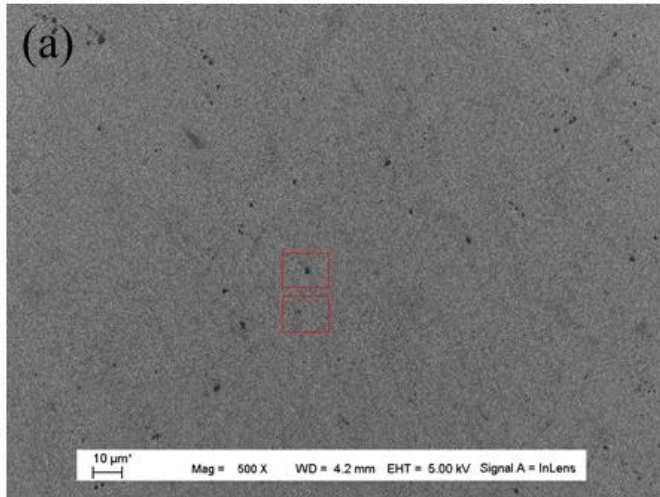


Figure 5.8. SEM observation of the surface topography of Cu-42Zn being anodically polarized in STW. $i_{ap} = 5 \mu\text{A cm}^{-2}$, $t = 1200 \text{ s}$.

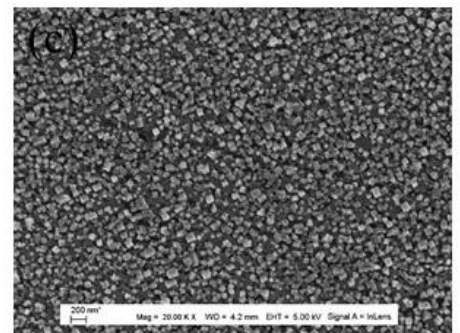
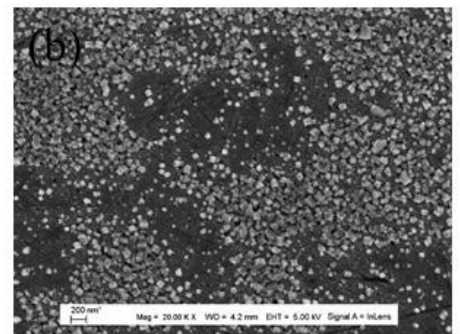
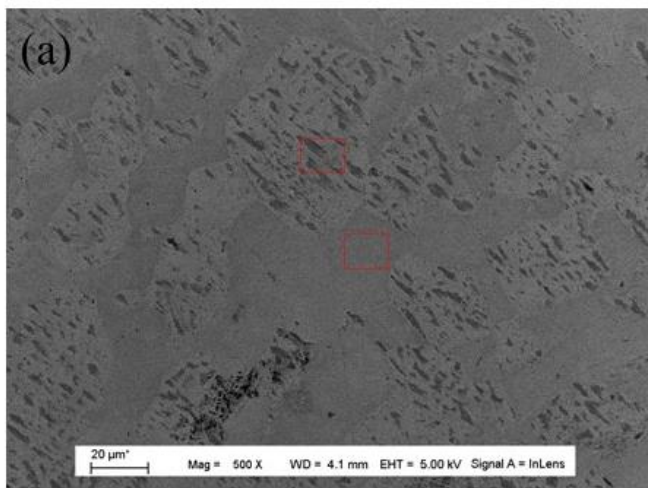


Figure 5.9. SEM observation of the surface topography of Cu-21Zn-3Si-P being anodically polarized in STW. $i_{ap} = 5 \mu\text{A cm}^{-2}$, $t = 1200 \text{ s}$.

5.5.6. Mass and Charge Balance

The quantity of the Cu oxide and of the residual metallic Cu layer as a function of time may be determined from a detailed mass/charge balance for the dissolution of Cu and Zn during the STW experiments. This requires knowledge of the oxidation states of the corrosion products. Based on the previous surface characterization, it's reasonable to assume that brass dissolution in STW leads primarily to the formation of aqueous Cu(II) species and solid Cu₂O, identical to the case of pure copper [155]. Zn dissolution of course occurs via the formation of aqueous Zn(II) species leaving behind a trivial amount of precipitated Zn(II) as an amorphous Zn oxide or Zn hydroxide [167-, 168, 116153]. These solid Zn species remained on the surface and were independent of galvanostatic current and time, as is shown in Figure 5.5. The Si in Cu-21Zn-3Si-P was assumed to be oxidized into Si(IV) species[169], although the quantity was low and does not significantly contribute to the total charge.

The validity of these assumptions- that the corrosion products consists of Cu(II) and Zn(II) aqueous and Cu(I) solid species- may be verified by comparing the total quantity of electricity, $Q_e(pstat)$ during the galvanostatic pulse, with the total equivalent electricity from the calculated from the elemental dissolution rates, $Q_e(ICP)$.

$$Q_e(ICP) = \sum n_{m,aq} Q_{m,an(aq)} + \sum n_{m,s} Q_{m,an(s)} \quad 5.1$$

where $Q_{m,an}$ represents the quantity of elemental dissolution of a metal, m (Cu, Zn and Si), contributed to either aqueous species (aq) or solid species (s), and $n_{m,aq}$, $n_{m,s}$ are the valence of each species in the form of aqueous or solid state. The two terms on the right of eq. 1, $Q_{m,an(aq)}$ and $Q_{m,an(s)}$, are the net quantity of aqueous and solid species attributed to the galvanostatic pulse, which can be further calculated through eq. 5.2-5.3.

$$Q_{m, an(aq)} = Q_m(STW) - Q_m(STW)(i_{ap} = 0); \quad 5.2$$

$$Q_{m, an(s)} = Q_m(CBS) - Q_m(CBS)(i_{ap} = 0). \quad 5.3$$

where $Q_m(STW)$ and $Q_m(CBS)$ correspond to the total quantities of elemental dissolution of m during the STW or CBS period. These values are determined by integration of the dissolution profiles. The quantity of elemental species formed during the open circuit exposure must be removed from this value in order to obtain the correct mass balance. In equation 5.2 & 5.3 this background mass was assumed to be given by $Q_m(STW)(i_{ap} = 0)$ and $Q_m(CBS)(i_{ap} = 0)$, the quantity of aqueous species of element m in STW, when $i_{ap} = 0$. The subtraction of these terms

from $Q_m(STW)$ and $Q_m(CBS)$ provides a net quantity of each species produced by the galvanostatic current, since all the experiments were performed on an identical time scale.

The comparison between $Q_e(ICP)$ and $Q_e(pstat)$ at various applied current or various time duration was shown in Figure 5.10A and 5.10B. The experimental data fits the $Q_e(ICP) = Q_e(pstat)$ (dashed line) fairly well within experimental error, though some deviation is observed at higher current, which may be due to the errors in background subtraction discussed above, or perhaps the existence of a trace amount of solid Cu(II) species. Nevertheless, the relatively good agreement of experimental points with the $Q_e(ICP) = Q_e(pstat)$ line corroborates the assumption of the oxidization state of each element in the aqueous and the solid phase.

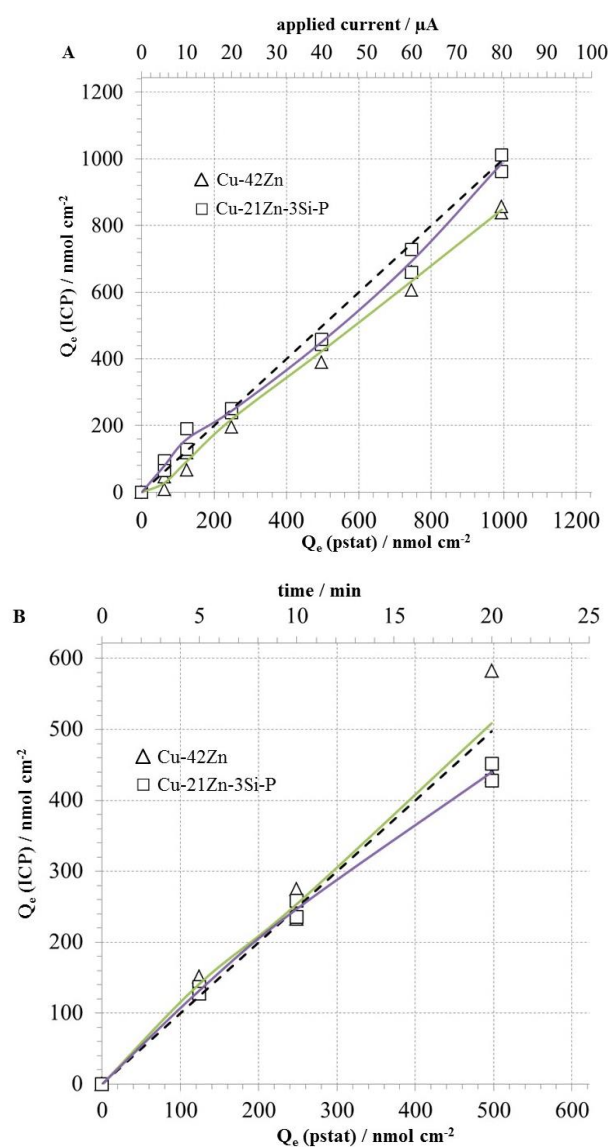


Figure 5.10. Comparison between $Q_e(pstat)$ and $Q_e(ICP)$ for Cu-42Zn (Δ) and Cu-21Zn-3Si-P (\square) respectively as a function of applied current (A) and as a function of time duration (B).

5.3.7. Growth of the dezincification and the oxide layers

It is of great mechanistic interest to investigate the rates of formation of aqueous Cu^{2+} , the solid Cu_2O corrosion product layer, and the Zn depleted metallic copper layer as a function of applied current or time. Figure 5.11 gives the values of $Q_{\text{Cu}}(\text{STW})$ representing the quantity of Cu dissolved, and $Q_{\text{Cu}}(\text{CBS})$ representing the quantity of solid Cu_2O oxide formed, plotted as a function of applied current for both alloys. In all cases the Cu_2O formation is clearly favored over Cu^{2+} dissolution, as was observed for pure Cu dissolution under identical experimental conditions [155]. Also, the growth rate of Cu_2O oxide film on both alloys decreased with the increase of i_{ap} , while the growth rate of Cu^{2+} began to increase at higher current.

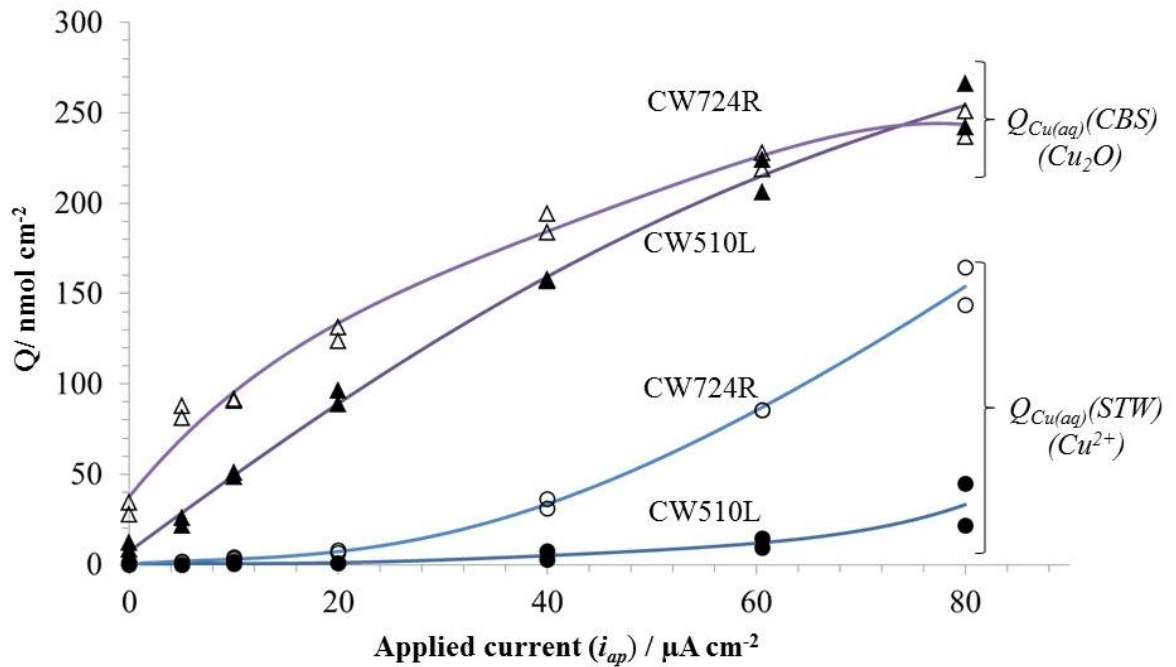


Figure 5.11. The increase of soluble species ($Q_{\text{Cu(aq)}}(\text{STW})$) and insoluble species ($Q_{\text{Cu(aq)}}(\text{CBS})$) as a function of applied current for Cu-42Zn and Cu-21Zn-3Si-P.

The establishment of mass/charge balance calculation allows us to estimate the thickness of the dezincified layer, assuming a compact pure Cu layer sandwiched by the outermost Cu_2O layer and the brass substrate. The thickness of the dezincified layer (δ_{Cu}) and residual oxide film ($\delta_{\text{Cu}_2\text{O}}$) can be estimated through eq. 5.4-5. 5:

$$\delta_{\text{Cu}} = \frac{M_{\text{Cu}} \{ \alpha [Q_{\text{Zn}}(\text{STW}) + Q_{\text{Zn}}(\text{CBS})] - [Q_{\text{Cu}}(\text{STW}) + Q_{\text{Cu}}(\text{CBS})] \}}{\rho_{\text{Cu}}}$$

5.4

$$\delta_{Cu_2O} = M_{Cu_2O} \frac{Q_{Cu(aq)}(CBS)}{\rho_{Cu_2O}} \quad 5.5$$

where α represents the molar ratio of Cu/Zn in the bulk; ρ_{Cu} and ρ_{Cu_2O} are the density of each component assuming that the dezincified layer and the corrosion product layer are both compact and dense; M_{Cu} and M_{Cu_2O} are the molar mass for each component. The growth of δ_{Cu} and δ_{Cu_2O} as a function of the applied current, are presented in Figure 5.12 assuming a $\rho_{Cu} = 8.90 \text{ g cm}^{-3}$ and $\rho_{Cu_2O} = 6.04 \text{ g cm}^{-3}$. This calculation definitely underestimates the thickness of the pure Cu layer and Cu_2O layer, considering the porous structures of both. However, the growth of both layers with the increase of applied current signifies that both the dezincified layer and the oxide layer thicken with current.

Also shown in Figure 5.12 is the dezincification factor (Z factor), Eq. 5.6 [87]:

$$Z = \frac{(Zn/Cu)_{oxidized}}{(Zn/Cu)_{metal}} = \alpha \frac{Q_{Zn(aq)}(STW) + Q_{Zn(aq)}(CBS)}{Q_{Cu(aq)}(STW) + Q_{Cu(aq)}(CBS)} \quad 5.6$$

From this definition, $Z = 1$ would represent perfect congruent dissolution. $Z > 1$ represents a preferential dissolution of Zn, the degree of which is quantified by the magnitude of Z . Figure 5.12 shows clearly that the Z factor decreases rapidly with increasing current for $i_{ap} < 20 \text{ } \mu\text{A cm}^{-2}$, and approaches $Z = 1.5$ for $i_{ap} > 20 \text{ } \mu\text{A cm}^{-2}$. Cu-21Zn-3Si-P has a smaller Z than Cu-42Zn at various current values, which corroborates the ISO dezincification test result, as is shown in Figure 5.1.

Also in Figure 5.12, δ_{Cu} , increased linearly with increasing applied current for each alloy. This result contrasts with that of Pchel'nikov [15] who reported that on an α -brass, the dezincified layer was independent of time and applied current. This result lead him to conclude that a dissolution/redeposition mechanism was operative as the steady state thickness would require both dissolution and redeposition.

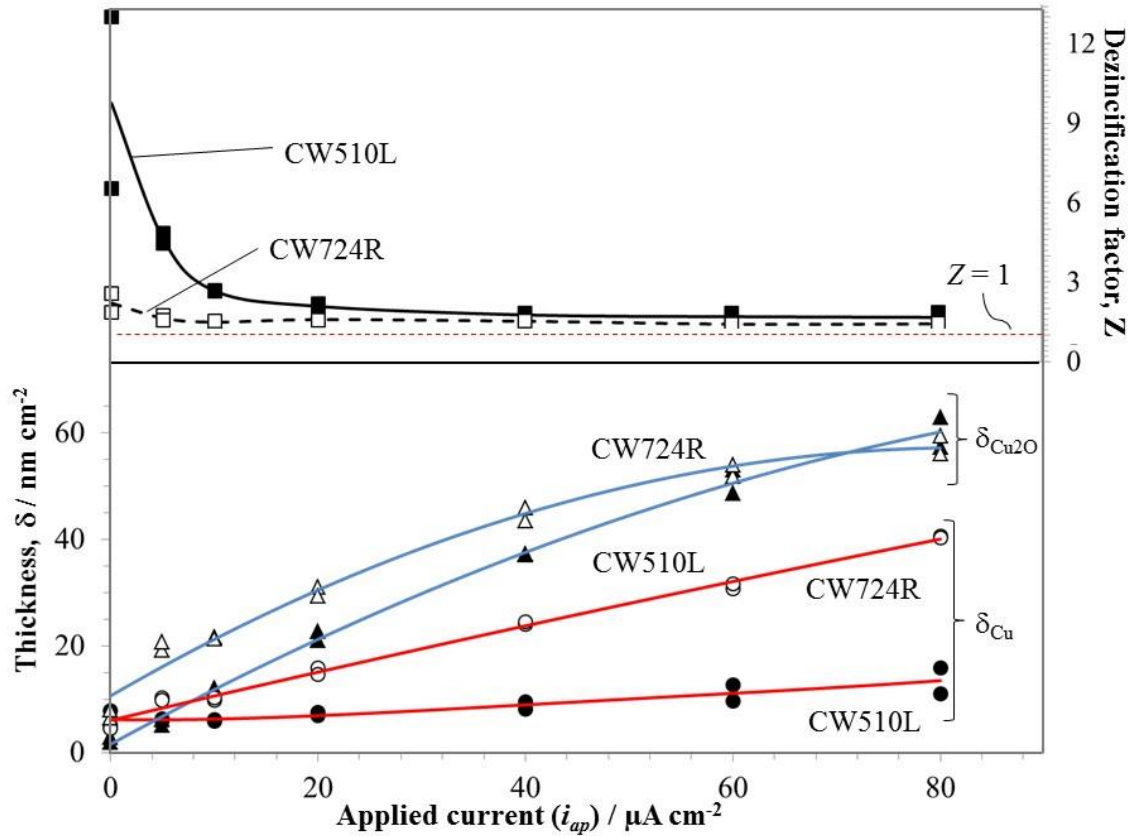


Figure 5.12. Thickness calculation of Cu_2O layer and dezincified layer, and dezincification factor (Z factor) as a function of applied current.

5.4. Kinetic analysis and Discussion

The results presented here demonstrate that the primary reactions involved in the corrosion of brass in tap water are as follows:



The formation of the Cu rich dezincification layer may be attributed to one of two broad classes of mechanisms: 1) redeposition due to the oxidation of Zn with Cu^{2+} or the disproportionation of Cu_2O [146], or 2) a selective dissolution of Zn via a surface diffusion [72] or percolation mechanism [81]. Insight into the mechanism of dealloying may be gained via a time resolved kinetic analysis of the elemental dissolution and film growth.

An example, the kinetic analysis of brass dissolution in STW under a $40 \mu\text{A cm}^{-2}$ galvanostatic pulse is shown in Figure 5.13. In this figure, the $v_{\text{Cu}(\text{aq})}$, $v_{\text{Zn}(\text{aq})}$ are the direct

dissolution profiles from ICP-OES. The growth rate of oxide film, v_{Cu_2O} , and the dezincified layer, v_{Cu} , was calculated via eq. 5.10-5.11.

$$v_{Cu_2O} = [v_e^* - 2 \sum v_{m(aq)}(STW)] / 2 \quad 5.10.$$

$$v_{Cu} = \alpha v_{Zn(aq)}(STW) - 2 v_{Cu_2O}(STW) - v_{Cu(aq)}(STW) \quad 5.11.$$

where v_e^* is the convoluted electrical current, $\sum v_{m(aq)}$ is the sum of elemental dissolution rates, such as $v_{Cu(aq)}(STW)$, $v_{Zn(aq)}(STW)$ and $v_{Si(aq)}(STW)$, α is the molar ratio of Cu/Zn in the bulk material. Also, the instantaneous dezincification factor, Z , as a function of time, is presented in this figure to demonstrate the instantaneous dezincification severity.

In Figure 5.13, the dashed curves represent the convoluted electrical current, normalized to the steady state value of each component. If dissolution and film growth followed directly the applied current, that is to say the rate increased in an instantaneous step to the steady state, it would be expected to follow this curve. The convolution of the current accounts for the broadening of the measured result due to mixing in the flow cell.

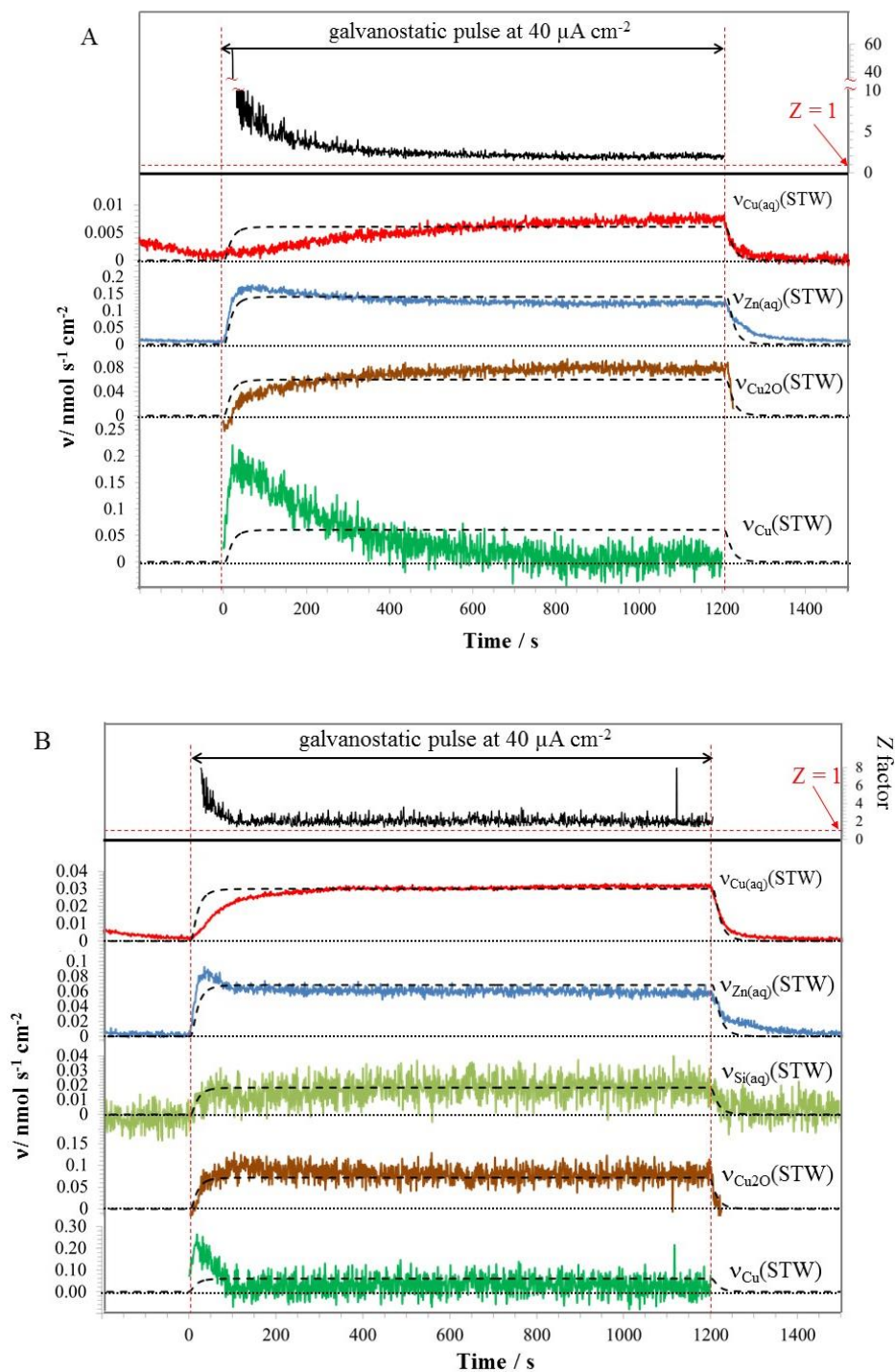


Figure 5.13. Kinetic analysis of elemental dissolution, oxide film and the dezincified pure copper layer growth of Cu-42Zn (A) and Cu-21Zn-3Si-P (B) at $i_{ap} = 40 \mu\text{A cm}^{-2}$. Dashed line represents the hypothetical curve for a step function after correcting for AESEC time constant.

The Zn dissolution rate increases very rapidly at the application of anodic current and actually passes through a maximum during the early stages of the experiment. In contrast, the Cu dissolution rate increases slowly only reaching steady state after several minutes. The increase of the Cu_2O film is in fairly good agreement with the convoluted current while the

formation of the metallic Cu-rich dealloyed layer (dezincified zone) shows an intense peak during the early period and drops off to a near zero value.

These results are consistent with the hypothesis that, at $t = 0$, Zn is oxidized more readily than Cu and a certain degree of Zn depletion must occur before Cu will oxidize directly to soluble Cu(II). Initially, Cu oxidation occurs via the formation of Cu_2O . Cu dissolution increases slowly as Zn depletion occurs, reaching a steady state only when the Cu film (dezincified layer) has also obtained a steady state configuration.

The selective dissolution of Zn was observed under all experimental conditions in STW, that is to say that the release of soluble Zn species (eq. 5.7) occurred more rapidly than the release of soluble Cu species (eq. 5.8), irrespective of the Cu to Zn ratio of the brass. When an anodic current was applied, a clear preferential formation of Cu_2O on the surface was observed on both alloys, especially in the lower current region. So, in the corrosion of Cu-Zn alloys, most Cu being oxidized will be present in the form of an oxide film; Zn is oxidized into both Zn soluble species that are released into STW and relatively small amounts of insoluble oxides/hydroxides that are deposited on the surface.

Under the conditions of the AESEC system, Cu-21Zn-3Si-P has a better corrosion resistance (Table 5.2) and dezincification resistance (Figure 5.12), especially at low anodic current ($i_{ap} \leq 10 \mu\text{A cm}^{-2}$). This may be attributed to the absence of the high zinc containing beta phase.

Nevertheless, the anodic dissolution transients of Cu and Zn in STW for the two alloys differ markedly from each other. This may likewise be attributed to the differences in their metallurgical phases. It is well known that the β' phase in brass is more sensitive to dezincification, due to the higher solubility of Zn in solid solution. The dezincification of α , β' -brass initiates firstly on the β' phase [170], and propagates along the crystal boundary or dislocations [147, 171], since the β' phase has a corrosion potential of 180 mV more negative than the α phase [99]. However, the SEM observation didn't show a clear composition contrast on Cu-42Zn that was due to the differentiation of dissolution rate among α and β' phase. On the contrary, the contrast may be observed on Cu-21Zn-3Si-P, which is not only due to the preferential distribution of Cu_2O particles, the chemical composition of the underlying phases must have changed significantly. Seuss et al [146] reported that in the exposure of CuZnSi3P to aggressive tap water, κ phase shows a corrosion potential of more than 50 mV more negative than α phase, γ phase has a value of 100 mV more negative than κ phase. This means that more severe dissolution occurred on some metallurgical phases. However, the average corrosion rate

of Cu-21Zn-3Si-P was still lower than Cu-42Zn, this can be explained by a relative small proportion of less noble phases in the CuZnSi₃P matrix. So it is reasonable to conclude that the difference in the dezincification performance was a direct result of the metallurgical phase difference. The γ phase, even the κ phase may contribute to the release of Cu²⁺ into tap water, also in turn promoting the formation of Cu oxides.

The kinetic analysis shown in Figure 5.13 demonstrates that the anodic dissolution of brass comprises two stages: a first stage where a growth peak of the dezincified layer can be found during the initial period of the galvanostatic pulse; and a second stage where the growth peak decreases to a very low rate, indicating a simultaneous dissolution of Cu and Zn or at least a less severe preferential dissolution of Zn, since the Z factor in this stage is close to 2 (Figure 5.13). Among the two alloys, obviously Cu-42Zn shows a more intense growth of the dezincified layer consistent with the accelerated test results of Figure 5.1.

The two-stage phenomenon found in the anodic dissolution of brass seems to support the dissolution-redeposition mechanism [147]. However, considering the complex metallurgical structure of the alloys investigated, the non-clarity as to the oxidation process of Cu to Cu₂O and Cu²⁺ species, and the possibility of galvanic corrosion among different metallurgical phases, a detailed conclusion regarding the mechanism is still yet to be made. Further work with pure phase samples of α brass, β' brass is in progress so as to address these questions.

5.5. Conclusions

In this work, the dezincification kinetics of two commercial brass samples, Cu-42Zn and Cu-21Zn-3Si-P, were investigated.

1. The main products of the anodic dissolution of brass in synthetic tap water (STW) were soluble Cu(II) and Zn(II) species, and a solid Cu₂O film. A Zn depleted metallic Cu film was formed due to the selective dissolution (dezincification) of Zn.
2. The partial dissolution rates of Cu and Zn as a function of time throughout the exposure of brass to a synthetic tap water solution were established. Zn dissolution was significantly enhanced during the first stages of the exposure indicative of a dezincification reaction.
3. The rates of formation of the Cu₂O layer and the Zn depleted metallic Cu layer were determined as a function of time via a mass/charge balance.
4. Cu oxidation during the early stages of the galvanostatic pulse formed Cu₂O; the rate of soluble Cu(II) formation increased slowly with time.

5. The dezincified layer grew rapidly during the early stages but slowed to almost zero at longer times as the rate of Cu dissolution increased.

6. The overall kinetic picture was similar for the two brass samples, however the Cu-42Zn, a duplex (α , β' -brass) showed a significantly more intense dezincification rate which was attributed to the presence of the β' phase with high Zn content.

6. The dissolution of Cu-Zn alloys in synthetic tap water: effect of Zn content on the elemental release, scale formation and dissolution mechanism.

6.1 Introduction

The selective dissolution of Zn from Cu-Zn alloys, known as dezincification of brass, is a major factor that precludes the application of Cu-Zn alloys. The mechanism of dezincification has been thoroughly investigated during the past decades [12-15,72,74,75,81,149-152,172,173]. Two categories of theories have been proposed: the theory of dissolution – redeposition [14,15] and the theory of the preferential dissolution [12,13]. These theories interpret the mechanism in terms of the atomic mobility, vacancy movement, surface rearrangement as well as electrochemical reaction. However, dezincification is a complex process that involves not only Cu and Zn cation release, but the growth of dezincification structure. A clear characterization of both would be helpful to explain the dezincification mechanism.

In neutral or alkaline electrolyte, dezincified brass has a complex structure: an outer residual layer consisting of Cu oxide and/or hydroxide, and an intermediate Zn depleted layer consisting of defect-rich metallic Cu. The dezincification structure varies with testing conditions and the chemical composition of the alloy and the electrolyte, making a direct comparison of published literature difficult. In order to better understand the dezincification process, much work has focused on the qualification of the dezincification interface, such as the characterization of different species by various surface spectroscopies such as *in situ* Raman spectroscopy [88], infrared reflection absorption spectroscopy (IRAS) [89], near normal incidence reflectance spectroelectrochemical technique (NNIRS) [90] and ultraviolet-visible (UV-vis) reflectance spectroscopy [91]. Layer mapping & depth profiling of Zn depleted layer, has been attempted using time-of-flight secondary ion mass spectroscopy (ToF-SIMS) [174] and laser induced breakdown spectroscopy (LIBS)[175].

The quantification of soluble species during dezincification has been performed by means of intermittent chemical analysis of Cu and Zn in the electrolyte, aiming at establishing a relationship between partial elemental current and potential [12], and by a channel flow double

electrode (CFDE) [95], which allows a simultaneous identification and quantification of soluble Cu(II) and Cu(I). While there are many advantages and disadvantages to these methodologies: the intermittent chemical analysis of electrolyte gives an average value of the dissolution rate over a relatively long period of time, transitional concentration changes may be missed, making correlation with electrical current, for example, difficult; the CFDE has the huge advantage of making it possible to identify the chemical state of downstream Cu, however it would be difficult to detect both Zn and Cu simultaneously. Previously, we utilized the atomic emission spectroelectrochemistry (AESEC) [118,126] to investigate the anodic dissolution of pure Cu [155] and commercial brass alloys [176] in tap water, a precise quantitative relationship of ion release, scale formation, growth of Zn depleted layer, together with kinetic information during a galvanostatic pulse were obtained and the dissolution mechanism was discussed. In this work, we extended our foregoing work to the anodic dissolution of brass with various Zn contents ranging from 0 wt% to 45 wt%, giving a metallurgical change from a single α brass, in between dual phase brass, to single β' brass. The effect of Zn content on the elementary dissolution kinetics were identified; the growth of residual oxide layer and the Zn depleted layer with the increase of anodic current were established; a different dissolution mechanism among α and β' phase in Cu-Zn alloys was discussed.

6.2 Experimental

Cu-Zn alloys with various Zn contents were used. The chemical composition of the alloys and their metallurgical phase compositions as characterized by XRD, are listed in Table 1. Most alloys were commercially fabricated except the single β' brass, Cu-45Zn, which was laboratory fabricated. For the galvanostatic dissolution experiments, all the samples were ground in water with SiC paper up to grit 800. For the potentiodynamic polarization experiments, samples were ground in water up to grit 1200, and then further ground in ethanol with a grit 2400 SiC paper.

Table 6.1. Composition of Cu-Zn alloys

ISO	Zn	Cu	Cu-10Zn	Cu-20Zn	Cu-30Zn	Cu-33Zn	Cu-37Zn	Cu-42Zn	Cu-45Zn	
UNS(1)	--	C10100	C22000	C24000	C26000	C26800	C27400	--	--	
CEN(2)	--	CW009A	CW501L	CW503L	CW505L	CW506L	CW508L	CW510L	--	
Chemical composition (wt%)	Cu	--	99.9	89.0-91.0	78.5-81.5	68.5-71.5	65.5-68.5	62.5-65.5	57-57.5	55.0
	Fe	--	--	0.1	0.1	0.1	0.1	0.2	0.1	--
	Pb	--	--	0.05	0.05	0.05	0.02	0.3	0.2	--
	Zn	99.9	--	remaining	remaining	remaining	remaining	remaining	remaining	remaining
phase	--	α	α	α	α	α	$\alpha + \beta'$	$\alpha + \beta'$	β'	

(1): Unified Numbering System

(2): Comité Européen de Normalisation, *i.e.*, European Committee for Standardization.

Synthetic tap water (STW) [160] with a natural pH of 7.5 ± 0.1 , was prepared using $\text{MgSO}_4 \cdot 7\text{H}_2\text{O}$ (31.92 mg L^{-1}), NaHCO_3 (36.00 mg L^{-1}), $\text{CaCl}_2 \cdot 7\text{H}_2\text{O}$ (102.9 mg L^{-1}) and Na_2SO_4 (275.5 mg L^{-1}); citrate buffer solution (CBS) with a pH of 4.9 ± 0.1 was prepared with 0.1 M citrate acid and 0.1 M citrate trisodium solution. The solutions were prepared by mixing reagent grade reagents into deionized water (Millipore™ system, $18.2 \Omega \text{ cm}$ at $25 \text{ }^\circ\text{C}$).

The atomic emission spectroelectrochemistry (AESEC) technique was utilized in this work, details of the instrumentation had been introduced in previous publications [176]. Briefly, a three-electrode electrochemical flow cell and an inductively coupled plasma - atomic emission spectroscopy (ICP-AES) constitute the AESEC device. The flow cell was divided into two separate compartments by a cellulose membrane (Zellu Trans/Roth), giving a small volume reaction compartment (*ca.* 0.3 ml) where 1.0 cm^2 of the sample was exposed. A large volume secondary compartment (*ca.* 10.0 cm^2) where the reference electrode (saturated calomel electrode, SCE) and the counter electrode (Pt foil) were placed. The electrolyte was introduced by a capillary from the bottom of the reaction compartment at a flow rate of $f = 3.0 \pm 0.1 \text{ ml / min}$, measured to better than 1% precision for each series of experiments. The electrolyte was immediately transported downstream to the ICP-AES system, which was used to measure the elemental concentrations.

Polarization experiments for Cu-Zn alloys were conducted in naturally aerated STW and were followed by AESEC. The experiments were divided into four stages: a) the samples were first exposed to STW at open circuit for 20 minutes; b) a cathodic potential of $-1.0 \text{ V}_{\text{vs. SCE}}$ was applied for 10 minutes for cleaning the surface; c) the potentiodynamic polarization of the sample from $-1.0 \text{ V}_{\text{vs. SCE}}$ to $0.6 \text{ V}_{\text{vs. SCE}}$ with a sweep rate of 0.5 mV s^{-1} ; d) a short time open circuit of 5 minutes was followed. For pure Zn, the sweep range was $-1.0 \sim 0.6 \text{ V}_{\text{vs. SCE}}$.

The synthetic tap water-citrate buffer solution (STW-CBS) experiments, were identical to these previously described [155]. Figure 6.1 demonstrates four stages of the STW-CBS experiment: a) the freshly ground Cu-Zn alloys were exposed to STW for 300 s allowing an open circuit dissolution of Cu and Zn; b) an anodic galvanostatic current (i_{ap}) ranging from 0 to $80 \mu\text{A cm}^{-2}$ was imposed for $\Delta t = 1200 \text{ s}$, resulting in an accelerated release of Cu and Zn ($v_{\text{Cu}(aq)}$ and $v_{\text{Zn}(aq)}$) into water and a simultaneous precipitation of residual scale on the surface; c) a second open circuit dissolution of 300 s was imposed allowing the elemental release to return to its low rate; and d) the electrolyte was replaced by the deaerated citrate buffer solution to dissolve the residual scale formed during the previous stages. The trick for using citrate buffer

solution to dissolve the scale is due to its excellent combination of either descaling capability and the minimal harm to the substrate [177].

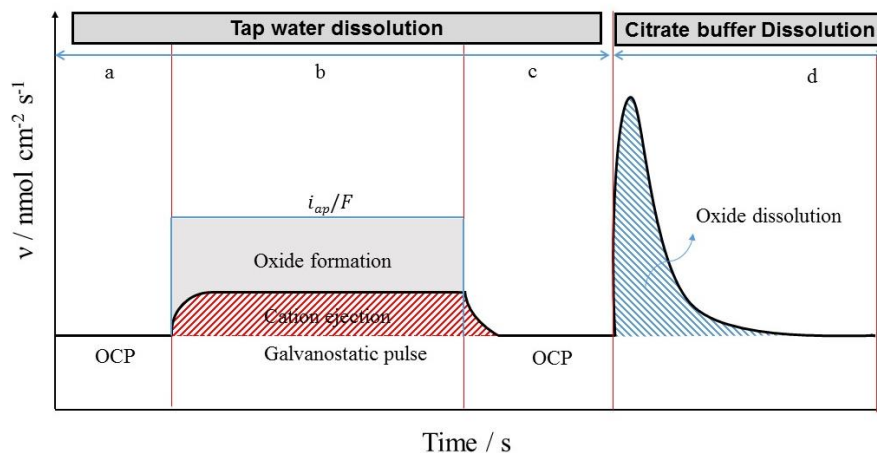


Figure 6.1. Schematic diagram of the STW-CBS experiment: a) open circuit dissolution in STW for 5 min; b) galvanostatic pulse in STW for 20 min; c) open circuit in STW for 5 min; d) open circuit dissolution of oxide in CBS for 25 min.

6.3 Results

6.3.1 Potentiodynamic polarization of Cu-Zn alloys

Figure 6.2 presents the AESEC polarization curve of nominally pure Cu (6.2A) and Zn (6.2B). The dissolution rates of Cu and Zn are both expressed as equivalent current densities, j_{Cu} and j_{Zn} , in units of $\mu\text{A cm}^{-2}$, since a clear knowledge of reaction factors had been obtained in previous publications [155, 176]. j_e^* represents the total current measured by the potentiostat, convoluted to simulate the hydrodynamic effect of the flow cell on the time resolution. In the AESEC polarization curve of pure Zn, j_{Zn} starts to rise above the detection limit (LOD) before $E_{j=0 \mu\text{A}}$, as is shown by the onset potential of Zn dissolution, $E_{Zn} = -1.06 \text{ V}_{\text{SCE}}$ and $E_{j=0 \mu\text{A}} = -0.98 \text{ V}_{\text{SCE}}$. Throughout the polarization curve, $j_{Zn} \geq j_e^*$, indicative of minimal oxide formation and the presence of a cathodic reaction throughout. At higher anodic polarizations, $j_{Zn} = j_e^*$ as predicted by Faraday's law, demonstrating the good quantitative relationship of the AESEC data as these measurements are completely independent. The polarization curve of pure Cu, however, showed $j_{Cu} < j_e^*$ even at a very high potential, indicating the formation of insoluble oxidized Cu species. Besides, the onset potential of Cu was identified to be very close to $E_{j=0 \mu\text{A}}$, suggesting that in this potential range, the formation of Cu^{2+} was kept at a very low rate, undetectable by ICP-AES.

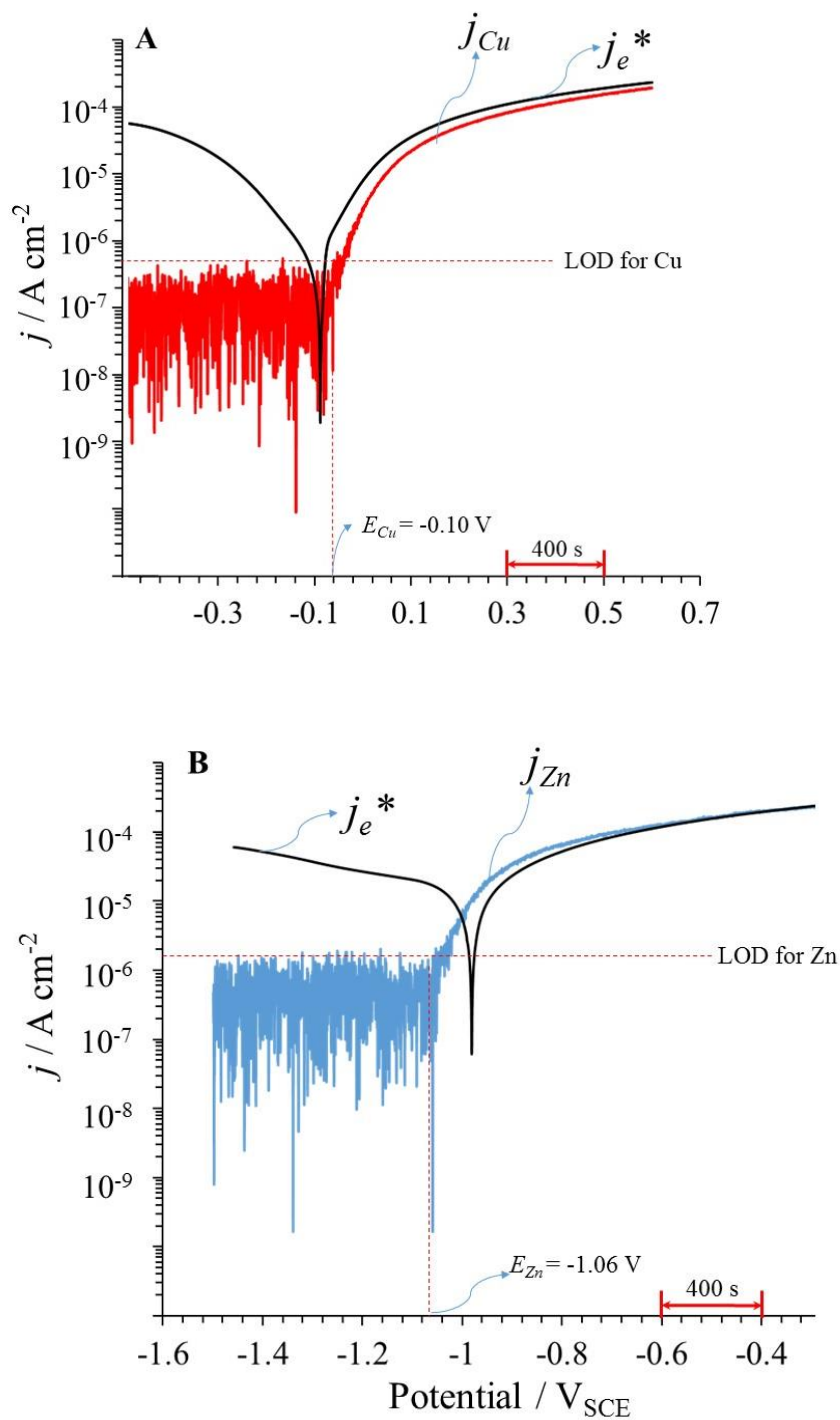


Figure 6.2. Potentiodynamic polarization of pure copper (A) and pure zinc (B).

Polarization curves of the Cu-Zn alloys are shown in Figure 6.3. Shown are j_{Cu} and j_{Zn} and $j_{\Sigma} = j_{\text{Cu}} + j_{\text{Zn}}$ respectively. In Figure 6.3A and 6.3B, $j_{\Sigma} < j_e^*$, indicative of the formation of solid oxidation products. However, the polarization curve of Cu-45Zn (Figure 6.3C) showed $j_{\Sigma} \approx j_e^*$, suggesting a direct dissolution mechanism which is logical since the only species dissolving is Zn.

Moreover, the onset potentials of Zn and Cu dissolution for Cu-10Zn (Figure 6.3A) were indistinguishable from each other, at $E_{Zn} = -0.05 \text{ V}_{SCE}$ and $E_{Cu} = -0.05 \text{ V}_{SCE}$. However, the separation increased with the Zn content: For Cu-33Zn (Figure 6.3B), $E_{Zn} = -0.11 \text{ V}_{SCE}$ and $E_{Cu} = -0.05 \text{ V}_{SCE}$. j_{Zn} reached a peak at E_{Zn} then decreased for a short period, then it resumed its increase. This is highlighted in the inset of Figure 6.3B. A similar feature could be observed from alloys containing Zn content up to 42 wt%.

But in the polarization curve of Cu-45Zn (Figure 6.3C), a different dissolution behavior of Cu was obtained: regardless of a low partial Cu current throughout the polarization, there was a valley on j_{Cu} at 0.11 V_{SCE} , which just corresponded to a peak on j_{Zn} . After the peak, j_{Cu} remained very near or below the LOD and j_{Zn} nearly equal to j_e , resulting a very good superimposition between j_{Zn} and j_{Σ} .

The polarization curves of Cu-Zn alloys can be categorized into three groups: a) a group in which the onset potential of Cu and Zn are less identifiable to be showed a clear sequential order, such as the case of Cu-10Zn, Cu-20Zn, as is shown in Figure 6.3A; b) a group in which the onset potential of Zn is well below the onset potential of Cu, such as the case of Cu-30Zn, Cu-33Zn, Cu-37Zn and Cu-42Zn, Figure 6.3B; and a group in which the partial current of Cu remains at a very low level throughout the whole range of potential scan, for example, Cu-45Zn, pure β' -brass, shown in Figure 6.3C.

Figure 6.4 gives the measured onset potential of Cu/Zn dissolution against the Cu (Zn) content. With the increase of Zn content in the alloy, the onset potential of Zn dissolution, distinguished from the potentiodynamic curve, E_{Zn} , shifted to a more negative value. And the onset dissolution potential of Cu, E_{Cu} , is shifted to a more positive value with the increase of Zn content.

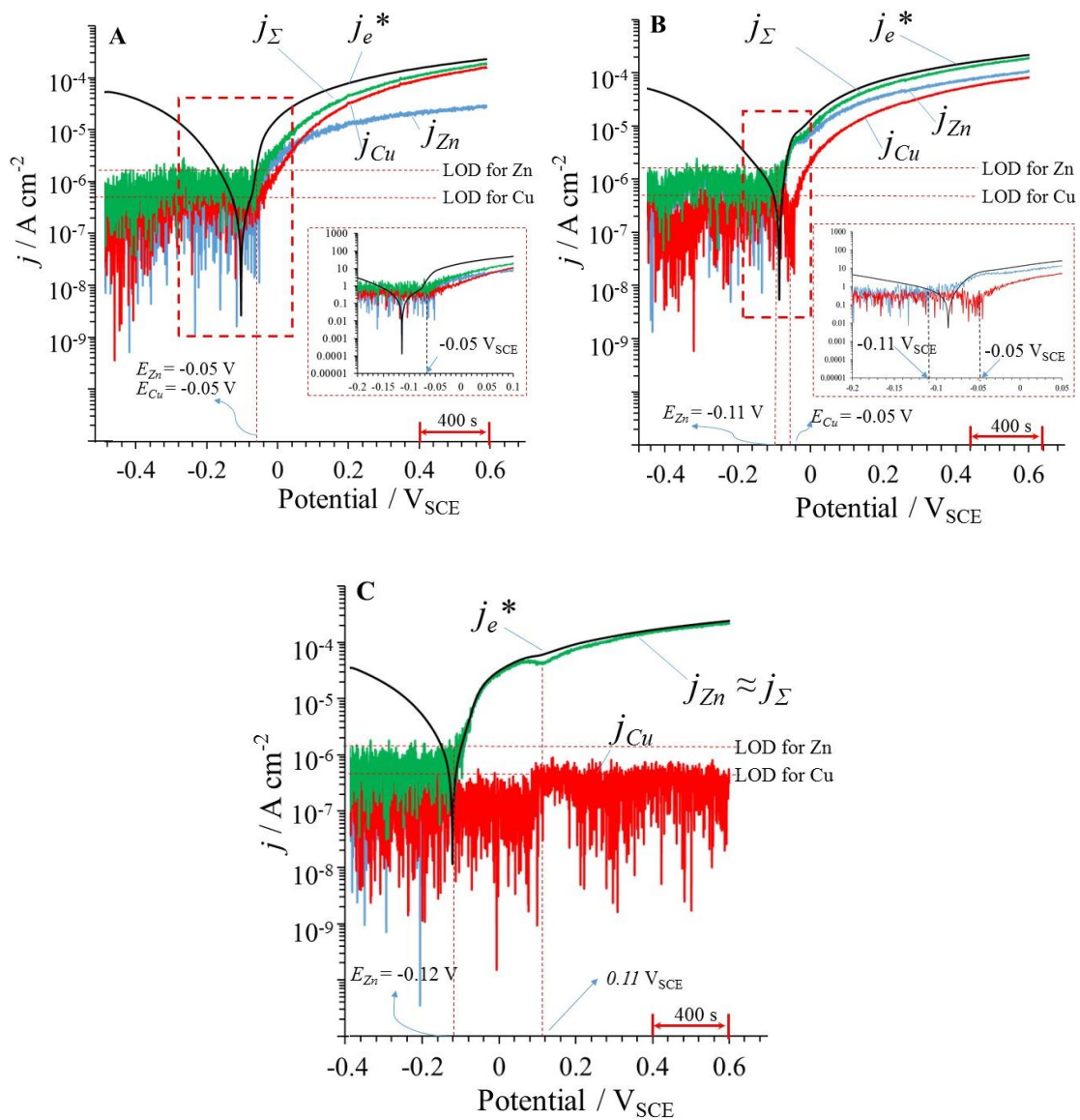


Figure 6.3. Potentiodynamic polarization curves of Cu-10Zn (A), Cu-33Zn (B) and Cu-45Zn (C). Note that j_{Zn} and j_{Σ} are nearly equal and are superimposed throughout most of the curve.

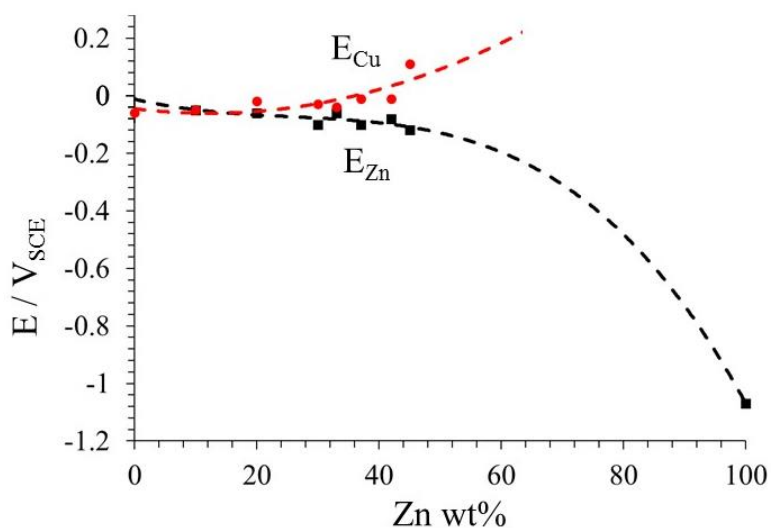


Figure 6.4. Plot of measured onset potential of Cu and Zn from the potentiodynamic polarization curve against Zn content (wt%)

The superimposition of the anodic branch of the polarization curves, j_e , is shown in Figure 6.5A. The polarization curves of Cu-Zn alloys showed a similar pattern with that of nominally pure Cu, and both deviated significantly from the polarization curve of nominally pure Zn. The superimposition of the j_{Zn} vs. E for various alloys is shown in Figure 6.5B. Besides a very good decreasing alignment of the partial current with the decrease of Zn content, an interesting peak can be found on alloys containing more than 30 wt% Zn, as shown by the inset in Figure 6.5B. The position of the peak shifted to more positive potential value with the increase of Zn content in the alloy. This peak correlates with the onset of Cu dissolution, as had been shown by the polarization curves in Figure 6.2-6.3. Figure 6.5C presents the superimposition of j_{Cu} . The dissolution of Cu was gradually inhibited by the increase of Zn content in the alloy, and it was completely inhibited when Zn content reach 45 wt%, corresponding to the β' -brass.

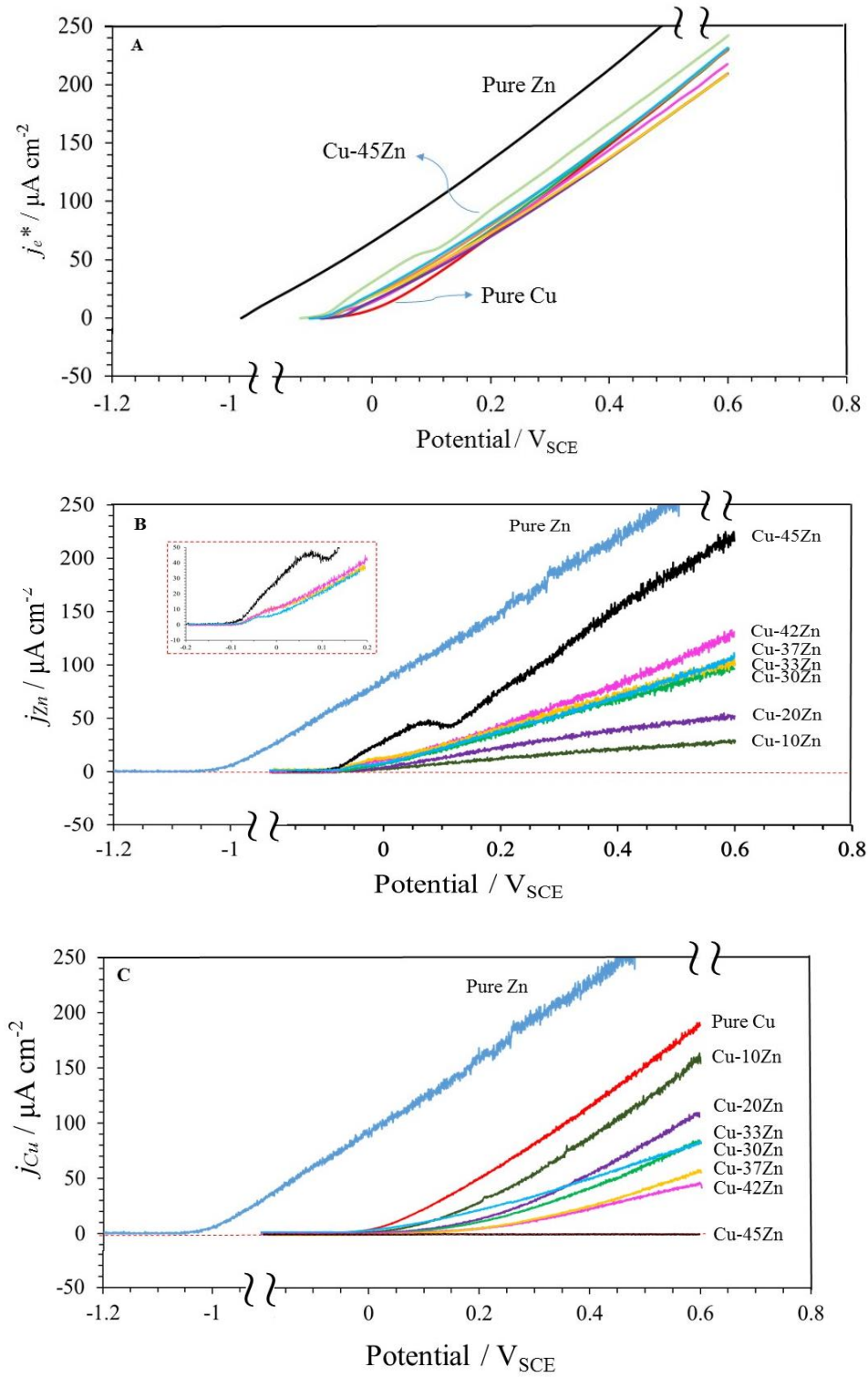


Figure 6.5. Superimposition of potential- j_e^* (A), potential- j_{Zn} (B) and potential- j_{Cu} (C) curves from various Cu-Zn alloys.

6.3.2 Galvanostatic dissolution behavior of Cu-Zn alloys in tap water

Figure 6.6 demonstrates the galvanostatic dissolution behavior of Cu alloys in tap water (part of stage a-b of the STW-CBS experiment shown in Figure 6.1). The open circuit dissolution rate of brass in tap water was very low, as can be seen in Figure 6.6 for both alloys: Cu and Zn dissolution rate, $v_{Cu}(STW)$ and $v_{Zn}(STW)$ were close to the detection limit. When the anodic current was imposed, at $t = 0$ s in these figures, both $v_{Cu}(STW)$ and $v_{Zn}(STW)$ increased significantly.

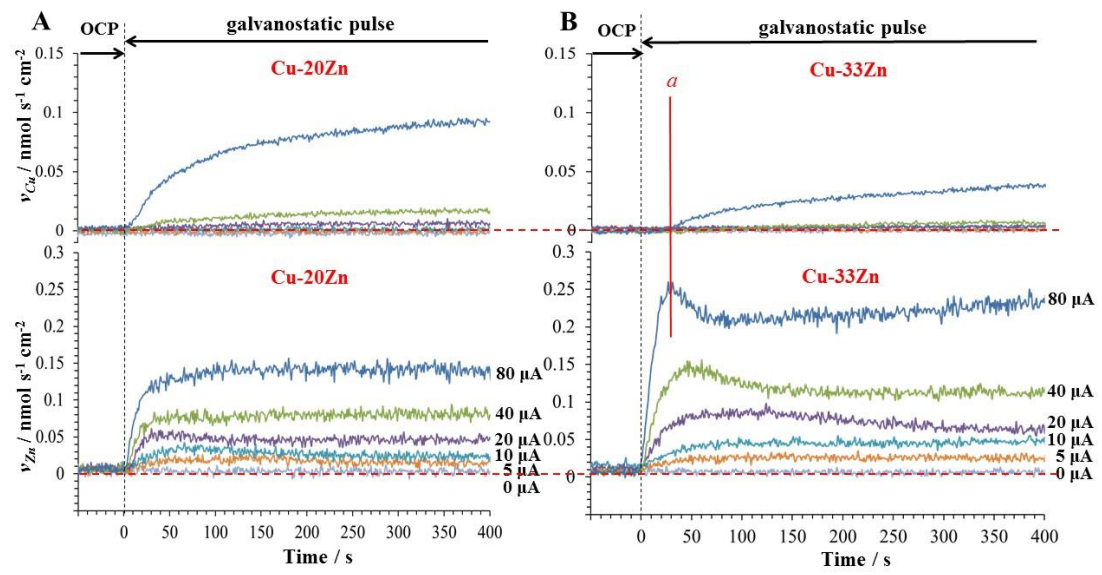


Figure 6.6. Elemental dissolution profile of Cu-20Zn (A) and Cu-33Zn (B) at various applied current.

The elemental dissolution behavior for the different Cu alloys differ from each other. In Figure 6.6, $v_{Zn}(STW)$ from Cu-20Zn reached a steady state after about 70 s of anodic polarization. Cu dissolution was kept at a low rate when the current was less than $40 \mu\text{A cm}^{-2}$ and no steady state could be reached even after 400 s of polarization. Cu dissolution was significantly enhanced when the current was higher than $40 \mu\text{A cm}^{-2}$, resulting in a rapid increase but still no stable state was achieved.

The dissolution profile of another α -brass, Cu-33Zn, showed some different features. $v_{Zn}(STW)$ showed a rather rapid increase of rate, leading to a peak at high current, as indicated as peak 'a' in Figure 6.6. Corresponding to the peak was the onset of Cu dissolution. Before the peak was reached, a time duration of about 35 s was observed where no soluble Cu release was detected.

Figure 6.7 shows a detailed dissolution kinetic analysis of Cu-20Zn and Cu-33Zn at an applied current density, $i_{ap} = 80 \mu\text{A cm}^{-2}$. The area filled with color is the difference between v_e^* and $2v_\Sigma$, which represents the formation of Cu_2O , as has been confirmed in previous work [155,176]. The growth of Cu_2O could be calculated via equation 6.1-6.2:

$$v_{\text{Cu}_2\text{O}} = v_e^* - 2v_\Sigma \quad 6.1$$

$$Q_{\text{Cu}_2\text{O}} = \int_0^t v_{\text{Cu}_2\text{O}} dt \quad 6.2$$

v_e^* is the applied current expressed as $\text{nmol cm}^{-2} \text{s}^{-1}$. The “*” indicates that the current density was numerically convoluted with the residence time distribution, $h(t)$ [126], of the flow cell to account for the loss of time resolution due to the hydrodynamic effect of the flow cell. $2v_\Sigma$ represents the sum of v_{Cu} and v_{Zn} being multiplied by a factor of 2, considering a maximum valence state for each element. The difference between the two terms, filled with color in the figure, gives the quantity of Cu_2O , which couldn't be directly detected by ICP-AES. The growth of Cu_2O could be obtained by an integral of $v_{\text{Cu}_2\text{O}}$ against time, equation 6.2. It is obvious that in Figure 6.7, $Q_{\text{Cu}_2\text{O}}$ started from $t = 0$ s, well prior to the onset of Cu^{2+} release. This suggests that during the first few tens of seconds of the dissolution of Cu-33Zn (Figure 6.7B), Cu was also oxidized, but its product exists in the form of Cu_2O , rather being oxidized into soluble Cu^{2+} .

The formation of Zn depleted layer, which is composed of metallic Cu, could also be evaluated as follows:

$$v_{\text{Cu}^*} = K v_{\text{Zn}}(\text{STW}) - 2v_{\text{Cu}_2\text{O}} - v_{\text{Cu}}(\text{STW}) \quad 6.3$$

$$Q_{\text{Cu}^*} = \int_0^t v_{\text{Cu}^*} dt \quad 6.4$$

Where K is the molar ratio of Cu/Zn in the bulk alloy. The integration of v_{Cu^*} gives the quantity of residual metallic Cu, Q_{Cu^*} . The growth of the Cu metallic layer also started from $t = 0$ s, with a steady rate for both alloys.

During the anodic dissolution, the potential decreased firstly rapidly through a minimum, rose through a peak, and then slowly decreased. The fast decrease and increase of potential during the initial tens of second forms a “bump” feature [65]. The existence of the “bump” suggests that the surface contains metallic Zn available for oxidation. The duration of the “bump” increased with increasing Zn content in the alloy, as can be seen in Figure 6.7A and B. After a

short time, atomic Zn on the surface are preferentially leached out, leaving a Cu rich layer on the surface, resulting in the potential increase. But with the onset of Cu^{2+} release, the atomic Cu layer starts to dissolve, exposing more atomic Zn from sublayers to the electrolyte. This results in the slow decrease of potential.

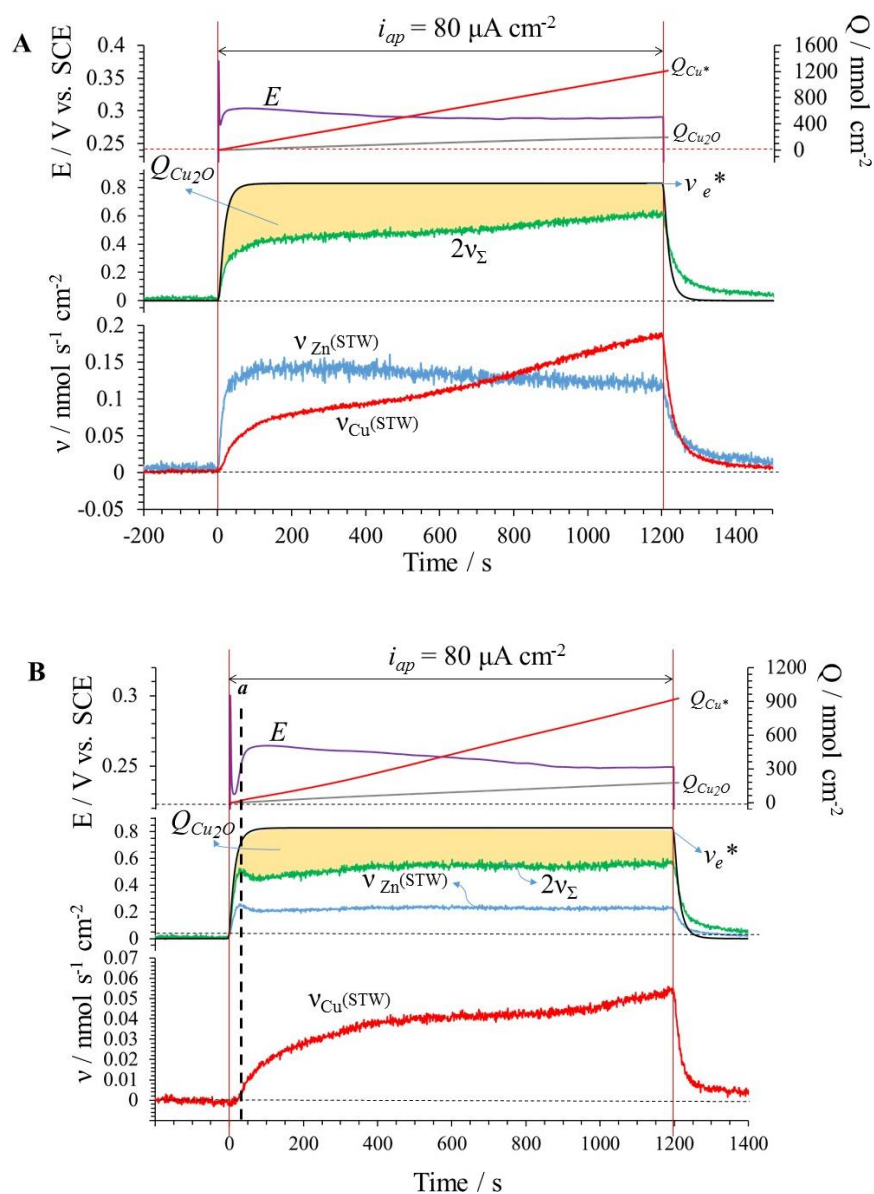


Figure 6.7. Comparison between the effective charge (v_e^*) and the sum of elemental dissolution rate ($2v_{\text{Zn}}$) for the dissolution of Cu-20Zn (A) and Cu-33Zn (B) in STW at $i_{ap} = 80 \mu\text{A cm}^{-2}$.

A similar “induction period” for Cu^{2+} release was also observed on alloys with Zn content up to 42 wt%. Figure 6.8 demonstrates the dissolution profile of Cu-37Zn (A) and Cu-45Zn (B). Cu-37Zn is a dual phase alloy that contains a small amount of β' . Cu-45Zn is a pure β' -brass. In Figure 6.8A, the “induction period” of Cu^{2+} is even more observable at $i_{ap} = 40 \mu\text{A cm}^{-2}$ (peak “a” and “b”). The detailed kinetic analyses of two alloys are presented in Figure 6.9.

It is obvious that the Cu_2O film started to form well prior to peak “a” and “b” in Figure 6.9A, indicating a similar dissolution behavior of Cu-37Zn with Cu-33Zn: in the initial stage of anodic dissolution, Zn is oxidized into soluble Zn^{2+} and Cu is oxidized into solid Cu_2O ; Cu^{2+} release started after metallic Zn was preferentially removed from the surface region. A two-stage dissolution behavior could be observed on alloys that contain α phase and the time duration of the first stage (induction period) is proportional to the Zn content. For alloys containing less than 20 wt% Zn, this period was not observed, Zn^{2+} and Cu^{2+} release followed each other closely on the time scale of these experiments.

The two-stage dissolution behavior was not observed for β' -brass, Cu-45Zn, Figure 6.8B and 6.9B. Figure 6.8B presents the dissolution profiles of pure Cu-45Zn. At lower current, $v_{\text{Zn}}(STW)$ increased steadily and remained constant after ≈ 50 s while $v_{\text{Cu}}(STW)$ remained below the detection limit. When the current increased to $80 \mu\text{A cm}^{-2}$, $v_{\text{Zn}}(STW)$ increased rapidly to form a peak, which is visible for the other alloys. Curiously, a small peak in $v_{\text{Cu}}(STW)$ correlates with the valley in $v_{\text{Zn}}(STW)$.

The kinetic analysis in Figure 6.9B shows a clear difference of this alloy as compared to the α phase alloys. The oxidation of Zn into $\text{Zn}^{2+}(aq)$ is the predominant reaction during anodic dissolution as indicated by the relatively small area between v_e^* and $2v_{\Sigma}$ (area filled with color). After the initial “induction period”, as being marked as peak “c”, $v_{\text{Cu}}(STW)$ increased to peak “c’” decreased again. In response, $v_{\text{Zn}}(STW)$ decreased and resumed its increase after peak “c’”. The potential signal in Figure 6.9B decreased more rapidly after the initial “bump feature”, suggesting that after the initial “induction period”, there was more metallic Zn available to be oxidized, which also resulted in a slow formation of Cu_2O from metallic Cu.

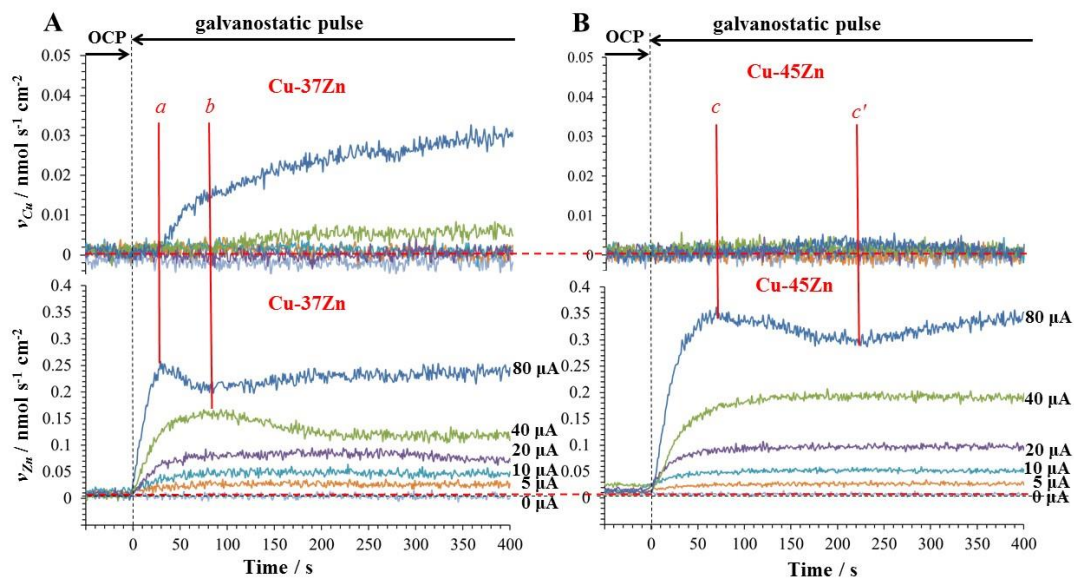


Figure 6.8. Elemental dissolution profile of Cu-37Zn (A) and Cu-45Zn (B) at various applied current.

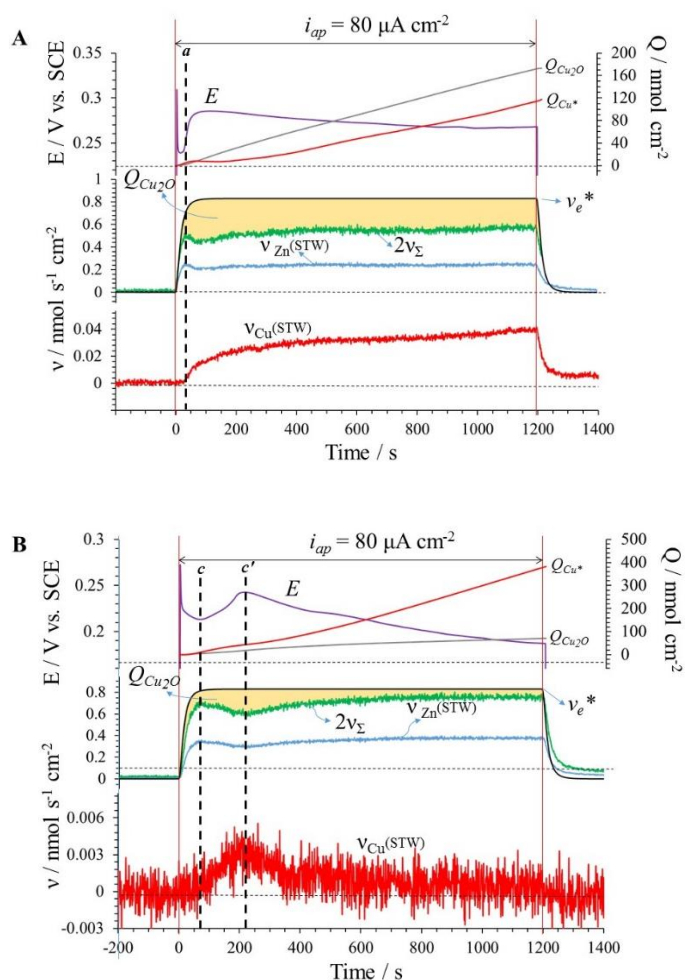


Figure 6.9. Comparison between the effective charge (v_e^*) and the sum of elemental dissolution rate ($2v_\Sigma$) for the dissolution of Cu-37Zn (A) and Cu-45Zn (B) in STW at $i_{ap} = 80 \mu\text{A cm}^{-2}$.

Figure 6.10 shows the semi-logarithmic plot of measured potential against applied current (i_{ap}) during the STW-CBS experiment for each alloy. Ohmic drop was manually corrected by subtracting the $i_{ap} \times R$ from the potential for each current (R was the system resistance, which could be obtained from the Nyquist plot of the impedance spectrum). The linear fitting of the measured potential-current curve gives an anodic Tafel slope, β_a . This value varied from 91 mV to 141 mV. Nawaz et al proposed that in the dissolution of brass in aggressive tap water, β_a varies from 81 to 107 mV when the pH was adjusted to be around 7 ~ 8 [178]. This value, however, is sensitive to the aggressiveness of tap water, which explains the larger value obtained in this work. Also, can be seen in this figure is the gradual decrease of measured potential at each applied current with the increase of Zn content in the alloy, which suggests the increase of Zn content promotes the dissolution of Cu-Zn alloys.

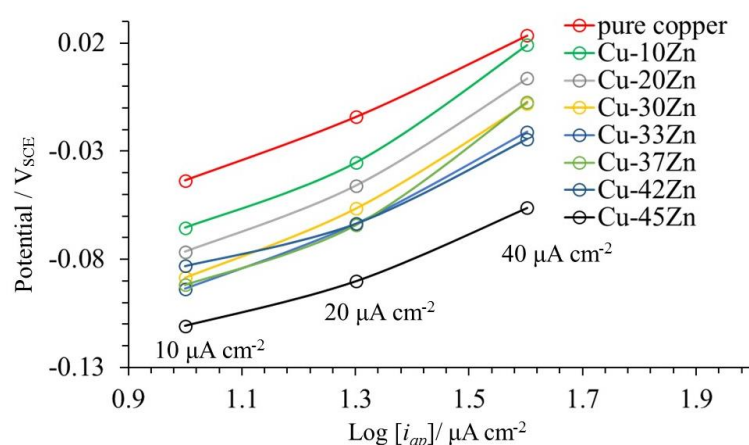


Figure 6.10. Plot of measured potential against applied current

6.3.3 Validation of the fate of elements by the mass/charge balance calculation

Previously we have demonstrated that in the dissolution of pure Cu [176] and the two Zn-Cu alloys in tap water [176], $\text{Cu} \rightarrow \text{Cu}^{2+}(\text{aq}) + 2e^-$ and $\text{Zn} \rightarrow \text{Zn}^{2+}(\text{aq}) + 2e^-$ contribute to the cation release; the residual oxides deposited on the surface are mainly composed of Cu_2O , with a negligible content of $\text{Zn}(\text{II})$ and $\text{Cu}(\text{II})$. These results were determined by AESEC and confirmed by XRD and Raman analysis.

The stoichiometry of dissolution may be discerned by comparing the total charge input, $Q_e(pstat)$, and the quantity of ions dissolved expressed as an effective charge, $Q_e(ICP)$. $Q_e(pstat)$ can be calculated using Faraday's law:

$$Q_e(pstat) = i_{ap} * \Delta t / F \quad 6.5$$

$Q_e(ICP)$ can be calculated using eq. 6.6:

$$Q_e(ICP) = \sum n_{m,aq} Q_{m,an(aq)} + \sum n_{m,s} Q_{m,an(s)} \quad 6.6$$

where $Q_e(pstat)$ is the total charge input, i_{ap} , represents the applied current, Δt is time duration of the galvanostatic pulse. In eq. 6.6, m represents either Cu or Zn; $Q_e(ICP)$ is the total charges output, $Q_{m,an(aq)}$ and $Q_{m,an(s)}$ represent the integral of dissolution in STW and in CBS species and solid species respectively, $n_{m,aq}$ and $n_{m,s}$ are the assumed valence states of the aqueous (aq) and the solid (s) species respectively.

Figure 6.11 shows the mass/charge calculation result of Cu-Zn alloys. In the figure, the dashed line represents the hypothetical case where $Q_e(pstat) = Q_e(ICP)$, i.e. a faradaic yield for dissolution of 100%. The experimental data, shown with different legends, followed closely the dashed line with increasing applied current. Especially at lower current than $20 \mu A cm^{-2}$, the deviation of the experimental data from the hypothetical case is negligible and reproducible for all alloys. At higher current, the experimental data deviated from the dashed line with a maximum discrepancy of 7.85% at $80 \mu A cm^{-2}$. However, this deviation can be explained by three different possibilities:

a) Cu(II) species existing in an amorphous state in the residual oxide film which cannot be detected by either Raman or XRD due to their low concentration and amorphous nature.

b) Error in the estimation of the background dissolution rate. The open circuit dissolution rates were subtracted from Q_M . In this subtraction, it was assumed that the anodic dissolution rate was kept unchanged even under anodic polarization. However, the mixed potential theory depicts an inhibition of the cathodic reaction when the sample is anodically dissolved. An overestimation of the cathodic contribution to the total charges input may play a significant role in the deviation;

c) as has been demonstrated in the previous publication, there were a small quantity of Zn containing solid species doped in the cuprite scale, its quantity decreased with the increase of anodic current. The subtraction of the open circuit contribution from the total quantity of different species definitely over counted this part. However, it's remarkable in Figure 6.7 that most alloys showed a feature that the calculated $Q_e(ICP)$ was smaller than $Q_e(pstat)$, resulting

in the dispersion of experimental data below the dashed line, except for the β' brass (Cu-45Zn), which dispersed above the dashed line at higher current.

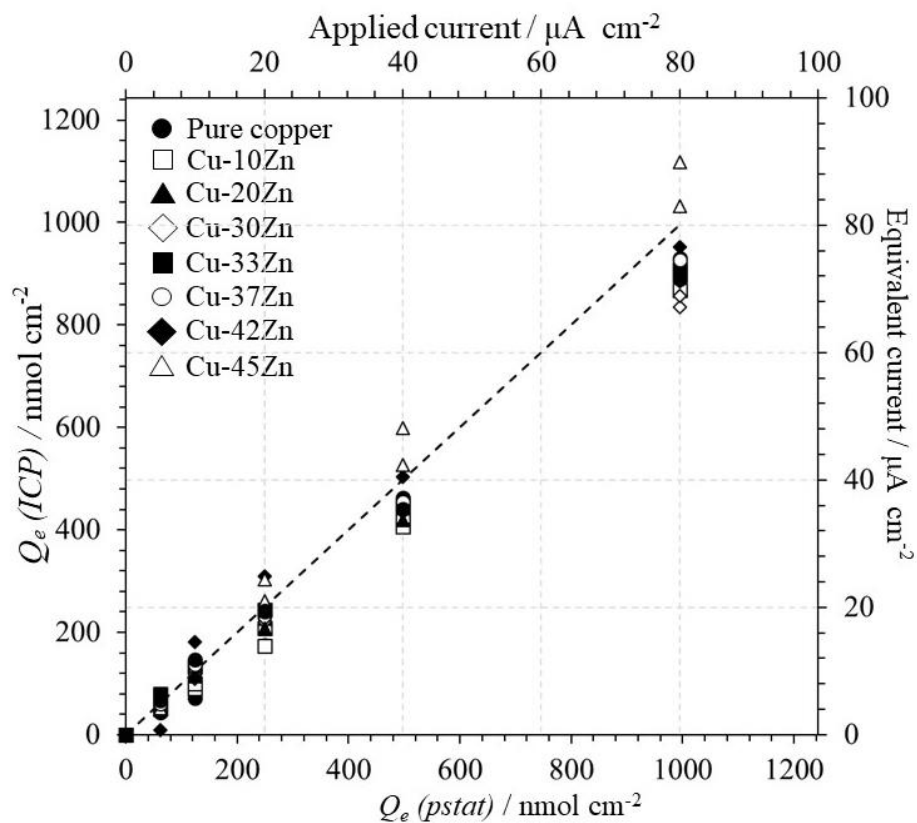


Figure 6.11. Mass/charge balance calculation of Cu-Zn alloys.

6.3.4 Effect of current on the formation of Cu^{2+} , Cu_2O and Zn^{2+}

In the previous section, we demonstrated the feasibility of quantifying soluble and solid Cu and Zn containing species [155,176] during galvanostatic dissolution with AESEC. A linear relationship between the total oxidized Cu, Q_{Cu} , (including $\text{Cu}^{2+}(\text{aq})$ and $\text{Cu}_2\text{O}(\text{s})$) and the total oxidized Zn, Q_{Zn} , and the applied current density, i_{ap} , was observed (Figure 6.12). Further, the slope of the respective Cu and Zn curves was directly proportional to Zn content in the alloy.

Cu oxidation was distributed between Cu^{2+} and Cu_2O . The formation of Cu_2O was favored over Cu^{2+} at lower current (Figure 6.13), but the slope of ν_{Cu} vs. i_{ap} increased with increasing i_{ap} while the formation rate of Cu_2O leveled off. Moreover, the increase of Zn content progressively inhibited the release of Cu^{2+} , and it was almost completely inhibited for the β' -brass, Cu-45Zn.

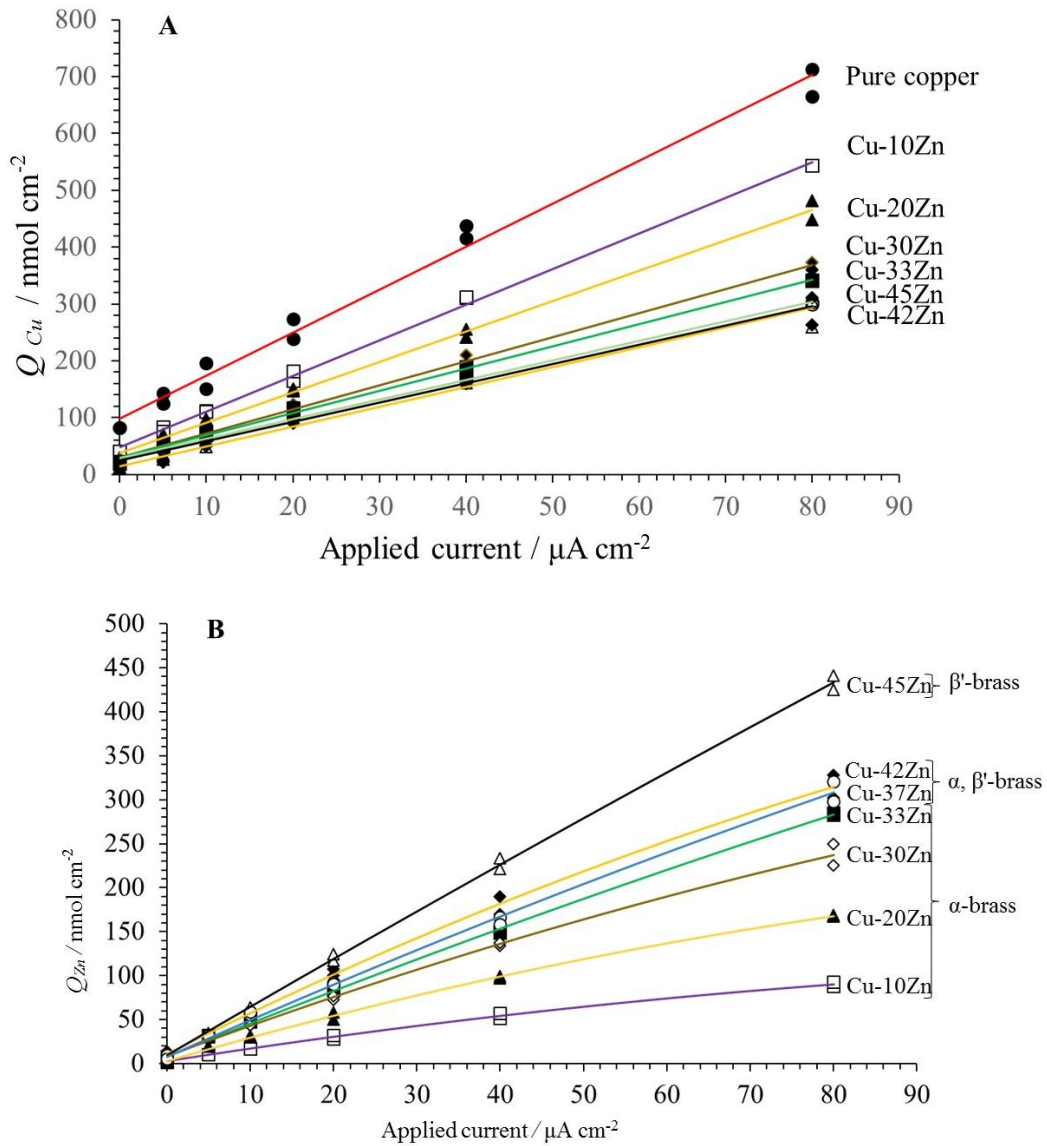


Figure 6.12. Quantitative relationship of oxidized Cu (A) and Zn (B) as a function of applied current.

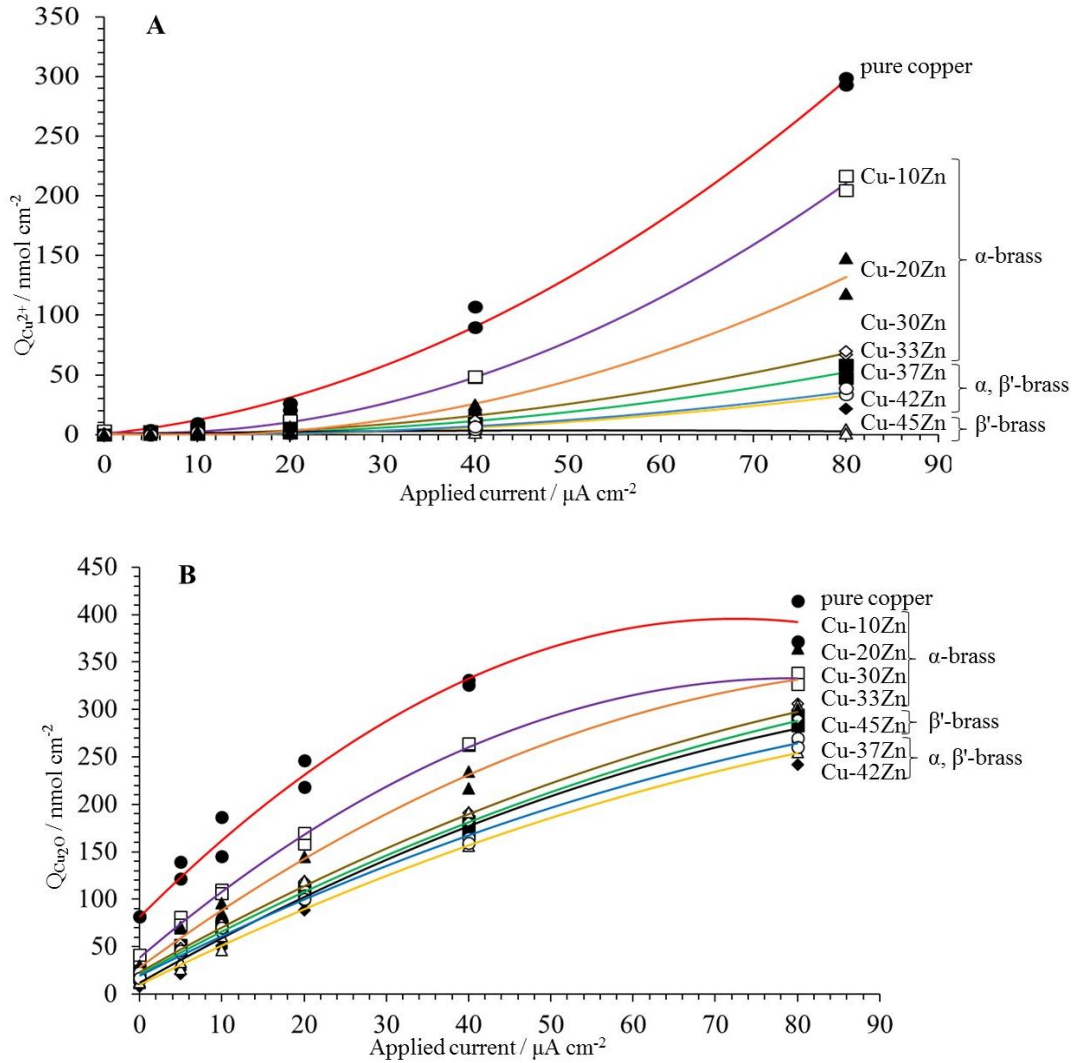


Figure 6.13. Quantitative relationship of Cu^{2+} (A) and Cu_2O (B) as a function of applied current.

6.3.5 Effect of Zn content on dissolution behavior

Figure 6.14A demonstrates the increase of Zn^{2+} release (Q_{Zn}) with increasing Zn content in the bulk. A steady increase in Q_{Zn} was observed when the Zn content was below 30 wt%, and then started to fluctuate with further increase, possibly due to a phase composition transition from α to α , β' and then β' . Also, the Zn release increased steadily with the increase of applied current. Figure 6.14B and 6.14C depict the change of Cu^{2+} and Cu_2O as a function of Cu content. It is noteworthy that though Cu^{2+} release was kept at a rather low rate and was even independent of the composition change in the alloy when the current was less than $20 \mu\text{A cm}^{-2}$, at higher current it was sensitive to the increase of Zn content. The Cu release was almost completely inhibited when the Zn content reached 45 wt%, corresponding to a β' -brass. On the other hand, the quantity of Cu_2O was less sensitive to the Cu content in then bulk alloy, especially at high

current. this feature demonstrates that the increase of Zn content in the alloy significantly affects the Cu^{2+} formation, and affects the formation of oxide scale to a lesser extent.

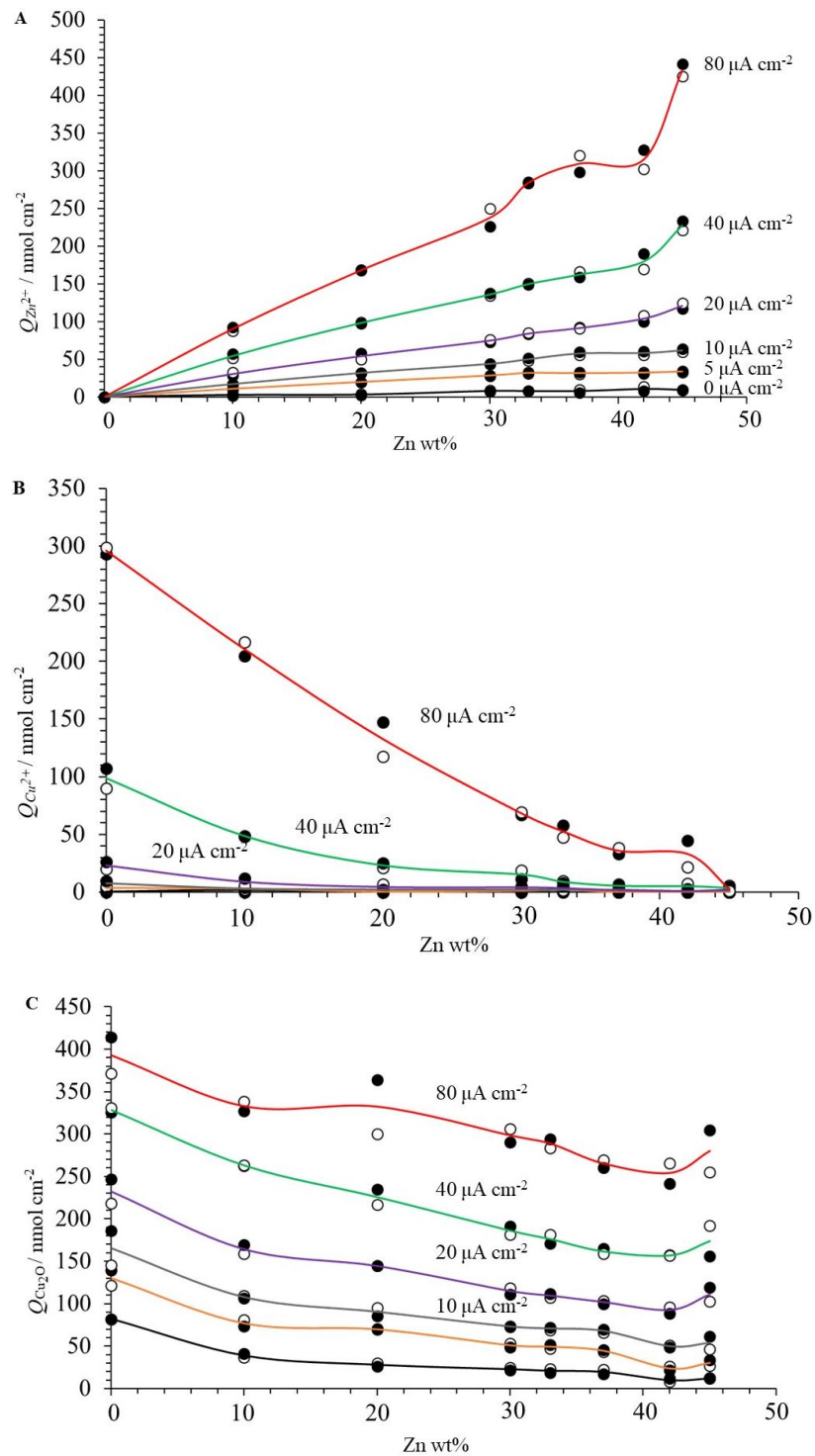


Figure 6.14. Effect of Cu (Zn) content on the dissolution behavior of Cu-Zn alloys. A: Zn^{2+} ; B: Cu^{2+} ; C: Cu_2O .

The percentage of oxidized Cu in the total quantity of elements being oxidized, can be calculated by:

$$K' = \frac{Q_{Cu^{2+}} + Q_{Cu_2O}}{Q_{Cu^{2+}} + Q_{Cu_2O} + Q_{Zn^{2+}} + Q_{ZnO}} \times 100\% \quad 6.7$$

Where K' represents the percentage of total Cu being oxidized, as compared to the atomic percentage of Cu in the bulk, K . A relationship between K' and Zn content is described in Figure 6.15. It is observed that the percentage of oxidized Cu decreased gradually with increasing of Zn content. The data at different current densities overlapped each other except for data at $0 \mu A \text{ cm}^{-2}$, which showed a smaller percentage of Cu being oxidized. The dashed line in the figure indicates a hypothetical congruent dissolution, where $K' = K$. The extent of selective Zn dissolution increases with increasing Zn content. Furthermore, the steady decrease of Cu percentage was broken when the Zn content increases to form dual phase structure, this may indicate that the dissolution mechanism of dual phase alloy was more complicated than the single phase alloy.

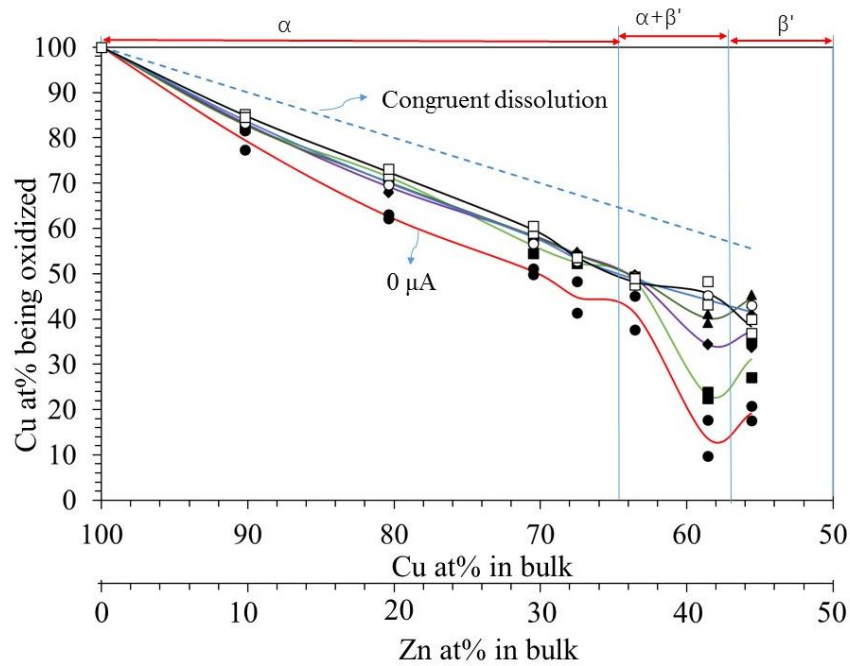


Figure 6.15. Quantitative comparison between the oxidized Cu and the Cu content in the bulk for alloys with various Zn content.

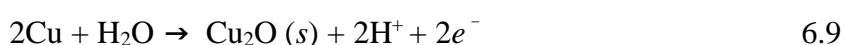
6.4 Discussion

6.4.1 Summary of findings

The major results of this study are summarized as follows:

The polarization curves demonstrate the asynchronous nature of the onset dissolution potential of Zn and Cu, E_{Zn} and E_{Cu} . With the increase of Zn content in the alloy, E_{Zn} shifted negatively and E_{Cu} shifted positively. Further, corresponding to E_{Cu} , the Zn dissolution profile decreased for a short potential range and then resumed its increase again, forming a peak. This peak was detected for alloys containing > 37 wt% Zn. The potentiodynamic curve of Cu-45Zn demonstrated that the oxidation was primarily due to the dissolution of Zn from the alloy into water, Cu dissolution was kept very low throughout the potential range.

The mass/charge calculation corroborated that, for all the Cu-Zn alloys investigated in this work, Cu was primarily oxidized into Cu^{2+} and $Cu_2O(s)$, and Zn was oxidized into Zn^{2+} :



The analysis of elemental dissolution profiles from STW-CBS experiment demonstrated the existence of an induction period at the beginning of the galvanostatic pulse, during which Cu was only oxidized essentially into Cu_2O and Zn was oxidized into Zn^{2+} . After this period, Cu^{2+} release was detected. A schematic diagram of dissolution process is presented in Figure 6.16. In this figure, a two-stage mechanism is proposed. A first stage in which the simultaneous oxidation of Zn into Zn^{2+} (reaction a) and Cu into Cu_2O (reaction b). In this stage, the dissolution rate of Zn is significantly higher than Cu, resulting in the formation of Zn depleted metallic Cu layer. The second stage sees the release of Cu^{2+} into tap water. However, the release of Cu^{2+} could be achieved either by the direct dissolution of metallic Cu in the bulk (reaction c), or the further dissolution of Cu_2O oxide (reaction d & e). However, two possible reactions regarding the dissolution of oxide are proposed: a direct oxidation of Cu_2O into soluble Cu^{2+} (reaction e) and a disproportionation reaction of Cu_2O into metallic Cu and Cu^{2+} (reaction d) [99, 178-180]:



The first stage is sensitive to Zn content in the alloy: for alloys containing less than 20 wt% of Zn, this period was undetectable up to $80 \mu A cm^{-2}$. With the further increase of Zn content, this stage is more distinctive and can be observed at lower current. The release of Cu^{2+} decreased gradually with the increase of Zn content. When Zn content reached 45 wt%, giving

a pure β' phase in the alloy, Cu^{2+} formation was almost entirely inhibited, with only a negligible dissolution peak being observed.

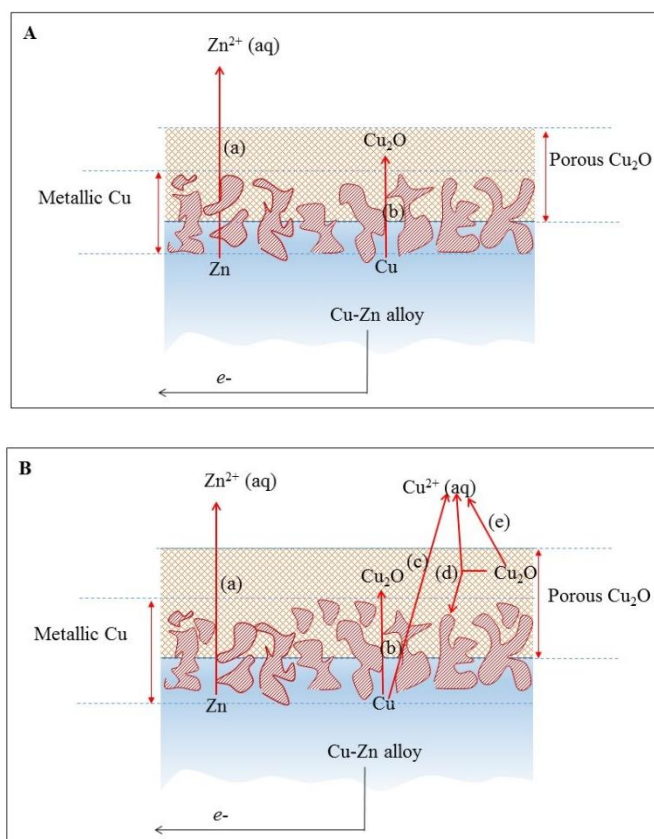


Figure 6.16. Schematic diagram of the dissolution of Cu-Zn alloy in tap water. A: the simultaneous oxidation of Cu and Zn, resulting in a direct release of Zn cation into water but Cu was deposited on the surface forming a Cu_2O layer; B: the release of Cu cation into water via the direct oxidation of bulk Cu or the further dissolution of Cu_2O layer.

The mass/charge balance calculation offers a quantitative relationship of the different species as a function of the applied current density, i_{ap} . In section 6.3.3 we discussed three possible factors that result in the difference between $Q_e(\text{ICP})$ and $Q_e(\text{pstat})$ shown in Figure 6.11. The mass balance of Figure 6.11 suggests that some solid Cu(II) may also be formed, estimated from the slope as $\sim 8\%$ of the solid Cu oxidation products. This Cu(II) oxide, however, could not be detected by GIXRD, considering its small amount. Raman spectroscopy couldn't distinguish Cu(II) from Cu(I) since the main peak of Cu(II) from Cu(I) are both centered at 650 cm^{-1} . The overestimation of background dissolution rate could also be ruled out from a significant contribution to the difference, since the polarization curve in Figure 6.12-6.13 showed that the open circuit dissolution rate was essentially zero. Zn(II) solid species also

contributed negligibly to the difference, with a maximum of 2%~3%, as can be seen in Figure 5.5 (Chapter 5)

The dissolution rate of Zn, v_{Zn} , increased linearly with the increase of current. The release of Cu^{2+} , v_{Cu} , only became significant at $i_{\text{ap}} > 20 \mu\text{A cm}^{-2}$.

The rate of Zn^{2+} release increased steadily with the increasing %Zn while the rate of Cu^{2+} release decreased with increasing %Zn. The quantity of Cu_2O also decreased with the increase of Zn content but much was much less sensitive to %Zn than v_{Cu} .

6.4.2. Dezincification mechanism

The STW-CBS and the potentiodynamic polarization experiments demonstrated the electrochemical reactions involved in the dissolution process: the oxidation of Zn into Zn^{2+} , the oxidation of Cu into Cu^{2+} and the formation of Cu_2O . The effect of Zn content and phase composition on the dissolution process is discussed below.

Effect of Zn content

Sugawara and Ebiko [147] investigated the dissolution behavior of Cu-Zn alloys ranging from 0 % to 100 wt% Zn in 3 wt% NaCl solution. They concluded that the increase of Zn content shifts the corrosion potential in the cathodic direction and increases the corrosion rate. But no detailed effect of Zn content on the specific electrochemical reactions was discussed.

In this work, we tested the anodic dissolution of Cu-Zn alloys containing Zn up to 45 wt% and a two-stage dissolution process was identified, Figure 6.16. The first stage, was observed on alloys containing more than 33 wt%, and corresponded to the induction period for Cu^{2+} dissolution and the initial negative drop of the potential. The duration of this period increases with increasing Zn content, as can be seen in Figure 6.7 and 6.9. This period was also observed at lower current for %Zn ≥ 37 %, as can be seen in Figure 6.7B and 6.9A, as well as Figure 5.5A (in Chapter 5). The increase of Zn content will increase the formation of Cu_2O during the first stage at the expense of Cu^{2+} dissolution. The same conclusion could also be drawn from Figure 6. 4, as the onset dissolution potential of Cu was shifted positively. The dissolution rate of Zn during the first stage reached a maximum value, indicating that the most severe selective dissolution of Zn occurs in this stage. This dezincification propensity is also proportional to %Zn, as can be seen from 6.14A. As a result, a typical dezincification structure consisting of an outmost cuprite scale, an inner Zn depleted metallic Cu layer was formed. In principle, this stage would terminate when no metallic Zn is available in the metallic layer.

The second stage starts with the release of Cu^{2+} . In this stage, Cu^{2+} could be formed either from the direct oxidation of metallic Cu (equation 6.6) or the further oxidation of Cu_2O layer (equation 6.11-6.12). The kinetic analyses in Figure 6.7 and 6.9 demonstrated that during this stage, the Zn dissolution rate remained constant and the Cu dissolution rate increased steadily. Therefore, the dissolution of metallic Cu (equation 6.6) is inevitable. Besides, the potential signal in Figure 6.7 and 6.9 also showed a steady decrease during the second stage, indicating a decrease of noble elements on the surface.

However, Figure 6.13 depicts a competitive relationship between Cu_2O and Cu^{2+} with increasing current density. This may indicate that at higher current density ($i_{ap} \geq 20 \mu\text{A cm}^{-2}$), the dissolution of residual Cu_2O scale also plays a critical role. The increase of Zn content in the alloy will inhibit both the formation of Cu_2O and Cu^{2+} , as shown in Figure 6.14. However, the inhibiting effect of Zn on Cu^{2+} release is more significant than the formation of Cu_2O especially at higher current. This phenomenon demonstrated that the increase of Zn will result in a more severe preferential dissolution of Zn (Figure 6.2), thus retarding both the formation of Cu_2O and Cu^{2+} . But the formation of Cu_2O is thermodynamically easier than Cu^{2+} [63], since equation 6.8 has a standard reduction potential of 0.342 V and equation 6.9 has a standard reduction potential of 0.028 V. Therefore, the inhibiting effect of Zn is less sensitive for Cu_2O formation than for Cu^{2+} dissolution.

The role played by Zn in affecting dissolution behavior of Cu-Zn alloy is complicated. On the one hand, the increase of Zn in the alloy increases the concentration of Zn on the surface, resulting in a direct preferential dissolution of Zn, which also inhibits the oxidation of Cu; on the other hand, the existence of Zn promotes the formation of kink, ledge and terrace, resulting in heterogeneity of surface energy. The former determines the first stage as mentioned before: the more Zn content in the alloy, the longer the first stage is; when Zn wt% is less than 20 wt%, this first stage is too short to be detected. The latter affects the whole process of corrosion, since surface rearrangement of Cu/Zn via surface and/or volume diffusion, or redeposition of Cu back on to the surface will altogether reduce surface energy, establishing a stable dissolution process. However, in the first stage, as discussed before, Cu is also involved in the electrochemical process, but it preferentially formed Cu_2O on the surface. This means that the dissolution rate due to the preferential removal of Zn is fast, it will be immediately replaced by the simultaneous oxidation of Cu and Zn.

Effect of phase composition

The increase of Zn content from 0 wt% to 45 wt% results in the phase composition varying from pure α phase (pure copper, Cu-10Zn, Cu-20Zn, Cu-30Zn and Cu-33Zn), via dual phase (Cu-37Zn and Cu-42Zn), to pure β' phase. It is known that the β' phase has a corrosion potential of 180 mV more negative than the α phase [99,146], and β' suffers more severe dezincification than α [86,170]. The effect of phase composition on dissolution behavior has seldom been investigated, but some authors proposed experimental evidence showing that the dissolution behavior of α and β' might be different. Polunin and Pchel'nikov [14,15] used isotopes to follow the dissolution of α brass and β brass, their results show that in the dissolution of β' brass, no Cu was released into the electrolyte whereas in α brass both Cu and Zn ions were released. Can utilized the rotating ring-disk to investigate the effect of rotating speed on the electrode current density for different alloys [100]. They found that the current of an α brass was independent of the rotating speed whereas the current depended on rotating speed for an α , β' brass. In this work, the first stage of the dissolution process could be found on all Cu-Zn alloys tested, regardless of the phase composition. However, the difference emerged on the second stage for β' -brass: there was almost no Cu^{2+} release from either the STW-CBS experiment or the potentiodynamic polarization experiment. This result confirms the isotopic investigation from Polunin and Pchel'nikov [14,15] that no soluble Cu was released from β' -brass. They proposed a multi-stage mechanism for α -brass, which involves a primary selective dissolution of Zn, controlled by the volume diffusion of Zn in the alloy, a subsequent simultaneous dissolution of both Cu and Zn, and a secondary preferential dissolution of Zn due to the redeposition of Cu back onto the surface. As to β' -brass, a simpler process involving the preferential dissolution of Zn due to the redeposition of Cu back onto the surface was proposed [100].

In this work, the initial stage of dissolution was indeed associated with a severe dezincification, indicated by a peak in the Zn dissolution profiles of Figure 6.2-6.5. In the second stage, the onset of Cu^{2+} release also demonstrated simultaneous dissolution. As to the redeposition process of oxidized Cu, it could be achieved either by the reverse reaction of equation 6.8 or by the disproportionation reaction of Cu_2O into Cu and Cu^{2+} , since the non-protective nature of Cu_2O would neither prevent the dissolution of Zn nor interfere with the redepositon process of Cu.

Moreover, it's noteworthy that the crystal structure difference between α and β' phase may also play a vital role in the difference of dissolution behavior. Modern advanced techniques provide a closer insight into the dissolution/corrosion on the nanoscale. It had been proven that grains with different orientation show different corrosion behavior [181,182]. For the corrosion of body centered cubic (bcc) stainless steel in NaCl solution, planes oriented $\sim 25^\circ$ away from

{001} exhibit the highest percentage of pitting events [183] while contrarily the {100} orientation was reported to have the highest corrosion rate in H_2SO_4 [184] and NO_3^- [185]; for the corrosion of face-centered cubic (fcc) Al in NaOH, orientations near {111} indicated the highest corrosion rate [186]; for the corrosion of hexagonal close packed (hcp) magnesium in chloride containing, alkaline environment, the thickest oxide was observed on the (1010), and (1120) planes while the thinnest oxide was found on the (0001) plane, and the thick oxide prevents the underlying substrate from severe corrosion [187]. Literature regarding the effect of crystalline orientation on corrosion of Cu alloys is lacking. It is commonly accepted that the difference in surface energy (γ) of various planes plays a critical role in corroding and pitting sample surface: a higher surface energy gives a higher corrosion rate [187]. However, as to the commercial polycrystalline alloy, the existence of grain boundary further confounds the corrosion behavior as a whole, since grain boundaries and phase boundaries have higher energy allowing corrosion to initiate preferentially. In this work, the involvement of surface oxide on the surface further perplexes the possible effect of crystalline orientation. Nevertheless, more in-depth investigation regarding the effect of crystalline orientation on corrosion property needs to be conducted.

Further, the semi-conductive nature of Cu_2O [188] may have a catalytic effect on the corrosion, and the existence of residual stress within the Cu metallic layer will also alter the reaction. A more in-depth investigation is needed in distinguishing the different mechanism of different metallurgical phases.

6.5 Conclusions

In this work, the dezincification mechanisms of Cu-Zn alloys with Zn content ranging from 0 wt% to 45 wt% in tap water were investigated using a synthetic tap water-citrate buffer solution experiment (STW-CBS) with the atomic emission spectroelectrochemistry technique (AESEC).

1. The main soluble products of anodic dissolution of Cu-Zn alloys in tap water were soluble Cu(II), Zn(II); the main solid products were Cu_2O and a negligible amount of Zn(II) and Cu(II) species.
2. The STW-CBS and potentiodynamic polarization experiments in tap water showed an “induction period” of Cu^{2+} for all alloys. In this period, Zn was oxidized into Zn^{2+} and Cu was oxidized into Cu_2O .
3. The mass/charge calculation offers a quantitative relationship of different

species against applied current. It showed a linear relationship of total oxidized Cu and Zn with the increase of applied current; but the distribution of total oxidized Cu into Cu^{2+} and Cu_2O showed a compensating relationship of each other: Cu^{2+} release was more favored at higher current and Cu_2O formation was preferred at lower current.

4. A two-stage dissolution mechanism was proposed for α phase in Cu-Zn alloy: an initial stage in which Cu and Zn are oxidized congruently, but only Zn^{2+} was released into water, Cu forming a Cu_2O film, and a second stage where Cu was released into water in the form of Cu^{2+} . For the β' phase, the second stage is the same to the initial stage.

5. The increase of Zn content in the alloy results in a time extension of the initial stage and retard the Cu^{2+} release.

7. Effect of alloying elements on the electrochemical Cu release from Cu-Sn alloys to artificial perspiration solution

7.1 Introduction

Cu ions have been demonstrated to be efficient in killing/inactivating antibiotic-resistant so-called ‘superbugs’, such as methicillin-resistant *Staphylococcus aureus* (MRSA), *Escherichia coli* O157, *Salmonella enterica*, *Campylobacter jejuni*, *Clostridium difficile*, *Listeria monocytogenes*, and *Mycobacterium tuberculosis* [189-198]. This has led to a renewed interest from the corrosion and the pathogenic microbiological communities in the exploitation of Cu alloys as functional antimicrobial materials. Cu alloys are considered undesirable for use in these high-touch applications due to tarnishing (surface discoloration from an oxide) from hand contact. Soluble ion release is required to maintain antimicrobial function and hence, metallic corrosion is compulsory. A critical balance is needed between corrosion and ion release: corrosion rates must be sufficient to release enough Cu ions for desired antimicrobial function and low enough to avoid undesired tarnish-forming and/or passivating oxides.

The effect of alloying content on the variation of structure, porosity and composition of oxide had been well documented [199-201], but has not been explained. It was recently demonstrated that the Cu-Sn alloys, *i.e.* bronze, exhibited an enhanced Cu release and an increased anti-microbial efficacy, regardless of the diluting effect of Sn on the Cu solid-solution compared to Cu alone [197]. It is of great interest to elucidate the role played by alloying elements, such as Sn, in the corrosion/dissolution mechanism of Cu-Sn alloys and Cu-Zn alloys. The investigation of Cu anti-microbial efficacy had usually been conducted in media such as soy broth [190], agar [191], and saline [202], these tests provide a precise bacterial culture growth but neglect the effect of corrosion. In order to better simulate a high-touch environment that causes a simultaneous appraisal of corrosion response and anti-microbial efficacy, simulated human perspiration [203] is a perfect substitute since it contains known complexing and Cu ion -chelating compounds [204] and offers a more representative electrolyte for high-touch environments.

Soluble cation release and oxide tarnish behavior on commercial Cu based alloys in artificial perspiration solution has been investigated in several publications [197,205,206,]. It was found that Cu-Sn alloys demonstrated an enhanced Cu cation release as compared to Cu despite having reduced Cu content. Similar phenomenon was also observed in the rainfall-induced run off of Cu-Sn alloys compared to pure Cu [207]. These phenomena have inspired interest in exploring the effect of Sn on the cation release property of Cu alloys, especially the dose-response relationship.

The objective of this work aims at investigating the corrosion response, the fate of cations, oxide growth and passivity of film, as well as their relationship to the Sn alloying content in the bulk. AESEC technique [208] was used to quantify the soluble species; insoluble species were characterized by XRD, Raman and XPS, and could be quantified by a mass/charge balance calculation. The mechanism by which the enhancing effect of Sn function on the Cu release was discussed.

7.2 Materials and experiments

Commercially pure Cu (99.9 wt%, UNS C11000), Cu-4.5Sn-0.1Zn (UNS C51000) and Cu-9.7Sn-0.1Zn were used. These wrought sheets were obtained from commercial suppliers and sectioned into a size of about 2.5 cm × 2.5 cm. In this chapter, only the effect of main alloying element Sn is highlighted, Zn and other impurities are not discussed. All samples were ground with up to 800 grit polishing paper under water and were further ground with 1200 grit polishing paper under ethanol.

Synthetic perspiration solution (SPS) was used as an appropriate analogue to a high-touch environment where Cu alloys may be of interest, it was used in a naturally aerated state. This solution is based on the BS EN 1811:2011 standard [203]. Citrate buffer solutions (CBS) was used to dissolve the oxide scale formed on the surface, it was prepared from mixed 0.1 M solutions of citric acid ($C_6H_8O_7$) and trisodium citrate ($Na_3C_6H_5O_7$) solutions to achieve a pH of 4.9 ± 0.1 . Buffer solution of citric/citrate was deaerated for a minimum of one hour by grade-5 pure N_2 gas bubbling prior to each test.

Table 7.1. Artificial perspiration solution composition. Based on [203].

Chemical Name	g/L	Molarity (mM)
NaCl – Sodium Chloride	5.00	85.6
CH ₄ N ₂ O - Urea	1.00	16.7
C ₃ H ₆ O ₃ - L(+) Lactic Acid (90%)	1.00	11.1
NH ₄ OH – Ammonium Hydroxide	pH Adjuster	~11

Atomic emission spectroelectrochemistry (AESEC) was used to investigate the elemental dissolution kinetics in artificial perspiration solution (APS), and citrate buffer solution (CBS). Details of this technique had been introduced in the introduction section. Cu dissolution was followed using a monochromator to detect the atomic Cu emission intensity at 324.75 nm. Zn and Sn were followed using a polychromator detecting the atomic emission intensity at 213.68 nm and 189.99 nm respectively. A conventional three-standard calibration was conducted for each element. The detection limit (LOD) was defined as three times the standard deviation of background noise divided by the sensitivity (α), which can be determined from the intensity – concentration calibration line. The LOD for Cu in SPS and CBS was 5 ppb, for Zn it was 24 ppb and for Si it was 150 ppb, corresponding to an equivalent current density of 0.4, 3.5, and 95 $\mu\text{A cm}^{-2}$ for each. Due to the minor content of Zn in the bulk alloy and the high detection limit of Sn, dissolution profiles of Zn and Sn could not be distinguished from the background noise. A Gamry Reference 600TM potentiostat was used to control and/or measure the current and potential. The analog output of the potentiostat was routed into the data acquisition system of the ICP spectrometer so that spectroscopic intensity and electrochemical data were on an identical time scale.

A typical SPS-CBS experiment was conducted as follow: a) an open circuit exposure of 10 min allowing a relative steady dissolution rate of Cu in APS; b) application of an anodic current varying from 0 $\mu\text{A cm}^{-2}$ to 80 $\mu\text{A cm}^{-2}$ for 20 min, allowing an accelerated cation release as well as oxide film formation; c) return to the open circuit potential for 10 min; and d) the perspiration solution was replaced by a deaerated citrate buffer solution to dissolve the oxide formed during the previous stages.

Potentiodynamic polarization experiment was conducted by the following steps: a) an open circuit exposure for 20 min, b) a 10-minute potentiostatic polarization of -1.0 V_{SCE}, c) a potentiodynamic scan was initiated from -1.0 V_{SCE} to 0.5 V_{SCE} at a sweep rate of 0.5 mV s⁻¹, d) return to the open circuit potential.

Crystalline products were identified using grazing incidence X-Ray diffraction (GIXRD, PANalytical X'Pert). Incidence grazing angle gave optimal signal/noise at $\omega = 0.5^\circ$ with a 10 mm width limiting mask. 2Θ ranged from 20° to 100° ; Raman spectroscopy measurements were acquired using a Renishaw InVia Raman microscope, utilizing a 514 nm line of an argon laser with 180° back scattering geometry and a 3000 l/mm grating; X-ray photoelectron spectroscopy (XPS) was employed using a Thermo-Scientific K-AlphaTM XPS system equipped with an Al K α monochromatic X-ray source and an Ar ion gun for sputting. High-resolution scans were taken with a pass energy of 20 eV and a spot size of $\sim 0.5 \text{ mm}^2$. Au 4f_{7/2} was used as an energy reference assigned to 84.0 eV. Peak fits were made using a Shirley background and a Gaussian-Lorentzian shape. Spin orbit energy splits were set as the only constraint with all other parameters unconstrained for the best software fit.

7.3 Results

7.3.1 Synthetic perspiration solution-citrate buffer solution experiment (SPS-CBS)

A typical dissolution profile for pure Cu exposed to synthetic perspiration solution, followed by citrate buffer solution (SPS-CBS) is shown in Figure 7.1. As the valence state of Cu in sweat solution was unclear, the applied current i_{ap} was expressed in $\text{nmol cm}^{-2} \text{ s}^{-1}$, allowing a direct quantitative comparison with the dissolution rate of Cu in synthetic perspiration solution, $v_{\text{Cu}}(\text{SPS})$. The experiment started at $t = 0 \text{ s}$, with the system at open circuit for 600 s (stage a). $v_{\text{Cu}}(\text{SPS})$ into the electrolyte reached a maximum within 100 s and it decreased gradually. When the anodic current density was applied, $v_{\text{Cu}}(\text{SPS})$ increased immediately to a maximum and then decreased sluggishly throughout the rest time in stage b. Note that the decrease of $v_{\text{Cu}}(\text{SPS})$ under anodic pulse roughly gave a continuation of the decrease of the open circuit dissolution rate, indicating a non-steady state for both the open circuit dissolution and the anodic dissolution. After another open circuit delay (stage c), the electrolyte was replaced by deaerated citrate buffer solution to dissolve the solid species (stage d), resulting in a well-defined dissolution peak.

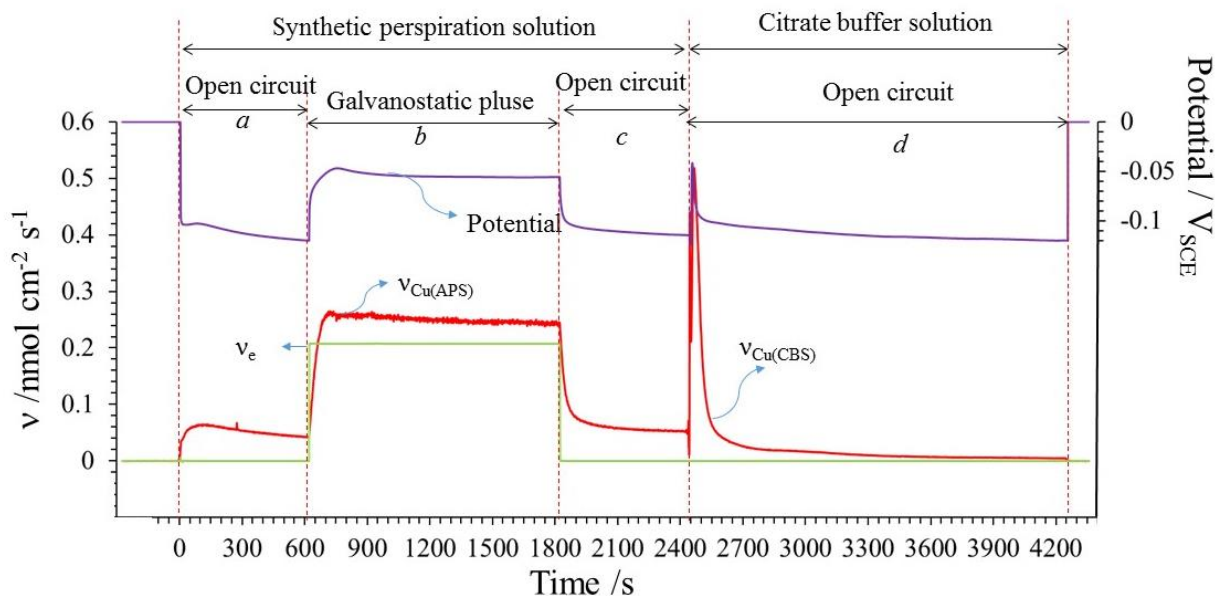


Figure 7.1. Synthetic perspiration solution-citrate buffer solution (APS-CBS) experiment of pure Cu at $i_{ap} = 20 \mu\text{A cm}^{-2}$

The dissolution profile of Cu-Sn alloys showed similar features to the profile of pure Cu, as is shown in Figure 7.2. However, the dissolution rates of Zn and Sn in sweat solution could hardly be detected, due to the minor Zn content in the alloy. But there is a small peak being observed for Zn and Sn when the corroded sample was exposed to citrate buffer solution, indicative of a minor quantity of oxidized Zn and Sn on the surface.

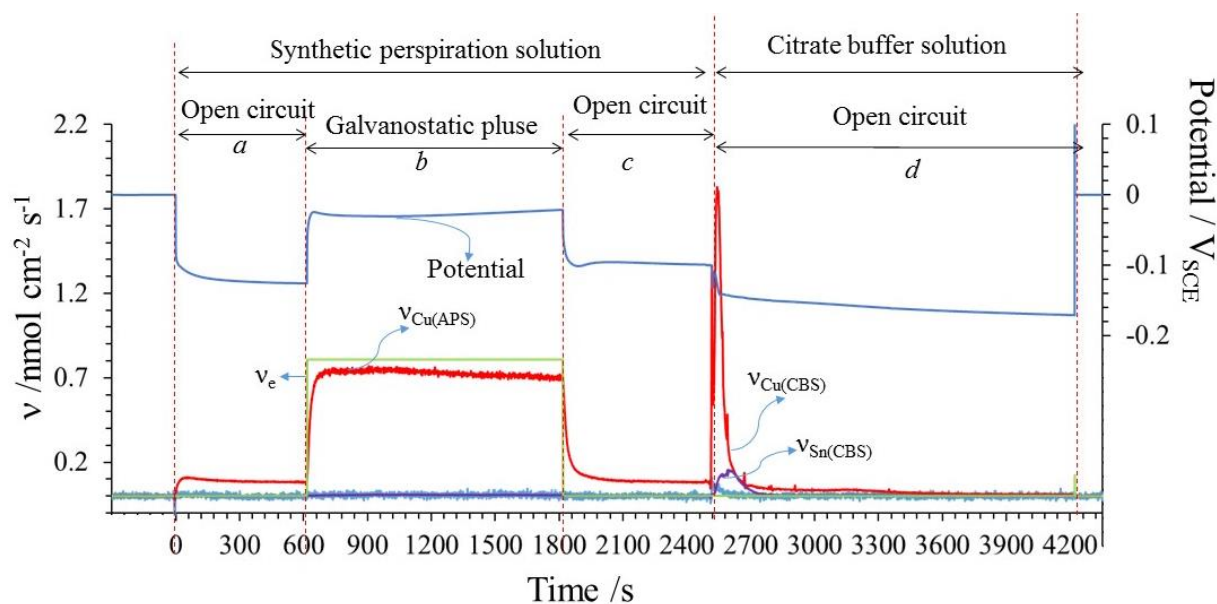


Figure 7.2. Synthetic perspiration solution-citrate buffer solution (APS-CBS) experiment of Cu-4.5Sn-0.1Zn at $i_{ap} = 80 \mu\text{A cm}^{-2}$

Figure 7.3 demonstrates that Cu dissolves as Cu(I) in the SPS electrolyte. The Cu dissolution profiles of stage b are shown, allowing a direct comparison between the applied current (expressed as v_e^*) and $v_{Cu(SPS)}$, indicating Cu release is the predominant reaction. Since the open circuit dissolution rate of Cu was not negligible, as had been shown in Figure 7.1-7.2, the applied current was offset by adding the open circuit dissolution rate, *i.e.* v_{corr} . The dissolution curve of Cu followed closely the applied current at $5 \mu\text{A cm}^{-2}$ and at $20 \mu\text{A cm}^{-2}$ indicative of a 1:1 release (*i.e.*, applied $e^- \text{ nmol s}^{-1} = \text{Cu nmol s}^{-1}$). However, a significant discrepancy between Cu dissolution and applied current was observed at $80 \mu\text{A cm}^{-2}$, suggesting the formation of solid Cu species, or the dissolution of Sn since the detection limit is more than $80 \mu\text{A cm}^{-2}$.

The dissolution profiles of various Cu-Sn alloys at $i_{ap}=80 \mu\text{A cm}^{-2}$ are shown in Figure 7.4. It is remarkable that the dissolution rate of soluble Cu was enhanced for Cu-Sn alloys as compared with pure Cu, regardless of the diluting effect of alloying addition in solid solution.

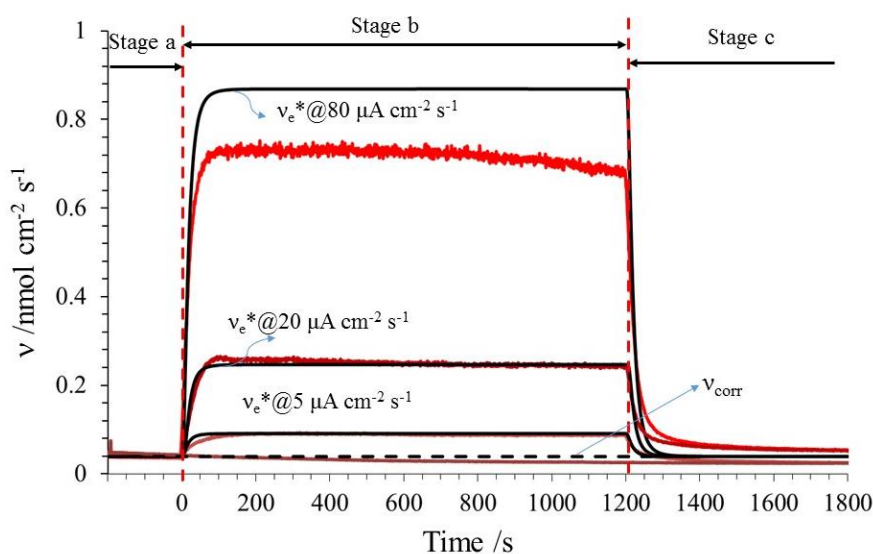


Figure 7.3. Superimposition of the dissolution profile of pure Cu in artificial perspiration solution, under anodic pulse from $0 \mu\text{A cm}^{-2} \text{ s}^{-1}$ to $80 \mu\text{A cm}^{-2} \text{ s}^{-1}$.

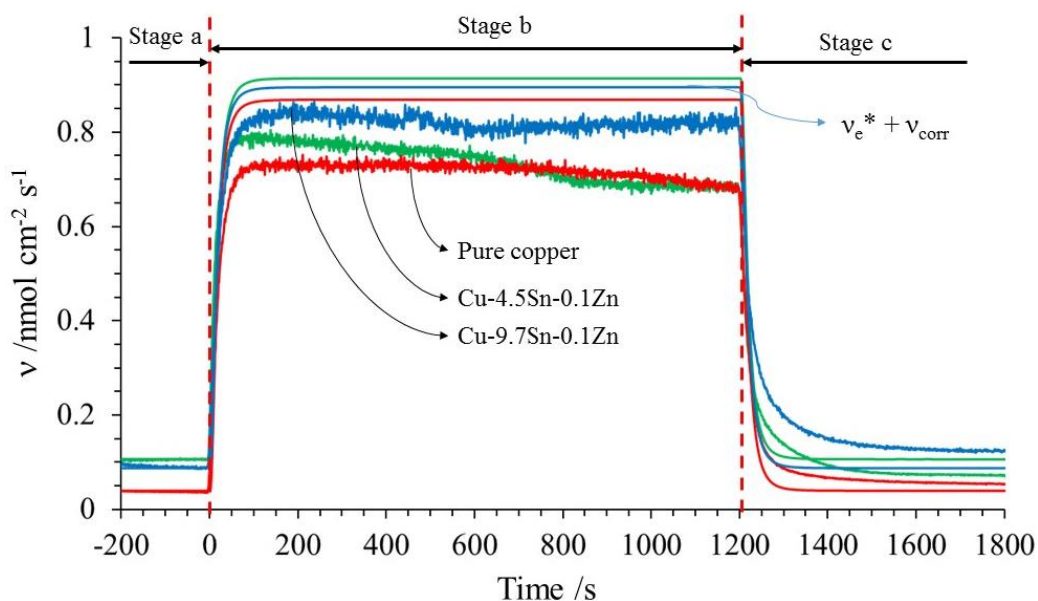


Figure 7.4. Superimposition of the dissolution profile of Cu-Sn alloys in artificial perspiration solution at $i_{ap} = 80 \mu\text{A cm}^{-2}$.

The effect of alloying Sn on the Cu release could also be seen by the relationship between the applied anodic current density and the anodic potential, Figure 7.5. This relationship followed a Tafel behavior with a slope of about 76 mV/dec. For each applied current, pure Cu required the highest polarization as compared with Cu-Sn alloys, indicative of the enhancing effect of Sn on Cu release. Cu-9.7Sn-0.1Zn showed a larger potential than Cu-4.5Sn-0.1Zn at each current, this phenomenon demonstrated that the addition of Sn did not promote Cu release monotonically.

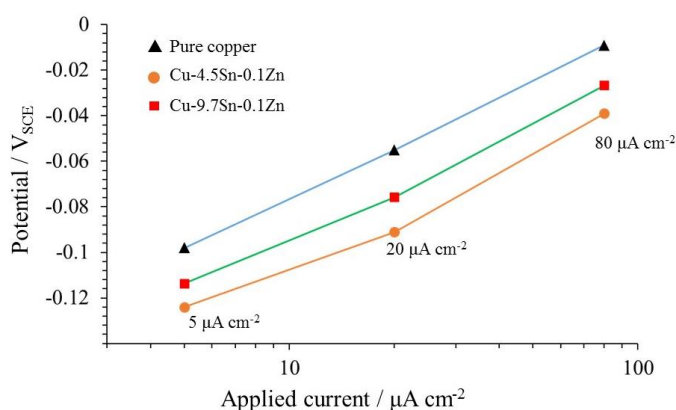


Figure 7.5. Measured potential plotted against applied current during anodic dissolution stage (stage b) of AESEC experiments.

The superimposition of the dissolution profiles of the residual corrosion products on pure Cu in citrate buffer solution is presented in Figure 7.5. A relatively large peak due to the dissolution of oxide scale at an anodic current of $80 \mu\text{A cm}^{-2}$ was shown in the figure, which was significantly larger than the peak at $20 \mu\text{A cm}^{-2}$. This phenomenon corroborates the discrepancy between v_e^* and $v_{Cu}(SPS)$ shown in Figure 7.3. Note that a small peak was observed prior to the major peak at each current, as is shown in the inset of Figure 7.6. This peak is an artefact of the experiment associated with the rinsing of the flow cell.

The Cu-Sn alloys also showed a major Cu dissolution peak indicating that Cu-containing species are the dominant solid corrosion products. Less intense peaks of Sn and Zn, (Figure 7.6, for Cu-9.7Sn-0.1Zn) were also detected. Sn and Zn accounted for only a small portion (~8%) of the total quantity of solid species dissolved in CBS, however, they showed another interesting feature: the nonsynchronous growth of their dissolution peaks. The dissolution profile of Cu and Zn started simultaneously when the electrolyte was replaced by citrate buffer solution, and reached a maximum value corresponding to the position 'a' and 'b' respectively. Sn dissolution however was quite different. Dissolution began later, initiating at position 'a', corresponding to the maximum point of the dissolution profile of Zn, and reached a maximum after 140 s, a time duration much longer than Zn or Cu.

This phenomenon corroborates the results from literature [209, 210] that the corrosion product layer formed on Cu and Cu-Sn alloys in perspiration solution consists of an outmost layer of CuCl, a sublayer of porous Cu_2O and an inner layer of hydrated cassiterite (SnO_2). A corrosion layer with similar structure was also found in environment such as atmospheric corrosion, marine corrosion as well as archeological sites. [211, 212,213].

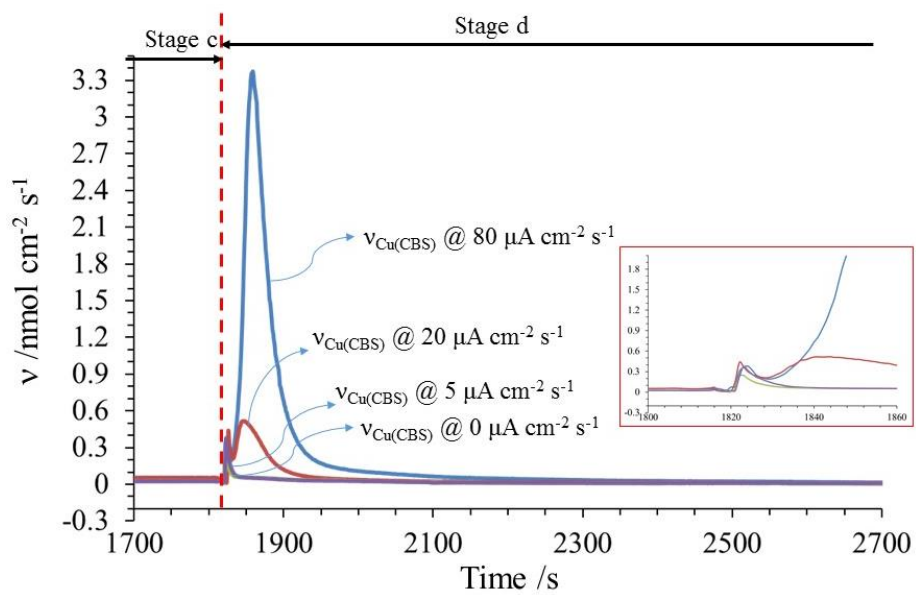


Figure 7.6. Superimposition of the dissolution profile of Cu scale of pure Cu in citrate buffer solution, after the anodic dissolution in synthetic perspiration solution.

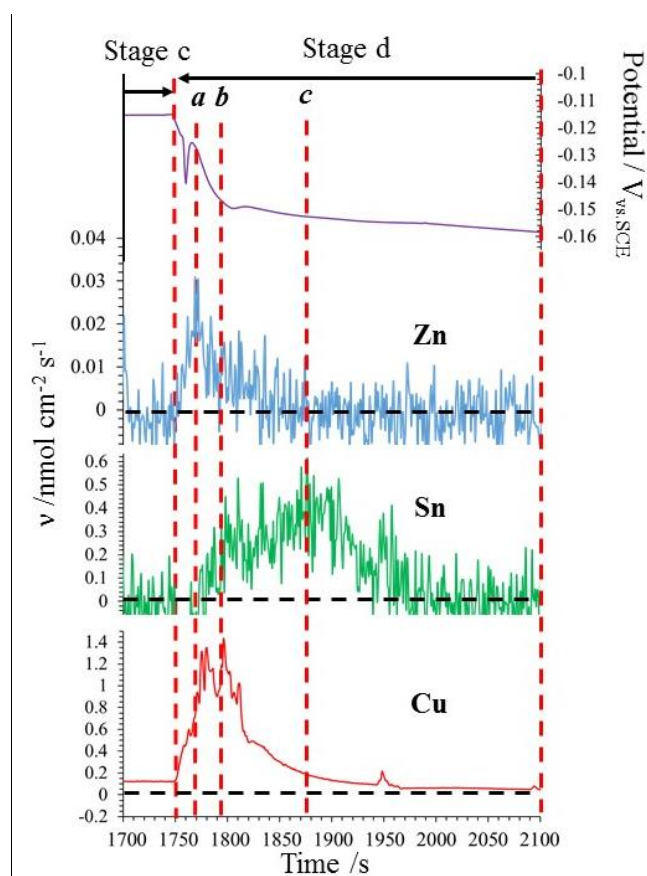


Figure 7.7. Superimposition of the open circuit dissolution profile of Cu scale in citrate buffer solution for Cu-9.7Sn-0.1Zn after exposure to SPS at $i_{ap} = 80 \mu\text{A cm}^{-2}$

7.3.2. Characterization of solid species

Characterization of surface solid products formed during long-time exposure to perspiration solution was conducted by Hutchison *et al.* [177] using grazing incidence X-ray diffraction (GIXRD), Raman spectroscopy, XPS as well as energy dispersive spectroscopy (EDS) [177]. Results are shown in Figure 7.7-7.9.

The primary solid product was cuprous oxide (Cu₂O), which could be revealed by all techniques: GIXRD analyses on pure metal and Cu-Sn alloys verified Cu₂O formation; Raman spectroscopy of alloys revealed all peaks with reference to Cu₂O powder, except for a peak centered at 525 cm⁻², which was due to a Cu-OH vibration in a defective Cu₂O [214]; X-Ray excited Auger Cu LMM transition photoelectric lines (Table 7.2) validated that oxidized Cu is in the cuprous state [215-221], together with the absence of the characteristic cupric 2p shift and shake-up satellite peaks in XPS which further confirmed the presence of cuprous oxide.

Table 7.2. XPS binding energies (eV), X-ray generated Auger electron energy (eV), and corrosion product assignment from fit of high-resolution photoelectron spectral data on Cu-4.5Sn-0.1Zn after 24 hours in artificial perspiration solution at open circuit. Literature values from: [215-221].

Chemical State	Orbital/Auger	Experiment (eV)	Literature (eV)	Assignment
Cu ⁰	2p _{3/2}	Not Detected	932.7	Cu, Cu ₂ O
Cu ⁺	2p _{3/2}	932.2	932.0, 932.5, 933.0	CuCl, Cu ₂ O
Cu ²⁺	2p _{3/2}	Not Detected	935.0, 934.9, 935.2	CuO, Cu(OH) ₂ , CuCl ₂
Cu _{Auger}	LMM	569.8	569.8	CuCl, Cu ₂ O
Sn ⁰	3d _{5/2}	484.7	484.8, 485.4	Sn
Sn ²⁺	3d _{5/2}	486.4	486.0, 486.6, 486.9	SnO
Sn ⁴⁺	3d _{5/2}	486.4	486.6, 486.7, 487.1	SnO ₂

GIXRD analyses on Cu-4.5Sn-0.1Zn showed a diffraction peak for nantokite (CuCl), and XPS also revealed Cl (2p orbital) on the surface of Cu-Sn alloys (not shown), collaborating the existence of minor quantity of CuCl. Further, Hutchison *et al.* [177] also observed a plateau on the potential-time curve of cathodic reduction of the surface oxide. CuCl could not be observed by Raman spectroscopy due to its easy degradation nature through thermal heating.

The existence of cassiterite (Sn_2O) was confirmed through XPS, as a pair of energy-shifted 3d photoelectron peaks assigned to oxidized Sn was observed on the corroded samples. SnCl_x species was excluded since a lack of Cl 2p photoelectrons (198.4 eV) [222].

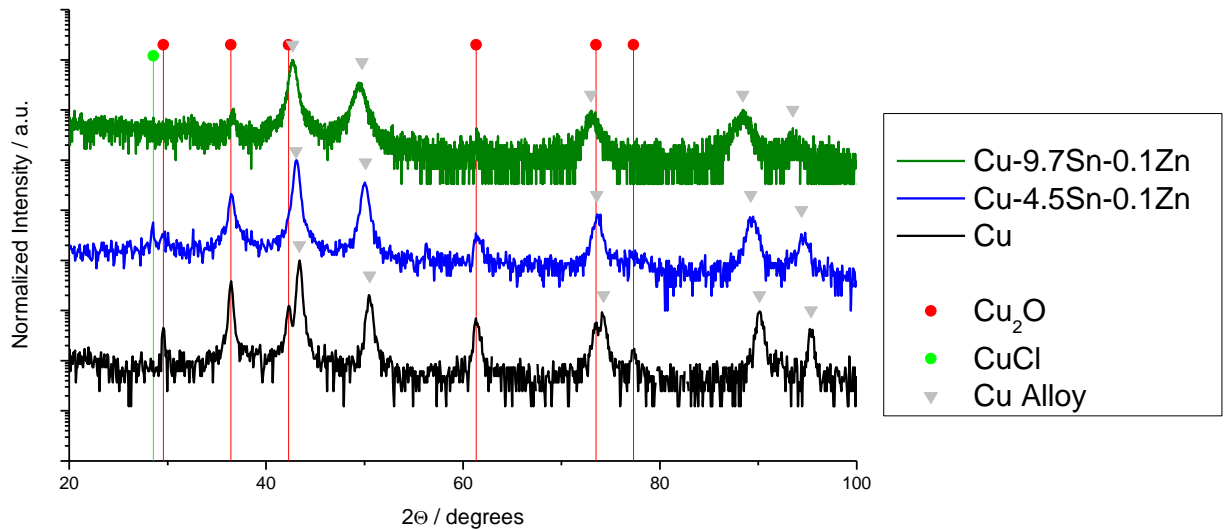


Figure 7.7. GIXRD of surface corrosion products on commercial Cu-Sn alloys compared to Cu following 130 h exposure to artificial perspiration solution at open circuit. Gray triangles represent base alloy FCC Cu peaks calculated with stretched lattice parameter fit of a substitutional solid solution alloy. Corrosion product identification was facilitated using standard X-Ray PDF cards (ICDD[®] PDF-4+).

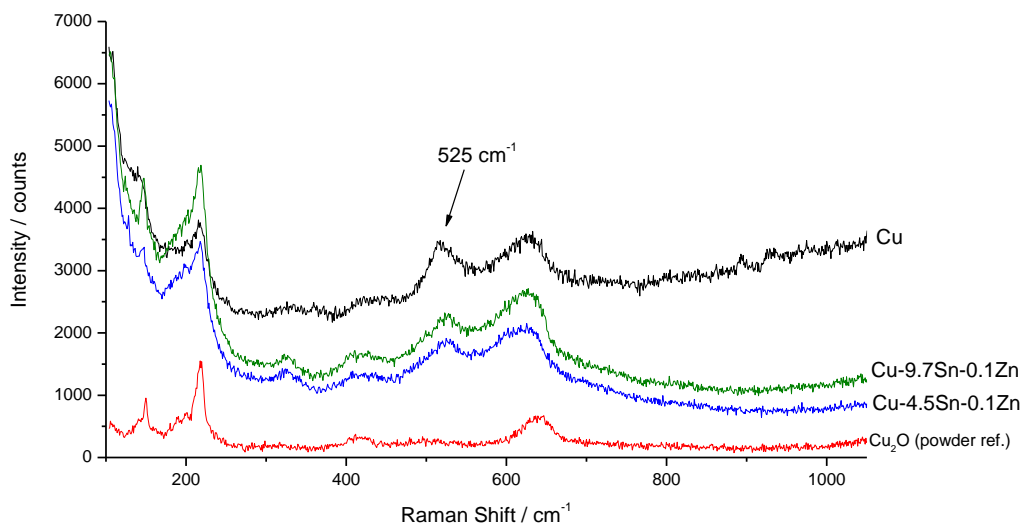


Figure 7.8. *Ex Situ* Raman spectroscopy of surface corrosion products on Cu and commercial Cu-Sn alloys following 130 h exposure to artificial perspiration solution at open circuit. Cuprite (Cu_2O) cold-pressed powder reference (red) displayed for comparison.

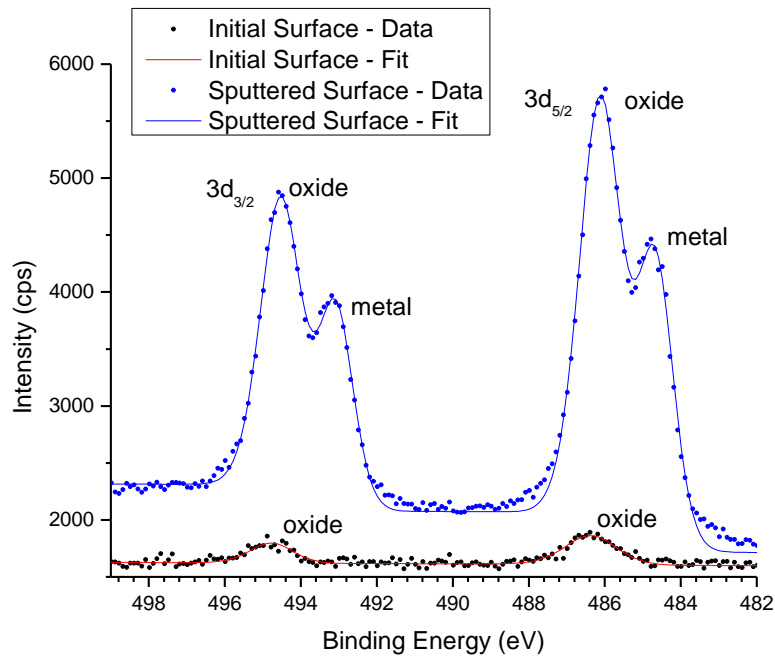


Figure 7.9. Initial and sputtered surface high-resolution XPS spectra of Cu-4.5Sn-0.1Zn sample exposed for 24 hours in artificial perspiration focused on Sn 3d range including 3d_{3/2} and 3d_{5/2} regions.

7.3.3. Mass/charge balance calculation

A mass/charge balance, as is similar to the calculation of Cu-Zn alloys in previous chapters, allows a verification of the prediction of valence state. The quantitative relationship between $Q_e(pstat)$ and $Q_e(ICP)$ could be obtained.

$$Q_e(pstat) = i_{ap} \Delta t / F \quad 7.1$$

$$Q_e(ICP) = \sum n_{m,aq} Q_{m,an(aq)} + \sum n_{m,s} Q_{m,an(s)} - Q_e(ICP)(i_{ap} = 0 \mu A cm^{-2}) \quad 7.2$$

where i_{ap} , Δt , n_m , Q_m have identical meaning to these terms in previous chapters. Figure 7.10 demonstrates a calculation assigning the reaction number for Cu equals 1, for Sn and Zn they were assigned to be 4 and 2 respectively. Due to the very low concentration of Zn and Sn detected by ICP, these elements didn't contribute significantly to the calculation. The results show that the experimental data followed the theoretical value with an error of 19% at 80 $\mu A cm^{-2}$. Although the error was larger at lower current, this could be explained by the possible overestimation of $Q_e(ICP)$ ($i_{ap} = 0 \mu A cm^{-2}$), which was significantly larger than the case of dezincification in tap water.

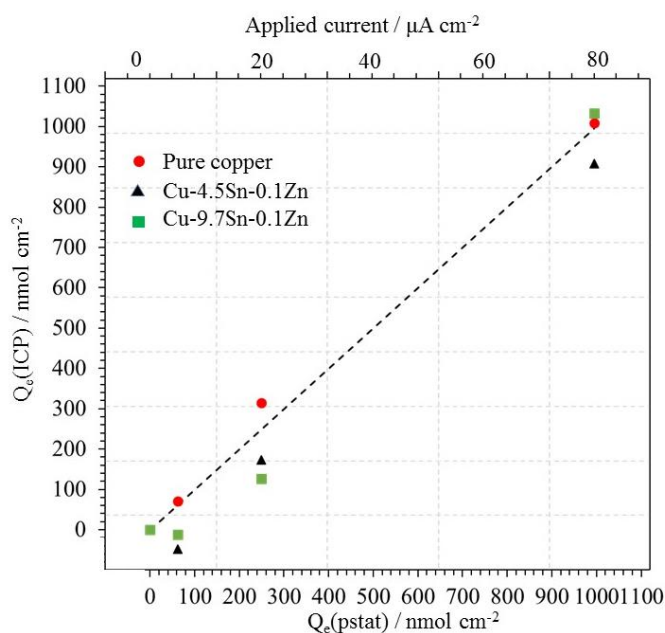


Figure 7.10. Mass/charge balance calculation of Cu-Sn alloys in perspiration solution.

7.3.4 Potentiodynamic polarization experiments

Potentiodynamic polarization curves of pure Cu and Cu-9.7Sn-0.1Zn are shown in Figure 7.11 and 7.12 respectively. The dissolution profile of Cu and Sn were converted to their equivalent current density ($\mu\text{A cm}^{-2}$) since a clear reaction stoichiometry had been determined either by the quantitative calculation from the AESEC data or the characterization of the surface solid species. j_e^* represents the total current density convoluted with consideration of the hydrodynamic effect inside the flow cell. j_{Cu} started to rise above the detection limit (LOD) at $E = 0.25 \text{ V}_{\text{SCE}}$, a potential value that was more negative than $E_{i=0 \mu\text{A}}$. The partial Cu current overlapped j_e^* from the start of the anodic polarization, until $E = 0.08 \text{ V}_{\text{SCE}}$. Within this potential range, Cu(I) was the predominant species. However, a deviation of the Cu partial current from the total current was observed, indicating the formation of solid species. For pure Cu, the partial current decreased for the next 100 mV and resumed its increase afterwards; for Cu-Sn alloy, the potential range for which the partial current decreased was much larger. Meanwhile, the Sn partial current (assuming a stoichiometry factor of 4) was kept at a low value and it only raised above the detection limit during the potential range that Cu partial current was decreasing. This opposite trend of partial current indicated the enhanced passivity of the surface oxide.

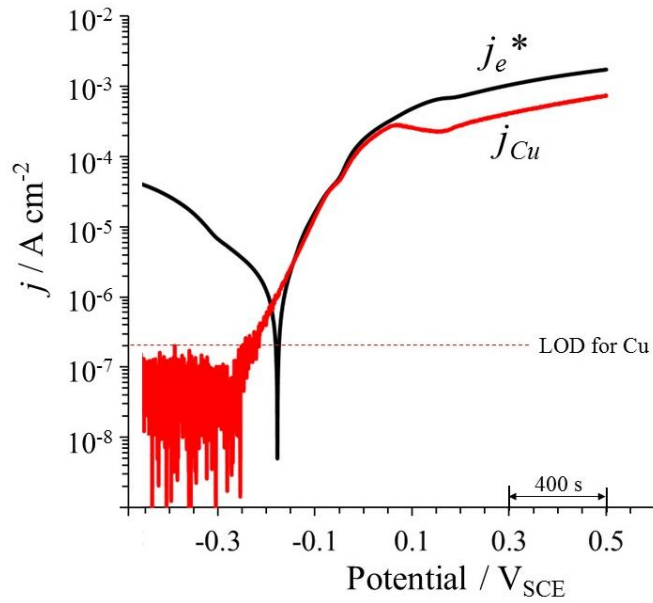


Figure 7.11. Potentiodynamic AESEC polarization curve of pure Cu in synthetic perspiration solution

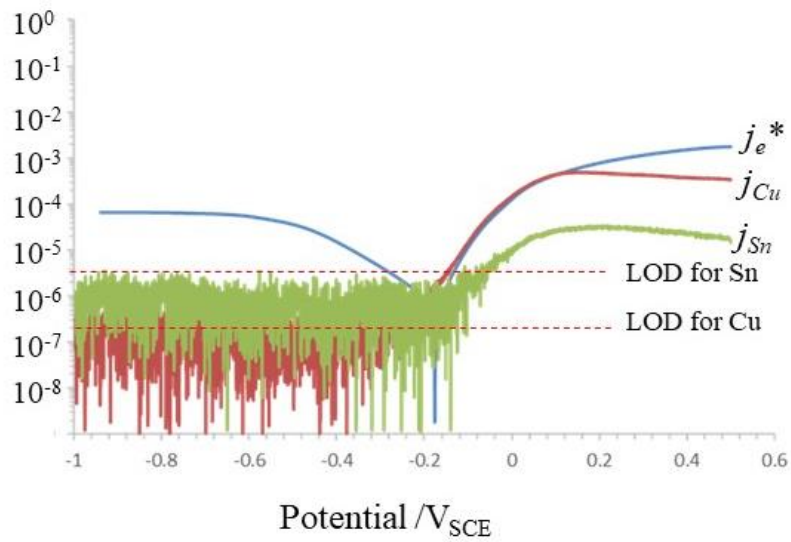
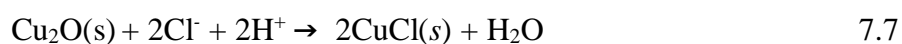
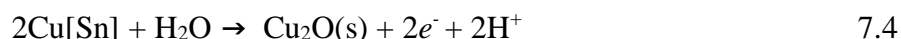


Figure 7.12. Potentiodynamic AESEC polarization curve of Cu-9.7Sn-0.1Zn in synthetic perspiration solution

7.4 Discussion

In Cu-Sn alloys, besides the major alloying element Sn, there are some minor alloying additions such as Zn, Pb and Fe. However, considering their negligible content and unmeasurable response to polarization, it is reasonable to ascribe the change of dissolution

behavior of Cu-Sn alloys to the major alloying element, Sn. The characterization of the surface solid products showed that Cu was simultaneously oxidized into both soluble Cu^+ into the electrolyte and solid Cu_2O , CuCl on the surface. Sn was oxidized into SnO_2 ; no soluble Sn species could be detected in perspiration solution. A series of electrochemical reactions were thus proposed:



Cu oxidation may follow reaction 7.3 and 7.4. Sn oxidation may follow reaction 7.5. the formation of CuCl could either follow reaction 7.6 or was due to the conversion from Cu_2O via reaction 7.7.

The enhanced Cu release from Cu-Sn alloys may be understood by considering the atomic bonding of Cu and Sn in solid solution [223]: Cu-Sn has a weaker atomic bonding ($\Delta H_{f, 298} = 177 \text{ kJ mol}^{-1}$, 224) than Cu-Cu bonding ($\Delta H_{f, 298} = 202 \text{ kJ mol}^{-1}$, 224). The addition of Sn in Cu solid solution weakens the bonding of surrounding Cu atoms, promoting Cu oxidation; besides, Sn has a strong affinity to oxide formation (SnO_2 : $\Delta G_{f, 298} = -519 \text{ kJ mol}^{-1}$, 212). In this way, the Cu atoms surrounding Sn would have an increased anodic activity, resulting an enhanced Cu release.

The addition of Sn in Cu solid solution significantly enhanced the Cu release into perspiration solution (Figure 7.4). However, the enhancement was not monotonic, as can be seen from either the open circuit dissolution rate (Figure 7.4) or the current- potential curve (Figure 7.5). A speculative interpretation would be to attribute this to an inhibiting effect of an Sn_2O layer on the surface.

Figure 7.13 depicts the structure of surface layer of Cu-Sn alloys and the electrochemical reactions involved. The corrosion structure consists of an outmost layer containing CuCl, a sublayer containing Cu₂O and an inner layer composed of SnO₂. Similar structure had been proposed by previous literature [211,212,213], it could also be supported by the “peak mismatch” shown in Figure 7.6. The oxidation of Cu into Cu⁺ (a) and Cu₂O (b) allows Cu release and oxide formation; the formation of an outmost CuCl layer could be achieved via the precipitation of Cu⁺ (c) or the conversion from Cu₂O (d). The oxidation of Sn into Sn oxide precipitated next to the bulk alloy allows the formation of a semi-passive layer. This layer, however, determines the efficacy of Cu release into the electrolyte: for Cu-4.5Sn-0.1Zn, a relative low Sn content provides insufficient Sn oxide to fully cover the bulk material, allowing an enhanced Cu release as well as a high corrosion rate; for Cu-9.7Sn-0.1Zn, a relative higher Sn content allows the formation of a Sn oxide layer that provides more protection, but this layer is far away from being compact, so the Cu release was inhibited but was still higher than pure Cu, due to the catalytic effect of Sn.

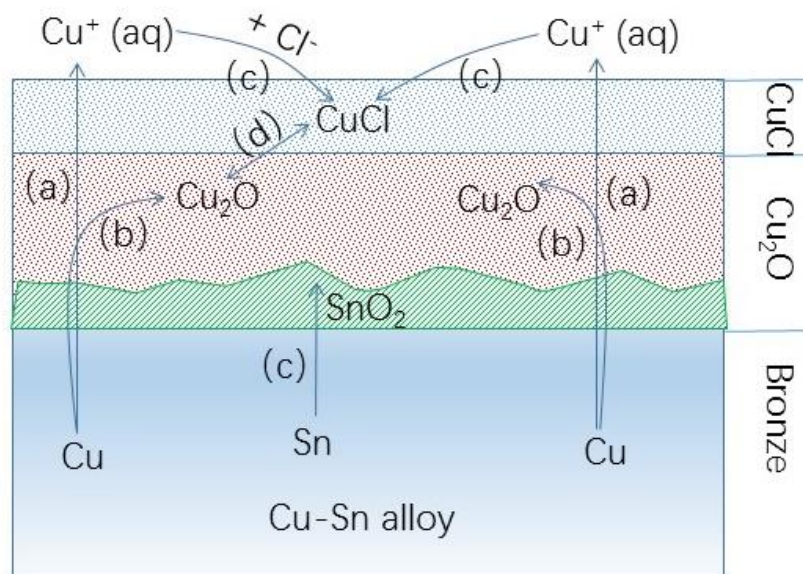


Figure 7.13. Schematic diagram illustrating the structure and electrochemical reactions involved during the dissolution of Cu-Sn alloys in perspiration solution.

7.5 Conclusions

1. In the dissolution of Cu-Sn alloys in synthetic perspiration solution, Cu was oxidized into Cu⁺ as the predominant soluble species and Cu₂O or CuCl as the solid Cu species; Sn

was oxidized into SnO₂ as the predominant solid Sn species, no Sn soluble species could be detected in perspiration solution due to the high detection limit.

2. The Cu release rate of Cu-Sn alloys were higher than pure Cu, indicating the enhanced effect of Sn; However, the increase of Sn content in the alloy didn't monotonically increase the Cu release efficacy of Cu-Sn alloys.

3. The role of Sn played in the enhancement of Cu release in Cu-Sn alloys was speculated to be the weaker atomic bonding of Cu-Sn, by which an increased anodic activity of Cu atoms was provided.

4. The efficacy of Cu release was determined by the compactness of the inner SnO₂ layer.

D. Concluding remarks

This section summarizes the major conclusions presented in previous chapters. The perspectives brought by the current work are also presented.

8. Conclusions and perspectives

8.1 Conclusions

In this thesis, the anodic dissolution behavior of Cu-Zn alloys in tap water, of Cu-Sn alloys in perspiration solution were investigated using AESEC technique. The soluble species and solid species were qualified and quantified. The relationship of different species against applied current or against the content of alloying additions were presented and discussed. The dissolution mechanism was proposed for Cu-Zn alloys and for Cu-Sn alloys.

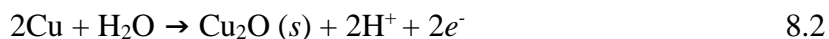
Dissolution mechanism of Cu

The results presented in Chapter 4 demonstrate that the AESEC method may be used to monitor the kinetics of anodic Cu dissolution. The instantaneous dissolution rate of Cu was measured in real time and compared with the simultaneous measurement of electrochemical current. From a mass / charge balance, it was revealed that the majority species formed during anodic polarization are soluble Cu(II) and insoluble Cu(I). The insoluble species was quantified after the experiment by dissolution in a citrate buffer solution.

The solid corrosion products were characterized by Raman and XRD analysis which confirmed that a Cu₂O film forms on the Cu surface at open circuit and during anodic polarization. Quantitative relationships of Cu(I), Cu(II) species vs. applied current and vs. time duration of galvanostatic pulse were presented. These results showed that the formation of Cu₂O is favoured at lower current than 20 $\mu\text{A cm}^{-2}$, Cu²⁺ release is favoured at higher current than 20 $\mu\text{A cm}^{-2}$ and a linear increase of the quantity of both Cu₂O and Cu²⁺ indicates a constant formation rate of both. The kinetic analysis of the dissolution profile demonstrated that the dissolution mechanism of Cu follows a simultaneous formation of Cu₂O and Cu²⁺, or a sequential formation of Cu₂O in the first place, the dissolution of Cu₂O into Cu²⁺ in the second place.

Dissolution mechanism of Cu-Zn alloys

The fate of Cu in the dissolution of Cu-Zn alloys in tap water was identical to that of Cu, with soluble Cu^{2+} , solid Cu_2O and a minor quantity (less than 8 at%) of Cu(II) solid species on the surface. Zn was oxidized into soluble Zn (II), leaving a minimal amount (less than 2 at%) of solid Zn(II) on the surface:



The formation of Cu_2O was more favoured at lower current than $20 \mu\text{A cm}^{-2}$, and the formation of Cu^{2+} was more favoured at higher current than $20 \mu\text{A cm}^{-2}$. The increase of Zn content in Cu-Zn alloy will inhibit both the formation of Cu_2O and Cu^{2+} , but promote Zn^{2+} release. So a more severe dezincification will be observed on alloys containing high Zn content. When Zn content increased to 45 wt%, forming a pure β' phase, Cu^{2+} release was almost completely inhibited. So a different dissolution mechanism was proposed for α and β' phase respectively.

A two-stage dissolution mechanism was proposed for α phase in Cu-Zn alloy: an initial stage in which Cu and Zn are oxidized congruently, but only Zn^{2+} was released into water, Cu forming a Cu_2O film, and a second stage where Cu was released into water in the form of Cu^{2+} . For the β' phase, the second stage is the same to the initial stage;

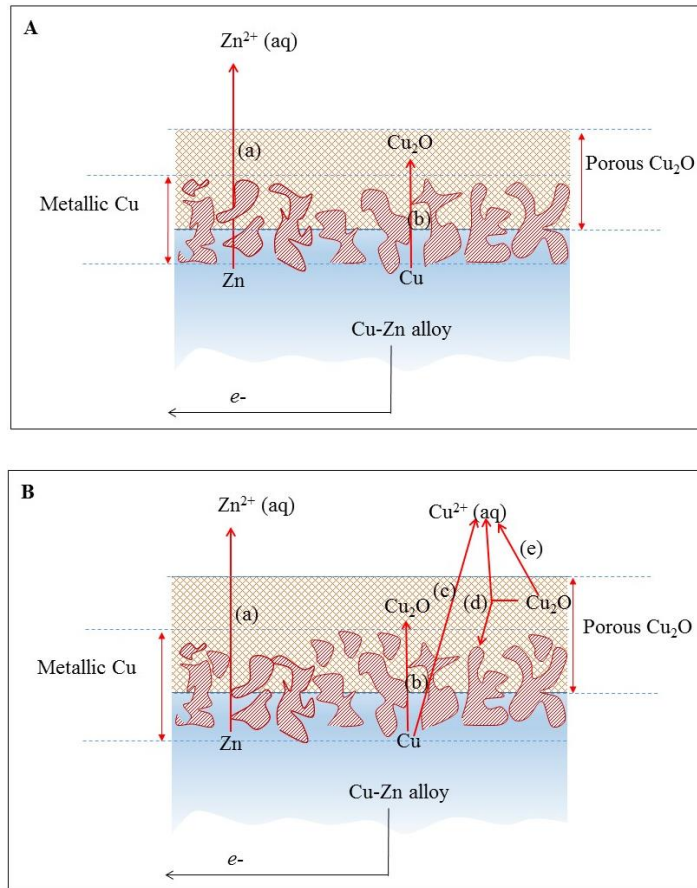


Figure 8.1. Schematic diagram of the dissolution of Cu-Zn alloy in tap water.

The addition of 3 wt% Si into a Cu-Zn alloy, forms a dezincification resistance Cu-21Zn-3Si-P. The dissolution behavior of Cu in this alloy was found different from Cu-Zn alloys with no alloying additions: Cu²⁺ release was remarkably promoted during anodic dissolution and the formation of Cu₂O was also slightly promoted. This was also attributed to the different dissolution mechanism of different phase.

Dissolution mechanism of Cu-Sn alloys

The dissolution of Cu-Sn alloys in synthetic perspiration solution was also investigated by AESEC. The mass/charge balance result, in combination with the surface corrosion product identification, showed that Cu was oxidized into Cu⁺, leaving some Cu(I) on the surface forming a multilayered structure consisting of an outmost CuCl layer, an immediate Cu₂O layer and an innermost SnO₂ layer.



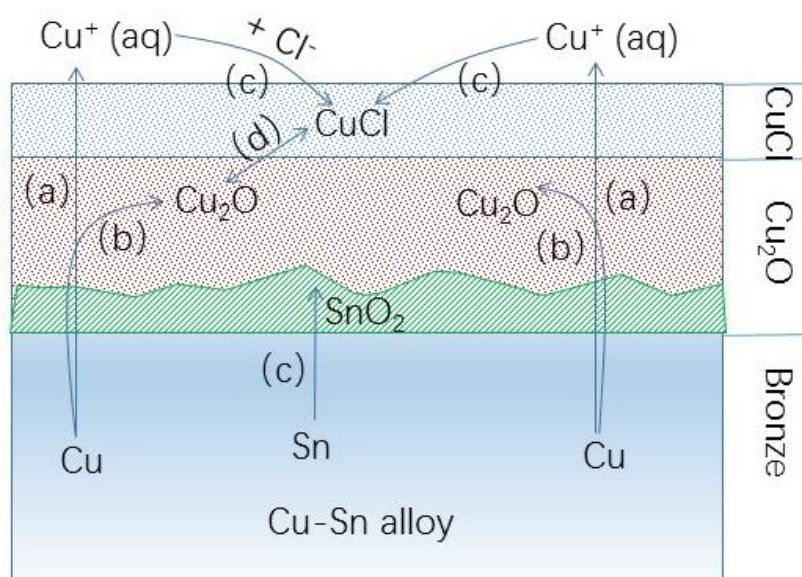
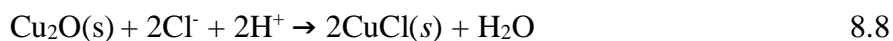
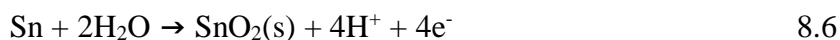
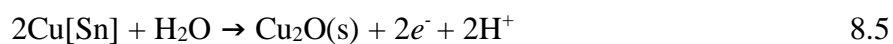


Figure 8.2. Schematic diagram illustrating the structure and electrochemical reactions involved during the dissolution of Cu-Sn alloys in perspiration solution.

The increase of Sn content in the alloy will not infinitely promote Cu^+ release, which is critical in the antimicrobial function of Cu-Sn alloys. Cu-4.5Sn-0.1Zn showed the largest quantity of Cu^+ , which was followed by Cu-9.7Sn-01Zn and then pure Cu. This was due to the passivity of SnO_2 , which will increase its protectiveness with the increase of Sn content. Cu-9.7Sn-01Zn has a thicker Sn_2O layer than Cu-4.5Sn-0.1Zn, resulting an inhibition of Cu^+ release.

8.2 Perspectives

Although this work has clarified some aspects of the mechanisms of the selective dissolution of Cu-Zn alloys and the effect of Sn on Cu release into perspiration solution, there are still more questions that could not be answered by the present data.

Firstly, we used mass/charge balance to quantify soluble/solid species and a reliable result has been obtained for alloys with various compositions. However, as we have discussed in Chapter 6, the existence of less than 8 at% solid Cu(II) on the surface could not be corroborated by GIXRD, Raman, but could be confirmed by the mass/charge balance. So did the existence of less than 2 at% solid Zn(II) species. The proposed dissolution mechanisms have been simplified without considering the possible incorporation of these minor species into the electrochemical reactions. But it will be of great interest to investigate whether Cu(II) and Zn(II) species are also involved in the electrochemical reactions.

Secondly, we have proposed a different dissolution mechanism for α and β' phases. But the origin of this difference is still unknown: whether it was a simple effect of the increase of Zn content that leads to the inhibition of Cu^{2+} release, or it was due to the lattice structure difference from a FCC to a BCC, or it was due to the difference in the oxide layer that has different catalytic effect on the dissolution of bulk alloy. More work needs to be conducted on the characterization of surface solid products, as well as localized corrosion on specific phases.

Moreover, the addition of Si significantly changes the dissolution behaviour of Cu-Zn alloys, majorly affecting the release of Cu^{2+} . However, the phase composition of Cu-Zn alloys is also changed from a single α phase composition to a triple α , κ and γ phase composition. It is difficult to distinguish the effect of Si and phase on the dissolution behaviour of Cu-Zn alloys. A simpler system, in which the alloying additions will not significantly change the phase composition of alloys, will be more interesting. For instance, Pb is another alloying addition that will effectively improve the dezincification resistance of Cu-Zn alloys. It exists in the grain boundary as isolated islets, thus have minimal influence on the phase composition. The investigation of the role played by Pb in the dezincification will be another project after the Ph. D. defence.

The investigation of the dissolution of Cu-Sn alloys in perspiration solution provide adequate information regarding the quantification and qualification of Cu. However, no detailed

information concerning the fate of could be obtained, since a very high detection limit of Sn in either SPS or CBS. The fate of Sn should be investigated in another system that has a high solubility of Sn as well as a low detection limit.

Finally, as we have demonstrated in this thesis that citrate buffer solution is a perfect descaling agent: it has a high descaling efficiency and do a minimal harm to the bulk alloy. A primary investigation (appendix B) shows that Cu-Zn alloys dissolving in CBS follow a congruent dissolution of both Cu and Zn. This was due to the formation of Cu-citrate complex. A detailed investigation of the dissolution of Cu-Zn alloys in CBS will be of great scientific significance. This work will be finished soon.

Appendix A: ISO-6509 dezincification test of Cu-Zn alloys.

ISO 6509-1:2014 specifies a method for the determination of dezincification depth of copper alloys with zinc exposed to fresh, saline waters or drinking water. The method is intended for copper alloys with a mass fraction of zinc more than 15 % [161,162]. Details of the test is listed as follows:

Solution: Freshly prepared CuCl_2 (1 wt%) was heated to 75 ± 5 °C;

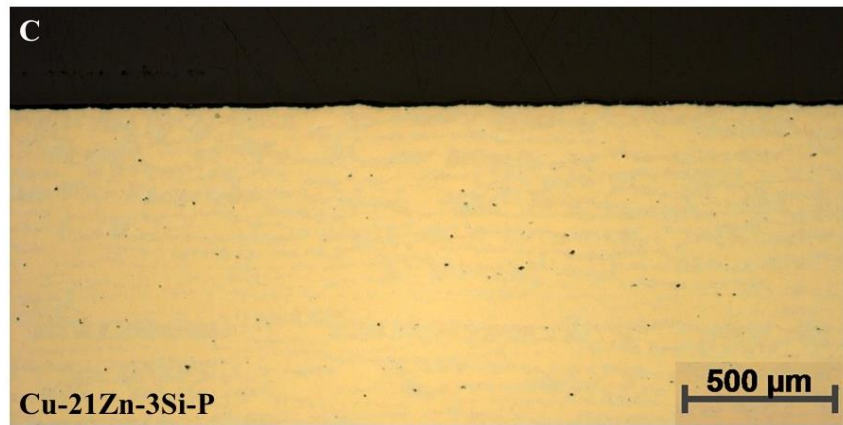
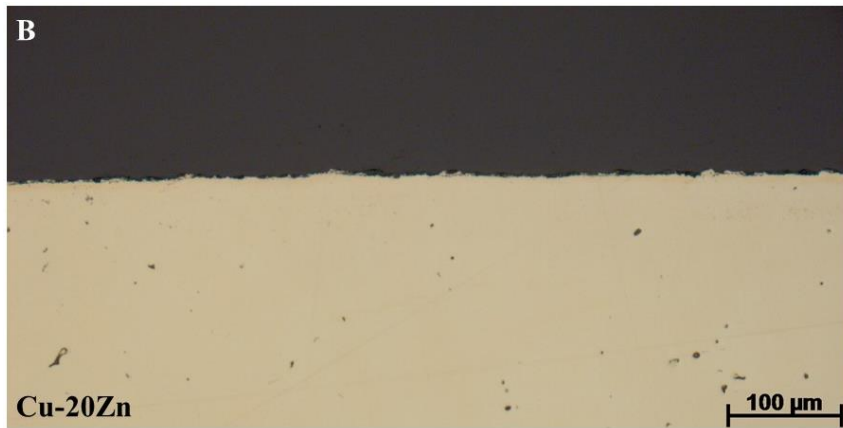
Sample preparation: Cu-Zn alloys was mounted by a phenolic resin and have an exposure area of 100 mm^2 ; it was freshly ground using wet abrasive paper, and then properly rinsed with water.

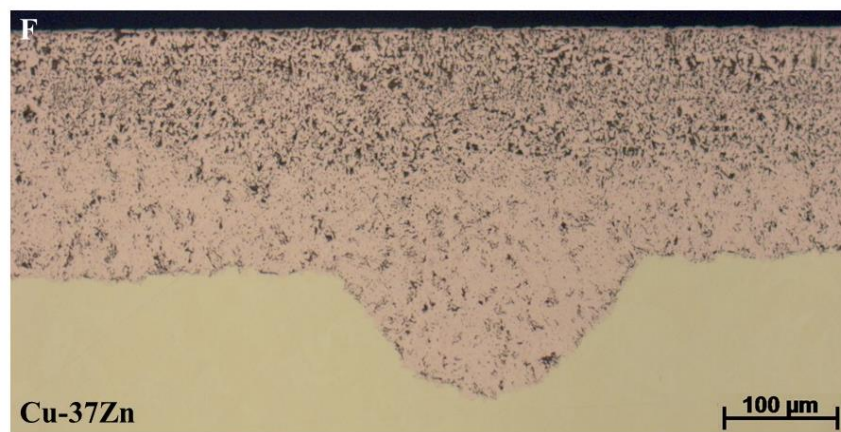
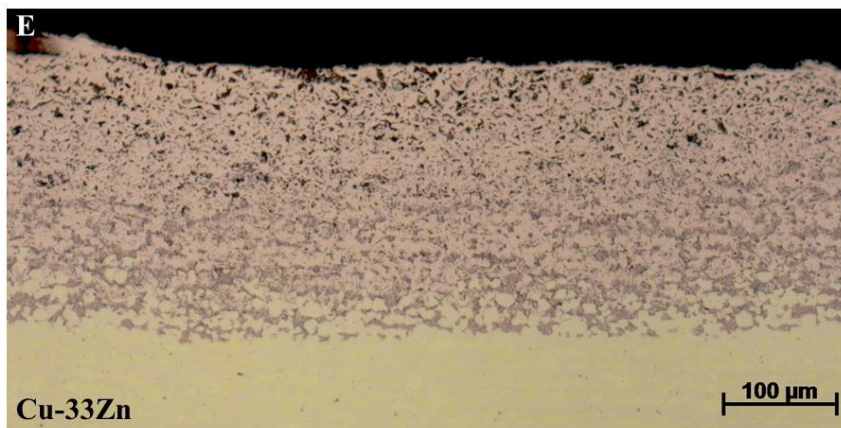
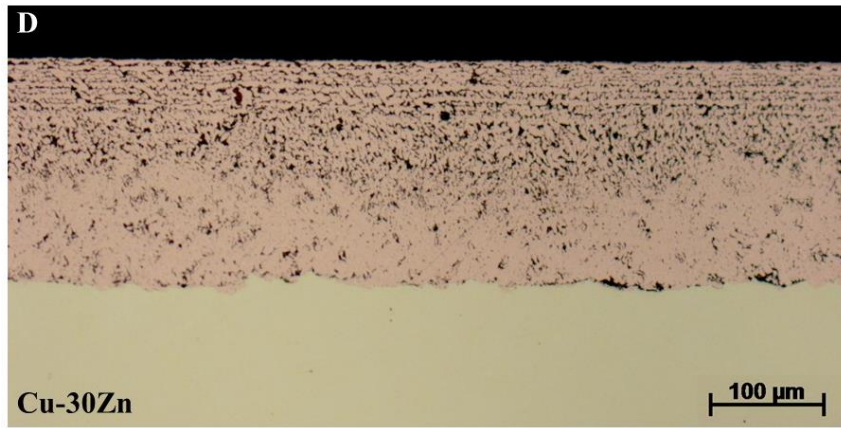
Positioning of tested specimens: 250 ml of the copper (II) chloride solution is required; The test specimens shall be placed in the beaker containing the copper (II) chloride solution so that the test surfaces are vertical and at least 15 mm above the bottom of the beaker. The plastic foil shall then be placed and secured.

Duration of test: The test specimens shall be exposed continuously for $24 \text{ h} \pm 30 \text{ min}$. At the end of this period, they shall be removed from the beaker, washed in water, rinsed in an appropriate solvent and allowed to dry.

Microscopic examination: The micro-section prepared from each test area shall be examined using an optical microscope provided with a scale for measurement of the dezincification depth and the maximum as well as the average depth of dezincification with respect to the final, corroded, surface shall be recorded. The appropriate magnification shall be used to provide the greatest accuracy of measurement.

The microscopic observations of all Cu-Zn alloys are listed in Figure 1. The maximum dezincification depth (L_{max} , μm) and the average dezincification depth (L_{mean} , μm) are presented in Figure 2.





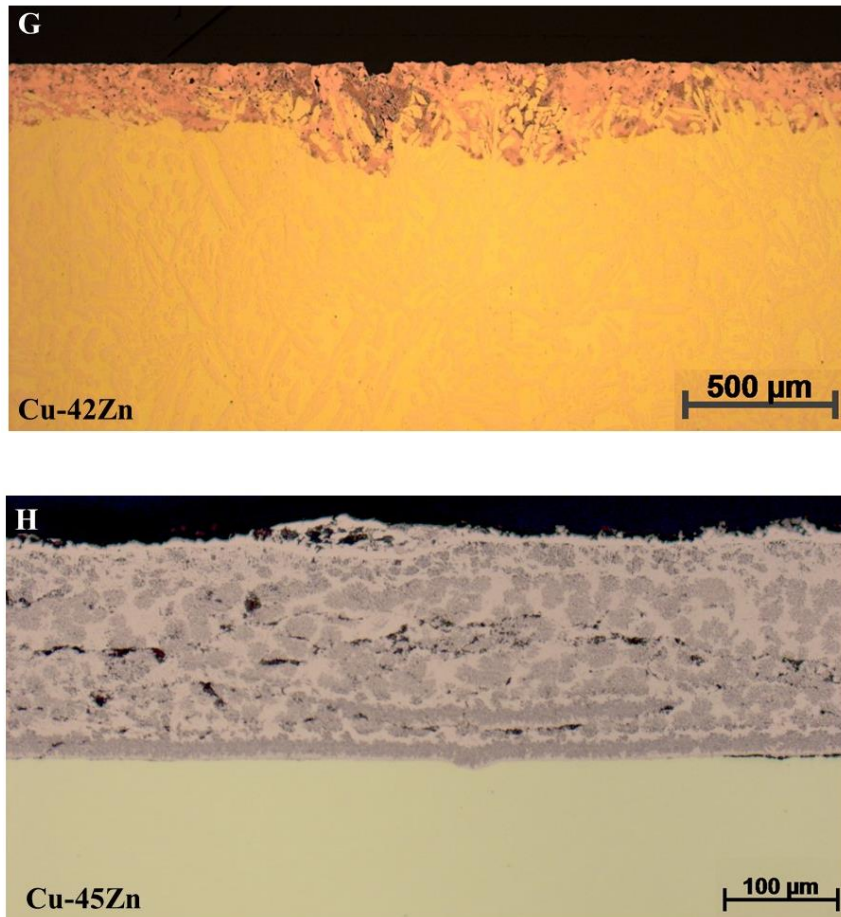


Figure 1. Microscopic observations of the cross-section of tested specimens. A. Cu-10Zn; B. Cu-20Zn; C. Cu-21Zn-3Si-P; D. Cu-30Zn; E. Cu-33Zn; F. Cu-37Zn; G. Cu-42Zn; H. Cu-45Zn.

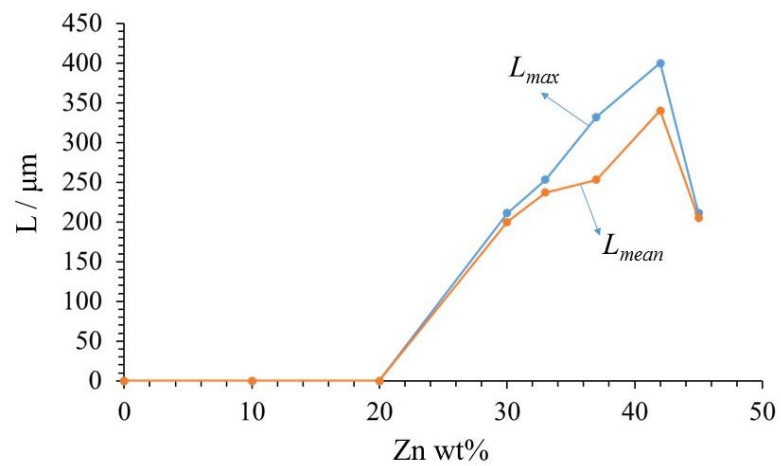


Figure 2. Measured maximum dezincification depth (L_{max}) and averaged dezincification depth (L_{mean}) against Zn content (wt%).

Appendix B: Investigation into the dissolution mechanism of Cu-Zn alloys in deaerated citrate buffer solution.

1. Introduction

A citrate buffer solution ($\text{pH} = 4.9 \pm 0.1$) has been used to dissolve Cu oxide films formed on Cu-Zn [] alloys and Cu-Sn alloys[177] for analysis by on-line ICP-AES (AESEC). Citric acid is a weak organic tricarboxylic acid having the chemical formula $\text{H}_3\text{C}_6\text{H}_5\text{O}_7$ occurring naturally in citrus fruits. In biochemistry, it is an intermediate in the citric acid cycle, which occurs in the metabolism of all aerobic organisms [225]. Due to its propensity to complex with Cu ions in solution, it has proven to be an efficient descaling agent for Cu alloys. It is well known that a metal complexing agent, such as metal - citrate is responsible for the loss of passivity during selective dissolution [226].

In this chapter, the dissolution behavior of pure metal (copper and zinc) and Cu-Zn alloys was investigated using the AESEC technique. Due to the solubility of Cu and Zn ions in the CBS electrolyte, it makes an excellent model system for the application of the AESEC technique.

2. Materials and experiments

2.1 Materials

Pure copper (99.99%, Goodfellow), pure Zn (99.99%, Goodfellow), Cu-10Zn (CW501L, Zn 10 wt%), Cu-33Zn (CW506L, Zn 33 wt%) and Cu-42Zn (CW510L, Zn 42 wt%) were used. They were sectioned into a size of $2.5 \text{ cm} \times 2.5 \text{ cm}$, ground with up to 800 grit polishing paper and cleaned with ethanol before each experiment. Citrate buffer solution was prepared by adjusting the pH value of 0.1 M citrate acid (AppliChem) solution to 4.9 ± 0.1 , using 0.1 M citrate trisodium solution (Amresco), and deaerated for at least 30 min with an argon bubbling system before use.

2.2 Experiments

Atomic emission spectroelectrochemistry (AESEC) was used in this work. Details of this technique had been introduced in the introduction section. Briefly, this technique consists of a customized ICP-OES (Horiba Jobin Yvon Ultima 2CTM) system allowing an *in situ* detection

of the concentration change, which was coupled to a potentiostat (Gamry Reference 600™), permitting a precise online detection of elemental concentration response to polarization (current or potential).

Stepwise anodic polarization of pure metal or Cu-Zn alloys was conducted as follows: a stepwise anodic current ranging from 0 to 80 $\mu\text{A cm}^{-2}$ was applied after an open circuit delay, for which the time interval was 10 min. Potentiodynamic polarization of pure metal or Cu-Zn alloys were conducted: an open circuit of 30 min was implemented allowing a relative steady state of the surface; the potentiodynamic scan was set to start from negative to positive within the range from -200 mV vs. E_{oc} to 200 mV vs. E_{oc} with a scan rate of 0.167 mV s^{-1} ; another 10 min open circuit delay was followed; finally a potentiostatic EIS was conducted at open circuit, permitting a manual IR compensation by subtracting the ohmic drop.

3. Results

3.1 Dissolution behavior under galvanostatic dissolution

Figure 1 shows the superimposition of the dissolution profile of pure Zn (upper) and pure Cu (lower). At open circuit, the corrosion rate of pure Cu was reproducibly very low at 7.2 $\text{pmol cm}^{-2} \text{s}^{-1}$ ($140 \text{ g m}^{-2} \text{y}^{-1}$). But the corrosion rate of pure Zn after each anodic current increased steadily from 120 $\text{pmol cm}^{-2} \text{s}^{-1}$ to 190 $\text{pmol cm}^{-2} \text{s}^{-1}$ (2400 to $3800 \text{ g m}^{-2} \text{y}^{-1}$), a value that is much larger than obtained for pure copper.

For Cu-42Zn, both Cu and Zn showed a reproducibly low dissolution rate after each anodic current, Figure 2. The corrosion rate of Cu-10Zn, of Cu-33Zn, and of Cu-42Zn were $260 \text{ g m}^{-2} \text{y}^{-1}$, $190 \text{ g m}^{-2} \text{y}^{-1}$ and $180 \text{ g m}^{-2} \text{y}^{-1}$ respectively. Under galvanostatic mode, both Cu and Zn showed an immediate response to the anodic polarization, which gradually increased with the increase of anodic current.

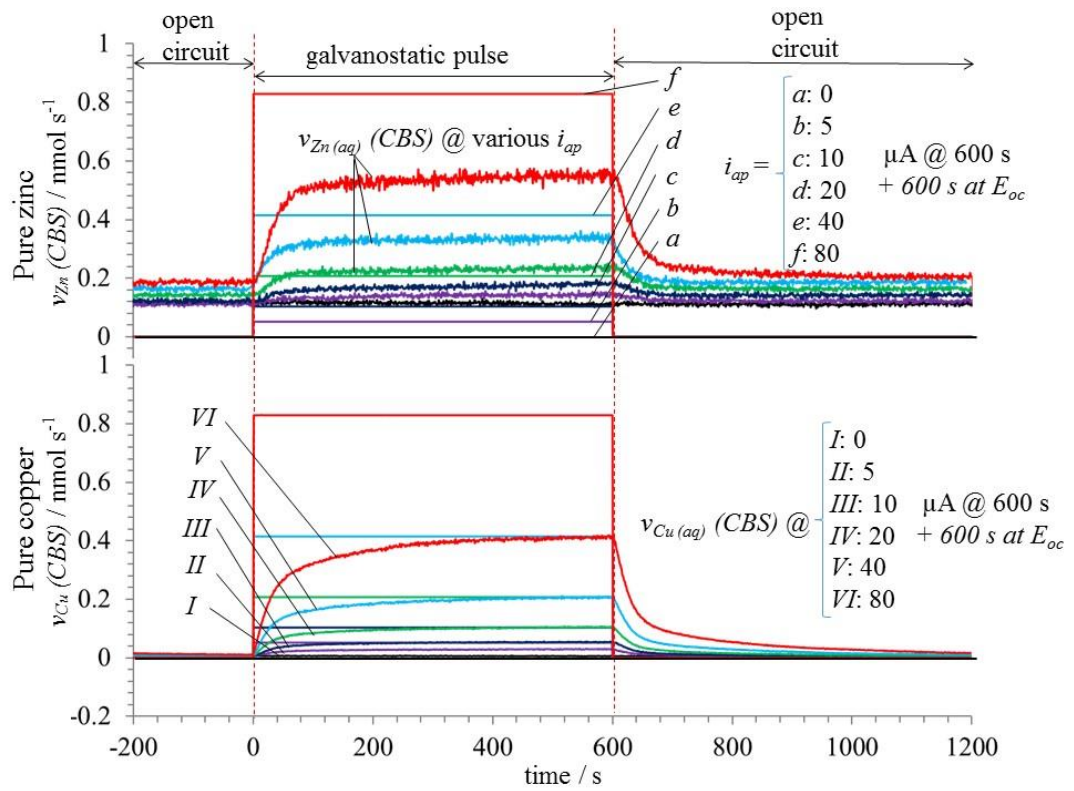


Figure 8.1. Superimposition of the anodic dissolution profile of Cu and Zn for pure zinc (upper) and pure copper (lower).

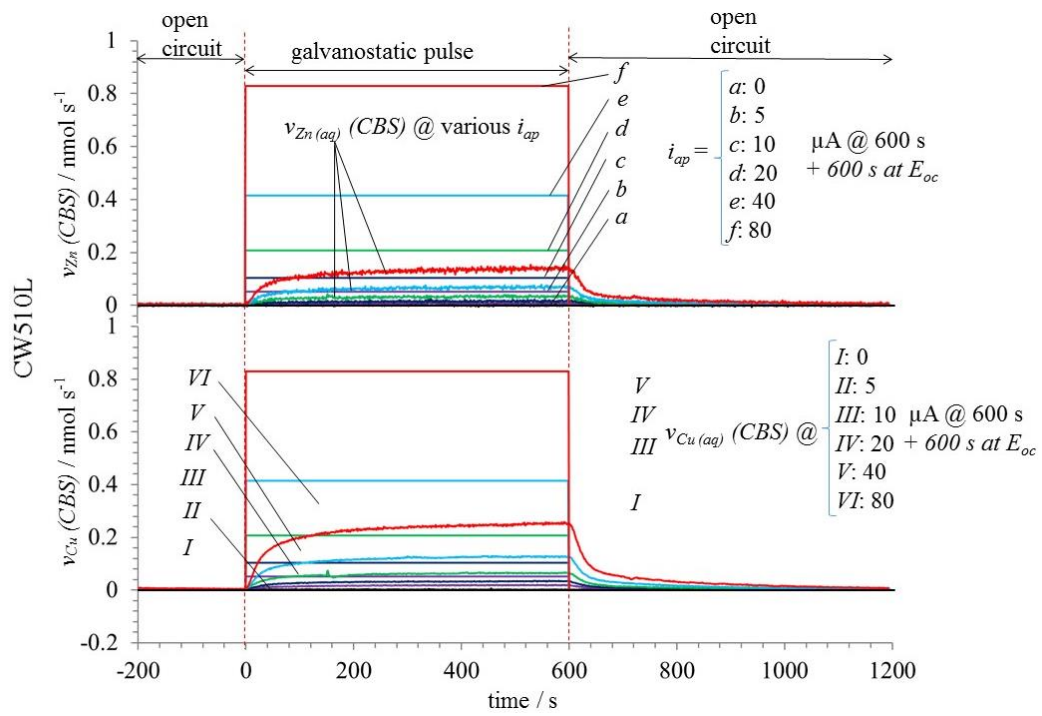


Figure 2. Superimposition of the anodic dissolution profile of Zn and Cu for CW510L (Cu-42Zn).

A mass/charge balance calculation established a direct comparison between the total quantity of charge being consumed ($Q_e(\text{pstat})$) and the quantity of charged yielded by oxidizing Cu and Zn ($Q_e(\text{ICP})$). For pure copper and Cu-Zn alloys, the calculation could be achieved through equation 1 - 4:

$$Q_e(\text{pstat}) = i_{ap} \Delta t / F \quad 1$$

$$Q_m(\text{CBS}) = \int_0^t v_m(\text{CBS}) dt \quad 2$$

$$Q_e(\text{ICP}) = \sum n_m Q_{m,an} \quad 3$$

$$Q_{m, an} = Q_m(\text{CBS}) - Q_m(\text{CBS})(i_{ap} = 0) \quad 4$$

where i_{ap} , Δt , F and $v_m(\text{CBS})$ represent applied current, the time interval, the Faraday constant and the elemental dissolution rate of metal (m) in CBS respectively. The integration started from $t = 0$ s till the end of the following open circuit dissolution, giving a range of $2\Delta t$, due to the fact that dissolution continues after Δt . n is the number of electrons exchanged for each element (m) and $Q_{m,an}$ is the net quantity of metal dissolution which is attributed to the anodic polarization. This is obtained by Eq. 4 where the quantity due to open circuit dissolution ($Q_m(\text{CBS})(i_{ap} = 0)$) is subtracted from the total quantity dissolved.

For pure Zn, since the open circuit dissolution rate after each anodic current changed significantly, the quantity of charges due to open circuit dissolution was subtracted via equation 5.

$$Q_{Zn, an} = Q_{Zn}(\text{CBS}) - v_{Zn, corr} * \Delta t \quad 5$$

where $v_{Zn, corr}$ represents the steady-state open circuit dissolution rate prior to the galvanostatic anodic current step, and Δt is the time interval.

Figure 3 demonstrates the mass/charge balance calculation assuming a $n = 2$ for both Cu and Zn. The dashed line represents the ideal condition that $Q_e(\text{pstat})$ equals $Q_e(\text{ICP})$. Both alloys follow closely the dashed line, with a maximum deviation of 10 % at $80 \mu\text{A cm}^{-2}$. This result clearly demonstrates that Cu and Zn are oxidized into soluble Cu(II) and Zn(II) respectively in the CBS electrolyte.

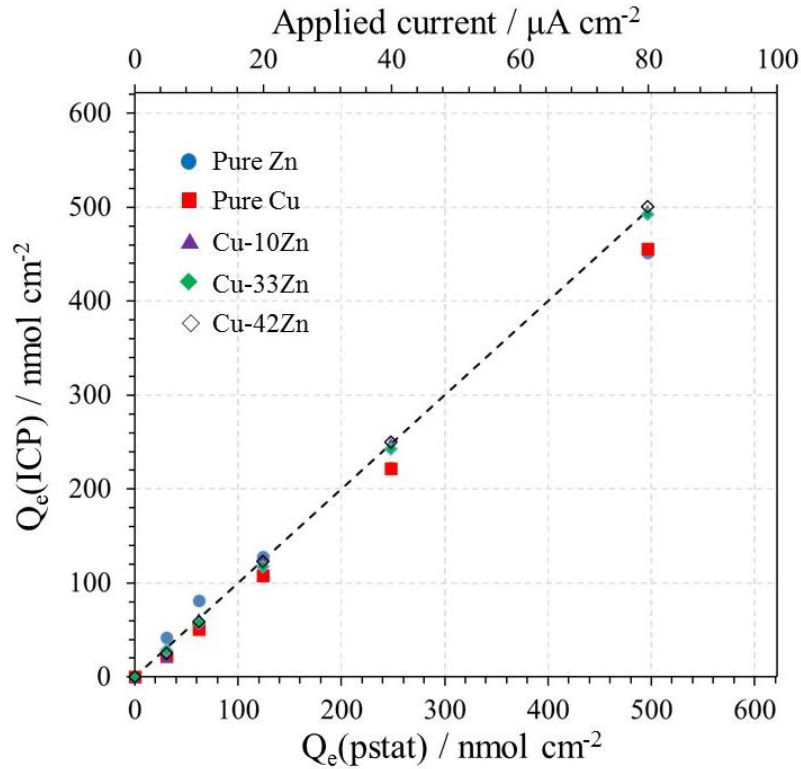


Figure 3. Mass/charge balance calculation of pure Cu, pure Zn, and Cu-Zn alloys.

Figure 4 and 5 depict the dissolution profile of pure metal at $80 \mu\text{A cm}^{-2}$. Also shown in these figures are the convoluted curve of applied current (expressed in nmol cm^{-2}). Note that the elemental dissolution rate, v_{Zn} (CBS) and v_{Cu} (CBS) have been multiplied by a factor of 2, the valence state determined from Figure 3. Also, the applied current, v_e^* was offset by adding $2v_{\text{Zn, corr}}$, allowing a visual comparison between the two profiles.

Both v_{Zn} (CBS) and v_{Cu} (CBS) deviated significantly from $v_e^* + 2v_{\text{Zn, corr}}$, either from the ascending stage during the anodic polarization or the descending stage after the polarization. No steady state was obtained for either elements and the increase of Zn was slower than Cu. Similar features were also observed on all Cu-Zn alloys.

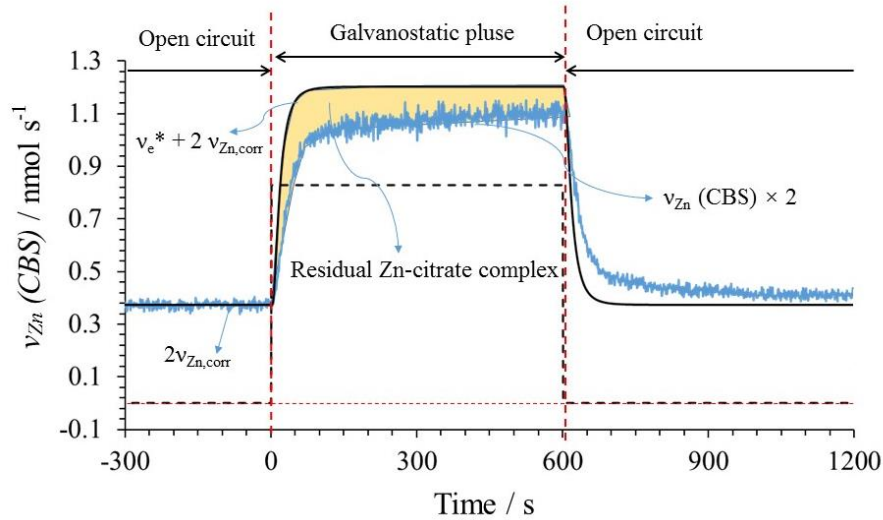


Figure 4. Dissolution profile of pure Zn in CBS at $80 \mu\text{A cm}^{-2}$.

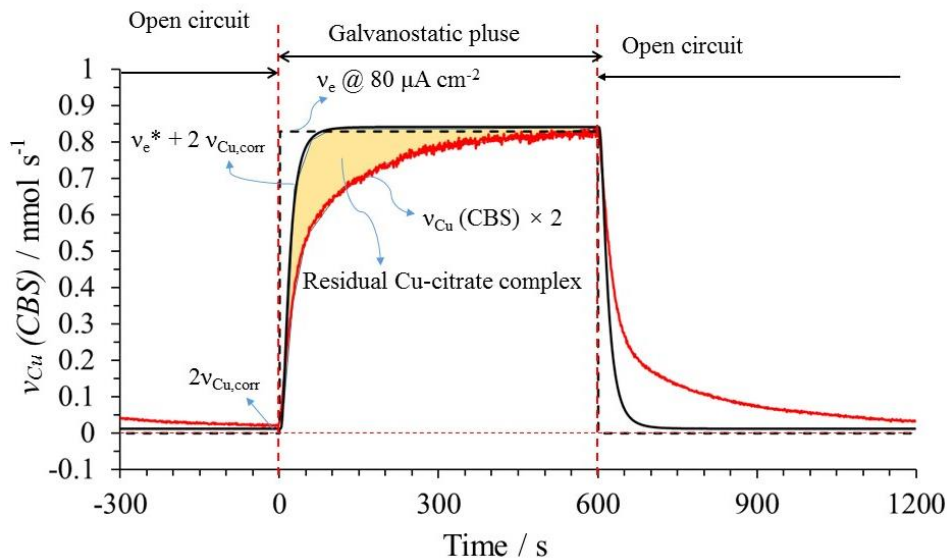


Figure 5. Dissolution profile of pure Cu in CBS at $80 \mu\text{A cm}^{-2}$.

The discrepancy between j_e and nM (Figure 8.4 and 8.5) may be attributed to a two-step mechanism involving the formation of an initial solid or adsorbed species, followed by its dissolution.

Figure 6 demonstrates the quantitative relationship of dissolved Cu and Zn as a function of applied current. Solid lines represent congruent dissolution by multiplying $Q_e(\text{pstat})$ with Cu at% and Zn% separately, allowing a breakdown of $Q_e(\text{pstat})$ into two parts. These lines allow a direct assessment of selective dissolution: when experimental data lies above the line, a selective dissolution of the element occurs; when experimental data lies below the line, an enrichment of this element occurs. It shows clearly in Figure 6 that for Cu-10Zn, a near perfect congruent dissolution occurred. For Cu-42Zn, a slight selective dissolution of Cu occurred

since these experimental points of Q_{Cu} lies above the solid line and points of Q_{Zn} lies below the solid line. The selective dissolution, *i.e.*, dezincification could not be observed for the dissolution of Cu-Zn alloys in CBS. This was attributed to the formation of metal complex, such as Cu citrate complex and Zn citrate complex.

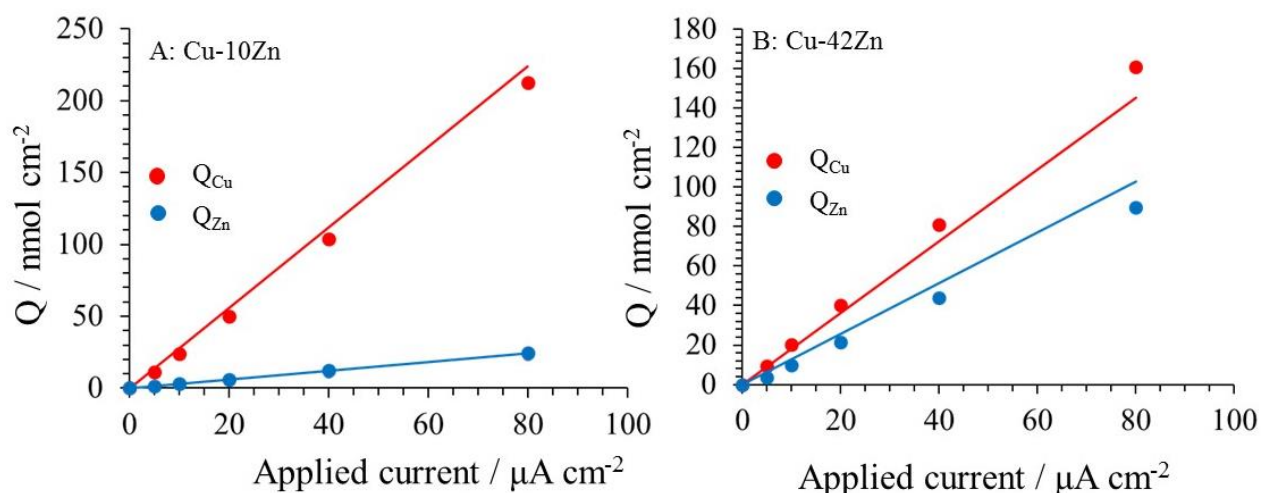


Figure 6. Relationship of dissolved Cu and Zn as a function of current: left Cu-10Zn and right Cu-42Zn.

8.3.2 Potentiodynamic polarization experiments

Polarization curves of pure Zn, pure Cu, and Cu-Zn alloy are presented in Figure 7-9 respectively. As described previously, these curves have been corrected for electrolyte resistance.

The polarization curve of pure Zn (Figure 7) shows that the dissolution rate during the cathodic branch was nearly constant at approximately $6.7 \mu\text{A cm}^{-2}$, significantly above the limit of detection (LOD) for Zn. It started to rise before reaching $E_{i=0}$ indicative of an intense cathodic reaction. At higher polarizations above $-1.11 \text{ V}_{\text{SCE}}$, j_{Zn} approaches j_e^* corroborating the previous assumption of $n = 2$.

The cathodic branch of the polarization curve was extracted based on the mixed potential theory, $j_c = j_e^* - j_{\text{Zn}}$. The intersection point between j_c and j_{Zn} yields a corrosion rate of $20.0 \mu\text{A cm}^{-2}$, a value comparable to the dissolution rate detected by ICP ($21.7 \mu\text{A cm}^{-2}$). However, no similar feature can be observed on the polarization curve of pure Cu (Figure 8). Here, the

dissolution rate of Cu was below the detection limit and only started to rise at $-0.17 \text{ V}_{\text{SCE}}$. There was a significant deviation with $j_e^* > j_{\text{Cu}}$ throughout the potential domain. This phenomenon was due to the existence of Cu citrate complex, which dissolves slower and accumulates on the surface, resulting in an underestimation of the oxidation rate via the concentration. The polarization curve of a Cu-Zn alloys showed a similar deviation of $j_{\Sigma} (= j_{\text{Zn}} + j_{\text{Cu}})$ from j_e^* . The dissolution of Cu started rose above the LOD at $-0.17 \text{ V}_{\text{SCE}}$, identical to the onset potential from pure copper. The dissolution of Zn started to raise above the LOD at $-0.15 \text{ V}_{\text{SCE}}$. However, due to the higher LOD of Zn (7.07 ppb) than Cu (2.76 ppb), the dissolution simultaneity of each element could not be distinguished at small potential. But it is observable that at higher potential, j_{Cu} was higher than j_{Zn} , indicating a congruent dissolution of Cu and Zn. Similar results were also found on the polarization curve of Cu-10Zn (not shown).

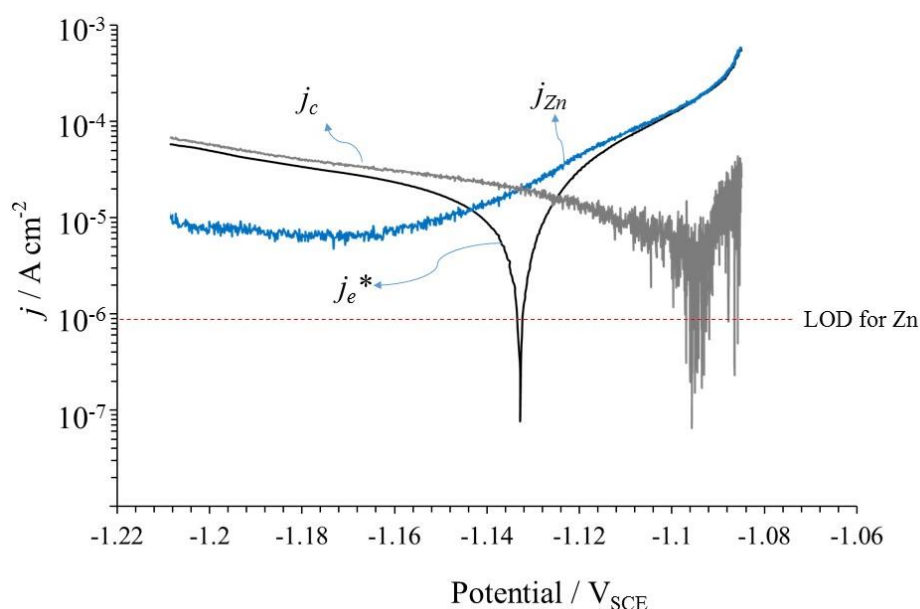


Figure 7. Potentiodynamic polarization experiment of pure zinc.

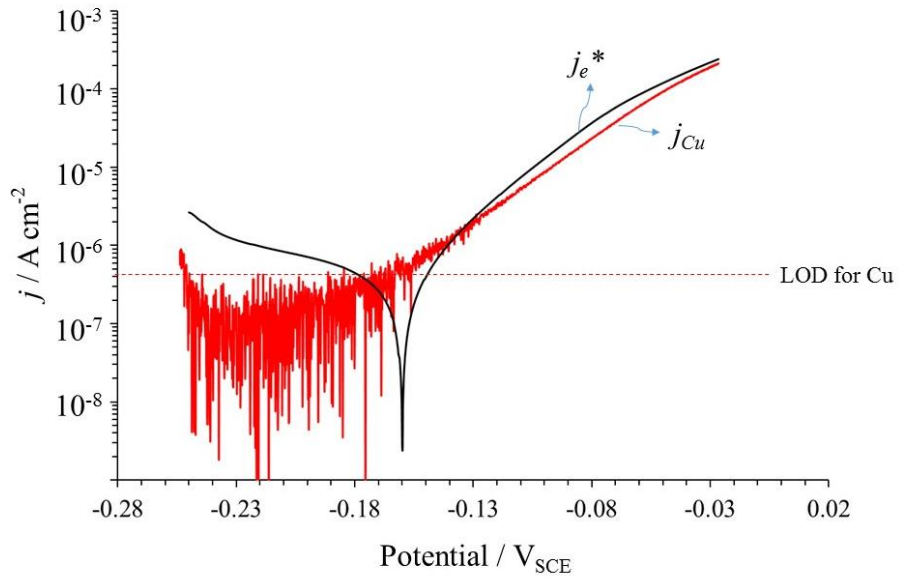
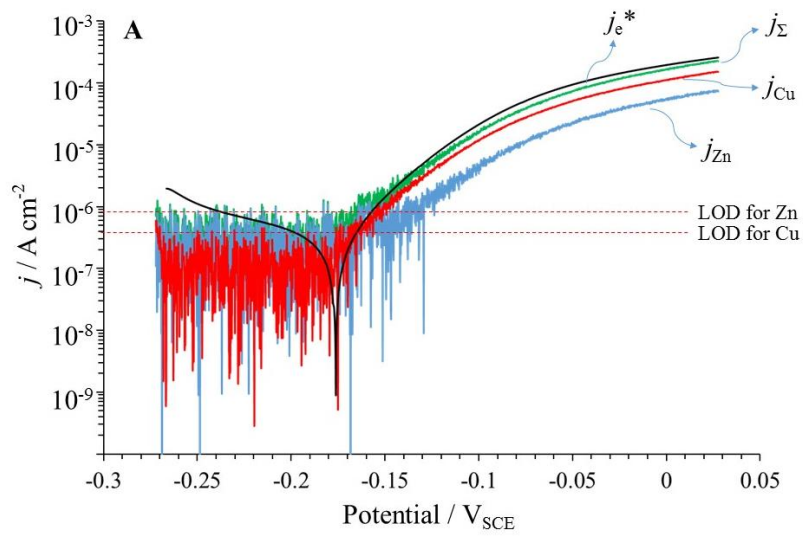


Figure 8. Potentiodynamic polarization experiment of pure copper.



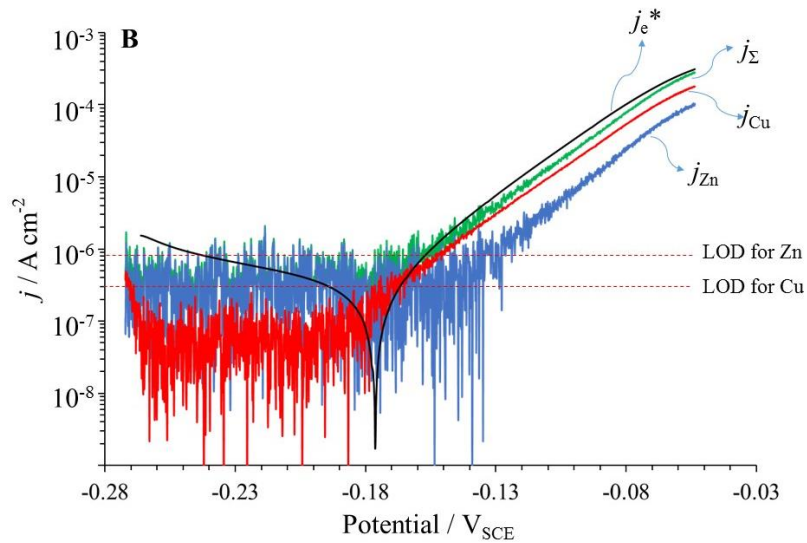


Figure 9. Potentiodynamic polarization experiment of Cu-33Zn (A) and Cu-42Zn (B).

4. Discussion

The use of citric acid or citrate solution as descaling agent of Cu and Cu alloys involves a minimal corrosion rate of the substrate and very little selective dissolution, *i.e.*, dezincification. The galvanostatic dissolution of pure metals and Cu-Zn alloys demonstrate that Cu and Zn were dissolved into Cu(II) and Zn(II) species and no significant quantity of solid species were formed. The quantification of dissolved Cu and Zn from Cu-Zn alloys suggested a congruent dissolution of both elements at a ratio almost the same to the bulk composition. These results demonstrated the dissolution simultaneity of Cu and Zn. The corrosion rates of Cu alloys were considerably lower than pure Zn, indicating a relative low corrosion rate.

The polarization curves showed that in Cu-Zn alloys, the onset potential of elemental dissolution was independent of alloy composition, which suggests that the electrochemical dissolution of Cu and Zn were independent. This also confirmed the existence of complexes acting as intermediate species that allows the congruent dissolution of Cu and Zn.

5. Conclusions

1. In the dissolution of Cu-Zn alloys, Cu and Zn were oxidized into Cu(II) and Zn(II) soluble species.

2. The dissolution of Cu and Zn followed a congruent dissolution at a ratio close to the bulk composition.
3. The existence of metal complexes, acting as intermediate species, allows the simultaneous dissolution of Cu and Zn.

Appendix C: Curriculum vitae of the author

<i>Profile</i>						
Name:	Peng ZHOU					
Citizenship:	P. R. China	Date of birth:	21 /02 /1989	Gender:	Male	
Research: Materials Corrosion Science						
Institution: IRCP-I2E, École Nationale Supérieure de Chimie de Paris						
Address: 11 Rue Pierre et Marie Curie 75231 PARIS Cedex 05, France						
Email address:	peng.zhou@chimie-paristech.fr		Phone number:	+33-7-53-71-00-18		
Personal Hobbies:	Tennis, basketball, fishing.					
<i>Language skills</i>						
English: IELTS 6.0;						
French: Primary Level;						
<i>Education</i>						
• Ph. D	Université Pierre et Marie Curie (UPMC), Paris, France				10 / 2014–Present	
	<ul style="list-style-type: none"> • Financed by China Scholarship Council for the duration of three years in UPMC. • Specialize in dealloying mechanism of alloys such as brass and bronze • Supervisor: Kevin Ogle 					
• Visiting	University of Virginia (UVA), Virginia, USA				07 / 2015 – 08 / 2015	
	<ul style="list-style-type: none"> • Working as a visiting scientist in Center for Electrochemical Science and Engineering, UVA; • Under the supervision of Prof. John R. Scully; • To finish the collaborative project of the US National Science Foundation under DMR-130999 and U.S. Office of Naval Research under Grant SP0028970-PROJ0007990 					
• Master	Liaoning Technical University (LNTU), Liaoning, China				09/2011 – 01/2014	
	<ul style="list-style-type: none"> • Officially Recommended as a Master Student of Materials Processing Engineering in School of Materials Science and Engineering • Supervisor: Prof. Zhuang MA • Co-supervisor: Shizhi DONG (Associate professor) • <i>Core courses:</i> Materials Surface and Interface, Equations of Mathematical Physics, Numerical Analysis, Reliability Evaluation and Failure Analysis of Welding Structure, Microscopic Theory of Strength of Materials, Thermodynamics and Dynamics of Materials, Diffusion and Solid State Phase Transformation • GPA: 3.55/4.0 Rank: 1 /20 					
• Bachelor	Liaoning Technical University (LNTU), Liaoning, China				09/2007–07/2011	
	<ul style="list-style-type: none"> • Bachelor's Degree of Materials Science and Engineering, • <i>Core courses:</i> Linear Algebra, Engineering Mechanics, Fundamentals of Mechanical Design, Materials Surface Technology, High Energy Beam Surface Processing, Materials Modern Analysis Techniques, Materials Performance and Test. • GPA: 3.43/4.0 Rank: 4/122 					
<i>Research and Project Experiences</i>						
<ul style="list-style-type: none"> • 02/2012-01/2014 Coal Ash-Derivative of Coal Resources in the Application of Activating Flux-Tungsten Inert Gas (A-TIG) - Major participant 						

<ul style="list-style-type: none"> • This project covers my master's dissertation. It is a project financed by Natural Science Foundation of China (NSFC: U1261123/E0422). • I have designed the semi-automatized welding device by installing the modified welding torch onto the moving unit of oxyacetylene cutting machine, from which precise welding speed and arc length can be acquired. Preliminary experiments had been conducted by my teammates. • Standards and criteria had been established based on my work, which played a critical role in launching the project.
<ul style="list-style-type: none"> • 03/2012-03/2013 Preparation of Fly Ash as Activating Flux of TIG – Project leader
<ul style="list-style-type: none"> • This project is a University Fund project for postgraduates (Y201200301), it is also a subsidiary project of the NSFC. • I wrote the thesis about our project and made the presentation for the final assessment.
Working & Practical Experience
<ul style="list-style-type: none"> • 02 /2014-06 /2014 in Shanghai Meishan Iron&Steel Co., Ltd. • As an assistant engineer in the Centre of Technology, responsible for the optimization of welding parameters, thus improving the applicability of steel products.
<ul style="list-style-type: none"> • 10/2012-10/2013 Managing Assistant of postgraduate college of LNTU. • As a part-time employee, participated in departmental affairs such as recruitment, recruit registration, and serving for the student employment.
Scholarships & Honors
<ul style="list-style-type: none"> • 11/2013: National scholarship for graduate students • 05/2013: The bronze prize for the Long Jump of 2013 University Olympic • 07/2013 Outstanding Member of Chinese Communist Party • 09/2011-07/2012 Scholarship for Excellent postgraduate student leader(First Prize) • 06/2011 Excellent graduate of LN.T.U. • 09/2007-07/2011 1st Prize Yearly Scholarship for Excellent undergraduate (3 times) 2nd Prize Yearly Scholarship for Excellent undergraduate (1 time) • 02/2011: Excellent undergraduate of LN.T.U. • 01/2009: National English Contest for College Students.(Second Prize) 1. 07/2007-07/2009: Yearly National Encouragement scholarship (2 times)
Publications (Latest three years)
<ol style="list-style-type: none"> 2. P. Zhou, M. J. Hutchison, J. R. Scully, K. Ogle, The anodic dissolution of copper alloys: Pure copper in synthetic tap water. <i>Electrochimica Acta</i>, 191 (2016), 548-557. 3. P. Zhou, M. J. Hutchison, J.W. Erning, J. R. Scully, K. Ogle. An in situ ICP-AES study of brass dezincification in synthetic tap water, <i>Electrochimica Acta</i>, 229(2017), 141-154. 4. M. J. Hutchison, P. Zhou, J. R. Scully, K. Ogle, Effect of Al and Sn on Corrosion Response and Cu Ion Release of Copper-Based Alloys, Implications towards Tarnish Resistant Antimicrobial Surfaces, <i>Electrochimica Acta</i>, 241 (2017) 73-88. 5. Peng Zhou, Kevin Ogle, Corrosion of Cu and Cu Alloys in Encyclopedia of Interfacial Chemistry - Surface Science and Electrochemistry, 2017, accepted. 6. P. Zhou, M. J. Hutchison, J.W. Erning, J. R. Scully, K. Ogle. The dissolution of Cu-Zn alloys in synthetic tap water: effect of metallurgical phase on the elemental release and scale formation and dissolution mechanism, <i>Electrochimica Acta</i>, in preparation. 7. P. Zhou, J.W. Erning, K. Ogle. Anodic dissolution of Cu-Zn alloys in citrate buffer solution, in preparation.
Conferences (Latest three years)

8. **Oral presentation:**

1. **Peng Zhou**, Kevin Ogle, *A new look into the selective dissolution of Cu-Zn alloys in tap water: elemental release, scale formation and dissolution mechanism, Eurocorr2016, Montpellier, France.*
2. **Peng Zhou**, Kevin Ogle, *Dissolution of Cu-Zn alloys in tap water: effect of metallurgical phase on the elemental release, scale formation and dissolution mechanism, NACE Corrosion 2017, New Orleans, USA.*

9. **Poster / Participant:**

1. K. Ogle, V. Shkirskiy, P. Volovitch, **P. Zhou** and A. Maltseva, *A Novel Coupling Between Atomic Emission Spectroelectrochemistry and Electrochemical Impedance Spectroscopy: Application to Zn, Zn-Cu and Zn-Al-Mg Alloys, 228th ECS Meeting, Oct, 2015, Phoenix, USA.*
2. M. J. Hutchison, **P. Zhou**, K. Ogle, J. R. Scully, *Effect of Sn on the Fate of Copper during Dissolution: A Comparison between Copper and Bronze Commercial Alloys, July 10-15, 2016, New London, New Hampshire, USA.*

Bibliography

- [1] T. Rosenqvist, Principles of Extractive Metallurgy, Tapir academic press, Trondheim, 2004.
- [2] W. O'Brien, Prehistoric copper mining in Europe: 5500-500 BC. OUP Oxford, 2014.
- [3] T. M. D. Lê, Some Aspects of Vietnamese Bronze Age (The Comparative Studies in East and Southeast Asian Context), (2001)
- [4] J.M. Day, The Bristol brass industry: furnace structures and their associated remains, The Journal of the Historical Metallurgy Society, 22(1988) 22–41.
- [5] J.S. Kharakwal and L.K. Gurjar. Zinc and brass in archaeological perspective. Ancient Asia Journal of the Society of South Asian Archaeology 1 (2006) 139–159.
- [6] M. Radetzki, Seven thousand years in the service of humanity-the history of copper, the red metal, Resources Policy 34 (2009) 176–184.
- [7] http://www.aalco.co.uk/datasheets/Copper-and-Copper-Alloys-Introduction-to-Copper-and-its-Alloys_68.ashx
- [8] R.C. Juvinall, K.M. Marshek, Fundamentals of machine component design, New York: John Wiley & Sons. 2006.
- [9] D.A. Lytle, M.N. Nadagouda, A comprehensive investigation of copper pitting corrosion in a drinking water distribution system. Corrosion Science 52 (2010) 1927–1938.
- [10] B.V. Salas, M.S. Wiener, *et al.*, Copper corrosion by atmospheric pollutants in the electronics industry, International Scholarly Research Notices 2013 (2013) 1–7.
- [11] <https://www.nace.org/Publications/Cost-of-Corrosion-Study/>
- [12] H.W. Pickering, P.J. Byrne, Partial currents during anodic dissolution of Cu-Zn alloys at constant potential, Journal of the Electrochemical Society 116 (1969) 1492–1496.
- [13] H. W. Pickering, Formation of new phases during anodic dissolution of Zn-rich Cu-Zn alloys, Journal of the Electrochemical Society 117(1970) 8–15.
- [14] A.V. Polunin, A.P. Pchel'nikov, V.V. Losev, I.K. Marshakov, Electrochemical studies of the kinetics and mechanism of brass dezincification, Electrochimica Acta 27 (1982) 467–475.
- [15] A.P. Pchel'nikov, A.D. Sitnikov, I.K. Marshakov, V.V. Losev A study of the kinetics and mechanism of brass dezincification by radiotracer and electrochemical methods. Electrochimica Acta 26 (1981) 591–600.

- [16] C. Chiavari, E. Bernardi, A. Balbo, et al., Atmosphere corrosion of fire-gilded bronze: corrosion and corrosion protection during accelerated ageing test, *Corrosion Science* 100 (2015) 435–447.
- [17] S. Voynick, A metal for all ages, *The World & I* 13 (1998) 182.
- [18] S. Forenbaher The late copper age architecture at Vučedol, Croatia. *Journal of field archaeology*, 21(1994) 307–323.
- [19] Q.H. Pan. Application of beryllium copper in automotive industry, *Automobile Technology & material* 6 (2003) 9–14.
- [20] J. A. Bares, N. Argibay, *et al.* High current density copper-on-copper sliding electrical contacts at low sliding velocities, *Wear* 267 (2009) 417–424.
- [21] World Health Organization: Copper in drinking-water, Background document for development of WHO Guidelines for Drinking-water Quality, WHO/SDE/WSH/03.04/88.
- [22] V. F. Lucey, Mechanism of pitting corrosion of copper in supply waters, *British Corrosion Journal* 2 (1967) 175–185.
- [23] M. A. Edwards, T. E. Meyer, *et al.*, Role of inorganic anions, NOM, and water treatment processes in copper corrosion, AWWARF, Denver, USA, 1996.
- [24] T.H. Merkel, H.J. Groß, *et al.*, Copper corrosion by-product release in long-term stagnation experiments, *Water Research* 36 (2002) 1547–1555.
- [25] R.A. Isaac, L. Gil, *et al.*, Corrosion in drinking water distribution systems: a major contributor of copper and lead to wastewaters and effluents. *Environmental science & technology* 31(1997) 3198–3203.
- [26] N. Boulay, M. Edwards, Role of temperature, chlorine, and organic matter in copper corrosion by-product release in soft water, *Water research* 35 (2001) 683–690.
- [27] M. Fabbicino, Copper release in drinking water due to internal corrosion of distribution pipes, *Global NEST Journal* 7 (2005) 163–171.
- [28] W. Xiao, S. Hong, *et al.*, Effects of blending on surface characteristics of copper corrosion products in drinking water distribution systems, *Corrosion science* 49 (2007) 449–468.
- [29] A.E. Broo, B. Berghult, T. Hedberg, Copper corrosion in water distribution systems - the influence of natural organic matter (NOM) on the solubility of copper corrosion products, *Corrosion science* 40 (1998) 1479–1489.
- [30] M. Edwards, J.F. Ferguson, S.H. Reiber, The pitting corrosion of copper, *Journal of the American Water Works Association*, 86(1994) 74–90.
- [31] M. Edwards, T. Meyer, J. Rehring, Effect of selected anions on copper corrosion rates, *Journal of the American Water Works Association* 86(1994) 73–81.

- [32] A.E. Broo, B. Berghult, T. Hedberg, Copper corrosion in drinking water distribution systems - the influence of water quality, *Corrosion Science* 39 (1997) 1119–1132.
- [33] H.P.K. Andrew, Y.Y. Macauley. Corrosion and leaching of copper tubing exposed to chlorinated drinking water, *Water, Air, and Soil Pollution* 108 (1998) 457–471.
- [34] J.H. Michel, I. Richardson, *et al.*, Development of copper alloys for seawater service from traditional application to state-of-the art engineering, *CORROSION 2017*. NACE International, 2017.
- [35] L.O. Werme, P. Sellin and N. Kjellbert, Copper canisters for nuclear high level waste disposal: corrosion aspects, *Svensk kärnbränslehantering* (1992) 1–30.
- [36] W.A. Lanford, P.J. Ding, *et al.*, Alloying of copper for use in microelectronic metallization, *Materials Chemistry and Physics* 41(1995) 192–198.
- [37] G. Hultquist, L. Gråsjö, Q. Lu, T. Åkermark. The analysis of gas consumption in the reaction of Fe and Cu in $\text{H}_2^{16}\text{O}/\text{H}_2^{18}\text{O}/\text{O}_2$ gas mixtures, *Corrosion Science* 36 (1994) 1459–1471.
- [38] T.M.H. Saber, A.A.E. Warraky, Electrochemical and spectroscopic studies on dezincification of α brass: Part 1: Effect of pretreatment on surface composition of 70-30 α brass, *Corrosion Engineering, Science and Technology* 26 (1991) 279–285.
- [39] D. Landolt, *Corrosion et chimie de surfaces des métaux*. (Reimpression corrigée). Lausanne: Presse Polytechniques et Universitaires Romandes, 1997, pp 28–29.
- [40] A. Palit and S.O. Pehkonen, Copper corrosion in distribution systems: evaluation of a homogeneous Cu_2O film and a natural corrosion scale as corrosion inhibitors, *Corrosion Science* 42 (2000) 1801–1822.
- [41] Y. Lu, H. Xu, J. Wang and X. Kong, Oxygen reduction mechanism on copper in a 0.5 M H_2SO_4 , *Electrochimica Acta* 54 (2009) 3972–3978.
- [42] N. Birbilis, M.K. Cavanaugh and R.G. Buchheit, Electrochemical behavior and localized corrosion associated with $\text{Al}_7\text{Cu}_2\text{Fe}$ particles in aluminum alloy 7075-T651, *Corrosion Science* 48 (2006) 4202–4215.
- [43] H.M. Obispo, L.E. Murr, R.M. Arrowood and E.A. Trillo, Copper deposition during the corrosion of aluminum alloy 2024 in sodium chloride solutions, *Journal of Materials Science* 35 (2000) 3479–3495
- [44] W. Qafsaoui, M.W. Kendig, H. Perrot and H. Takenouti, Coupling of electrochemical techniques to study copper corrosion inhibition in 0.5 mol l^{-1} NaCl by 1-pyrrolidine dithiocarbamate. *Electrochimica Acta* 87 (2013) 348–360.
- [45] O. Gharbi, N. Birbilis and K. Ogle, *In-situ* monitoring of alloy dissolution and residual film formation during the pretreatment of Al-alloy AA2024-T3, *Journal of The Electrochemical Society* 163 (2016) C240–C251.

- [46] G. Hultquist, Hydrogen evolution in corrosion of copper in pure water, *Corrosion Science* 26 (1986) 173–177.
- [47] G. Hultquist, Why copper may be able to corrode in pure water, *Corrosion Science* 93 (2015) 327–329
- [48] C. Cleveland, S. Moghaddam and M.E. Orazem, Nanometer-scale corrosion of copper in de-aerated deionized water, *Journal of The Electrochemical Society* 161 (2014) C107–C114.
- [49] G. Hultquist, P. Szak los, *et al.*, Water corrodes copper, *Catalysis Letters* 132(2009) 311–316.
- [50] (a) J. P. Simpson and R. Schenk, Hydrogen evolution from corrosion of pure copper, *Corrosion Science* 27 (1987) 1365–1370; (b) T.E. Eriksen, P. Ndalamba and I. Grenthe, On the corrosion of copper in pure water, *Corrosion science* 29 (1989) 1241–1250; (c) L.O. Werme and P.A. Korzhavyi, Comment on Hultquist *et al.* ‘Water Corrodes Copper’ [*Catal. Lett.* 132(2009)311]”, *Catalysis Letters* 135 (2010) 165–166.
- [51] T. Aastrup, M. Wadsak, M. Schreiner and C. Leygraf, Experimental *in situ* studies of copper exposed to humidified air, *Corrosion Science* 42 (2000) 957–967.
- [52] (a) D. G. Ives and A. E. Rawson, Copper corrosion: I. thermodynamic aspects. *Journal of The Electrochemical Society* 109 (1962) 452–457; (b) Copper corrosion: II. kinetic studies, *ibid*, 458–462; (c) Copper Corrosion: III. Electrochemical theory of general corrosion, *ibid*, 462–466.
- [53] U. Collisi and H.H. Strehblow, A photoelectrochemical study of passive copper in alkaline solutions, *Journal of Electroanalytical Chemistry* 210 (1986) 213–227.
- [54] U. Collisi and H.H. Strehblow, The formation of Cu₂O layers on Cu and their electrochemical and photoelectrochemical properties, *Journal of Electroanalytical Chemistry* 335 (1990) 55–65.
- [55] Y. Feng, K.S. Siow, *et al.*, Corrosion mechanisms and products of copper in aqueous solutions at various pH values, *Corrosion* 53(1997) 389–398.
- [56] J.M. Bastidas, A. Lopez-Delgado, *et al.*, Copper corrosion mechanism in the presence of formic acid vapor for short exposure times, *Journal of the Electrochemical Society* 147 (2000) 999–1005.
- [57] Y. Feng, W.K. Teo, *et al.*, The corrosion behavior of copper in neutral tap water part I: corrosion mechanisms. *Corrosion Science* 38 (1996) 369–385.
- [58] T. Hurlen, Dissolution of cuprous chloride in acid chloride solution. *Acta Chemica Scandinavica* 16 (1962) 279–282.
- [59] T. Hurlen, Film growth on copper in acidified cupric chloride solutions. *Acta Chemica Scandinavica* 15 (1961) 1246–4254.

- [60] H. Lal and H.R. Thirsk, The anodic behavior of copper in neutral and alkaline chloride solutions, *Journal of the Chemical Society* 538 (1953) 2638–2644
- [61] J.R. Davis, *ASM specialty handbook-copper and copper alloys*. ASM International, 2001: Materials Park, Ohio.
- [62] S.L. Chawla and R.K. Gupta, *Materials selection for corrosion control*, 1st ed. ASM International, 1993 Materials Park, Ohio.
- [63] P. Vanysek, Electrochemical series in W.M. Haynes “*CRC Handbook of Chemistry and Physics*”, 91th ed., CRC Press, 2010.
- [64] L. Burzynska, Comparison of the spontaneous and anodic processes during dissolution of brass, *Corrosion Science* 43 (2001) 1053–1069.
- [65] R.K. Dinnappa and S.M. Mayanna, The dezincification of brass and its inhibition in acidic chloride and sulphate solutions, *Corrosion Science* 27(1987) 349–361.
- [66] Q. Liu, H. Luo, *et al.*, The electrochemical behavior of brass in NaHSO₃ solution without and with Cl⁻. *International Journal of Electrochemical Science* 7 (2012) 11123–11136.
- [67] L. Yohai, W.H. Schreiner, M. Vázquez and M.B. Valcarce, Surface characterization of copper, zinc and brass in contact with tap water inhibited with phosphate ions, *Applied Surface Science* 257 (2011) 10089–10095.
- [68] E.E. Langenegger, F.P.A. Robinson, A study of the mechanism of dezincification of brases, *Corrosion* 25 (1969) 59–66.
- [69] R.M. Horton, New Metallographic Evidence for dezincification of brass by redistribution of copper, *Corrosion* 26 (1970) 260–264.
- [70] R. Natarajan, P.C. Angelo, N.T. George, R.V. Tamhankar, Dezincification of cartridge brass, *Corrosion* 31 (1975) 302–304.
- [71] A.J. Forty, Corrosion micromorphology of noble metal alloys and depletion gilding, *Nature* 282 (1979) 597–598.
- [72] A.J. Forty, G. Rowlands, A possible model for corrosion pitting and tunneling in noble-metal alloys. *Philosophical Magazine A*, 43 (1981) 171–188.
- [73] I. McCue, E. Benn, B. Gaskey, J. Erlebacher, Dealloying and dealloyed materials, *Annual Review of Materials* 46 (2016) 263–286.
- [74] G.T. Burstein, G. Gao, The first stages of dezincification of freshly generated brass surfaces in sulfuric acid solution, *Journal of The Electrochemical Society*, 141 (1994) 912–921.
- [75] H.W. Pickering. Volume diffusion during anodic dissolution of a binary alloy, *Journal of the Electrochemical Society* 115 (1968) 143–147.

- [76] L. Yao, W. Qiu, F. Gan, H. Guo, On the volume diffusion mechanism during dezincification of brass, *Corrosion Science and Protection technique* 4 (1992) 217–222. (in Chinese)
- [77] J.Y. Zou, D.H. Wang, W.C. Qiu, Solid-state diffusion during the selective dissolution of brass: chronoamperometry and positron annihilation study, *Electrochimica Acta* 42 (1997) 1733–1737.
- [78] W.C. Fort, Mechanisms and inhibition of dealloying in an alpha brass, Ph.D. dissertation, University of Florida, 1975.
- [79] J. Laurent, D. Landolt, Time dependent selective dissolution of gold-copper alloys at sub-critical potentials, *Materials Science Forum* 44-45 (1989) 213-222.
- [80] J. Laurent, D. Landolt, Anodic dissolution of binary single phase alloys at subcritical potential. *Electrochimica Acta* 36 (1991) 49–58.
- [81] K. Sieradzki, R.R. Corderman, K. Shukla and R.C. Newman, Computer simulations of corrosion: selective dissolution of binary alloys. *Philosophical Magazine A* 59 (1989) 713–746.
- [82] C. Berne, E. Andrieu, *et al.*, Dissolution kinetics of α , β' -brass in basic NaNO_3 solutions. *Journal of The Electrochemical Society* 163 (2016) C7–C15.
- [83] R.W. Revie, H.H. Uhlig, An introduction to corrosion science and engineering, 4th Ed., John Wiley & Sons, Inc., Hoboken, NJ, USA, 2008
- [84] R.W. Cahn, Percolation frustrated, *Nature* 389 (1997) 121–122.
- [85] J. Wang, X. Jiang, S. Li, Synergistic mechanism of boron and arsenic in preventing dezincification of brass, *Chinese Science Bulletin* 42 (1997) 1135–1139.
- [86] K.R. Trethewey, I. Pinwill, The dezincification of free-machining brasses in sea water, *Surface and Coatings Technology* 30 (1987) 289–307.
- [87] R.H. Heidersbach, E.D. Verinkm, The dezincification of alpha and beta brasses, *Corrosion* 28 (1972) 397–418.
- [88] J.C. Rubim, Surface enhanced Raman scattering (SERS) from benzotriazole adsorbed on brass electrodes, *Chemical Physics Letters* 167 (1990) 209–214.
- [89] P. Qiu, C. Leygraf, Initial oxidation of brass induced by humidified air, *Applied Surface Science* 258 (2011) 1235–1241.
- [90] B.S. Kim, T. Piao, S.N. Hoier, S.M. Park, *In situ* spectro-electrochemical studies on the oxidation mechanism of brass, *Corrosion Science* 37 (1995) 557–570.
- [91] M.B. Valcarce, S.R. de Sanchez, M. Vazquez, A comparative analysis of copper and brass surface films in contact with tap water, *Journal of Materials Science* 41 (2006) 1999–2007.

- [92] M.B. Valcarce, S.R. de Sanchez, M. Vazquez, Brass dezincification in a tap water bacterial suspension, *Electrochimica Acta* 51 (2006) 3736–3742.
- [93] S.M. Awadh, F.M.A. Kharafi, B.G. Ateya, Selective dissolution of alpha brass in acid non-complexing media, *Journal of the Electrochemical Society* 156 (2009) C114–C121.
- [94] K. Satendra, T.S.N. Sankara Narayanan, M. Suresh Kumar, A. Manimaran, Dezincification of brass in sulfide polluted sodium chloride medium: evaluation of the effectiveness of 2-mercaptobenzothiazole, *International Journal of Electrochemical Science* 1 (2006) 456–469.
- [95] Y. Hoshi, T. Oda, I. Shitanda and M. Itagaki, Real-time surface observation of copper during anodic polarization with channel flow double electrode, *Journal of the Electrochemical Society* 164 (2017) C450–C452.
- [96] Y. Hoshi, M. Itagaki, K. Tabeisao and I. Shitanda, Anodic dissolution of brass and dezincing-resistant brass investigated using channel flow double electrode, *Journal of Solid State Electrochemistry* 19 (2015) 3551–3557.
- [97] R. Cerrato, A. Casal, *et al.*, Dealloying evidence on corroded brass by laser-induced breakdown spectroscopy mapping and depth profiling measurements, *Spectrochimica Acta Part B: Atomic Spectroscopy* 130 (2017) 1–6.
- [98] V.F. Lucey, The mechanism of dezincification and the effect of arsenic. I, *British Corrosion Journal* 1 (1965) 9–14.
- [99] V.F. Lucey, The mechanism of dezincification and the effect of arsenic. II, *British Corrosion Journal* 1 (1965) 53–59.
- [100] F. Can, J. Zou, L. Yao, A study of the mechanism of dezincification of $\alpha+\beta$ bi-phase brass(II), *Journal of Chinese Society for Corrosion and Protection*, 03 (1983) 217–223.
- [101] H.H.A. Dollwet and J.R.J. Sorenson, Historic uses of copper compounds in medicine, *Trace elements in Medicine*, 2 (1985), 80–87.
- [102] G. Grass, C. Rensing and M. Solioz, Metallic copper as an antimicrobial surface, *Applied and environmental microbiology* 77 (2011) 1541–1547.
- [103] P.J. Kuhn, Doorknobs: a source of nosocomial infection? Copper Development Association, 1983, New York, NY. <http://www.copperinfo.co.uk/antimicrobial/downloads/kuhn-doorknob.pdf>.
- [104] V.B.P Sudha, K.O. Singh, S.R. Prasad, and P. Venkatasubramanian, Killing of enteric bacteria in drinking water by a copper device for use in the home: laboratory evidence, *Transactions of The royal society of tropical Medicine and Hygiene*, 103 (2009) 819–822.
- [105] US Environment Protection Agency, Office of Pesticide Program, Copper facts, 2008.
- [106] K. Helbig, C. Bleuel, G. J. Krauss, and D.H. Nies. Glutathione and transition-metal homeostasis in *Escherichia coli*. *Journal of Bacteriology*, 190 (2008) 5431–5438

- [107] D. Schomburg and M. Salzmann, Dihydroxy-acid dehydratase In *Enzyme Handbook 1*. Springer Berlin Heidelberg, 1990, pp 617-621
- [108] G.B. Kohlhaw, β -Isopropylmalate dehydrogenase from yeast. *Methods in enzymology*, 166 (1988) 429–435.
- [109] O. Yogev, A. Naamati, and O. Pines, Fumarase: a paradigm of dual targeting and dual localized functions, *The FEBS Journal* 278 (2011) 4230–4242.
- [110] W.T. Blevins, T.W. Feary, P.V. Phibbs, 6-Phosphogluconate dehydratase deficiency in pleiotropic carbohydrate-negative mutant strains of *Pseudomonas aeruginosa*, *Journal of bacteriology* 121 (1975) 942–949.
- [111] C. Manzl, J. Enrich, H. Ebner, R. Dallinger, G. Krumschnabel, Copper-induced formation of reactive oxygen species causes cell death and disruption of calcium homeostasis in trout hepatocytes, *Toxicology*, 196 (2004) 57–64..
- [112] B. Halliwell and J.M. Gutteridge. Toxicité de l'oxygène, des radicaux d'oxygène, des métaux de transition et les maladies, *Biochemical Journal*, 219 (1984) 1–14.
- [113] B. Halliwell and J.M. Gutteridge, Le rôle des radicaux libres et des ions métalliques catalytiques dans les maladies humaines: une vue d'ensemble. *Methods in Enzymology*, 186 (1990) 1–85.
- [114] E.R. Stadtman, oxydation des protéines et le vieillissement, *Sciences* 257 (1992) 1220–1224.
- [115] L. Yohai, M. Vázquez, M.B. Valcarce. Brass corrosion in tap water distribution systems inhibited by phosphate ions, *Corrosion Science* 53 (2011) 1130–1136.
- [116] L. Yohai, W.H. Schreiner, M. Vázquez, M.B. Valcarce, Surface characterization of copper, zinc and brass in contact with tap water inhibited with phosphate ions, *Applied Surface Science* 257 (2011) 10089–10095.
- [117] G. M. Ingo, E. Angelini, *et al.*, Study of long-term corrosion layers grown on high-tin leaded bronzes by means of the combined use of GDOES and SEM+ EDS, *Surface and interface analysis* 34 (2002) 337–342.
- [118] K. Ogle, S. Weber, Anodic dissolution of 304 stainless steel using atomic emission spectro-electrochemistry, *Journal of the Electrochemical Society* 147 (2000) 1770–1780.
- [119] J. Świątowska, P. Volovitch, K. Ogle, The anodic dissolution of Mg in NaCl and Na₂SO₄ electrolytes by atomic emission spectroelectrochemistry, *Corrosion Science* 52 (2010) 2372–2378
- [120] A. Stáhlavská The use of spectrum analytical methods in drug analysis. 1. Determination of alkaline metals using emission flame photometry, *Pharmazie* (in German), 28 (1973) 238–239.

- [121] K. Ogle, J. Baeyens, J. Swiatowska, P. Volovitch, Atomic emission spectroelectrochemistry applied to dealloying phenomena: I. The formation and dissolution of residual copper films on stainless steel, *Electrochimica Acta* 54 (2009) 5163–5170
- [122] B. Laurent, N. Gruet, *et al.*, A direct measurement of the activation potential of stainless steels in nitric acid, *Journal of The Electrochemical Society* 164 (2017) C481–C487
- [123] K. Ogle, S. Morel, N. Meddahi, An electrochemical study of the delamination of polymer coatings on galvanized steel, *Corrosion science* 47 (2005) 2034–2052
- [124] O. Gharbi, N. Birbilis, K. Ogle, Li reactivity during the surface pretreatment of Al-Li alloy AA2050-T3, *Electrochimica Acta* 243 (2017) 207–219
- [125] T.J. Manning, W.R. Grow, Inductively coupled plasma–atomic emission spectrometry, *The Chemical Educator*, Springer-Verlag New York, Inc. 2 (1997) pp 1-19.
- [126] V. Shkirskiy, P. Marciel, J. Deconinck, K. Ogle, On the time resolution of the atomic emission spectroelectrochemistry method, *Journal of electrochemical society* 163 (2016) C1–C8.
- [127] H. Cong, H.T. Michels, J.R. Scully, Passivity and pit stability behavior of copper as a function of selected water chemistry variables, *Journal of the Electrochemical Society* 156 (2009) C16–C27.
- [128] E. Mattsson, Counteraction of pitting in copper water pipes by bicarbonate dosing, *Materials and Corrosion* 39 (1988) 499–503.
- [129] M. Drogowska, L. Brossard H. Ménard, Influence of anions on the passivity behavior of copper in alkaline solutions, *Surface and Coatings Technology* 34 (1988) 383–400.
- [130] G. Schmitt, P. Plagemann, E. Slavcheva, ECN-measurements at copper in artificial tap water - Investigation of anion-effects. *Materials and Corrosion* 52 (2001) 439–444.
- [131] Y.P. Feng, S.K. Sinha, C.A. Melendres, D.D. Lee, X-ray off-specular reflectivity studies of electrochemical pitting of Cu surfaces in sodium bicarbonate solution, *Physica B: Condensed Matter* 221 (1996) 251–256.
- [132] S.A. Imran, J.D. Dietz, G. Mutoti, J.S. Taylor, A.A. Randall, Modified Larsons ratio in incorporating temperature, water age, and electroneutrality effects on red water release, *Journal of Environmental Engineering* 131 (2005) 1514–1520.
- [133] E.J. Singley, The search for a corrosion index, *Journal of American Water Works Association* 73 (1981) 579–582.
- [134] J.R. Rossum, T.M. Douglas, An evaluation of the calcium carbonate saturation indexes, *Journal of American Water Works Association* 75 (1983) 95–100.
- [135] E. Sarver, K. Dodson, *et al.*, Copper pitting in chlorinated, high-pH potable water, *Journal of American Water Works Association* 103 (2011) 86–98.

- [136] H. Cong, J.R. Scully, Effects of aluminum solids on the under deposit corrosion of copper in synthetic potable water: the arguments for and against a semi-permeable membrane. *Journal of the Electrochemical Society* 160 (2013) C403–C413.
- [137] M. Drogowska, L. Brossard, H. Ménard, Copper Dissolution in NaHCO_3 and $\text{NaHCO}_3 + \text{NaCl}$ Aqueous Solutions at pH 8, *Journal of Electrochemical Society* 139 (1992) 39–47.
- [138] S. Nakayama, Mechanistic study by electrochemical impedance spectroscopy on reduction of copper oxides in neutral solutions, *SEI Technical Review* (2009) 62–68.
- [139] P. Szakalos, G. Hultquist, G. Wikmark, Corrosion of copper by water, *Electrochemical and Solid-State Letters* 10 (2007) C63–C67.
- [140] G. Hultquist, P. Szakalos, *et al.*, Detection of hydrogen in corrosion of copper in pure water. In *International Corrosion Congress* (2008) paper No. 3884.
- [141] T.E. Eriksen, P. Ndalamba, I. Grenthe, On the corrosion of copper in pure water, *Corrosion Science* 29 (1989) 1241–1250.
- [142] S. Jacobs, M. Edwards, Sulfide scale catalysis of copper corrosion, *Water Research* 34 (2000) 2798–2808.
- [143] C. Ackfeld, O. von Franqué W. Siedlarek. Electrochemical potential measurements of commercial copper tubes with different surfaces, *Materials and Corrosion* 1997 (48) 624–630.
- [144] K. Ogle. Atomic emission spectroelectrochemistry: a new look at the corrosion, dissolution and passivation of complex materials. *EuroCorr 2011*, Stockholm, Sweden, (2011) 60–67.
- [145] J. Lin, M.Z. Liu, Detergent for steel, aluminium and copper materials, CN1101950 (A) (1995) (in Chinese).
- [146] F. Seuss, N. Gaag, S. Virtanen, Corrosion mechanism of CuZn21Si3P in aggressive tap water, *Materials and Corrosion* (2016) DOI: 10.1002/maco.201609018.
- [147] H. Sugawara, H. Ebiko, Dezincification of Brass, *Corrosion Science* 7 (1967) 513–523.
- [148] H. Lu, K.W. Gao, W.Y. Chu, Determination of tensile stress induced by dezincification layer during corrosion for brass, *Corrosion Science* 40 (1998) 1663–1670.
- [149] H.W. Pickering, P.J. Byrne, On preferential anodic dissolution of alloys in the low-current region and the nature of the critical potential, *Journal of the Electrochemical Society* 118 (1971) 209–215.
- [150] H.W. Pickering, Electrolytic dissolution of binary alloys containing a noble metal, *Journal of the Electrochemical Society* 114 (1967) 698–706.
- [151] B. Assouli, A. Srhiri, and H. Idrissi, Characterization and control of selective corrosion of α , β' -brass by acoustic emission, *NDT & E International* 36 (2003) 117–126.

- [152] R.C. Newman, T. Shahrabi, K. Sieradzki, Direct electrochemical measurement of dezincification including the effect of alloyed arsenic, *Corrosion science* 28 (1988) 873–886.
- [153] T.L. Barr, J.J. Hackenberg, Determination of the onset of the dezincification of alpha-brass using x-ray photoelectron (ESCA) spectroscopy, *Journal of the American Chemical Society* 104 (1982) 5390–5394.
- [154] Y.M. Kolotyркиn, Use of radioactive indicator and electrochemical methods for determining low corrosion rates, *Electrochimica Acta* 18 (1973) 593–606.
- [155] P. Zhou, M. J. Hutchison, J.R. Scully, K. Ogle, The anodic dissolution of copper alloys: Pure copper in synthetic tap water, *Electrochimica Acta* 191 (2016) 548–557.
- [156] C. Nobel, F. Klocke, D. Lung, S. Wolf, Machinability enhancement of lead-free brass alloys, *Procedia CIRP* 14 (2014) 95-100.
- [157] C. Nobel, U. Hofmann, F. Klocke, D. Veselovac, H. Puls, Application of a new, severe-condition friction test method to understand the machining characteristics of Cu-Zn alloys using coated cutting tools, *Wear* 344 (2015) 58–68.
- [158] E. Brandl, R. Malke, T. Beck, A. Wanner, T. Hack, Stress corrosion cracking and selective corrosion of copper-zinc alloys for the drinking water installation, *Materials and Corrosion* 60 (2009) 251–258.
- [159] M.A. Taha, T.M. Mousa, R.M. Hamouda, A.F.A.G. Yousef, Microstructure and castability of lead-free silicon brass alloys. *Materialwissenschaft und Werkstofftechnik* 43 (2012) 699–704.
- [160] C. Ackfeld, O. von Franqu é W. Siedlarek, Elektrochemische untersuchungen von handels üblichen kupferrohren mit verschiedenen oberfl ächenzust änden, *Materials and Corrosion* 48 (1997) 624–630. (in German)
- [161] International Organization for Standardization, ISO 6509-1: 2014, Corrosion of metals and alloys - Determination of dezincification resistance of copper alloys with zinc - Part 1: Test method, 2014.
- [162] International Organization for Standardization, ISO 6509-1: 2014, ISO 6509-2, Corrosion of metals and alloys — Determination of dezincification resistance of copper alloys with zinc - Part 2: Acceptance criteria, 2014.
- [163] K. Ogle, M. Mokaddem, P. Volovitch, Atomic emission spectroelectrochemistry applied to dealloying phenomena II. Selective dissolution of iron and chromium during active-passive cycles of an austenitic stainless steel, *Electrochimica Acta* 55 (2010) 913–921.
- [164] J.C. Hamilton, J.C. Farmer, R.J. Anderson, *In situ* Raman spectroscopy of anodic films formed on copper and silver in sodium hydroxide solution, *Journal of the Electrochemical Society* 133 (1986) 739–745.

- [165] M. Biton, G. Salitra, D. Aurbach, P. Mishkov, D. Ilzyer, On the electrochemical behavior and passivation of copper and brass (Cu70/Zn30) electrodes in concentrated aqueous KOH solutions, *Journal of the Electrochemical Society* 153 (2006) B555–B565.
- [166] F. Ospitali, C. Chiavari, C. Martini, E. Bernardi, F. Passarini, L. Robbiola, The characterization of Sn-based corrosion products in ancient bronzes: a Raman approach, *Journal of Raman Spectroscopy* 43 (2012) 1596–1603.
- [167] P.L. Kazansky, Y.E. Pronin, I.A. Arkhipushkin, XPS study of adsorption of 2-mercapto benzothiazole on a brass surface, *Corrosion Science* 89 (2014) 21–29.
- [168] M.H. Saber; A.A. El Warraky, Electrochemical and spectroscopic studies on dezincification of α -brass Part II. Effect of polarization on the dezincification process, *Desalination* 93 (1993) 473–486
- [169] L.B. Railsback. *Some Fundamentals of Mineralogy and Geochemistry*. Georgia, 2006.
- [170] N.T. Rochman, K. Yamada, R. Fujimoto, S.I. Suehiro, H. Sueyoshi, Effects of microstructural factors and alloying elements on dezincification of brass, *Journal of Advanced Science* 13 (2001) 277–280.
- [171] G. Joseph, M.T. Arce, Contribution to the study of brass dezincification, *Corrosion Science* 7 (1967) 597–605.
- [172] J.E. Holliday, H.W. Pickering, A Soft X-Ray Study of the Near Surface Composition of Cu₃₀Zn Alloy during Simultaneous Dissolution of Its Components, *Journal of the Electrochemical Society* 120 (1973) 470–475.
- [173] B.G. Atey, H.W. Pickering, The effects of potential and kinetic parameters on the formation of passivating noble metal rich surface layers during the selective dissolution of binary alloys, *Corrosion Science* 38 (1996) 1245–1267.
- [174] M.L. Carvalho. *Corrosion of copper alloys in natural seawater: effects of hydrodynamics and pH*. Ph.D. dissertation, Université Pierre et Marie Curie - Paris VI, 2014.
- [175] R. Cerrato, A. Casal, M. P. Mateo, *et al.*, Dealloying evidence on corroded brass by laser-induced breakdown spectroscopy mapping and depth profiling measurements, *Spectrochimica Acta Part B: Atomic Spectroscopy* 130 (2017) 1–6.
- [176] P. Zhou, M. J. Hutchison, J.W. Erning, J. R. Scully, K. Ogle. An *in situ* kinetic study of brass dezincification in synthetic tap water, *Electrochimica Acta* 229 (2017) 141–154.
- [177] M.J. Hutchison, P. Zhou, K. Ogle, J.R. Scully, Enhanced Electrochemical Cu Release from Commercial Cu-Sn Alloys: Fate of the Alloying Elements in Artificial Perspiration, *Electrochimica Acta* 241 (2017) 73–88.
- [178] A. Nawaz, K.M. Deen, A. Farooq, R. Ahmed, Investigating the electrochemical behavior of α brass in acidic and alkaline tap water. *Materials Today: Proceedings* 2 (2015) 5170–5176.

- [179] R.M. El-Sherif, K.M. Ismail, W.A. Badawy. Effect of Zn and Pb as alloying elements on the electrochemical behavior of brass in NaCl solutions. *Electrochimica Acta* 49 (2004) 5139–5150.
- [180] D.J.G. Ives, and A.E. Rawson, Copper corrosion I. Thermodynamic aspects, *Journal of The Electrochemical Society* 109 (1962) 447–451.
- [181] H.E. Troiani, J.L. Pelegrina, M. Ahlers, The dezincification of α -Cu-Zn. *Physica Status Solidi (a)*, 156 (1996) 93–106.
- [182] E.V. Koroleva, G.E. Thompson, P. Skeldon and B. Noble, Crystallographic dissolution of high purity aluminum, *Proceedings of the Royal Society. A.* 463 (2007) 1729–1748
- [183] A. Shahryari, S. Orriano, The influence of crystallographic orientation distribution on 316LVM stainless steel pitting behavior, *Corrosion Science* 51 (2009).
- [184] K. Fushimi, K. Miyamoto, H. Konno, Anisotropic corrosion of iron in pH 1 sulphuric acid, *Electrochimica Acta* 55 (2010) 7322–7327.
- [185] A. Schreiber, C. Rosenkranz, M.M. Lohrengel Grain-dependent anodic dissolution of iron, *Electrochimica Acta* 52 (2007) 7738–7745.
- [186] B. Holme, N. Ljones, A. Bakken, O. Lunder, J.E. Lein, L. Vines, T. Hauge, Ø. Bauger and K. Nisancioglu, Preferential grain etching of AlMgSi(Zn) model alloys, *Journal of the Electrochemical Society* 157 (2010) C424–C427.
- [187] L. Bland, K. Gusieva, J.R. Scully, Effect of crystallographic orientation on the corrosion of magnesium: comparison of film forming and bare crystal facets using electrochemical impedance and raman spectroscopy, *Electrochimica Acta* 227 (2017) 136–151.
- [188] M. Nolan, S.D. Elliott, The p-type conduction mechanism in Cu₂O: a first principles study. *Physical Chemistry Chemical Physics* 8 (2006) 5350–5358.
- [189] G. Grass, C. Rensing, M. Solioz, Metallic Copper as an Antimicrobial Surface, *Appl. Environ. Microbiol* 77 (2011) 1541–1547.
- [190] H.T. Michels, J.O. Noyce, C.W. Keevil, Effects of temperature and humidity on the efficacy of methicillin-resistant *Staphylococcus aureus* challenged antimicrobial materials containing silver and copper, *Lett. Appl. Microbiol.* 49 (2009) 191–195.
- [191] J.O. Noyce, H. Michels, C.W. Keevil, Potential use of copper surfaces to reduce survival of epidemic methicillin-resistant *Staphylococcus aureus* in the healthcare environment, *J. Hosp. Infect.* 63 (2006) 289–297.
- [192] S. Mehtar, I Wiid, S. D. Todorov, The antimicrobial activity of copper and copper alloys against nosocomial pathogens and *Mycobacterium tuberculosis* isolated from healthcare facilities in the Western Cape: an in-vitro study. *J. Hosp. Infect.* 68 (2008) 45-51.

- [193] J. Elguindi, J. Wagner, C. Rensing, Genes involved in copper resistance influence survival of *Pseudomonas aeruginosa* on copper surfaces. *J. Appl. Microbiol.* 106 (2009) 1448–1455.
- [194] G. Faúndez, M. Troncoso, P. Navarrete, G. Figueroa, Antimicrobial activity of copper surfaces against suspensions of *Salmonella enterica* and *Campylobacter jejuni*. *BMC Microbiol.* 4 (2004) 19.
- [195] J. O. Noyce, H. Michels, C.W. Keevil. Potential use of copper surfaces to reduce survival of epidemic methicillin-resistant *Staphylococcus aureus* in the healthcare environment. *J. Hosp. Infect.* 63 (2006) 289–297.
- [196] J. O. Noyce, H. Michels, C.W. Keevil. Use of copper cast alloys to control *Escherichia coli* O157 cross-contamination during food processing. *Appl. Environ. Microbiol.* 72 (2006) 4239–4244.
- [197] L. Weaver, H. T. Michels, C. W. Keevil, Survival of *Clostridium difficile* on copper and steel: futuristic options for hospital hygiene. *J. Hosp. Infect.* 68 (2008) 145–151.
- [198] S.A. Wilks, H.T. Michels, C.W. Keevil. Survival of *Listeria monocytogenes* Scott A on metal surfaces: implications for cross-contamination. *Int. J. Food Microbiol.* 111 (2006) 93–98.
- [199] D.J. Horton, H. Ha, L.L. Foster, H.J. Bindig, J.R. Scully, Tarnishing and Cu Ion release in Selected Copper-Base Alloys: Implications towards Antimicrobial Functionality, *Electrochimica Acta* 169 (2015) 351–366.
- [200] D. Quaranta, T. Krans, C.E. Santo, C.G. Elowsky, D.W. Domaille, C.J. Chang, G. Grass, Mechanisms of Contact-Mediated Killing of Yeast Cells on Dry Metallic Copper Surfaces, *Appl. Environ. Microbiol.* 77 (2011) 416–426
- [201] C.E. Santo, E.W. Lam, C.G. Elowsky, D. Quaranta, D.W. Domaille, C.J. Chang, G. Grass, Bacterial Killing by Dry Metallic Copper Surfaces, *Appl. Environ. Microbiol.* 77 (2011) 794–802.
- [202] D. Quaranta, T. Krans, C. E. Santo, C. G. Elowsky, D. W. Domaille, C. J. Chang, G. Grass, Mechanisms of Contact-Mediated Killing of Yeast Cells on Dry Metallic Copper Surfaces, *Appl. Environ. Microbiol.* 77 (2011) 416–426.
- [203] BS EN. Reference test method for release of nickel from all post assemblies which are inserted into pierced parts of the human body and articles intended to come into direct and prolonged contact with the skin. London, United Kingdom: (2008) 1811.
- [204] I. Milošev, T. Kosec, Metal ion release and surface composition of the Cu–18Ni–20Zn nickel–silver during 30 days’ immersion in artificial sweat, *Appl. Surf. Sci.* 254 (2007) 644–652.
- [205] S. Caporali and U. Bardi, Corrosion Mechanism in artificial sweat solution of in-bearing white bronze alloy, *Corrosion*, 68 (2012) 025001-1–025001-8.

- [206] N. Fredj, J.S. Kolar, D.M. Prichard, T.D. Burleigh, Study of relative color stability and corrosion resistance of commercial copper alloys exposed to hand contact and synthetic hand sweat, *Corrosion Science*, 76 (2013) 415–423
- [207] S. Goidanich, I. Odnevall Wallinder, G. Herting, C. Leygraf, Corrosion induced metal release from copper based alloys compared to their pure elements, *Corros. Eng. Sci. Technol.* 43 (2008) 134–141.
- [208] L. Jiang, P. Volovitch, U. Sundermeier, M. Wolpers, K. Ogle, Dissolution and passive film formation of Sn and Sn coated steel using atomic emission spectroelectrochemistry, *Electrochimica Acta* 58(2011) 322–329
- [209] G. Herting, S. Goidanich, I.O. Wallinder, C. Leygraf, Corrosion-induced release of Cu and Zn into rainwater from brass, bronze and their pure metals. A 2-year field study, *Environ. Monit. Assess.* 144 (2008) 455–461.
- [210] X. Zhang, I. Odnevall Wallinder, C. Leygraf, Mechanistic studies of corrosion product flaking on copper and copper-based alloys in marine environments, *Corros. Sci.* 85 (2014) 15–25.
- [211] C. Debiemme-Chouvy, F. Ammeloot, E.M.M. Sutter, X-ray photoemission investigation of the corrosion film formed on a polished Cu–13Sn alloy in aerated NaCl solution, *Appl. Surf. Sci.* 174 (2001) 55–61
- [212] L. Robbiola, K. Rahmouni, C. Chiavari, C. Martini, D. Prandstraller, A. Texier, H. Takanouti, P. Vermaut, New insight into the nature and properties of pale green surfaces of outdoor bronze monuments, *Appl. Phys. A*. 92 (2008) 161–169.
- [213] M.C. Squarzialupi, G.P. Bernardini, V. Faso, A. Atrei, G. Rovida, Characterisation by XPS of the corrosion patina formed on bronze surfaces, *J. Cult. Herit.* 3 (2002) 199–204.
- [214] F. Ospitali, C. Chiavari, C. Martini, E. Bernardi, F. Passarini, L. Robbiola, The characterization of Sn-based corrosion products in ancient bronzes: a Raman approach, *Journal of the Raman Spectroscopy* 43 (2012) 1596–1603.
- [215] I. Milošev, T. Kosec, Metal ion release and surface composition of the Cu–18Ni–20Zn nickel–silver during 30 days’ immersion in artificial sweat, *Appl. Surf. Sci.* 254 (2007) 644–652
- [216] S. Colin, E. Beche, R. Berjoan, H. Jolibois, A. Chambaudet, An XPS and AES study of the free corrosion of Cu-, Ni- and Zn-based alloys in synthetic sweat, *Corros. Sci.* 41 (1999) 1051–1065.
- [217] M.C. Squarzialupi, G.P. Bernardini, V. Faso, A. Atrei, G. Rovida, Characterisation by XPS of the corrosion patina formed on bronze surfaces, *J. Cult. Herit.* 3 (2002) 199–204.
- [218] G. Masi, C. Chiavari, J. Avila, J. Esvan, S. Raffo, M.C. Bignozzi, M.C. Asensio, L. Robbiola, C. Martini, Corrosion investigation of fire-gilded bronze involving high surface resolution spectroscopic imaging, *Appl. Surf. Sci.* 366 (2016) 317–327.

- [219] C. Debiemme-Chouvy, F. Ammeloot, E.M.M. Sutter, X-ray photoemission investigation of the corrosion film formed on a polished Cu–13Sn alloy in aerated NaCl solution, *Appl. Surf. Sci.* 174 (2001) 55–61.
- [220] R. Walker, Aqueous Corrosion of Tin-Bronze and Inhibition by Benzotriazole, *Corrosion* 56 (2000) 1211–1219.
- [221] F. Ammeloot, C. Fiaud, E.M.M. Sutter, Characterization of the oxide layers on a Cu–13Sn alloy in a NaCl aqueous solution without and with 0.1 M benzotriazole. Electrochemical and photoelectrochemical contributions, *Electrochimica Acta* 44 (1999) 2549–2558.
- [222] S. Men and P. Licence, Probing the electronic environment of binary and ternary ionic liquid mixtures by X-ray photoelectron spectroscopy. *Chemical Physics Letters*. (2017) <https://doi.org/10.1016/j.cplett.2017.08.034>
- [223] B. Malki, S. Saedlou, I. Guillotte, B. Baroux, Ab Initio Monte Carlo Simulations of the Acidic Dissolution of Stainless Steels: Influence of the Alloying Elements, *J. Electrochem. Soc.* 163 (2016) C807–C814.
- [224] J.G. Speight, *Lange's Handbook of Chemistry: Bond Dissociation Energies*, New York: McGraw-Hill, 2005.
- [225] R. K. Thauer, Citric-acid cycle, 50 years on modifications and an alternative pathway in anaerobic bacteria. *The FEBS Journal* 176 (1988) 497–508.
- [226] J. C. Lin, J. Y. Lin, S. P. Jou, Selective dissolution of the cobalt binder from scraps of cemented tungsten carbide in acids containing additives. *Hydrometallurgy*, 43(1996) 47–61.